Biomaterials for Soft Tissue Applications

A Dissertation Presented for the

Doctor of Philosophy

Degree

The University of Tennessee, Knoxville

Alisha Potter Pedersen

May 2021

Dedication

No words can express the thanks in my heart for the support and encouragement of my mother, husband, family, friends, and precious mentors in my pursuit of seemingly unsurmountable goals and despite my frequent faithlessness and stubbornness. Yet, the greatest thanksgiving of all I extend to my Lord for His providential guidance that has granted me opportunities and blessings so far beyond what I deserve or could have imagined. To these, this culminating work is dedicated.

Acknowledgements

Having had the privilege to work alongside members of the Regenerative Medicine Team at the University of Tennessee College of Veterinary Medicine for nearly five years, I have as a result gained a wealth of experience and knowledge from a handful of individuals who so willingly share their wisdom and give of their time so that others can grow and succeed. My first and foremost recognition is extended to Dr. David Anderson, who not only gave me the first opportunity to be involved in research as a naïve veterinary student, but made possible a way for me to continue in that path upon making the decision to enroll in the dual-degree program. He has consistently been a great mentor to me and never fails to give advice as I need it. I also extend much appreciation to several other faculty and staff members who have served as great mentors to me over the past several years, whether in matters associated with my education or research: Drs. Linden Craig, Madhu Dhar, Pierre-Yves Mulon, Dustin Crouch, Stacy Stephenson, and Robert Donnell. Groupmates who have helped me immensely and whom I extend much gratitude to include Drs. Austin Bow, Rebecca Rifkin, and Remi Grzeskowiak; soon-to-be Drs. Steven Newby, Lisa Amelse, and Amber MacDonald; and the various COE and summer research students who have been temporary yet meaningful gems of our group. I especially thank Steven for his patience as he has taught me the ABC's of bioprinting and working with cells and materials, and Rebecca and Remi for those particularly difficult few days with the pigs (I needn't elaborate, just know they were nightmares). A special thanks is extended to our group technician, and my dear friend, Elizabeth Croy, for her constant willingness to help and the relief she imparts when we know that *she's* the one that prepared for a surgery day. Lastly, I give a sincere note of appreciation to Dr. Steven Kania and Kim Rutherford of the Comparative and Experimental Medicine Program, who have opened a great opportunity for me and have kept me on track to succeed.

Abstract

Biomaterial applications in the biomedical field have resulted in great advancements in the availability and efficacy of medical devices and therapeutic options for a host of conditions. Applications of biomaterials span all organ systems and tissue types, and have served a range of purposes including mechanical support, drug delivery, tissue regeneration, and reduction of surgical complications. Biomaterials are delineated by their ability to be utilized on or within the body with minimal-to-no adverse reaction and can be manipulated to feature various structures, degradative properties, topographies, and inclusion of bioactive substances or drugs. Soft tissue applications of biomaterials is an expansive area with a vast array of promising devices, and this document serves to provide a brief overview of some of these materials, along with their constituents, manipulations, and applications. The gastrointestinal and peripheral nervous systems are highlighted as individual research projects pertaining to these body systems follow the initial review. In the research project-vein, first is described the conceptualization of a novel anastomotic guide for utilization in end-to-end small intestinal anastomosis, along with an *ex vivo* experimental phase and initial *in vivo* application of the device in a swine model. Successful results of this study led to a follow-up *in vivo* project with a second-generation anastomotic guide, which is described thereafter. Results of this study suggest that the anastomotic guide may be useful for refinement of the surgical procedure. The discussion then transitions to an evaluation of a peripheral nerve scaffold for utilization in peripheral neuropathic disorders and injury sites. This study focused on conceptualization, fabrication, and *in vitro* evaluation of poly(lactic-co-glycolic) acid and graphene oxide composites for the proposed nerve scaffold, along with development of a growth factor-eluting hydrogel adjunct. The collective research performed in these studies exemplifies the magnitude of possibilities for biomaterial uses in soft tissue applications.

Table of Contents

CHAPTER 1 : A Brief Introduction to Biomaterials, with Special Emphasis on Soft Tissue Applications 1
Abstract 2
Introduction to Biomaterials 3
Biomaterials Defined 3
Biomaterial Classifications, Advantages, & Disadvantages 3
Chemical Properties of Biomaterials & Their Influences on Bioactivity 5
Physical & Mechanical Properties of Biomaterials & Their Influences on Bioactivity 10
Gastrointestinal Pathologies & Biomaterial-Based Therapeutic Advancements 19
Anatomy of the Gastrointestinal System 19
Healing Mechanisms of the Lower Gastrointestinal Viscera 21
Pathologies and Aberrant Healing of the Lower Gastrointestinal Viscera 22
Brief Overview of Materials Used for Surgical Intervention of the Lower Gastrointestinal System 24
Peripheral Neuropathic Disorders & Biomaterial-Based Therapeutic Advancements 28
Anatomy of the Peripheral Nervous System 28
Peripheral Nerve Regeneration 29
Injury & Pathologic Healing in the Peripheral Nervous System 30
Surgical Repair of Peripheral Nerve Injury 31
Nerve Conduits 34
References 41
Tables & Figures 54
CHAPTER 2 : *Pilot Study*: Collapsible Guide for Use in Small Intestinal Anastomosis 67
Abstract 69
Introduction 70
Materials and Methods 72
Ex Vivo *Investigation* 72
Anastomotic Guide Composition and Fabrication 73
In Vivo *Investigation* 74
Results 76
Ex Vivo *Investigation* 76
Anastomotic Guide Characteristics 77
In Vivo *Investigation* 77
Discussion 79
Acknowledgements 81
References 82
Tables & Figures 85
CHAPTER 3 : *Feasibility Study*: Second-Generation Collapsible Guide for Use in Small Intestinal Anastomosis 95
Abstract 97
Introduction 98

Materials and Methods 100
Anastomotic Guide Fabrication & Hydration/Degradation Testing 100
Surgical Procedure 101
Post-Mortem Data Collection 103
Statistical Analysis 104
Results 104
Anastomotic Guide Material Characteristics 104
Intra-Operative Data 105
Postmortem Data 106
Discussion 108
References 113
Figures 115
CHAPTER 4 : Design, Fabrication, & Preliminary *In Vitro* Validation of a Degradable Scaffold for Peripheral Nerve Defects 126
Abstract 127
Background, Significance, & Innovation 128
Scaffold Design Conceptualizations 131
Design Phase 131
Material Selection 132
Composite Fabrication Techniques 133
Assessment of Composite Formulations for Bioprinting Compatibility 133
Fabrication of Material with Variable Graphene Oxide Proportions 134
In Vitro Analyses of Composites for Delineation of Optimal Neuroinductivity 138
Cell Culture Conditions 138
WST-8 Assay for Assessment of Cell Viability 139
Calcein Green AM for Morphology & Qualitative Assessment of Cell Proliferation 142
Results & Discussion 143
Preliminary Experiments for Development of a Growth Factor-Eluting Hydrogel 145
Growth Factor Hydrogel Conceptualization 145
In Vitro *Growth Factor Experiments* 148
In Vitro *Growth Factor Results & Discussion* 150
Hydrogel Optimization & Elution Studies 152
Hydrogel Studies Results & Discussion 158
Conclusions & Future Steps 161
Acknowledgements 162
References 163
Tables & Figures 170
Vita 205

List of Tables

Table 1-1: Selection of Soft Tissue Biomaterial Applications 54
Table 1-2: Gastrointestinal System Classifications of a Selection of Species 55
Table 2-1: Comparison of Completion Time, Burst Pressure, and Diameter Difference for Each Anastomotic Technique (Ex Vivo) 85
Table 2-2: Comparison of Adhesion Number, Burst Pressure, and Maximum Diameter for Each Anastomotic Technique (In Vivo) 86
Table 4-1: Growth Factors Utilized in the Nervous System 170
Table 4-2: Subjective Qualities of Hydrogel Samples 171

List of Figures

Figure 1-1: Hydrolytic breakdown of poly(D,L-lactide-co-glycolide) 56
Figure 1-2: Foreign body response to a biomaterial implant 57
Figure 1-3: Comparison of gastrointestinal gross anatomy between several common species 58
Figure 1-4: Small & large intestinal microanatomy 59
Figure 1-5: Fibrous tissue and ulcer formation in the intestine 60
Figure 1-6: Neuronal & glial cells 61
Figure 1-7: Microanatomy of the peripheral nerve 62
Figure 1-8: Peripheral nerve regeneration process 63
Figure 1-9: Drawings of early peripheral nerve repair techniques 64
Figure 1-10: Structure of several members of the graphene family 65
Figure 1-11: Example nerve conduit features 66
Figure 2-1: Ex vivo intestinal anastomoses 87
Figure 2-2: Ex vivo burst pressure testing 88
Figure 2-3: 3D-printed non-degradable intraluminal guide designs 89
Figure 2-4: Intestinal guide fabrication protocol 90
Figure 2-5: Fabricated intestinal anastomotic guide 91
Figure 2-6: End-to-end anastomosis procedure 92
Figure 2-7: 3D LSCM results for the porous polymer laminate used to fabricate the device 93
Figure 2-8: Water uptake and swelling behavior of the device 94
Figure 3-1: Steps for fabrication of the device 115
Figure 3-2: Images of pre-sterilized anastomotic guide 116
Figure 3-3: Images of anastomotic guide placement during surgery 117
Figure 3-4: Representative 3D laser microscopy images of polymer 118
Figure 3-5: Mechanical compression results 119
Figure 3-6: Hydration testing 120
Figure 3-7: Surgical duration comparison 121
Figure 3-8: Fecal scoring results 122
Figure 3-9: Return to fecal production 123
Figure 3-10: Post-mortem anastomotic site diameter results 124
Figure 3-11: Burst pressures achieved by each anastomosis 125
Figure 4-1: CAD images of proposed nerve scaffold constructs 172
Figure 4-2: Wettability assessment of potential solvents for drop-coating 173
Figure 4-3: SEM and TEM images of polymer-GO composites of varying % wt. GO 174
Figure 4-4: Appearance of PLGA-GO smears 175
Figure 4-5: Reduction mechanism of MTT assay reagent 176
Figure 4-6: WST-8 assay results for PLGA-GO smears 177
Figure 4-7: Day 7 CAM images of PLGA-GO composites exposed to neuroinduction media 178
Figure 4-8: Day 7 CAM images of PLGA-GO composites exposed to standard media 180
Figure 4-9: WST-8 calibration with Schwann cells 182

Figure 4-10: WST-8 assay results for growth factor experiments 183
Figure 4-11: Day 2 CAM images of NSCs (750 cells/well), exposed to growth factors 184
Figure 4-12: Day 4 CAM images of NSCs (2000 cells/well), exposed to growth factors 187
Figure 4-13: WST-8 assay results for CNTF concentration gradient experiments 190
Figure 4-14: Day 6 CAM images of NSCs (seeded at 750 cells/well), exposed to CNTF..... 191
Figure 4-15: Day 4 CAM images of NSCs (seeded at 2000 cells/well), exposed to CNTF..... 193
Figure 4-16: Bradford's assay initial calibration data 195
Figure 4-17: Appearances of colorimetric assays..... 196
Figure 4-18: Appearances of Gel Forumla 1 and 2 in varying conditions 197
Figure 4-19: Appearances of Gel Forumla 3 and 4 in varying conditions 198
Figure 4-20: Hydrogel elution results for Trials 1-3..... 199
Figure 4-21: Bradford's assay calibration data with higher concentrations of BSA..... 200
Figure 4-22: BCA assay calibration data..... 201
Figure 4-23: Bradford's and BCA assays (corrected) with divided trendlines..... 202
Figure 4-24: Absorbance values for Trial 4 hydrogel samples..... 203
Figure 4-25: Total BSA mass release Trial 4 hydrogel samples 204

CHAPTER 1 : A Brief Introduction to Biomaterials, with Special Emphasis on Soft Tissue Applications

Abstract

Biomaterials, or materials utilized in the assemblage of medical devices, have been a topic of interest for centuries. As the wealth of knowledge has grown regarding the processes and limitations of natural tissue healing, investigations into the capacity for implants to bridge these difficulties has taken place in parallel. The prospect of biomaterials to mitigate failed or suboptimal healing processes has fueled extensive research in this area, particularly over the past several decades, and has resulted in great achievements in the understanding of how the body responds to different materials, what applications such materials can be successfully utilized for, what properties are inherent to these materials, and effective and efficient fabrication and manipulation techniques that can be employed. Additionally, much has been learned about physical and mechanical features (e.g. topography, surface charge, porosity), independent to materials' inherent chemical properties, that evoke particular responses within the body. Biomaterials can broadly be categorized into products of natural or synthetic origin, and further classified as soft tissue-derived, hard tissue-derived, cellular, metallic, ceramic, or polymeric in nature. Additionally, a growing area of interest is in the development of composite materials, featuring two or more materials from different sub-categories or even of both natural and synthetic origins, which take advantage of the benefits of each individual material while reducing the magnitude or propensity of their disadvantages. The field of biomaterials is simultaneously experiencing advancements in fabrication technology, application of new and novel materials, and investigations into biomolecular effects on host tissues, resulting in a discipline that has become a fusion of materials science, engineering, biology, and biochemistry. With the wealth of accumulated knowledge from these distinct disciplines, it is apparent that the chemical, physical, and mechanical aspects of biomaterials are all equally relevant to their behavior within the host, and ultimately to the successful outcome in their utilization for therapeutic applications. This chapter initially reviews biomaterials broadly in terms of their classifications and properties, followed by distinct considerations of biomaterials when utilized for soft tissue applications. The latter half of the chapter focuses on two particular soft tissue body systems, the gastrointestinal and peripheral nervous systems, in regards to their unique requirements for applications of biomaterials.

Introduction to Biomaterials

Biomaterials Defined

Trends over the years and variances in the opinions of biomedical researchers have presented alternative concepts in the designation of individual materials to the class of "biomaterials", largely distinguished by an emphasis on materials that are *derived* from living systems versus materials that are *applied* to living systems [1]. In reviewing the wealth of literature in this field, it is apparent that biomaterials have a wide range of etiologies and applications, and that there is a greater tendency to view them as materials which can be applied to living systems, irrespective of their origin. In the simplest of terms, a biomaterial can be defined as a substance incorporated in the assemblage of a medical device that is purposed to interact with a biological system [1, 2]. Major applications of biomaterials include replacement of a diseased or injured tissue, correction of a functional abnormality or cosmetic defect, enhancement in the healing or functionality of a repair, and assistance in the diagnosis or treatment of a condition [3].

Biomaterial Classifications, Advantages, & Disadvantages

Biomaterial Classifications

In the broadest classifications, biomaterials are divided into natural products, synthetic products, or hybrid composites [4, 5]. Natural biomaterials are classified into products derived from soft tissues, hard tissues, or cells [4]. Synthetic biomaterials are divided into categories based on the chemical nature of the product, being a metal, ceramic, or polymer [4, 5]. Hybrid products can be composites fabricated with multiple natural products, multiple synthetic products, or products of both origins. Within these categories are further subcategories. For example, metals may be pure or alloys; ceramics may be glasses, glass-ceramics, or carbon-based; polymers may be thermosets, thermoplastics, elastomers, or textiles [1]. Coinciding with great advancements and novel experimentation, distinct boundaries between class divisions have become less distinct in some cases of materials featuring extensive structural complexity and a variety of interatomic and intermolecular bonding, including some nanomaterials and self-assembly materials [1].

Advantages & Disadvantages of Biomaterial Subcategories

Just as biomaterials are representative of a wide range of classifications, they vary greatly in their utility and application. Important considerations to be taken into account when selecting an ideal biomaterial for a particular application include their inherent advantages and disadvantages when applied within a living system. There are particular benefits and pitfalls to each individual material, but there are some common themes represented within the classifications and subcategories of biomaterials that can aid in narrowing down material selection for a particular application. In the historic vein, a transition has taken place in the utilization of predominantly natural-origin biomaterials to synthetic materials due to the wealth of beneficial properties of synthetic materials that have been discovered [2], largely owing to the coinciding progression of advanced fabrication and characterization techniques and proven performance in *in vitro* and *in vivo* studies.

Natural biomaterials feature the advantages of absent cytotoxicity and foreign body response, degradation *via* inherent enzymes, and biological functionality [4]. Some natural materials also express bioactivity, stimulating particular cellular responses within the tissues to which it they are applied. Disadvantages of natural biomaterials include the potential for adverse immunologic reaction, high variability due to individual differences in donors, and more extensive considerations in manipulation due to complex structure [4]. Metals, ceramics, and synthetic polymers are exceptionally different in their properties, and hence have unique advantages and disadvantages from one another. Metallic biomaterials can beneficially feature high strength, extensive hardness, resistance to fatigue, wear, and impact, easy sterilizability, and may be fabricated or manipulated by methods with ready availability [4, 6]. Unfortunately, metals can corrode and wear over time, have a low strength to weight ratio, and may present toxicity or sensitivity concerns due to harmful corrosion products [3, 4]. Ceramic biomaterials advantageously can endure high levels of compression, possess a notable elastic modulus, are resistant to wear and corrosion, and can be bioactive or inert, which may be a beneficial feature to specific applications depending on the precise purpose of the implant [4, 5]. High biocompatibility and biofunctionality make ceramic materials one of the most ideal classes of biomaterials [7, 8]. Disadvantages include a high modulus (incomparable with the modulus of bone), low tensile strength, brittleness, and challenging fabrication methods [4]. Synthetic polymers, a subcategory of biomaterials that has attracted much popularity in recent years, feature favorable degradability

potential, simpler and readily-available fabrication and manipulation practices, and easy modification to display a wide range of properties [3, 4]. Downfalls to utilizing synthetic polymers in biomaterial applications include their propensity to swell with extraneous fluid and proteins within the implantation site, wear at a suboptimal rate, and degrade into less compatible by-products (in select cases), as well as their difficulty to sterilize without modifying the materials' properties or the implant structure [4]. Note that there are also numerous naturally-occurring polymers (e.g. collagen), some of which are also commonly utilized for biomaterial applications [5].

Chemical Properties of Biomaterials & Their Influences on Bioactivity

Chemical Properties of Biomaterials

At the most minute level in the hierarchy of a biomaterial construct is its chemical makeup. All properties that a biomaterial evokes within the biological system to which it is applied are first originated from the elements used to compose the material [5]; hence, understanding the elemental constituents of the material, along with their interactions with one another and the local environment, are imperative to the development of an effective material. Areas related to the chemical properties that affect the design, fabrication, and application of biomaterials include materials chemistry, chemical synthesis, chemical bonding, surface chemistry, chemical biology, and computational modeling of biological systems [5]. Some of the considerations pertaining to the chemical properties of biomaterials include specific elements incorporated, bonding to other molecules or cells, degradability, response to pH and temperature, affinity for water, surface charge, and functionalization. Some of these factors play more apparent roles in how the material inherently behaves, whereas others play pivotal roles in the bioactivity of the material once implanted, though there is often much crossover.

In consideration of the properties of biomaterials from the simplest aspects to the most complex, individual atoms, molecules, or monomers must be first reflected upon. These building blocks translate materials into their specific subcategories, afford them their inherent bonding schemes, and elicit distinct responses, whether chemical, physical, or biological. There may be great variability between these responses in respect to individual units versus entire constructs of

a material, as well as in respect to even slight modifications of bonding or arrangement of subunits. The molecular weight and elemental composition of polymers can directly affect biocompatibility, as this may influence the density of charges, conformation of the polymer units and sequence (e.g. block, random, linear, branched, cross-linked), and flexibility of the bonds between units and segments [9]. Cytotoxic effects as a result of employing higher or lower molecular weight versions of a particular material vary greatly depending on the material [9]. Bonding within the material also greatly affects its performance. Arrangement of polymer units within a polymer chain or the relationship of chains with one another varies depending on the intermolecular bonding and physical cross-linking that takes place, and can result in linear, branched, hyperbranched, and dendrimer arrangements [10]. In cases of biodegradable polymers, these arrangements directly influence steric-conformation and bonding rotation capacity, which ultimately impacts the mechanism and speed at which the material is degraded [10].

Depending on the nature of the biomaterial(s) used, an implant may be bioresorbable or biodegradable, or non-bioresorbable or non-biodegradable [7, 8]. Bioresorption is somewhat distinct from biodegradation in that the material is removed as it is replaced by advancing tissue [7], versus dissolution by various tissue environmental factors [8]. Degradability of biomaterials is an extremely beneficial aspect for many applications, eliminating the necessity for follow-up surgeries to remove implants and prevention of long-term adverse effects associated with foreign material remaining in the body. Additionally, biomaterials with degradative properties permit the fabrication of implants with the goal of serving as scaffolding temporarily during the tissue regeneration process [3]. The timeframe and method of degradation is largely dependent upon the chemical composition and interactions of the material and the conditions of the environment surrounding the implant. Two of the most common degradation processes that occur in biomaterials are water-soluble degradation and enzyme-mediated degradation [5].

Poly(lactic-co-glycolic acid) (PLGA) is the most frequently used of the biodegradable and biocompatible polymers [11]. Degradation of PLGA in an aqueous environment occurs by hydrolysis of ester bonds and subsequent auto-catalysis by carboxylic functional groups to form lactic acid, glycolic acid, and other acidic groups (Figure 1-1) [11, 12]. Strength, swelling behavior, and degradation of PLGA are affected by its crystallinity, which varies between the different molar ratio products, and the higher the proportion of glycolide groups, the faster the

material degrades [13, 14]. Similar degradation *via* hydrolysis of ester bonds occurs in other commonly used synthetic polymers, including polylactic acid (PLA), polycaprolactone (PCL), and polyvinyl alcohol (PVA), as well as natural polymers like cellulose [3]. Bioglasses are another class featuring bioresorbable materials, and while different bioglasses have many properties in common, the specific chemical composition of each greatly affects the degradation rate, simultaneously affecting ion release rate and the elution profile of any pore-imbedded therapeutic products [5]. An imperative consideration when predicting the degradative process of a biomaterial is the consequent by-products produced [5]. It is possible for a material to be inherently biocompatible, but to produce cytotoxic by-products as the material degrades.

Response to environmental pH and temperature are two additional considerations in respect to the chemical properties of a biomaterial. Presence of an acidic or basic tissue environment may ultimately affect the bioactivity or degradability of a material, resulting in a performance contrary to results seen *in vitro* or in normal *in vivo* tissue environments. The possibility of such environmental conditions should be considered when preparing to implant a material, to include the presence of bacterial infection, chronic inflammation, exposure to various bodily fluids, etc. Temperature is another important factor with direct implications to *ex vivo* versus *in vitro* or *in vivo* performance, as materials may not perform the same at room temperature versus physiologic temperature. An interesting line of research currently being given great attention is the potential for materials to undergo modification when exposed to certain pH levels or temperatures and subsequently display favorable properties for the particular application [15]. For example, pH-sensitive hydrogel particulates can serve as drug delivery platforms to targeted tissue sites [16], and dual pH- and temperature-sensitive polymers have been developed that can self-degrade on mildly acidic wound surfaces [17]. pH-sensitive bonds include imines, hydrazones, oximes, amides, acetals, and orthoesters [17]. Temperature-sensitive materials are defined by their ability to feature one phase or volume below a particular threshold temperature, and another above that temperature, with this phase or volume transition often being reversible [18]. In the development of temperature-sensitive biomaterials, the target temperature for this threshold is typically 35-37ºC, and some commonly investigated materials that have demonstrated transitional behavior in this range include the poly(*N*-isopropylacrylamide) family (PNIPAAMs), poly(2-oxazoline) family (POxs), and cellulose-derived polymers [18].

Chemical Properties of Biomaterials with Implications in Their Bioactivity

At the onset of biomaterials being a distinct discipline, the primary goals were for their facilitation of mechanical functionality while remaining relatively inert in order to prevent host rejection [2]. While prevention of adverse immunogenicity remains at the forefront of biomaterial development, interest has grown in developing materials that are not only compatible with host tissues, but elicit particular responses that can stimulate cellular recruitment, encourage integration, and enhance overall healing. "Bottom-up" approaches to implant fabrication are often employed, though ultimately tissue response is dependent on the multifactorial physical and chemical aspects of a biomaterial [2].

A common method of encouraging integration between an implanted material and the host tissue is by modifying the binding interactions taking place between the implant surface and host cell surface receptors or tissue components [2]. Bioactive glasses and glass-ceramics have demonstrated an inherent bioactivity that permits direct chemical bonding with bone tissue at the site of implantation [19]. Chemical adsorption of biological molecules or nanomaterials onto a material's surface *via* covalent bonding, prior to implantation, may facilitate better host integration as the tissue first encounters the modified, bioactive surface [20]. The strong chemical bonds formed between the surface and covalently bound molecules are more likely to maintain their position compared to adsorption processes that rely on physical bonds. This is an example of functionalization, a technique commonly employed to manipulate protein and cell interactions at the biomaterial interface. A common application of functionalization is in the production of non-fouling surfaces, where the bulk implant is functionalized with highly hydrophilic groups [21]. Most often, the bulk material is a neutral polymer, such as poly(ethylene glycol) (PEG), poly(2-hydroxyethyl methacrylate) (PHEMA), or poly(*N*-vinyl-2-pyrrolidone) (PVP) [21, 22]. One of the most common functionalizations is the grafting of integrin-binding peptides, such as RGD, to entice adhesion of cells to biomaterials [2]. Alternatively, metals that are frequently implanted (e.g. titanium, stainless steel), as well as some ceramics (e.g. alumina, zirconia) and highly hydrophilic polymers (e.g. poly(ethylene glycol)), have bioinert surfaces that typically prevent adherence of cells [3, 7, 23], unless the surface is modified in some manner to encourage protein adsorbance or cell attachment. Depending on the particular application, prevention or encouragement of protein or cell attachment may be favorable.

Stimulation of protein adsorption on the implant surface after implantation is described by the Vroman effect [22], which can be directly affected by surface chemistry and topography [2]. The Vroman effect describes the propensity for small, highly mobile proteins from blood plasma, such as albumin, to adsorb and desorb from an implant surface, until weightier proteins with higher affinity for the surface adhere more securely [22]. Implants featuring surfaces that do not repel proteins from blood plasma are highly prone to becoming coated in a provisional matrix of these proteins, which alters the surface characteristics of the implant and entices greater cell interaction [22, 24]. This may be favorable in some cases where integration is encouraged, but may prove disfavorable in cases where the materials' biofunctionality is impeded. Depending on the requirements and goals of the material, tactics can be employed that lead to resistance of nonspecific protein adsorption and enticement of favorable proteins that mimic the extracellular matrix of the implantation environment [2]. While the initial mechanisms are similar, these processes are contrasted against the often disadvantageous foreign body response to an implant. When a material is implanted that incites an adverse immunogenic reaction, a cascade of phases often takes place, beginning with protein adsorption and acute inflammation, followed by a prolonged period of chronic inflammation and foreign body giant cell formation, and finally fibrous tissue formation surrounding the implant (Figure 1-2) [22].

Utilization of materials with inherent opposition to protein adsorption or that have been tailored to feature surface characteristics that oppose protein deposition may be favorable in certain applications. Materials such as PEG, PHEMA, PVP, poly(acrylamide) (PAA), and poly(carboxybetaine methacrylate) (PCBMA) have been shown to display a decreased propensity for protein adsorption due to their hydrophilic nature [22]. Surfaces with extreme wettability, or a high affinity for water, may prevent protein adsorption by the establishment of a barrier of tightly bound water molecules through which proteins and cells have difficulty penetrating [22]. For this reason, hydrophilic materials in general may be predisposed to reduced protein adsorption; however, studies have shown that hydrophilic and hydrophobic materials may experience similar propensities for protein adsorption, which is heavily reliant on other factors such as surface charge and topography [22]. For example, fibrinogen and vitronectin are attracted to both positively and negatively charged hydrophobic surfaces [22]. One possible mitigation of these effects is to incorporate a balance between hydrophilic and hydrophobic groups present on the surface, a tactic

being investigated by researchers [9]. Lee, Kopecek, and Andrade (1989) evaluated a PEG and poly(propylene glycol) (PPG) copolymer, the constituents of which are hydrophilic and hydrophobic, respectively, and found that there was reduced protein adsorption on the material [9, 24]. Hydrophilic and hydrophobic diblock copolymers are also known to form micellar structures, which may facilitate delivery of solubilized or impregnated substances when utilized in drug delivery applications [9, 25]. In a general sense, neutral and anionic polymers tend to demonstrate greater cytocompatibility than cationic polymers, largely owing to the reduced absorbance of proteins, which often display a net negative charge, on the surface [9]. Some cationic materials, such as poly(L-lysine), have been shown to induce cellular damage and morphologic changes in various cell lineages [9]. The quantity of charges displayed by a polymer is affected by the molecular weight used [9], so applications of the same material, but utilizing different molecular weights, may result in different outcomes. Surface charge of an implant is affected not only by the materials used to fabricate the implant, but by the pH and small ions present in the surrounding aqueous tissue environment [22].

Physical & Mechanical Properties of Biomaterials & Their Influences on Bioactivity

Tissue-Specific Considerations

In developing a biomaterial implant for a particular application, it is not only imperative to consider the chemical properties of the material when applied, but the physical and mechanical requirements inherent to the tissue site. While many biological considerations apply to both tissue spaces, soft tissue is highly distinct from bone in that materials often must be flexible, with the ability to expand and contract, and must be especially resistant to protein adsorption due to high contact with proteinaceous fluids. Hard tissue biomaterials often require extreme durability and very limited brittleness as they undertake high compressive and tensile forces.

Physical Properties of Biomaterials with Implications in Their Bioactivity

Advanced comprehension of the microanatomic and sub-cellular features of biological systems has propagated an appreciation of their complexity and functionality which has fueled inspiration for biomaterial design [2]. As the inherent mechanisms of normal tissue development,

maintenance, and healing are “gold standard” models to which we compare biomaterial-based therapeutic outcomes, tailoring materials to elicit similar, or even enhanced, effects on tissues has become a leading area of research in the field. One of the most prevalent approaches to instigating this “mimicry” is by fabricating biomaterials to feature physical features similar to natural host tissue. As biological systems operate on nanometer and micrometer scales in order to cumulatively produce more readily apparent results, biomaterials must also be fabricated with consideration of how cells and individual molecules within the body will perceive and interact with the material [2]. Some approaches to inducing biomimetic effects in materials by taking advantage of their physical properties include manipulating surface topography, reproducing microstructures found within the extracellular matrix, encouraging formation of physical bonds with host tissues, and incorporating non-chemical components, such as mechanical action or electrical signals [2].

While a material’s chemical composition and general structure may be ideal for the intended application, a suboptimal surface texture can nullify these and prevent successful cell adherence upon implantation. Surface topography, even down to the nano- or micro-scale, can have a profound influence on cells, and optimizing the topography of implants can facilitate their integration into the host tissue [26]. Surface roughness has been shown to encourage cell adhesion and differentiation [22]. For example, osteoblast-like bone marrow cells preferentially adhere to and proliferate on rough surfaces, with an increase in these behaviors as roughness increases [19, 27]. Surface roughness may impact the propensity for protein deposition, with nano-topographic features potentially influencing protein conformation as the proteins are adsorbed [22]. There are, however, conflicting results from studies evaluating this [21]. Some researchers have described that protein arrangement is dependent on the nanotopographic features of the surface [28], whereas others have found that neither the quantity of protein nor the structural stability of the adsorbed protein is influenced by these [29]. Such confounding results are likely accounted for by the high variability in experimental conditions, but it has been suggested that proteins of a size corresponding to the same magnitude of surface roughness may more often maintain their conformation, and proteins of smaller or larger dimensions are more likely to be altered once adsorbed; this may further be impacted by the original protein morphology (strand-like versus globule) [21].

Not only roughness and size of features on a surface can impact protein adsorption and cell

adherence and response, but the pattern or shape of the features. Physical features of extracellular matrices are common sources for bio-inspired topographic design. Investigators have assessed how grooves, pits, pillars, fibers, etc. can impact behavior in biological systems, including cell differentiation and morphology [30]. Fate of stem cells [30], when applied to materials of varying topographic features, is a particularly interesting evaluation as these cells have the potential to differentiate into multiple lineages. Grooved patterns have been shown to facilitate alignment and elongation of cells, whereas micro-scale pits and pillars both appear to enhance differentiation to an osteogenic lineage [31]. Evidence of adoption to a distinct lineage in the presence of particular surface features may provide extensive justification for further evaluation of those features in implants for tissue-specific applications. Tissue-specific cell lineages have also been shown to demonstrate compatibility with particular surface features; for example, silicone material with parallel grooves has shown the capacity to orient dermal fibroblasts, as well as adsorbed proteins, into a more even conformation [22, 32], and micropatterned ridges and grooves have been shown to contribute to neural cell alignment and facilitate linear growth [33]. Modifying the surface texture of an implant may ultimately be a final processing step in the fabrication of a biomaterial implant, but the implications can be dramatic. Mechanisms of modifying the physical topography of implant surfaces, not including functionalization with other ions or molecules, include photolithography, electrospinning, soft lithography, hot embossing, ion-bean or electron-beam lithography, thermal-based nanoimprinting, laser ablation and irradiation, and dip-coating [30, 34-36].

Surface topography may also have implications on the potential for bacterial colonization, or the potential to aid in preventing this. It is estimated that 80% of nosocomial infections are the result of biofilm formation on implants and medical devices [37]. Instituting antibacterial characteristics within biomaterials, whether that be inherent to the material employed, the implant structure, or adjunctive therapeutics utilized with the implant, is an area that has gained increasing attention as concerns arise regarding antibacterial resistance and ethical infection prophylaxis measures. Adherence of bacteria to implants is heavily influenced by surface chemistry and functionalization, as well as surface topography [38]. Antibacterial coatings on biomaterial implants, whether based on antimicrobial release or relying on photoactive metal oxides or cations, are possible mechanisms of preventing infection that have been explored [39]. Certain

topographies utilized in implants to encourage tissue integration have been found to contrarily promote bacterial adherence, but a potential mitigation of this, and an interesting alternative to utilization of antimicrobial agents that present a risk for bacterial resistance, is manipulation of surface topography with inspiration from biological structures, including shark skin, leaves, and insect wings [40]. A variety of nano- and micron-scale topographies have been explored with varying results, but the general consensus is that micron-scale features are not bactericidal but may reduce the propensity for bacteria to adhere to the material surface, and that many nano-scale features can directly damage bacterial cell membranes, leading to cell death [40]. Particular topographic features may also serve as a barrier to bacterial motility on surfaces, potentially impacting their ability to colonize, replicate, seek nutrients, and produce biofilms [41]

One of the leading areas of research in the biomaterial field is in the production of materials that mimic the extracellular matrix (ECM) of target tissues. Production of an artificial ECM serves to support infiltration, adherence, migration, proliferation, and differentiation of cells, ultimately facilitating tissue integration and regeneration [42, 43]. Inclusion of ECM structural features is not merely restricted to implants that serve a distinct, long-term functional purpose, such as for mechanical support, but materials that are temporary platforms for new tissue formation. This latter application is highly prevalent in the field of tissue engineering. Williams (2009) defines tissue engineering as "the creation (or formation) of new tissue for the therapeutic reconstruction of the human body, by the deliberate and controlled stimulation of selected target cells through a systematic combination of molecular and mechanical signals." Collagen constitutes the majority of connective tissues in mammals [42], and while collagen itself can be utilized as a biomaterial [44], the benefits of certain synthetic products encourages the production of artificial ECM-mimicking materials with a similar fiber structure to collagen, eliciting biomimetic effects such as cell attachment, proliferation, and differentiation *in vitro* [42]. Porous structure may also be simulated in ECM-like materials for encouragement of cellular recruitment and infiltration, but can also serve as a local delivery mechanism for therapeutic products [5]. Hydrogels are especially intriguing for applications of ECM-mimicry as they can feature an extensive range of physical properties and can incorporate a host of potential additives bonded to the structure or imbedded within the matrix, making them easily tailored for application to a wide variety of tissue environments [5, 15, 45]. Stem cells can be simultaneously delivered in such applications, with

the goal of encouraging cell differentiation that facilitates integration of the material with the host tissue or enhances tissue regeneration [2]. Alternatively, naturally-sourced materials can be utilized in ECM-like materials [3], solely or in combination with synthetic products, taking advantage of nano- and micro-structures already present in the material to elicit the target effect.

Physical adsorption of materials onto a bulk implant, whether for protein or cell attraction or repulsion, is a common modification of surfaces, but may present challenges in applications of long-term implants [21]. Layering the material onto the surface by physical adsorption results in a coating that relies on relatively weak intermolecular forces, such as electrostatic forces, hydrogen bonds, and van der Waals forces, and over time these coatings may become eroded [21]. For short-term, bioresorbable materials, however, this may be a highly beneficial method of increasing the bioactivity of the surface. For example, Campbell *et al.* (1994) demonstrated that a physisorbed coating of various material surfaces with phosphorylcholine, a lipid constituent found on cell membrane surfaces, mimics biomembrane appearance within the host and can greatly reduce fibrinogen and platelet adsorption. Methods of applying substances to a material's surface by physical techniques include layer-by-layer assembly, co-electrospinning, and nanoparticle assembly, but quite often simple adsorption by submersion in solutions with adhesive molecules is employed [20]. Physical adsorption can also be used for temporary adherence of growth factors to an implants' surface; however, release kinetics can greatly vary based on protein-surface interactions and underlying properties of the material (e.g. surface charge, degradation) [20].

Apart from inclusion of bioactive molecules into biomaterial constructs, whether by incorporation or application to the surface (*via* chemical or physical processes), there are several techniques for eliciting a greater host response from biomaterials that are especially popular in the present-day. With advancements in molecular biology, especially since the 1970s, the understanding of how many growth factors operate within the body has subsequently driven interest in utilizing growth factors for therapeutics in a similar capacity to administered drugs [2]. Biomaterial applications of growth factor or drug delivery have since grown in interest, with the prospect that certain materials may have the capacity be functionalized or imbedded with such additives and may be capable of being tailored to optimized release rates. The leading methods for addition of therapeutic additives into the matrix of a biomaterial for delivery upon implantation are chemical immobilization, physical encapsulation, or direct incorporation into the material [46,

47]. Encapsulating additives into polymer-based spheres is an especially promising tactic in the prevention of premature degradation/denaturation and manipulation of release rates [46]. Polymer nanospheres as alternatives to colloidal drug carriers for site-specific drug delivery is also an approach [25], and hydrophilic and hydrophobic copolymers, which have been shown to form micellar conformations, may be able to serve as vehicles for solubilized drug [9, 25]. One of the hindrances to developing optimal drug delivery materials is that the release kinetics may not be consistent [16]. For example, production of particulate-based drug delivery polymers, such as hydrogel microspheres, can often result in variable particulate size ranges which do not release drug uniformly [16].

Considerations & Specific Biomaterials Employed in Soft Tissue Applications

There are a multitude of biomaterial applications within each body system, the listing of which is extensive and out of the scope of this overview. Coinciding with advancements in materials science and discoveries of unique material properties and functionalities, novel soft tissue applications for biomaterials are being investigated that may dramatically change therapeutic options for a host of conditions. While biomaterial applications for hard tissues have dominated the field in recent years, interestingly, The National Institute of Biomedical Imaging and Bioengineering, a branch of the National Institutes of Health, has highlighted several prominent research foci that their funded researchers are currently exploring, virtually all of which are soft tissue targeted; these include lung sealant patches, smart wound dressings for chronic diabetic ulcers, laser welding for intestinal anastomosis, dissolvable burn wound dressings, and zinc-based dissolvable vascular stents [48]. A brief description of biomaterials and their applications for several of the major soft tissue body systems are described to follow, and an abbreviated listing is provided in Table 1-1. Following this section, biomaterials utilized for lower gastrointestinal and peripheral nerve applications are discussed in-depth as they directly pertain to studies described in later chapters.

The advancement of biomaterial applications in soft tissue body systems has been primarily aided by the availability of a vast number of synthetic polymers that display a wide range of chemical and physical properties [49]. Polymers are more commonly employed for soft tissue applications rather than hard tissue applications due to their mechanical limitations [5].

Alternatively, soft tissue biomaterials often require a degree of flexibility as the tissues to which they are applied typically experience some form of motility, expansion, or contraction, making the mechanical properties of polymers highly favorable [49]. Some of the most common polymer families utilized for biomaterial applications are aliphatic poly(esters), poly(anhydrides), poly(orthoesters), poly(amides), poly(amino acids), and poly(phosphazenes) [5].

There are distinct considerations in the selection of which polymer to utilize for a specific soft tissue application, largely centered around the nature of the anticipated tissue environment, the purposed functionality of the implant, and the optimal degradation period (or lack thereof). As proteins adsorb to most material surfaces, soft tissue biomaterials anticipated to be in contact with blood or heavily proteinaceous fluid should be selected on the basis of their ability to repel proteins by high hydrophilicity, extreme wettability, or ability to be functionalized with anti-protein adsorption molecules [24, 50]. This is especially important in cardiovascular applications where the implant is in constant contact with blood, as proteins and platelets can accumulate overtime and predispose to thrombus formation [50]. Additionally, surface features may damage blood cells and other blood constituents, and so featureless or highly repellant surfaces are imperative in these applications [49]. Exposure to certain bodily fluids, including urine, stomach acid, and digesta, is another consideration that should impact material selection, as the materials' functionality and degradation may be greatly altered within these more acidic environments. Activity of the tissue should also be accounted for in order to prevent mismatch between the mechanical capacity for the polymer and the mechanics of the tissue. For example, integument, vasculature, and heart valves all display high mechanical activity [51]. A phenomenon encountered in vascular implants is failure due to a mismatch between the compliance of the graft and host tissue, termed intimal hyperplasia [51]. Bladder, lung, and intestinal tissue display extensive expansion and contraction mechanics, and so polymers for these applications often necessitate marked elastic properties. Other tissue-specific requirements for polymer applications include simultaneous toughness and high elastic modulus (artificial tendons and ligaments), optical clarity (artificial corneas and lenses), fluid retainment (hydrating wound dressings), polymerization *in situ* (tissue reconstruction), long-term fatigue resistance (artificial heart valves and vessels), selective adsorption of toxic by-products (dialysis membranes), and gas permeability (heart assist devices) [49, 51].

As discussed previously, implants that mimic native ECM can serve a variety of functional purposes, but have an especially valuable potential to serve as tissue regeneration platforms in soft tissue applications. Polymers commonly used to fabricate soft tissue scaffolds include natural products like collagen, gelatin, and elastin, and synthetic products like PCL, poly(glycolic acid) (PGA), PLA, and poly(hydroxy alkenoates) (PHAs), along with various copolymer composites [51]. Hydrogels, which are essentially lattices of polymer and water, are a subset of polymers with great prospect for soft tissue scaffolds. Hydrogels have acquired extensive popularity in recent years as the range of polymers from which they can be developed and their extremely diverse manipulation potential have been more deeply understood. Hydrogels can be composed of natural or synthetic polymers and can vary greatly in their density, viscosity, tissue adherence, degradability, and capacity to elute additives over time, making them prospective materials for a wide range of applications including ECM substitution, wound regeneration, drug delivery, and tissue sealants/barriers [5, 15, 48]. Properties elicited by individual hydrogel formulations rely heavily on the constituent polymer(s) used, type and prevalence of cross-linkages, polymerization method employed, and surface features that may permit topographic connections with tissues [52]. Cross-linkages formed in the gelation of the hydrogel allow it to maintain water and prevent premature dissolution [15]. Two especially common targets for tissue adherent hydrogels are amino groups and mucin glycoprotein on tissue surfaces [52, 53].

Metals are especially employed in the replacement and repair of hard tissues [5]; however, there are unique applications of metals in soft tissue body systems that have arisen due to their beneficial biocompatibility, malleability, and fatigue resistance properties [4, 5]. Metals are necessary components of biological systems, being required for such processes as proper enzyme function and redox reactions, and hence may also serve a bioactive function when utilized in biomaterials [5]. For example, substitution of materials with cobalt ions (Co^{2+}) have been shown to enhance angiogenesis, mitigated through the metal's induction of hypoxia in the local environment and stimulation of vascular endothelial growth factor expression [54]. Excessive exposure to cobalt can result in adverse systemic effects, however, so (as is true in all cases of biomaterial implantation), variances in local versus systemic responses and appropriate dosaging must be scrutinized [5]. Zinc, magnesium, and iron have demonstrated biodegradability *in vivo*, and have hence gained popularity in the development of absorbable biomedical devices [55]. Of

these three, magnesium is especially attractive due to its high biocompatibility and beneficial mechanical properties [55]. Soft tissue applications of these metals include bioresorbable stents and surgical staples [55-58]. While traditional staples are also metal, typically titanium alloy, these either remain *in situ* or necessitate removal due to their non-biodegradability [57, 58].

Metals have also been implicated in featuring beneficial properties in the realm of infection prophylaxis. Several metal ions have been shown to elicit antibacterial properties, including strontium, zinc, copper, cerium, and silver [59-61]. Applications of silver ions for this purpose have been of particular interest. While each metal type may utilize a unique mechanism for its bacteriostatic or bactericidal action, nanoscopic silver particulates, when incorporated into a material and encountering a bacterium, can induce membrane and cell wall damage, thereby destroying cell integrity and survival [59]. Additionally, silver can bind to the bacterial DNA and RNA, prevent reproduction, and interfere with proper electron transport chain function [59].

Ceramics, similar to metals, are mostly employed for hard tissue applications owing to their hardness, compression endurance, and resistance to wear and corrosion [4, 5]. Calcium phosphates, calcium silicates, and bioactive glasses, however, are particular ceramics that have shown promising results for both hard and soft tissue applications [5, 62]. Nanoapatites, under the umbrella of calcium phosphates, have demonstrated potential for regeneration of skin, muscle, and gums, in addition to the more traditionally recognized stimulation of bone and dental growth [62]. Calcium silicates offer the potential to induce tissue regeneration and angiogenesis as well, *via* release of SiO_4^{4-} ions, especially within the integument [62]. Bioglasses are a class of ceramics that are comprised of silica, calcium oxide, sodium oxide, and phosphorous pentoxide in varying proportions, often comparable to the proportions of calcium and phosphorous oxides found within bone [62, 63]. Despite this, these materials can serve as effective soft tissue scaffolds or delivery apparatuses [62]. For example, mesoporous bioglasses feature a unique porous structure, with pores ranging from 2-50 nm, into which bioactive or therapeutic products can be loaded and subsequently delivered to the implant site [5].

Gastrointestinal Pathologies & Biomaterial-Based Therapeutic Advancements

Anatomy of the Gastrointestinal System

Gross Anatomy – Comparative Perspectives

While many organs and physiologic processes of the gastrointestinal system are common between species, each species has its own unique features or proportionalities that add to the richness in diversity of the animal world. The major classifications of animals as distinguished by their gastrointestinal system include monogastrics, ruminants, pseudo-ruminants, and avians [64]. While the stomach is consistently the organ in the digestive system responsible for the initial bulk breakdown of food *via* enzymes, acidic juices, and peristalsis, plus or minus symbiotic bacteria, the monogastric system is distinguished by the presence of a single stomach compartment, whereas ruminants have a four-compartment stomach, and pseudo-ruminants a three-compartment stomach [64]. Aborad from the stomach, the animals amongst these three classifications have a tubular organ system for progressive digestion and nutrient/fluid absorption broadly divided into the small intestine, cecum, and large intestine, with subdivisions, proportionalities, and gross morphologies distinct to each species. The avian digestive system is quite distinguished from all others by the presence of a crop (in most birds) for temporary storage of unmasticated food, dual-chambered stomach first delineated as the proventriculus, which secretes digestive juices, followed by the gizzard, which physically breaks down food, and subsequent small intestine, cecum, and large intestine [65, 66]. There are other organs which constitute the gastrointestinal system, particularly for initial feed intake, excretion, and which contribute to production of digestive enzymes and bile, but discussion of these is out of the scope of this work.

Another classification of the gastrointestinal system pertinent to numerous animal species that feed on vegetation pertains to the location of cellulose degradation, the process of which is termed “fermentation” [66]. The site of fermentation is typically either within the stomach compartment(s), characterizing “foregut” fermenters, or within the intestines and cecum, as characteristic of “hindgut” fermenters, and in either location the fermentation process is driven by microbial action [66]. Hindgut fermenters often have an exceptionally long intestinal tract and large cecum so that a greater volume of feed can be contained for the extended fermentation

process [66]; however, this process of fermentation actually contributes minimally to the overall energy derived from the feed [67]. One important consideration in the utility of animals in gastrointestinal or nutritional research is the inherent commonalities and differences between the model species and any other species that the results may be translated to. The gastrointestinal system classifications and gross appearance of several species are elucidated in Table 1-1 and Figure 1-3, respectively.

Microanatomy of the Lower Gastrointestinal System

The small and large intestines can collectively be viewed as the location for the majority of nutrient breakdown and subsequent absorption, though each region has distinct microanatomic features that permit more specific and specialized actions. Additionally, the small intestine itself features differences in the histologic appearance and functionality of each of its segments (i.e. duodenum, jejunum, ileum), but the following is a general overview of the histologic features that are relatively similar between the regions [68, 69]. The small intestine is not merely a slender tube, but its interior is covered in a lining of mucosal folds coated in epithelial cell-covered projections called villi, as well as epithelial cell-covered crypts (Figure 1-4-A) [70-72]. The membrane of these epithelial cells is further covered in microvilli, often termed the "brush border", cumulatively accounting for the small intestines' extensive absorptive surface area (approximately 250 m^2 in humans) [70]. Several cell types constitute the epithelial lining, including stem cells, which permit rapid cell turnover and differentiation into cells necessary for all digestive functions; enteroendocrine cells (G, I, and K cells), which secrete hormones in response to substances within the intestinal lumen; goblet cells, which secrete mucus for improved digesta transit; Paneth cells, which serve as a defense mechanism against pathogens; and enterocytes, which are the mature absorptive cells that deliver digested nutrients into the systemic blood or lymph circulation [70-72]. As enterocytes are sloughed every few days, progressively differentiating enterocytes migrate from crypts up and along villi in order to briefly perform their absorptive roles [70, 71]. Absorption takes place either transcellularly, across the membrane of the cells, or paracellularly, across tight junctions between cells [73]. An additional feature within the small intestine is the presence of Peyer's patches, specifically within the ileum, which contain mucosal-associated lymphatic tissue (MALT) and serve to prevent translocation of pathogens from the intestinal contents into the host's

circulation [74].

Though the large intestinal gross appearance varies greatly from species to species, as previously mentioned, it functions similarly regardless of the host in that it permits the final phases of water and electrolyte absorption, fecal production, and microbial fermentation [75]. The mucosa of the large intestine appears somewhat similar to that of the small intestine, but without the presence of villi [76]. Rather, the luminal surface is relatively flat, with abundant openings into crypts, and the epithelium is infiltrated with a greater proportion of goblet cells than within the small intestine (Figure 1-4-B) [70].

The histologic cross-sectional tissue layers within the small and large intestine are the same, being comprised of four main layers [74]. The layer in contact with the lumen is the mucosa, which contains three sublayers: an epithelial cell layer, which is exposed to the luminal contents; the lamina propria, which is one layer deep; and the muscularis mucosae, which is two layers deep [74]. Deep to the mucosa is the submucosa, a connective tissue layer containing the circulatory vessels, followed by the muscularis externa, which is comprised of two smooth muscle layers that perform peristaltic functions [74]. The adventitia is the outer layer, made up of fibroblasts, collagen, vessels, and nerves, and which is coated in a mesothelial layer called the serosa [74].

Healing Mechanisms of the Lower Gastrointestinal Viscera

Healthy intestinal wound healing following injury is a balance between debris removal and migration, proliferation, and differentiation of new healthy tissue [77]. When the innermost layer of intestinal epithelium is injured, the cells surrounding the wound site adopt a flattened morphology and migrate into the wound *via* reorganization of the actin cytoskeleton, which ultimately re-establishes the intestinal barrier in a process called “epithelial restitution” [77]. Proliferation, maturation, and differentiation of new epithelial cells then takes place, resurfacing the wound and restoring proper tissue functionality [77]. In instances of intestinal injury that provoke a more pronounced inflammatory response, macrophages and neutrophils infiltrate, releasing reactive oxygen species and enzymes that damage and degrade the local tissue [78]. Pro-inflammatory cytokines and peptides with chemotactic and cell-activating properties are then released, and myofibroblasts arrive in order to contract the wound and aid in production of ECM

for tissue repair [78]. Growth factors and cytokines that are employed in these healing processes include transforming growth factors alpha and beta (TGF-α and TGF-β), epidermal growth factor (EGF), fibroblast growth factor (FGF), keratinocyte growth factor (KGF), insulin-like growth factor (IGF-I), and cytokine interleukins 1 beta and 2 (IL-1β and IL-2) [77]. Local and migratory inflammatory cells secrete both ECM-modifying and ECM-degrading enzymes [78], which simultaneously remove tissue debris and damaged cells and induce regeneration of new healthy tissue. Enzymes that contribute to ECM degradation include serine proteases, such as elastases and collagenases, and matrix metalloproteinases (MMPs) [78]. MMP activity is balanced with the activity of the enzymes that inhibit them, called tissue inhibitors of metalloproteinases (TIMPs), and this balance directly impacts the severity of damage that takes place during inflammatory events [78].

Surgical repair of transected intestinal tissue follows a progression of steps for restoration of the full thickness of the bowel. After apposition of the severed edges or ends of bowel, granulation tissue forms, followed by epithelial cell migration and proliferation at the mucosal level for sealing of the defect site [79]. This sealing may take place in as little as three days with primary healing (i.e. edges being in precise apposition), but is delayed in cases of secondary healing, typically due to mucosal eversion or inversion [79-81]. As primary healing is rarely feasible, the first several days of healing post-surgery are usually dominated by inflammatory cell infiltration and collagen lysis, then followed by fibroplasia and subsequent immature collagen deposition [80, 82]. Finally, tissue remodeling takes place with collagen content being relatively stable by five to six weeks post-repair [80, 82].

Pathologies and Aberrant Healing of the Lower Gastrointestinal Viscera

Aberrant healing of the intestinal tissue can be of two main types: insufficient healing, resulting in fistula or ulcer formation, or excessive tissue repair, resulting in fibrosis and stricture (Figure 1-5) [78]. As described by Rieder *et al.* (2007), instigators of more dramatic inflammatory responses induce enzyme and chemical mediator release from monocytes, macrophages, and granulocytes, resulting in sloughing of epithelial cells and destruction of ECM within the lamina propria, even extending into the submucosal tissue in severe cases. The resulting tissue damage appears

clinically as ulcerations on the luminal surface. Ulcerations may also be present due to impaired recruitment of myofibroblasts. Growth and chemotactic factor release serves as a dose-dependent solicitation for myofibroblast recruitment, and so a reduction in this gradient compared to the requirement for healthy tissue maintenance or post-injury repair can result in insufficient quantities of migrated myofibroblasts. Chronic inflammation may also alter myofibroblast function, including their ability to contract the wound site and produce ECM for repair.

Inflammation following acute injury is a normal process instigated in order to recruit cells to the injury site for debris removal and tissue repair. Intestinal epithelium may experience acute injury due to toxins, pathogen invasion, oxidative stress, pharmaceutical agents, or normal digestion [77], in addition to a multitude of inflammatory conditions. Mucosal damage is a frequent occurrence in cases of inflammatory bowel disease (IBD), which includes two conditions, Crohn's disease and ulcerative colitis, within which the mucosal damage can be especially severe and for which the etiologies are still elusive [77, 78]. Proposed etiologies, in a broad sense, include deranged intestinal flora, excessive or abnormal reactivity of the intestinal immune response, diet, environmental factors, and genetic factors [83]. The weakened intestinal lining caused by these conditions predisposes the individual to infiltration from inflammation-inducing luminal contents, including bacteria, which results in a chronic battle between fighting invaders with inflammatory cells and their released products and damaging the host tissue due to the persistent presence of these cells and products [83]. The constant inflammatory environment can result in focal regions of intestinal fibrosis, however. Intestinal fibrosis occurs as a result of chronic or recurrent episodes of inflammatory cell infiltration and mediator release [78], and is essentially an over-exuberance of normal repair processes. Repeated or persistent stimulation of myofibroblast recruitment and activation can induce excessive ECM production by the cells, with mismatch of the normal degradation mechanisms that take place in acute inflammatory processes [78]. Roughly 75% of individuals with Crohn's disease require surgery at least once in their lifetime, with half of these being indicated for obstruction and stricture [78]. Apart from IBD-related conditions, other causes of severe mucosal damage include radiation therapy and chronic ischemia, and strictures may also be induced by colonic wall thickening and fibrotic colonopathy secondary to cystic fibrosis, collagenous colitis, and rarely in cases of recurrent diverticulitis [78].

Factors affecting the healing of gastrointestinal surgical repairs include the approach and

materials used, achievement of adequate blood supply, tension on the repair, bacterial contamination, distal obstruction, medications (e.g. steroidal drugs, non-steroidal anti-inflammatories), patient nutrition and hydration status, and the presence of other systemic disorders [79]. Such factors may alter the timeline of tissue regeneration, prevent proper recovery and functionality, or induce complications.

Brief Overview of Materials Used for Surgical Intervention of the Lower Gastrointestinal System

One of the most common approaches utilized in the surgical management of disorders of the lower gastrointestinal system is intestinal anastomosis, permitting the removal of diseased bowel or restoration of continuity following severe trauma. Pertaining to this surgical technique and others encountered within the gastrointestinal system, suturing and stapling methods are the predominant approaches employed by surgeons. Details of distinct suturing and stapling methods are discussed more thoroughly in Chapters Two and Three of this dissertation; however, suture materials utilized for such applications are discussed here. Other biomaterials used in gastrointestinal procedures, particularly intraluminal implants, are also briefly reviewed.

Sutures are one of the most commonly used biomaterials. Historically, sutures have consisted of a wide range of materials, including iron and steel wires, desiccated animal intestinal tissue, horse hair, silk, and plant fibers, but have largely transitioned into synthetic polymer composition [84]. Suture materials can be divided into broad overarching subcategories in regards to their structural characteristics, including cross-sectional size (ranging from 11-0 to 6), filament structure (multifilament, monofilament, pseudo-monofilament), and surface texture (smooth, barbed), as well as subcategories pertaining to their physical characteristics, including tensile strength (knot-pull strength, straight-pull strength), degradability (absorbable versus non-absorbable), and stiffness/flexibility [84, 85]. The particular application impacts the selection of suture material, influenced by such factors as tissue thickness, tissue environment, bodily fluid exposure, and the anticipated timeframe of surgical site healing. Regardless of the specific material used, sutures must be strong, yet flexible, pliable, and able to endure tensile forces [84].

Absorbable sutures used most commonly in gastrointestinal procedures include chromic

catgut, polyglactin 910 (Vicryl), lactomer (Polysorb, Velosorb), polyglycolic acid (Dexon), Polyglytone 6211 (Caprosyn), Polygliocaprone 25 (Monocryl), polyglycolic acid/polycaprolactone (Quill, Monoderm, Stratafix PGA-PCL Plus), Glycomer 631 (Biosyn, V-Loc 90), polyglyconate (Maxon), and polydioxanone (PDS, V-Loc 180, Stratafix PDO, Quill PDO) [86]. All of these degrade by hydrolysis and evoke no more than a minimal foreign body response, except for catgut which is eliminated by enzymatic degradation and phagocytosis and is known to elicit a moderate inflammatory response [86]. Degradation timeframes are highly variable between materials; for example, polyglactin 910 is maintained for only approximately forty-two days, whereas polydioxanone can last for 6 months [86]. These timeframes can also be impacted by the presence of body fluids of a higher pH, including digesta. Degradation timeframe is one of the main factors that influences suture selection, as the suture should remain at the repair site minimally for the anticipated duration the tissues are expected to heal and regain integrity, but not an excessively long duration in order to prevent the risk of complications from foreign material. Strength of intestinal repairs begins to increase around day five post-surgery, and approximately 50-70% of the original bursting strength is regained within two to three weeks [86, 87].

Nonabsorbable sutures used in gastrointestinal surgeries include polyamide (Ethilon, Dermalon, Surgilon, Nurolon, Quill Nylon), polybutester (Novafil, V-Loc PBT), polypropylene (Prolene, Surgipro, Quill Polypropylene, Stratafix Polypropylene), hexafluoropropylene VDF (Pronova), stainless steel (Surgical Stainless Steel (mono or multi), Steel, Flexon), silk (Permahand, Sofsilk), and polyester (Mersilene, Ethibond Excel, Ticron, Surgidac) [86]. Fortunately, despite these sutures remaining within the tissues indefinitely, they rarely evoke a significant foreign body response [86]. Such sutures may be most appropriate for long-term implants.

Most cases of intestinal surgery are best facilitated by 4-0 to 3-0 synthetic absorbable monofilament suture varieties, as these degrade at a favorable rate, are less traumatic to the delicate bowel wall than multifilament suture, and are of a small enough cross-sectional size that they are at a low risk of inciting an adverse inflammatory response [85, 88]. Biosyn and Monocryl are especially good options as they retain approximately half of their tensile strength for three weeks post-surgery [88].

While suturing and stapling methods remain at the forefront of mechanisms for intestinal

repair, alternative options or adjuncts to improve outcomes have been evaluated over the past several decades. A common theme of many of these implants is intraluminal placement, whether to act as an expansion/dilatation device for prevention or mitigation of stenosis, or shielding of the fresh surgical site from contact with digesta. Various implants have been fabricated with features that vary depending on the segment of intestine to which they are to be implanted, invasiveness of the surgery, and intended longevity of the device. Many of these implants found within the literature are either no longer utilized or have not advanced to common utility as they have been replaced by more advanced implants or results have either been suboptimal or not significant enough to warrant inclusion in traditional repair methods.

Various intestinal stents have been investigated over the years, with the goals of maintaining lumen patency, shielding the anastomotic repair from fecal contaminants, preventing stricture, or even supporting apposition of the cut ends of the bowel [89]. Long-term metallic stents have long been considered the most successful of these implants for palliative treatment of obstruction, but benefits to alternative polymer-based stents include minimization of tissue trauma, optional removability at a later date (in the case of non-degradable polymers), and degradability [90-92]. Degradability is an especially positive aspect as one of the leading concerns associated with non-degradable stents is the potential for migration and subsequent obstruction or perforation [93]. Arora & Okolo (2006) describe successful utility of a Polyflex (Boston Scientific) self-expanding stent, typically used within the esophagus, for treatment of intestinal obstruction. Wang *et al.* (2011) and Winkeltau (1993) each investigated application of polymer-based degradable stents or tubes following operative procedures within the intestinal tract and found that such implants may be acceptable additions to traditional techniques. Magnesium alloys are an alternative material for application to intestinal stents that may present the structural advantages of a metallic implant, but beneficially degrade and prevent delayed adverse tissue reaction that could ultimately restrict the lumen diameter [93]. Several commercially-available stent products have been developed, many of which share commonalities such as mesh-like form, flexibility, expandability, and flared ends. Products include WallFlex Duodenal Stent (Boston Scientific), WallFlex Colonic Stent (Boston Scientific), Evolution Colonic Controlled-Release Stent (Cook Medical), and Evolution Duodenal Controlled-Release Stent (Cook Medical). Biliary duct, pancreatic duct, and pancreatic psuedocyst stents are also available with similar forms and

functions as intestinal stents, and include the AXIOS Stent (Boston Scientific), WallFlex Biliary Transhepatic Stent System (Boston Scientific), and WallFlex Biliary RX Stent (Boston Scientific). These products are typically formed from either a flexible biocompatible metal, polymer, or a combination of metal and polymer.

Colonic anastomotic leakage has been reported to occur in 2.5 to 20% of cases, with estimated leakage rates being greater in the most distal regions of the colon [94, 95]. Protective stomas are a common method of diverting fecal material from the surgical site during the immediate post-operative period, but intraluminal implants have been investigated as alternative options [94, 95]. One such device, the Coloshield, is a soft, collapsible tube that is sutured within the lumen of the colon following a colonic repair and acts much like a glove, shielding the mucosal wall from fecal flow and protecting the surgical site [89]. The implant also features woven mesh at one end, reinforcing the construct, and spontaneously breaks free from its attachment site between two and three weeks post-surgery [89]. In a modified technique, surgeons were able to implant the Coloshield through a colotomy following the colonic anastomosis procedure [96]. High rates of anastomotic leakage in procedures performed very distally within the gastrointestinal tract have encouraged development of transanal stents (TAS) for reduction in intra-luminal pressure at the surgical site [97]. Amin *et al.* (2003) evaluated a 4-cm radio-opaque soft silicone tube-shaped TAS with large flanges at either end, and found that patients receiving the implant experienced lower morbidity and a reduced hospital stay when compared to others with a diverting stoma; however, leakage rates were similar and follow-up surgery was more often required in those with a TAS. Bülow *et al.* (2006) similarly found that a silicone TAS did not prevent leakage at the surgical site [98]. Other transanal stents, transanal tubes, and rectal tubes have been evaluated as well [94].

Peripheral Neuropathic Disorders & Biomaterial-Based Therapeutic Advancements

Anatomy of the Peripheral Nervous System

Brief Overview of Gross Anatomy

The peripheral nervous system (PNS) is a continuation of the central nervous system which traverses and reaches all areas of the body and allows for performance of a multitude of functions, including voluntary motor activity and involuntary sympathetic and parasympathetic operations [99]. One division of the PNS, the somatic nervous system, features nerves that communicate with the skin and muscles and which are directly involved in voluntary and conscious actions [100]. The other primary division of the PNS, the autonomic nervous system, is comprised of nerves that communicate with the visceral organs and which facilitate involuntary actions (e.g. heartbeat, respiration, digestion) [100].

One grouping of the peripheral nerves is the cranial nerves, of which there are twelve pairs that descend directly from the brain, and each of which is specialized for a particular region of the head and neck (with a partial exception for the vagus nerve) and greatly vary in their motor and/or sensory capacities; these nerves permit the senses of smell, sight, taste, and audition, and aid in equilibrium and proprioception [100]. Another grouping of peripheral nerves is the spinal nerves, of which there are thirty-one pairs that are connected to the spinal cord by dorsal and ventral roots, which are fused together into individual nerves just prior to exiting the spinal cord on opposing lateral sides [100]. The dorsal and ventral roots are specific to sensory and motor capabilities, respectively, and hence all spinal nerves serve both of these functionalities [100].

Microanatomy

There are two cell groups that constitute the structures of the nervous system tissue: neurons, which conduct impulses from one region of the body to another, and glia, which support the neurons [99]. A neuron is composed of a cell body from which extends dendrite(s) that meet other nearby neurons at synaptic clefts, as well as one to two axons (in most cases) which propagate signals for transference to other neurons *via* the synaptic clefts [99]. These clefts are the site of chemical release that permits the transmission of messages from one neuron to another and ultimately

facilitates signal transduction. There are four main classifications of neurons which vary based on the positioning and number of their axons: unipolar, having a single structure extending from the neuronal cell body; bipolar, having one axon and one dendrite; multipolar, which has one axon and multiple dendrites and is the most commonly found type of neuron; and pseudounipolar, which has a single structure extending from the cell body, but which later branches into two [99] (see Figure 1-6). Glial cells are supportive to neurons, and the PNS specifically features satellite glia that provide nutrients and structure and Schwann cells that wrap around axons and supply myelin [99].

While peripheral nerves vary in fiber composition and fascicle number depending on the region of the body, the microanatomy of nerve trunks is relatively consistent [101] (see Figure 1-7). Nerve fibers are the most minute functional unit of peripheral nerves and are composed of either single axons surrounded by myelin and Schwann cells or several smaller ($\leq$ 2 μm) unmyelinated axons collectively enveloped by Schwann cells [101]. Myelin allows for nerve impulses to be conducted 20 to 100 times faster than in comparable unmyelinated axons [102]. Nerve fibers are grouped together by loose connective tissue called endoneurium and are collectively surrounded by a perineurial sheath to form a fascicle [103]. Fascicles, along with blood vessels traversing between, are secured together with epineurium to form the complete peripheral nerve [103].

Peripheral Nerve Regeneration

Understanding the mechanisms and timeline inherent to peripheral nerve regeneration is essential in the selection of the proper therapy (Figure 1-8) [104, 105]. When damage has taken place that disrupts the axon or transects the nerve, chromatolysis and swelling ensues within the neuron's nucleus and body within a few hours after injury, and proceeds within the axonal stump over the next several days [104, 105]. Wallerian degeneration, the disintegrative process of the axon and myelin, begins in the first two to three days in both anterograde and retrograde directions, and proceeds in the anterograde direction over the following several weeks, facilitated by Schwann cells and macrophages which eliminate the degradation products [104]. Once the basement membrane alone remains, Schwann cells proliferate and serve to guide and myelinate axonal

sprouts between basement membranes of the nerve ends [104, 105]. The proximal axon then sprouts a growth cone, which elongates along the tube at 1 to 3-mm per day with the aid of cytoplasmic extensions and actin [104].

Injury & Pathologic Healing in the Peripheral Nervous System

Peripheral neuropathy and injury consists of a wide range of potential etiologies, including physical damage, thermal intolerance, chemical agent exposure, ischemia, degenerative disorders, neoplasia, infection, and autoimmune disease [105, 106]. The extent of the injury, to include the anatomic location of the nerve, the span and microanatomic region of the nerve affected, and manner in which the nerve is damaged, directly corresponds to the resulting functional impairment [105]. Classifications of nerve injury, on the microanatomic scale, were first distinguished by Seddon (1943), who claimed the three types of nerve injury were neurapraxia, where there is partial demyelination of the nerve but axons remain intact, axonotmesis, where the axon is severed but the endoneurium remains intact, and neurotmesis, where the nerve is completely transected and scar tissue formation has occurred [105, 107]. Shortly thereafter, Sunderland (1951) described a five-degree injury classification model, with first-degree and second-degree injuries being equivalent to neurapraxia and axonotmesis, respectively, third-degree injury representing perineurial and fascicular preservation and endoneurial disruption, fourth-degree injury representing axonal, endoneurial, and perineurial disruption, with only the epineurium remaining intact, and fifth-degree injury being equivalent to neurotmesis [105, 108].

Sunderland (1951) describes the prognosis of the five degrees of nerve injury in reference to their microanatomic characteristics as follows: first-degree injury, or neuropraxia, is quickly reversible as no Wallerian degeneration is required to take place; second-degree injury, or axonotmesis, features some extent of Wallerian degeneration, but is also reliably reversible due to the ability for the damaged axon to be directed back to its end-organ *via* the remaining endoneurial tube; third-degree injury is complicated by such intrafunicular disorganization that fibrosis may ensue within the bundle and impede regeneration and appropriate axonal direction; fourth-degree injury features extensive destruction of axons and their surrounding environment, with any surviving axons facing difficulties in reconjoining to the end-organ and many forming scar tissue;

and fifth-degree injury results in permanent separation of the damaged segments, or after a long period of time and under very particular conditions, a strand of tissue may form containing fibroblasts and Schwann cells along which axons may be capable of traversing [108].

Abnormal healing may occur even in cases where nerve regeneration does proceed, leaving a multitude of adverse effects. Scar tissue may form along the pathway in which the axon is extended, serving as an impediment to further growth [104]. If the regenerating nerve is incapable of traversing the scar tissue, a neuroma may form, which can lead to atrophic muscle innervation or abnormal sensory impulses [105]. Motor and sensory axons may also become misaligned and attempt reconjoining with inappropriate targets, which can result in preferential motor reinnervation, or "pruning" of the axon, or innervation of incorrect muscles [104]. There are a multitude of side effects that may ultimately be displayed due to neuropathy or aberrant healing following peripheral nerve injury, including poor motor and/or sensory functionality, chronic pain, deranged temperature sensitivity, muscle atrophy, weakness, loss of reflexes, and incoordination, all of which greatly affect a person's ability to remain self-sufficient and affect quality of life [102, 106].

Surgical Repair of Peripheral Nerve Injury

Historic

Understanding the progression of peripheral nerve repair throughout history affords a greater appreciation for the availability of current therapeutic options and optimism for further advancement. Incredibly, during the Hippocratic era, in which much anatomic and medical knowledge was being accumulated, there was no distinct differentiation between nerve and tendon [109]. Hippocrates (460-370 B.C.) was aware of the impediments to nerve regrowth and reconjoining after transection, and although many of his accounts evoke pessimism in the tissues' regenerative capabilities, roughly 1400 years later, a single account was depicted in a surgical treatise describing a peripheral nerve repair procedure that he may have practiced [109]. Apart from this account, documented repair of peripheral nerves and the prospect of their regenerative capacity dates back to the second century A.D., with detailed descriptions of suturing methods for transected nerves having been first penned in the 1500s [110]. Evidence of successful outcomes in

peripheral nerve repair surgery continued to be published into the 1700s, and then with great advancements in histologic techniques in the 1800s, the improved capacity to understand peripheral nerve microanatomy led to a grander interest in seeking methods by which peripheral nerve regeneration may be supported [110].

The first autograft nerve reconstruction was documented in 1870, followed shortly by descriptions for allograft nerve repair [110]. Soon thereafter, attempts were made at bridging peripheral nerve defects with tissue other than that of nerve origin, specifically decalcified bone [110, 111]. These "nerve tubulation" procedures were initially unsuccessful due to scar tissue propagation, but in 1882, a 3-cm gap in the sciatic nerve of a dog was successfully bridged [110]. The 1900s featured a great interest in experimental surgeries with intense studying of the outcomes of nerve grafting, anastomosing, and crossing, and refinement of these techniques [110] (see Figure 1-9). One such technique that gained much interest was termino-lateral anastomosis (also called end-to-side neurorrhaphy), which experienced a steep rise in exploration during this time, followed by a near-complete elimination for over fifty years until rediscovery in the 1990s [112]. Due to the highly variable results of peripheral nerve repair, pessimism ensued, resulting in a decline in collaboration efforts between basic and clinical scientists, and a subsequent shift in focus from novel nerve regeneration efforts to enhancements in the surgical reconstruction process [110]. As microsurgical capabilities enhanced, intricate procedures such as group fascicular repair were attempted in order to facilitate more accurate alignment of axons; however, results demonstrated minimal evidence of superior outcomes compared to the more traditional, though less precisely aligned, epineural repair [103]. Fortunately, in the last several decades, coinciding with the growing interest in regenerative medicine and tissue engineering efforts in the biomedical field overall, an increased interest in methods by which peripheral nerve regeneration can be supported and enhanced has taken place which has revitalized the field and led to a great number of advancements.

Present-Day & Prospective Therapeutics

When a peripheral nerve injury necessitates repair that is incapable of mitigation by anastomosis, a variety of therapeutic options are available; however, due to suboptimal outcomes and high complication rates, alternative options are being heavily investigated by biomedical researchers.

Approximately 33% of all PNIs ultimately result in inadequate recovery, often due to aberrant healing and propagation of scar tissue which impedes Schwann cell proliferation and axon sprouting [102, 113]. One of the major impediments to surgical outcomes pertains to the timeframe in which treatment is pursued; in many cases, surgery may not be pursued until months following injury after inherent nerve regeneration mechanisms and medical management do not result in adequate healing [104]. Surgical therapeutic options can be broadly classified into groups based on the nature of the implant; specifically, grafts or nerve conduits [105]. Grafts are derived from biological sources and include autologous grafts, which are sourced from another region of the same individual receiving the graft, allogenic grafts, sourced from a human donor, and xenogeneic grafts, sourced from an animal of another species [105]. Nerve conduits can either be composed of decellularized nerve tissue or be manufactured from biomaterials, including biological products, such as proteins and polysaccharides, synthetic materials, such as polyesters and polyurethanes, or hybrid composites of both biological and synthetic materials [105].

The leading method of repair in the present-day is utilization of an autologous nerve graft. While this method is beneficial in regards to elimination of the potential for an adverse immunogenic reaction to the graft and ready availability, notwithstanding any co-morbid conditions that may prevent surgery at the donor site, additional morbidities may be associated with the harvesting procedure itself. Allogeneic nerve grafts are an alternative that may be convenient, but pose the risk of inducing an adverse immunogenic reaction which may result in rejection of the graft. Patients receiving an allogeneic graft typically undergo a systemic immunosuppression regimen to prevent this complication, but such drugs are often administered for months or years and may induce their own side effects; for example, tacrolimus can induce nephrotoxicity, neurotoxicity, and gastrointestinal disorders [114]. Similarly to allogeneic grafts, xenogeneic grafts pose a risk of adverse immunogenicity, as well as the potential for zoonotic disease transmission [105].

Nerve conduits, also termed “scaffolds”, “wraps”, or “guides”, are an alternative to nerve grafts that have the prospect of convenience and minimal risk of eliciting an adverse immunogenic reaction. Additionally, there is the proposal that utilization of a conduit in establishing a short gap between nerve ends permits beneficial cell and extracellular matrix accumulation that can ultimately hasten Wallerian degeneration and facilitate appropriate axonal guidance, and studies

have demonstrated successful outcomes corroborating with these concepts [115, 116]. There are several commercially-available nerve conduit products (e.g. Integra LifeSciences NeuraGen, Synovis Micro Companies Alliance Neurotube, Salumedica Salutunnel) [105], composed of materials such as type I collagen, polyglycolic acid, and porcine small intestinal submucosa; however, no option has successfully displayed the ideal properties needful for this application [117]. The increasingly exciting possibilities of nerve conduits has led to a dramatic increase in the production of non-autologous prototypes in the past 15 years, with a stark transition in fabrication methods and materials employed [118].

Nerve Conduits

Fabrication Methods

While nerve conduits have been investigated for decades, advancements in tissue engineering efforts and optimistic results from prior nerve regeneration studies have fueled deeper investigation into materials and constructs that may perform effectively for this application. Fabrication methods utilized in nerve conduit studies in the mid-1980s through mid-1990s strictly employed dipping for formation of the conduit structure, but this trend began to decrease over the next decade, where sheet rolling, non-neural tissue processing, lumen filling, and molding became extensively evaluated [118]. The past 15 years has seen a diversity of methods employed in addition to those aforementioned, such as 3D printing/bioprinting, electrospinning, surface coating, porogen extraction, braiding/weaving, machining, phase separation, mechanical pulling/stretching, directional freezing, solvent casting, melt extrusion, and photolithography [118]. It is common for more than one method to be employed for the fabrication of a single conduit prototype [118].

Materials

Highly successful outcomes have been reported with utilization of non-degradable materials for nerve conduits, such as median and ulnar nerve repairs employing silicone tubes [115]; however, concern lies in the possibility that maintenance of implanted material *in situ* following the period of utilization may result in complications such as local scar tissue formation, nerve compression

[115], delayed foreign body reaction, or future infection. A host of studies have revealed that some iterations of nerve conduits composed of biodegradable materials are as effective as the gold-standard autologous nerve graft, or result in even better outcomes [115]. Biodegradable materials evaluated in experimental studies include PGA, PLA, glycolide trimethylene carbomate (Maxon), collagen, PCL, chitosan, poly(3-hydroxybutyrate), alginate, hyaluronic acid, silk fibroin protein, and PLGA [105, 115, 119, 120]. Composites of more than one biomaterial may be highly beneficial in the introduction of optimal components from individual products, and is a method often employed in fabrication of biomaterial-based implants. While an extensive review of all of these materials is out of the scope of this work, several are described more thoroughly as they have substantiated a wealth of interest based on their promising results in applications for peripheral nerve repair to-date.

Chitosan, a polymer of acetyl glucosamine derived from chitin, has been found to feature high biocompatibility, degradability, antibacterial properties, and affordability [115]. Applications of chitosan in nerve conduits have demonstrated that the material has highly favorable mechanical properties, hydrophilicity, which prevents scar tissue propagation and improves affinity of neural cells, and slow degradability suitable to the region and which can be tailored depending on the proportion of deacetylation and molecular weights employed [116, 119]. Chitosan in combination with other appropriate materials may amplify neural cell affinity as alone it does not perform as an ideal substrate [119]. Mingyu *et al.* (2004) found that films of chitosan and poly-L-lysine featured enhanced nerve cell attachment, differentiation, and growth, likely owing to the favorable hydrophilicity and increased surface charge. Chitosan in combination with gelatin appears to result in a composite with improved elasticity and enhanced neural cell affinity and differentiation [116, 121]. Chitosan-PGA composite grafts have also been utilized for successful functional recovery of a 3-cm nerve defect in dogs [116, 122].

Collagen is the most prevalent material utilized in commercially-available nerve conduits, and for good reason, as this material takes advantage of the preserved fibrillar structure found within the natural host tissue in order to induce biomimetic effects, including cell adhesion and migration [105, 123]. Collagen conduits have shown such properties as resorption, non-friability, and flexibility, which aids in the prevention of compression and scar tissue formation [105]. Additionally, collagen conduit walls are semi-permeable, allowing diffusion of nutrients between

the external nerve environment and the lumen in the range of 0.1 to 0.5 μm [105]. Pitfalls of the material, which include weak manipulability and disadvantageous resistance to mechanical forces, suggest that application of collagen in composites with other more durable materials may be a more advantageous approach [123]. Xu *et al.* (2016) developed silk fibroin/collagen scaffolds and seeded them with Schwann cells and adipose-derived stem cells prior to *in vivo* implantation. The results were comparable to autologous grafts, but superior to scaffolds in the absence of cells, and none of the animals displayed signs of inflammation at their implant sites [123]. Stang *et al.* (2005) evaluated collagen type I and III composite scaffolds of different physical structures with infused Schwann cells and found that, while autologous grafts performed the best, hollow tubes and tubes with a reduced lumen demonstrated noteworthy nerve growth, and tubes with an internal skeleton impeded growth [124]. These results, and the evidence that the commercially-available collagen conduits do not perform as optimally as warranted, suggest that collagen may best be utilized in nerve conduits as composites with other advantageous materials. Gelatin, which is denatured collagen, has also been used in nerve regeneration applications after cross-linking the material to other chemicals in order to evoke more optimal properties [105].

Silk, another biologically-derived polymer, is a promising material for nerve regeneration applications due to its favorable physicochemical, mechanical, and biological properties, including oxygen and fluid permeability, minimal swelling, and simultaneous strength and flexibility, with a minimal inflammatory response comparable to many other degradable polymers [125, 126]. Silk also features favorable degradation profiles that can be easy tailored to a desired timeframe, making it feasible to produce variants for different nerve defect lengths [126]. This may ultimately translate to a reduced risk of nerve constriction or foreign body response that may otherwise occur due to the material remaining at the repair site longer than is needed. Silk has demonstrated the capacity for adherence and proliferation of both Schwann cells and neurons without altering their morphology, and silk products can display favorable peptide sequences, either dependent on the silk origin or fabricated as such [125]. Ghaznavi *et al.* (2011) applied porous silk fibroin conduits to 8-mm nerve defects in rats and found a greater number of proximal axon sprouts and distal connections in those animals receiving the silk conduits in comparison to commercial collagen guides [126]. Yang *et al.* (2007) applied silk fibroin conduits with oriented filaments into 10-mm nerve defects in rats, and found that after 6 months, the conduits promoted functional and

morphological recovery nearly comparable to autologous grafts [127].

Poly-ε-caprolactone (PCL) is a synthetic polymer that has gained much attention for applications in peripheral nerve repair, owing to it structural properties, non-immunogenicity, easy sterilizability, simultaneous strength and flexibility, and the low cost associated with manufacturing constructs by solvent casting [128]. While PCL has an inherently slow degradation rate, potentially in terms of years, it is an exceptional option for co-polymer composites which often can reduce the degradation timeframe while imparting favorable properties inherent to the PCL [129]. Sun *et al.* (2009) fabricated ultrathin PCL conduits with a pitted, microporous structure that demonstrated the capacity for nerve tissue growth and Schwann cell penetration across the entire 10-mm structure after only two weeks of *in vivo* implantation [129]. A follow-up study of eighteen weeks revealed histologic outcomes of the PCL conduits comparable to those of the autologous nerve grafts, as well as demonstrated re-innervation of end organ muscle and skin similar between both groups [128]. PCL scaffolds have also shown the capacity to serve as *in vitro* platforms for differentiation of stem cells exposed to neuronal growth factors, as evidenced by their expression of the neuron-specific markers nestin, β-tubulin-III, and neuron-specific enolase [130].

PLGA is a popular synthetic polymer that has shown great potential for use in nerve conduits due to its manipulatable degradation timeframes and significant biocompatibility [131]. Enhanced nerve regeneration has been demonstrated in various studies using PLGA-based conduits, but especially when they feature inclusion of growth factors, Schwann cells, or interior support structures [131]. When seeded with neural stem cells, the material has been shown to facilitate attachment and growth, as well as differentiation into neurons [132]. Bini *et al.* (2004) fabricated an electrospun nanofiber PLGA tube, which demonstrated no swelling or inflammatory response and successful nerve regeneration in five out of eleven rats after only one month post-implantation into a 10-mm defect [133]. Lee *et al.* (2006) fabricated PLGA-coated collagen conduits with the intention of enhancing structural integrity and elasticity of the more traditional collagen-only construct, which can break or collapse during the regeneration process at larger nerve defects [134]. Twelve weeks following implantation into a 15-mm nerve defect in rabbits, the conduit showed superior morphologic and electrophysiologic outcomes compared to collagen-filled vein grafts.

Inclusion of bioactive molecules or nanomaterials into nerve conduits is one possible mechanism of enhancing nerve regenerative capacity. Common approaches include incorporation of or functionalization with laminin, neural growth factors, or graphene [120]. Graphene is a carbon lattice monolayer (2D) nanomaterial that has acquired great intrigue in the biomedical field over the past several years due to its biocompatibility, flexibility, transparency, favorable mechanics, bioactivity, and thermal and electrical conductive capacity, leading it to be a prospective material for drug delivery, bioelectrodes, stem cell differentiation, and tissue engineering applications [135-137]. Graphene-related materials come in several compositions, including single- and few-layered graphene, graphene oxide (GO), high oxygen graphene (HOG), and reduced graphene oxide (Figure 1-10) [105, 120]. While each composition has the potential to evoke different effects from one another in biomedical applications [117], GO has gained special attraction with its abundant hydrophilic oxide groups [138]. GO applications have become especially promising in the realm of peripheral nerve repair. GO materials in composites with polymers have demonstrated enhanced adherence, proliferation, and differentiation of neural stem cells and Schwann cells [136, 139, 140], and have shown to positively modulate axonal outgrowth *in vitro* [141]. These positive cellular responses may be largely owing to surface factors of the material including nanotopography, versatile surface chemistry, electrical conduction, and functionalization capacity [142, 143]. For peripheral nerve applications, GO is often incorporated into or applied to the surface of materials with other favorable characteristics, including polymers previously mentioned [142]. Wang *et al.* (2019) found that GO-coated silk fibroin/(poly(L-lactic acid-co-caprolactone) scaffolds not only enhanced Schwann cell migration, proliferation, and myelination *in vitro*, but successfully repaired a 10-mm sciatic nerve defect *in vivo*. Wang *et al.* (2017) also demonstrated that GO-decellularized scaffolds could facilitate nerve regeneration *in vivo*, with significantly improved sciatic nerve action potentials, myelin sheath thickness, axon diameter, and muscle rehabilitation level than other scaffolds evaluated [144]. GO incorporated into materials and functionalized with therapeutic agents can also serve as drug delivery vehicles [142].

Structural Features, Adjuncts, & Manipulations

Apart from the materials employed for conduit fabrication, there are a multitude of ways in which

nerve conduits can be manipulated to evoke enhance nerve regeneration. Conduit structure should ultimately support and guide axonal growth, thwart fibrous tissue ingrowth within the lumen or at the nerve stumps, and facilitate diffusion of nutrients between the lumen and external environment [145]. Most often, nerve conduits are cylindrical tubes, but this does not imply hollowness. Conduits have been designed with complex internal features such as fibers, channels, scaffolding, micropatterning, and grooving (Figure 1-11) [105, 125]. Longitudinal channels essentially mimic native endoneural tubes, promoting axonal guidance in a contained environment until reaching the distal nerve stump [146]. These channels may also ease adhesion of Schwann cells and release of growth factors [132]. Microgrooving not only increases surface area, but can also facilitate axon guidance, stimulate firm adherence of Schwann cells, induce spreading of cellular processes, and lead to optimal cell orientation [132]. The microarchitecture of the interior directly impacts the growth cone attachment and propensity for extension in a particular direction during the regeneration process [132]. Mimicking of ECM fibrillar structure is one tactic in the production of a favorable biomimetic surface, and can often be achieved with electrospinning techniques [132]. One important consideration when including intraluminal structures or surface features in the conduit design is predicting the swelling behavior of the material and how that may alter the structure when exposed to fluid. Nerve scaffolds are often fabricated at very small dimensions for initial small mammal *in vivo* testing, and constructs at such minute dimensions may incur lumen obstruction at even minute levels of swelling.

Porosity of the conduit walls is an imperative feature as this allows proper nutrient exchange, but not all pore sizes evoke the same results [105, 145]. Lower porosity materials may maintain luminal growth factors better, but prevent proper diffusion of oxygen to cells [145]. The benefits of highly porous walls, including better nutrient diffusion and higher structural flexibility, without loss of small intraluminal soluble factors, can be mitigated by manipulation of wall thickness; specifically, increasing wall thickness displays an inhibitory effect on extraluminal diffusion [145]. Wall thickness also plays an important role, as it has been shown that wall thickness in excess of 0.81-mm impedes axonal outgrowth, predisposing to neuroma formation [147]; this may actually be owing to a reduction in the wall porosity simultaneous with increased wall thickness [147].

Inclusion of electrical or magnetic properties in nerve conduits are other possibilities that

have gained much attention [132]. Electrical stimulation of conductive materials has demonstrated the ability to assist in regenerating peripheral nerve [146]. Polyaniline and polypyrrole are conductive polymers that feature tunable conductivity and biocompatibility [146]. Magnetic nanoparticles have been incorporated into composites with the intent of aligning fibrils of collagen, fibrin, and/or laminin during fabrication, facilitated with application of a magnetic field, under the basis that unidirectional fibers have demonstrated enhanced axon regeneration [132]. Additional adjunctive components to nerve conduits include infusion of cells, neurotrophic factors, or pharmacologic agents into the lumen [105, 146]. Addition of Schwann cells or MSCs intraluminally may contribute to promotion of axon regeneration, and MSCs may be successfully differentiated into neural-lineage cells in the presence of simultaneously-delivered neural growth factors [146].

References

[1] Williams, D.F., *On the nature of biomaterials.* Biomaterials, 2009. **30**(30): p. 5897-5909.

[2] Huebsch, N. and Mooney, D.J., *Inspiration and application in the evolution of biomaterials.* Nature, 2009. **462**(7272): p. 426-432.

[3] Parida, P., Behera, A., and Chandra Mishra, S., *Classification of Biomaterials used in Medicine.* International Journal of Advances in Applied Sciences, 2012. **1**(3).

[4] Ali, S.H.R., Almaatoq, M.M., and Mohamed, A.S.A., *Classifications, Surface Characterization and Standardization of Nanobiomaterials.* International Journal of Engineering & Technology, 2013. **2**(3): p. 187.

[5] Kargozar, S., Ramakrishna, S., and Mozafari, M., *Chemistry of biomaterials: future prospects.* Current Opinion in Biomedical Engineering, 2019. **10**: p. 181-190.

[6] Festas, A., Ramos, A., and Davim, J., *Medical devices biomaterials – A review*. Proceedings of the Institution of Mechanical Engineers, Part L: Journal of Materials: Design and Applications, 2020. **234**(1): p. 218-228.

[7] Heness, G. and Ben-Nissan, B. *Biomaterials - Classifications and Behaviour of Different Types of Biomaterials*. 2004 [cited 2021 Mar 17]; Available from: https://www.azom.com/article.aspx?ArticleID=2630.

[8] Kiradzhiyska, D. and Mantcheva, R., *Overview of Biocompatible Materials and Their Use in Medicine.* Folia Medica, 2019. **61**: p. 34-40.

[9] Wang, Y.-X., Robertson, J.L., Spillman, J.W.B., and Claus, R.O., *Effects of the Chemical Structure and the Surface Properties of Polymeric Biomaterials on Their Biocompatibility*. Pharmaceutical Research, 2004. **21**(8): p. 1362-1373.

[10] Ghaffar, A., Schoenmakers, P.J., and Van Der Wal, S., *Methods for the Chemical Analysis of Degradable Synthetic Polymeric Biomaterials.* Critical Reviews in Analytical Chemistry, 2014. **44**(1): p. 23-40.

[11] Park, J.J., Yu, E.J., Lee, W.-K., and Ha, C.-S., *Mechanical properties and degradation studies of poly(D,L-lactide-co-glycolide) 50:50/graphene oxide nanocomposite films.* Polymers for Advanced Technologies, 2014. **25**(1): p. 48-54.

[12] Darestani, M., Entezami, A., Mobedi, H., and Abtahi, M., *Degradation of Poly(D,L-lactide-co-glycolide) 50:50 Implant in Aqueous Medium.* Iran Polym J, 2005. **14**.

[13] Makadia, H.K. and Siegel, S.J., *Poly Lactic-co-Glycolic Acid (PLGA) as Biodegradable Controlled Drug Delivery Carrier.* Polymers, 2011. **3**(3): p. 1377-1397.

[14] Vey, E., Rodger, C., Booth, J., Claybourn, M., Miller, A.F., and Saiani, A., *Degradation kinetics of poly(lactic-co-glycolic) acid block copolymer cast films in phosphate buffer solution as revealed by infrared and Raman spectroscopies.* Polymer Degradation and Stability, 2011. **96**(10): p. 1882-1889.

[15] Shah, R., Saha, N., and Saha, P., *Influence of temperature, pH and simulated biological solutions on swelling and structural properties of biomineralized (CaCO3) PVP–CMC hydrogel.* Progress in Biomaterials, 2015. **4**(2-4): p. 123-136.

[16] Yang, S., Fu, S., Zhou, Y., Xie, C., and Li, X., *Preparation and Release Properties of a pH-Tunable Carboxymethyl Cellulose Hydrogel/Methylene Blue Host/Guest Model.* International Journal of Polymeric Materials, 2010. **60**(1): p. 62-74.

[17] Zhuo, S., Zhang, F., Yu, J., Zhang, X., Yang, G., and Liu, X., *pH-Sensitive Biomaterials for Drug Delivery.* Molecules, 2020. **25**(23): p. 5649.

[18] Kim, Y.-J. and Matsunaga, Y.T., *Thermo-responsive polymers and their application as smart biomaterials.* Journal of Materials Chemistry B, 2017. **5**(23): p. 4307-4321.

[19] Li, X., Cai, S., Zhang, W., Xu, G., and Zhou, W., *Effect of pH values on surface modification and solubility of phosphate bioglass-ceramics in the CaO–P2O5–Na2O–SrO–ZnO system.* Applied Surface Science, 2009. **255**(22): p. 9241-9243.

[20] Amani, H., Arzaghi, H., Bayandori, M., Dezfuli, A.S., Pazoki-Toroudi, H., Shafiee, A., and Moradi, L., *Controlling Cell Behavior through the Design of Biomaterial Surfaces: A Focus on Surface Modification Techniques.* Advanced Materials Interfaces, 2019. **6**(13): p. 1900572.

[21] Poncin-Epaillard, F., Vrlinic, T., Debarnot, D., Mozetic, M., Coudreuse, A., Legeay, G., El Moualij, B., and Zorzi, W., *Surface Treatment of Polymeric Materials Controlling the Adhesion of Biomolecules.* Journal of Functional Biomaterials, 2012. **3**(3): p. 528-543.

[22] Klopfleisch, R. and Jung, F., *The pathology of the foreign body reaction against biomaterials.* Journal of Biomedical Materials Research Part A, 2017. **105**(3): p. 927-940.

[23] Wu, J., Zhao, C., Lin, W., Hu, R., Wang, Q., Chen, H., Li, L., Chen, S., and Zheng, J., *Binding characteristics between polyethylene glycol (PEG) and proteins in aqueous solution.* Journal of Materials Chemistry B, 2014. **2**(20): p. 2983.

[24] Lee, J.H., Kopecek, J., and Andrade, J.D., *Protein-resistant surfaces prepared by PEO-containing block copolymer surfactants.* Journal of Biomedical Materials Research, 1989. **23**(3): p. 351-368.

[25] Kim, S.Y., Lee, Y.M., Baik, D.J., and Kang, J.S., *Toxic characteristics of methoxy poly(ethylene glycol)/poly(ε-caprolactone) nanospheres; in vitro and in vivo studies in the normal mice.* Biomaterials, 2003. **24**(1): p. 55-63.

[26] Hulshof, F., Schophuizen, C., Mihajlovic, M., Blitterswijk, C., Masereeuw, R., Boer, J., and Stamatialis, D., *New insights into the effects of biomaterial chemistry and topography on the morphology of kidney epithelial cells.* Journal of Tissue Engineering and Regenerative Medicine, 2018. **12**(2): p. e817-e827.

[27] Montanaro, L., Arciola, C.R., Campoccia, D., and Cervellati, M., *In vitro effects on MG63 osteoblast-like cells following contact with two roughness-differing fluorohydroxyapatite-coated titanium alloys.* Biomaterials, 2002. **23**(17): p. 3651-9.

[28] Galli, C., Collaud Coen, M., Hauert, R., Katanaev, V.L., Gröning, P., and Schlapbach, L., *Creation of nanostructures to study the topographical dependency of protein adsorption.* Colloids and Surfaces B: Biointerfaces, 2002. **26**(3): p. 255-267.

[29] Han, M., Sethuraman, A., Kane, R.S., and Belfort, G., *Nanometer-Scale Roughness Having Little Effect on the Amount or Structure of Adsorbed Protein.* Langmuir, 2003. **19**(23): p. 9868-9872.

[30] Zhang, K., Xiao, X., Wang, X., Fan, Y., and Li, X., *Topographical patterning: characteristics of current processing techniques, controllable effects on material properties and co-cultured cell fate, updated applications in tissue engineering, and improvement strategies.* Journal of Materials Chemistry B, 2019. **7**(45): p. 7090-7109.

[31] Zhang, P.-X., Han, N., Kou, Y.-H., Zhu, Q.-T., Liu, X.-L., Quan, D.-P., Chen, J.-G., and Jiang, B.-G., *Tissue engineering for the repair of peripheral nerve injury.* Neural regeneration research, 2019. **14**(1): p. 51-58.

[32] Broughton, G., 2nd, Janis, J.E., and Attinger, C.E., *Wound healing: an overview.* Plast Reconstr Surg, 2006. **117**(7 Suppl): p. 1e-S-32e-S.

[33] Agarwal, J., Li, C.-W., Davis, B., Shea, J., Sant, H., and Gale, B., *Optimization of micropatterned poly(lactic-co-glycolic acid) films for enhancing dorsal root ganglion cell orientation and extension.* Neural Regeneration Research, 2018. **13**(1): p. 105.

[34] Donik, Č., Kocijan, A., Paulin, I., Hočevar, M., Gregorčič, P., and Godec, M., *Improved biodegradability of Fe–Mn alloy after modification of surface chemistry and topography by a laser ablation.* Applied Surface Science, 2018. **453**: p. 383-393.

[35] Shaikh, S., Singh, D., Subramanian, M., Kedia, S., Singh, A.K., Singh, K., Gupta, N., and Sinha, S., *Femtosecond laser induced surface modification for prevention of bacterial adhesion on 45S5 bioactive glass.* Journal of Non-Crystalline Solids, 2018. **482**: p. 63-72.

[36] GhavamiNejad, A., Aguilar, L.E., Ambade, R.B., Lee, S.-H., Park, C.H., and Kim, C.S., *Immobilization of silver nanoparticles on electropolymerized polydopamine films for metal implant applications.* Colloids and Interface Science Communications, 2015. **6**: p. 5-8.

[37] Raut, H.K., Das, R., Liu, Z., Liu, X., and Ramakrishna, S., *Biocompatibility of Biomaterials for Tissue Regeneration or Replacement.* Biotechnology Journal, 2020. **15**(12): p. 2000160.

[38] Lorenzetti, M., Dogša, I., Stošicki, T., Stopar, D., Kalin, M., Kobe, S., and Novak, S., *The Influence of Surface Modification on Bacterial Adhesion to Titanium-Based Substrates.* ACS Applied Materials & Interfaces, 2015. **7**(3): p. 1644-1651.

[39] Francolini, I., Vuotto, C., Piozzi, A., and Donelli, G., *Antifouling and antimicrobial biomaterials: an overview.* APMIS, 2017. **125**(4): p. 392-417.

[40] Lee, S.W., Phillips, K.S., Gu, H., Kazemzadeh-Narbat, M., and Ren, D., *How microbes read the map: Effects of implant topography on bacterial adhesion and biofilm formation.* Biomaterials, 2021. **268**: p. 120595.

[41] Chang, Y.-R., Weeks, E.R., and Ducker, W.A., *Surface Topography Hinders Bacterial Surface Motility.* ACS Applied Materials & Interfaces, 2018. **10**(11): p. 9225-9234.

[42] Woo, K.M., Chen, V.J., and Ma, P.X., *Nano-fibrous scaffolding architecture selectively enhances protein adsorption contributing to cell attachment.* Journal of Biomedical Materials Research, 2003. **67A**(2): p. 531-537.

[43] Ghanavati, Z., Neisi, N., Bayati, V., and Makvandi, M., *The influence of substrate topography and biomaterial substance on skin wound healing.* Anatomy & Cell Biology, 2015. **48**(4): p. 251.

[44] Chattopadhyay, S. and Raines, R.T., *Collagen-based biomaterials for wound healing.* Biopolymers, 2014. **101**(8): p. 821-833.

[45] Bahram, M., Mohseni, N., and Moghtader, M., *An Introduction to Hydrogels and Some Recent Applications*. 2016, InTech.

[46] Blackwood, K.A., Bock, N., Dargaville, T.R., and Ann Woodruff, M., *Scaffolds for Growth Factor Delivery as Applied to Bone Tissue Engineering.* International Journal of Polymer Science, 2012. **2012**: p. 1-25.

[47] Lee, K., Silva, E.A., and Mooney, D.J., *Growth factor delivery-based tissue engineering: general approaches and a review of recent developments.* Journal of The Royal Society Interface, 2011. **8**(55): p. 153-170.

[48] Bioengineering, N.I.o.B.I.a. *Biomaterials*. 2017 [cited 2021 Mar 18]; Available from: https://www.nibib.nih.gov/science-education/science-topics/biomaterials.

[49] Park, J.B., *Soft Tissue Replacement Implants*. 1984, Springer US. p. 305-355.

[50] Campbell, E.J., O'Byrne, V., Stratford, P.W., Quirk, I., Vick, T.A., Wiles, M.C., and Yianni, Y.P., *Biocompatible surfaces using methacryloylphosphorylcholine laurylmethacrylate copolymer.* Asaio j, 1994. **40**(3): p. M853-7.

[51] Pei, B., Wang, W., Fan, Y., Wang, X., Watari, F., and Li, X., *Fiber-reinforced scaffolds in soft tissue engineering.* Regenerative Biomaterials, 2017. **4**(4): p. 257-268.

[52] Yang, J., Bai, R., Chen, B., and Suo, Z., *Hydrogel Adhesion: A Supramolecular Synergy of Chemistry, Topology, and Mechanics.* Advanced Functional Materials, 2020. **30**(2): p. 1901693.

[53] Gao, L., Zhou, Y., Peng, J., Xu, C., Xu, Q., Xing, M., and Chang, J., *A novel dual-adhesive and bioactive hydrogel activated by bioglass for wound healing.* NPG Asia Materials, 2019. **11**(1).

[54] Kargozar, S., Lotfibakhshaiesh, N., Ai, J., Mozafari, M., Brouki Milan, P., Hamzehlou, S., Barati, M., Baino, F., Hill, R.G., and Joghataei, M.T., *Strontium- and cobalt-substituted bioactive glasses seeded with human umbilical cord perivascular cells to promote bone regeneration via enhanced osteogenic and angiogenic activities.* Acta Biomaterialia, 2017. **58**: p. 502-514.

[55] Venezuela, J.J.D., Johnston, S., and Dargusch, M.S., *The Prospects for Biodegradable Zinc in Wound Closure Applications.* Advanced Healthcare Materials, 2019. **8**(16): p. 1900408.

[56] Sezer, N., Evis, Z., Kayhan, S.M., Tahmasebifar, A., and Koç, M., *Review of magnesium-based biomaterials and their applications.* Journal of Magnesium and Alloys, 2018. **6**(1): p. 23-43.

[57] Qu, S., Xia, J., Yan, J., Wu, H., Wang, H., Yi, Y., Zhang, X., Zhang, S., Zhao, C., and Chen, Y., *In vivo and in vitro assessment of the biocompatibility and degradation of high-purity Mg anastomotic staples.* Journal of Biomaterials Applications, 2017. **31**(8): p. 1203-1214.

[58] Amano, H., Hanada, K., Hinoki, A., Tainaka, T., Shirota, C., Sumida, W., Yokota, K., Murase, N., Oshima, K., Chiba, K., Tanaka, Y., and Uchida, H., *Biodegradable Surgical Staple Composed of Magnesium Alloy.* Scientific Reports, 2019. **9**(1).

[59] Yuan, Q., Xu, A., Zhang, Z., Chen, Z., Wan, L., Shi, X., Lin, S., Yuan, Z., and Deng, L., *Bioactive silver doped hydroxyapatite composite coatings on metal substrates: Synthesis and characterization.* Materials Chemistry and Physics, 2018. **218**: p. 130-139.

[60] Jing, H., Wu, X., Liu, Y., Lu, M., Yang, K., Yao, Z., and Ke, W., *Antibacterial property of Ce-bearing stainless steels.* Journal of Materials Science, 2007. **42**(13): p. 5118-5122.

[61] Yuan, Q., Qin, C., Wu, J., Xu, A., Zhang, Z., Liao, J., Lin, S., Ren, X., and Zhang, P., *Synthesis and characterization of Cerium-doped hydroxyapatite/polylactic acid composite coatings on metal substrates.* Materials Chemistry and Physics, 2016. **182**: p. 365-371.

[62] Mazzoni, E., Iaquinta, M.R., Lanzillotti, C., Mazziotta, C., Maritati, M., Montesi, M., Sprio, S., Tampieri, A., Tognon, M., and Martini, F., *Bioactive Materials for Soft Tissue Repair.* Frontiers in Bioengineering and Biotechnology, 2021. **9**.

[63] Krishnan, V. and Lakshmi, T., *Bioglass: A novel biocompatible innovation.* Journal of advanced pharmaceutical technology & research, 2013. **4**(2): p. 78-83.

[64] Boundless, *34.1D: Vertebrate Digestive Systems*. MindTouch: LibreTexts libraries.

[65] *Digestive Anatomy and Physiology of Birds*. VIVO Pathophysiology [cited 2021 Feb 5, 2021]; Available from: http://www.vivo.colostate.edu/hbooks/pathphys/digestion/otherspp/birds.html.

[66] Mukherjee, D., *Comparative Anatomy of Digestive System in Vertebrates*, in *B.Sc. (H), SEM II: ZOOL-H-DC4-T*. 2020, S.B.S. Government College, Hili: S.B.S. Government College, Hili.

[67] Cherian, G., *II. Gastrointestinal Tract, Digestive Organs, and Processes*, in *A Guide to the Principles of Animal Nutrition*. Oregon State University Open Educational Resources: Oregon State University Open Educational Resources.

[68] Crumbie, L. *Histology of the lower digestive tract*. Histology 2021, Feb 23 [cited 2021 Mar 12]; Available from: https://www.kenhub.com/en/library/anatomy/histology-of-the-lower-digestive-tract.

[69] *Small and Large Intestine*. Michigan Histology and Virtual Microscopy Learning Resources [cited 2021 Mar 12]; Available from: https://histology.medicine.umich.edu/resources/small-large-intestine.

[70] Bowen, R. *Gross and Microscopic Anatomy of the Small Intestine*. VIVO Pathophysiology [cited 2021 Mar 11]; Available from: http://www.vivo.colostate.edu/hbooks/pathphys/digestion/smallgut/anatomy.html.

[71] Bowen, R. *Villi, Crypts and the Life Cycle of Small Intestinal Enterocytes*. [cited 2021 Mar 11]; Available from: http://www.vivo.colostate.edu/hbooks/pathphys/digestion/smallgut/lifecycle.html.

[72] OpenStax, *The Small and Large Intestines*, in *Anatomy and Physiology*. 2019, OpenStax CNX.

[73] Bowen, R. *Overview of Transport Across the Intestinal Epithelium*. [cited 2021 Mar 11]; Available from: http://www.vivo.colostate.edu/hbooks/pathphys/digestion/smallgut/transport.html.

[74] Turicchi, J. *Histology and Cellular Function of the Small Intestine*. TeachMePhysiology 2021, Jan 27 [cited 2021 Mar 12]; Available from: https://teachmephysiology.com/gastrointestinal-system/small-intestine/histology-and-cellular-function/.

[75] Bowen, R. *The Large Intestine: Introduction and Index*. [cited 2021 Mar 11]; Available from: http://www.vivo.colostate.edu/hbooks/pathphys/digestion/largegut/index.html.

[76] Bowen, R. *Gross and Microscopic Anatomy of the Large Intestine*. VIVO Pathophysiology [cited 2021 Mar 12]; Available from: http://www.vivo.colostate.edu/hbooks/pathphys/digestion/largegut/anatomy.html.

[77] Iizuka, M., *Wound healing of intestinal epithelial cells.* World Journal of Gastroenterology, 2011. **17**(17): p. 2161.

[78] Rieder, F., Brenmoehl, J., Leeb, S., Scholmerich, J., and Rogler, G., *Wound healing and fibrosis in intestinal disease.* Gut, 2007. **56**(1): p. 130-139.

[79] Thornton, F.J. and Barbul, A., *HEALING IN THE GASTROINTESTINAL TRACT.* Surgical Clinics of North America, 1997. **77**(3): p. 549-573.

[80] Ashkanani, F. and Krukowski, Z.H., *Intestinal Anastomosis.* Surgery (Oxford), 2002. **20**(5): p. 104-107.

[81] Kuo, W.-Y., Huang, H.-C., Huang, S.-W., Yu, K.-H., Cheng, F.-P., Wang, J.-H., and Wu, J.-T., *Benefits of Intraluminal Agarose Stents during End-to-End Intestinal Anastomosis in New Zealand White Rabbits.* Comparative medicine, 2017. **67**(6): p. 504-507.

[82] Lundy, J.B., *A primer on wound healing in colorectal surgery in the age of bioprosthetic materials.* Clinics in colon and rectal surgery, 2014. **27**(4): p. 125-133.

[83] Genentech. *Mechanisms of Healing*. 2016 [cited 2021 Mar 12]; Available from: https://www.gene.com/stories/mechanisms-of-healing?topic=behind-the-science.

[84] Dennis, C., Sethu, S., Nayak, S., Mohan, L., Morsi, Y.Y., and Manivasagam, G., *Suture materials - Current and emerging trends.* Journal of Biomedical Materials Research Part A, 2016. **104**(6): p. 1544-1559.

[85] Hochberg, J., Meyer, K.M., and Marion, M.D., *Suture choice and other methods of skin closure.* Surg Clin North Am, 2009. **89**(3): p. 627-41.

[86] Smeak, D.D., *Suture Materials, Staplers, and Tissue Apposition Devices*, in *Gastrointestinal Surgical Techniques in Small Animals*. 2020. p. 9-21.

[87] Monnet, E. and Smeak, D.D., *Gastrointestinal Healing*, in *Gastrointestinal Surgical Techniques in Small Animals*. 2020. p. 1-8.

[88] Monnet, E. *How to Perform a Safe Gastrointestinal Surgery*. in *World Small Animal Veterinary Association World Congress*. 2015. Colorado State University, Fort Collins, CO, USA: VIN.

[89] Ravo, B., *The Coloshield®.* Diseases of the Colon & Rectum, 1988. **31**(7): p. 579-580.

[90] Arora, M. and Okolo, P., *Polyflex Stent for Relief of Obstruction in a Patient With a Benign Anastomotic Colonic Stricture and Description of Nonfluoroscopic Technique.* 766 Gastroenterology & Hepatology Volume, 2006. **2**.

[91] Winkeltau, G.J., Treutner, K.H., Kleimann, E., Lerch, M.M., Ger, R., Haase, G., and Schumpelick, V., *Protection of intestinal anastomoses by biodegradable intraluminal bypass tubes under the condition of general peritonitis: an experimental study on the CLP model in rats.* Dis Colon Rectum, 1993. **36**(2): p. 154-60.

[92] Wang, Y., Cai, X., Jin, R., Liang, Y., Huang, D., and Peng, S., *Experimental study of primary repair of colonic leakage with a degradable stent in a porcine model.* J Gastrointest Surg, 2011. **15**(11): p. 1995-2000.

[93] Wang, Z., Li, N., Li, R., Li, Y., and Ruan, L., *Biodegradable intestinal stents: A review.* Progress in Natural Science: Materials International, 2014. **24**(5): p. 423-432.

[94] Morks, A.N., *Can intraluminal devices prevent or reduce colorectal anastomotic leakage: A review.* World Journal of Gastroenterology, 2011. **17**(40): p. 4461.

[95] Sciuto, A., Merola, G., Palma, G.D.D., Sodo, M., Pirozzi, F., Bracale, U.M., and Bracale, U., *Predictive factors for anastomotic leakage after laparoscopic colorectal surgery.* World Journal of Gastroenterology, 2018. **24**(21): p. 2247-2260.

[96] Ravo, B., Reggio, D., and Frattaroli, F.M., *Insertion of the coloshield through a colotomy after completion of a colonic anastomosis.* International Journal of Colorectal Disease, 1991. **6**(1): p. 46-48.

[97] Amin, A.I., Ramalingam, T., Sexton, R., Heald, R.J., Leppington-Clarke, A., and Moran, B.J., *Comparison of transanal stent with defunctioning stoma in low anterior resection for rectal cancer.* British Journal of Surgery, 2003. **90**(5): p. 581-582.

[98] Bulow, S., Bulut, O., Christensen, I.J., and Harling, H., *Transanal stent in anterior resection does not prevent anastomotic leakage.* Colorectal Disease, 2006. **8**(6): p. 494-496.

[99] *Neurons and Glial Cells*. Boundless Biology [cited 2021 Jan. 6]; Available from: https://courses.lumenlearning.com/boundless-biology/chapter/neurons-and-glial-cells/.

[100] *SEER Training Modules, The Peripheral Nervous System*. U.S. National Institutes of Health, National Cancer Institute [cited 2021 Feb. 26]; Available from: https://training.seer.cancer.gov/anatomy/nervous/organization/pns.html.

[101] Geuna, S., Raimondo, S., Ronchi, G., Di Scipio, F., Tos, P., Czaja, K., and Fornaro, M., *Chapter 3 Histology of the Peripheral Nerve and Changes Occurring During Nerve Regeneration*, in *International Review of Neurobiology*. 2009, Academic Press. p. 27-46.

[102] Wang, M.L., Rivlin, M., Graham, J.G., and Beredjiklian, P.K., *Peripheral nerve injury, scarring, and recovery.* Connective Tissue Research, 2019. **60**(1): p. 3-9.

[103] Lee, S. and Wolfe, S., *Peripheral Nerve Injury and Repair.* The Journal of the American Academy of Orthopaedic Surgeons, 2000. **8**: p. 243-52.

[104] Griffin, M.F., Malahias, M., Hindocha, S., and Khan, W.S., *Peripheral Nerve Injury: Principles for Repair and Regeneration.* The Open Orthopaedics Journal, 2014. **8**(1): p. 199-203.

[105] Arslantunali, D., Dursun, T., Yucel, D., Hasirci, N., and Hasirci, V., *Peripheral nerve conduits: technology update.* Medical devices (Auckland, N.Z.), 2014. **7**: p. 405-424.

[106] NINDS, N.I.o.N.D.a.S. *Peripheral Neuropathy Fact Sheet*. 2018 [cited 2020 October 8]; Available from: https://www.ninds.nih.gov/Disorders/Patient-Caregiver-Education/Fact-Sheets/Peripheral-Neuropathy-Fact-Sheet#3208_1.

[107] Seddon, H.J., *THREE TYPES OF NERVE INJURY.* Brain, 1943. **66**(4): p. 237-288.

[108] Sunderland, S., *A CLASSIFICATION OF PERIPHERAL NERVE INJURIES PRODUCING LOSS OF FUNCTION.* Brain, 1951. **74**(4): p. 491-516.

[109] Belen, D., Aciduman, A., and Er, U., *History of peripheral nerve repair: may the procedure have been practiced in Hippocratic School?* Surgical Neurology, 2009. **72**(2): p. 190-193.

[110] Battiston, B., Papalia, I., Tos, P., and Geuna, S., *Chapter 1 Peripheral Nerve Repair and Regeneration Research: A Historical Note*, in *International Review of Neurobiology*. 2009, Academic Press. p. 1-7.

[111] Ijpma, F.F.A., Van De Graaf, R.C., and Meek, M.F., *The Early History of Tubulation in Nerve Repair.* Journal of Hand Surgery (European Volume), 2008. **33**(5): p. 581-586.

[112] Papalia, I., Geuna, S., D'Alcontres, F.S., and Tos, P., *Origin and history of end-to-side neurorrhaphy.* Microsurgery, 2007. **27**(1): p. 56-61.

[113] Lopez, J., Xin, K., Quan, A., Xiang, S., Leto Barone, A.A., Budihardjo, J., Musavi, L., Mulla, S., Redett, R., Martin, R., Mao, H.-Q., Lee, W.P.A., Ibrahim, Z., and Brandacher, G., *Poly(ε-Caprolactone) Nanofiber Wrap Improves Nerve Regeneration and Functional Outcomes after Delayed Nerve Repair.* Plastic and Reconstructive Surgery, 2019. **144**(1): p. 48e-57e.

[114] Fox, I.K. and Mackinnon, S.E., *Experience with nerve allograft transplantation.* Seminars in plastic surgery, 2007. **21**(4): p. 242-249.

[115] Battiston, B., Raimondo, S., Tos, P., Gaidano, V., Audisio, C., Scevola, A., Perroteau, I., and Geuna, S., *Chapter 11 Tissue Engineering of Peripheral Nerves*, in *International Review of Neurobiology*. 2009, Academic Press. p. 227-249.

[116] Shirosaki, Y., Hayakawa, S., Osaka, A., Lopes, M.A., Santos, J.D., Geuna, S., and Mauricio, A.C., *Challenges for nerve repair using chitosan-siloxane hybrid porous scaffolds.* BioMed research international, 2014. **2014**: p. 153808-153808.

[117] Rebowe, R., Rogers, A., Yang, X., Kundu, S.C., Smith, T.L., and Li, Z., *Nerve Repair with Nerve Conduits: Problems, Solutions, and Future Directions.* Journal of hand and microsurgery, 2018. **10**(2): p. 61-65.

[118] Dixon, A.R., Jariwala, S.H., Bilis, Z., Loverde, J.R., Pasquina, P.F., and Alvarez, L.M., *Bridging the gap in peripheral nerve repair with 3D printed and bioprinted conduits.* Biomaterials, 2018. **186**: p. 44-63.

[119] Mingyu, C., Kai, G., Jiamou, L., Yandao, G., Nanming, Z., and Xiufang, Z., *Surface Modification and Characterization of Chitosan Film Blended with Poly-L-Lysine.* Journal of Biomaterials Applications, 2004. **19**(1): p. 59-75.

[120] Yi, S., Xu, L., and Gu, X., *Scaffolds for peripheral nerve repair and reconstruction.* Experimental Neurology, 2019. **319**: p. 112761.

[121] Cheng, M., Deng, J., Yang, F., Gong, Y., Zhao, N., and Zhang, X., *Study on physical properties and nerve cell affinity of composite films from chitosan and gelatin solutions.* Biomaterials, 2003. **24**(17): p. 2871-80.

[122] Wang, X., Hu, W., Cao, Y., Yao, J., Wu, J., and Gu, X., *Dog sciatic nerve regeneration across a 30-mm defect bridged by a chitosan/PGA artificial nerve graft.* Brain, 2005. **128**(8): p. 1897-1910.

[123] Xu, Y., Zhang, Z., Chen, X., Li, R., Li, D., and Feng, S., *A Silk Fibroin/Collagen Nerve Scaffold Seeded with a Co-Culture of Schwann Cells and Adipose-Derived Stem Cells for Sciatic Nerve Regeneration.* PLOS ONE, 2016. **11**(1): p. e0147184.

[124] Stang, F., Fansa, H., Wolf, G., Reppin, M., and Keilhoff, G., *Structural parameters of collagen nerve grafts influence peripheral nerve regeneration.* Biomaterials, 2005. **26**(16): p. 3083-3091.

[125] Magaz, A., Faroni, A., Gough, J.E., Reid, A.J., Li, X., and Blaker, J.J., *Bioactive Silk-Based Nerve Guidance Conduits for Augmenting Peripheral Nerve Repair.* Advanced Healthcare Materials, 2018. **7**(23): p. 1800308.

[126] Ghaznavi, A.M., Kokai, L.E., Lovett, M.L., Kaplan, D.L., and Marra, K.G., *Silk Fibroin Conduits: A Cellular and Functional Assessment ofPeripheral Nerve Repair.* Annals of Plastic Surgery, 2011. **66**(3): p. 273-279.

[127] Yang, Y., Ding, F., Wu, J., Hu, W., Liu, W., Liu, J., and Gu, X., *Development and evaluation of silk fibroin-based nerve grafts used for peripheral nerve regeneration.* Biomaterials, 2007. **28**(36): p. 5526-5535.

[128] Reid, A.J., De Luca, A.C., Faroni, A., Downes, S., Sun, M., Terenghi, G., and Kingham, P.J., *Long term peripheral nerve regeneration using a novel PCL nerve conduit.* Neuroscience Letters, 2013. **544**: p. 125-130.

[129] Sun, M., Kingham, P.J., Reid, A.J., Armstrong, S.J., Terenghi, G., and Downes, S., *In vitro and in vivo testing of novel ultrathin PCL and PCL/PLA blend films as peripheral nerve conduit.* Journal of Biomedical Materials Research Part A, 2009. **9999A**: p. NA-NA.

[130] Barbarisi, M., Marino, G., Armenia, E., Vincenzo, Q., Rosso, F., Porcelli, M., and Barbarisi, A., *Use of polycaprolactone (PCL) as scaffolds for the regeneration of nerve tissue.* Journal of Biomedical Materials Research Part A, 2015. **103**(5): p. 1755-1760.

[131] Labroo, P., Shea, J., Edwards, K., Ho, S., Davis, B., Sant, H., Goodwin, I., Gale, B., and Agarwal, J., *Novel drug delivering conduit for peripheral nerve regeneration.* Journal of Neural Engineering, 2017. **14**(6): p. 066011.

[132] Jahromi, M., Razavi, S., and Bakhtiari, A., *The advances in nerve tissue engineering: From fabrication of nerve conduit toin vivonerve regeneration assays.* Journal of Tissue Engineering and Regenerative Medicine, 2019. **13**(11): p. 2077-2100.

[133] Bini, T.B., Gao, S., Tan, T.C., Wang, S., Lim, A., Hai, L.B., and Ramakrishna, S., *Electrospun poly(L-lactide-co-glycolide) biodegradable polymer nanofibre tubes for peripheral nerve regeneration.* Nanotechnology, 2004. **15**(11): p. 1459-1464.

[134] Lee, D.-Y., Choi, B.-H., Park, J.-H., Zhu, S.-J., Kim, B.-Y., Huh, J.-Y., Lee, S.-H., Jung, J.-H., and Kim, S.-H., *Nerve regeneration with the use of a poly(l-lactide-co-glycolic acid)-coated collagen tube filled with collagen gel.* 2006. **34**(1): p. 50-56.

[135] Bramini, M., Alberini, G., Colombo, E., Chiacchiaretta, M., Difrancesco, M.L., Maya-Vetencourt, J.F., Maragliano, L., Benfenati, F., and Cesca, F., *Interfacing Graphene-Based Materials With Neural Cells.* Frontiers in Systems Neuroscience, 2018. **12**.

[136] Zhang, Y., Liu, X., Michelson, K., Trivedi, R., Wu, X., Schepp, E., Xing, Y., Darland, D., and Zhao, J.X., *Graphene Oxide-Based Biocompatible 3D Mesh with a Tunable Porosity and Tensility for Cell Culture.* ACS Biomaterials Science & Engineering, 2018.

[137] Wang, J., Cheng, Y., Chen, L., Zhu, T., Ye, K., Jia, C., Wang, H., Zhu, M., Fan, C., and Mo, X., *In vitro and in vivo studies of electroactive reduced graphene oxide-modified nanofiber scaffolds for peripheral nerve regeneration.* Acta Biomaterialia, 2019. **84**: p. 98-113.

[138] Wang, J., Zheng, W., Chen, L., Zhu, T., Shen, W., Fan, C., Wang, H., and Mo, X., *Enhancement of Schwann Cells Function Using Graphene-Oxide-Modified Nanofiber Scaffolds for Peripheral Nerve Regeneration.* ACS Biomaterials Science & Engineering, 2019. **5**(5): p. 2444-2456.

[139] Zhao, Y., Wang, Y., Niu, C., Zhang, L., Li, G., and Yang, Y., *Construction of polyacrylamide/graphene oxide/gelatin/sodium alginate composite hydrogel with bioactivity for promoting Schwann cells growth.* Journal of Biomedical Materials Research Part A, 2018. **106**(7): p. 1951-1964.

[140] Li, G., Zhao, Y., Zhang, L., Gao, M., Kong, Y., and Yang, Y., *Preparation of graphene oxide/polyacrylamide composite hydrogel and its effect on Schwann cells attachment and proliferation.* Colloids and Surfaces B: Biointerfaces, 2016. **143**: p. 547-556.

[141] Verre, A.F., Faroni, A., Iliut, M., Silva, C., Muryn, C., Reid, A.J., and Vijayaraghavan, A., *Improving the glial differentiation of human Schwann-like adipose-derived stem cells with graphene oxide substrates.* Interface Focus, 2018. **8**(3): p. 20180002.

[142] Reina, G., González-Domínguez, J.M., Criado, A., Vázquez, E., Bianco, A., and Prato, M., *Promises, facts and challenges for graphene in biomedical applications.* Chemical Society Reviews, 2017. **46**(15): p. 4400-4416.

[143] Nezakati, T., Cousins, B.G., and Seifalian, A.M., *Toxicology of chemically modified graphene-based materials for medical application.* Archives of Toxicology, 2014. **88**(11): p. 1987-2012.

[144] Wang, Q., Chen, J., Niu, Q., Fu, X., Sun, X., and Tong, X., *The application of graphene oxidized combining with decellularized scaffold to repair of sciatic nerve injury in rats.* Saudi Pharmaceutical Journal, 2017.

[145] Kokai, L.E., Lin, Y.-C., Oyster, N.M., and Marra, K.G., *Diffusion of soluble factors through degradable polymer nerve guides: Controlling manufacturing parameters.* Acta Biomaterialia, 2009. **5**(7): p. 2540-2550.

[146] Pedrosa, S.S., Caseiro, A.R., Santos, J.D., and Maurício, A.C., *Scaffolds for Peripheral Nerve Regeneration, the Importance of In Vitro and In Vivo Studies for the Development of Cell-Based Therapies and Biomaterials: State of the Art*. 2017, InTech.

[147] Du, J., Chen, H., Qing, L., Yang, X., and Jia, X., *Biomimetic neural scaffolds: a crucial step towards optimal peripheral nerve regeneration.* Biomaterials Science, 2018. **6**(6): p. 1299-1311.

[148] Bravo, P.W., *Camelidae*. 2015, Elsevier. p. 592-602.

[149] Godoy-Vitorino, F., Goldfarb, K.C., Karaoz, U., Leal, S., Garcia-Amado, M.A., Hugenholtz, P., Tringe, S.G., Brodie, E.L., and Dominguez-Bello, M.G., *Comparative analyses of foregut and hindgut bacterial communities in hoatzins and cows.* The ISME Journal, 2012. **6**(3): p. 531-541.

[150] McWilliams, S.R. *S37.2: Digestive strategies of avian herbivores*. in *22nd International Ornithological Congress*. 1998. Durban, South Africa: International Ornithologists' Union.

[151] Kararli, T.T., *Comparison of the gastrointestinal anatomy, physiology, and biochemistry of humans and commonly used laboratory animals.* Biopharmaceutics & Drug Disposition, 1995. **16**(5): p. 351-380.

[152] Stevens, C.E. and Dukes, H.H., *Comparative physiology of the digestive system*, in *Dukes' Physiology of Domestic Animals*, Swenson, M.J., Editor. 1977, Comstock Pub. Associates: Comstock, Ithaca, NY and London. p. 216-232.

[153] Lundborg, G., *Nerve Injury and Repair*. 1988: Churchill Livingstone.

[154] Babcock, W.W., *A standard technique for operations on peripheral nerves with special reference to closure of large gaps.* Surgery Gynec. Obstet., 1927. **45**: p. 364.

Appendix
Tables & Figures

Table 1-1: Selection of Soft Tissue Biomaterial Applications

Body System	Biomaterial-Based Implant
Nervous System	Nerve conduit
Musculoskeletal System	Artificial tendon
Ocular	Contact lens
	Artificial intraocular lens
Cardiovascular	Pacemaker
	Artificial heart valve
	Artificial blood vessel
	Catheter
	Vascular stent
Gastrointestinal & Abdominal	Esophageal stent
	Hernia mesh
Renal/Urinary	Stent
	Catheter
	Dialysis membrane
Integumentary	Wound dressing
	Artificial skin
	Tissue adhesives
Other	Sutures
	Staples

Information compilated from Parida, Behera, & Mishra (2012), Chattopadhyay & Raines (2014), Kiradzhiyska & Mantcheva (2019), Festas, Ramos, & Davim (2020), and Park (1984)

Table 1-2: Gastrointestinal System Classifications of a Selection of Species

	Monogastric	Ruminant	Pseudo-Ruminant	Avian
Non-Herbivorous (Limited Fermentation)	Human			
	Canine			
	Feline			
Foregut Fermenters		Bovine	Elk	Hoatzin (dual)
		Caprine	Deer	
		Ovine	Camelid	
Hindgut Fermenters	Equine			Hoatzin (dual)
	Lagomorph			Chicken
	Porcine			Emu

This table depicts the designations of several species in regards to their gastrointestinal system classifications, including limited, foregut, and hindgut fermenters, as well as monogastric, ruminant, pseudo-ruminant, and avian organ systems [67, 148-152].

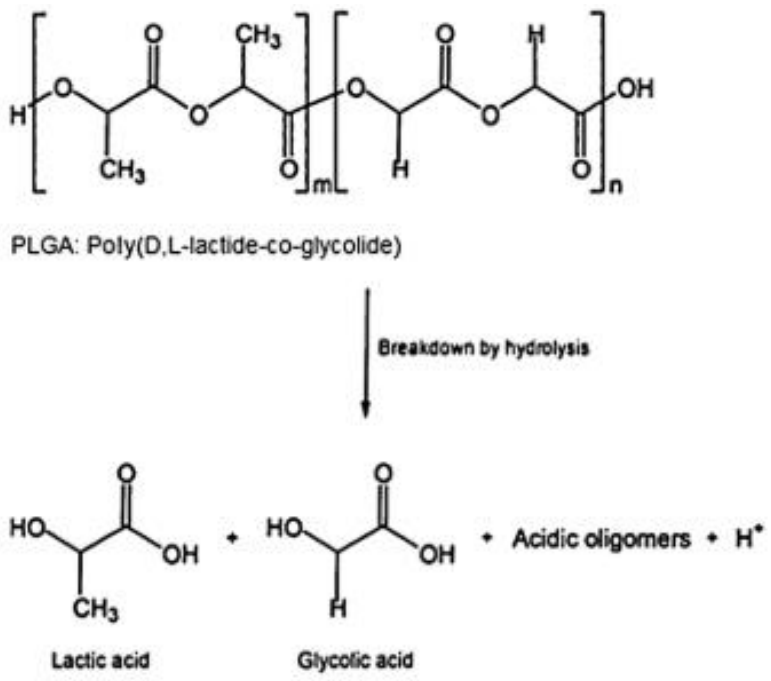


Figure 1-1: Hydrolytic breakdown of poly(D,L-lactide-co-glycolide)

Degradation of PLGA in an aqueous environment occurs by hydrolysis of ester bonds and subsequent auto-catalysis by carboxylic functional groups to form lactic acid, glycolic acid, and other acidic groups [11, 12]. Image courtesy of Park *et al.* (2014).

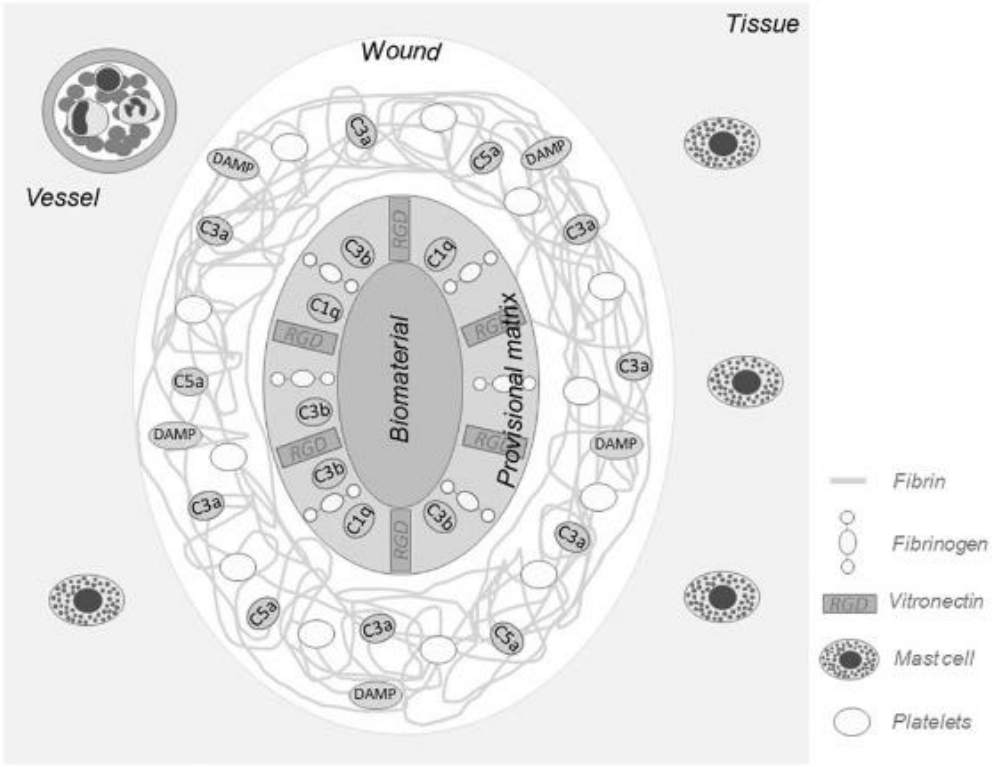


Figure 1-2: Foreign body response to a biomaterial implant

The cascade of a foreign body response to a biomaterial implant includes initial protein adsorption on the surface of the biomaterial and recruitment of acute inflammatory cells, followed by a period of chronic inflammation and foreign body giant cell formation, and ultimately formation of a fibrous tissue capsule around the implant [22]. Image courtesy of Klopfleisch & Jung (2017).

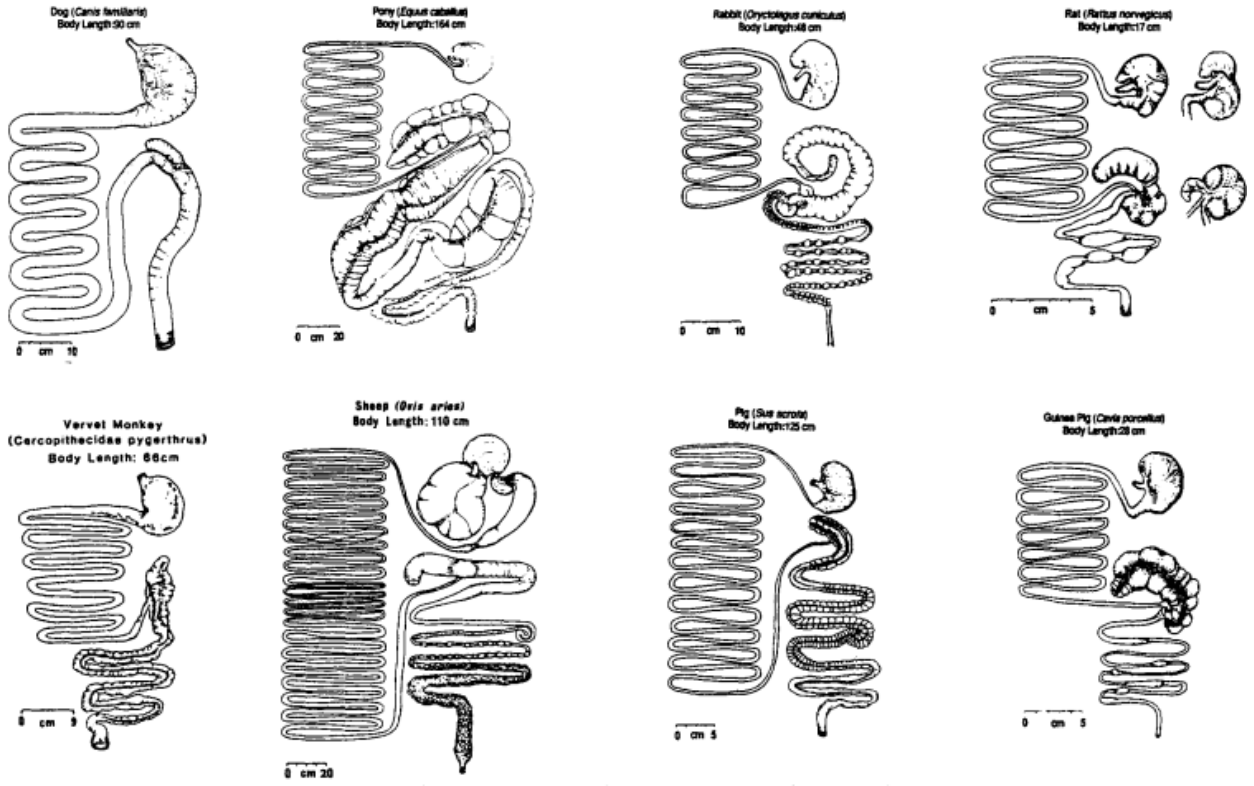


Figure 1-3: Comparison of gastrointestinal gross anatomy between several common species

Species represnted, from left to right: (*top row*) dog, pony, rabbit, rat; (*bottom row*) vervet monkey, sheep, pig, guinea pig. Image taken from Kararli (1995) [151], originally published in *Dukes' Physiology of Domestic Animals* (1977) [152].

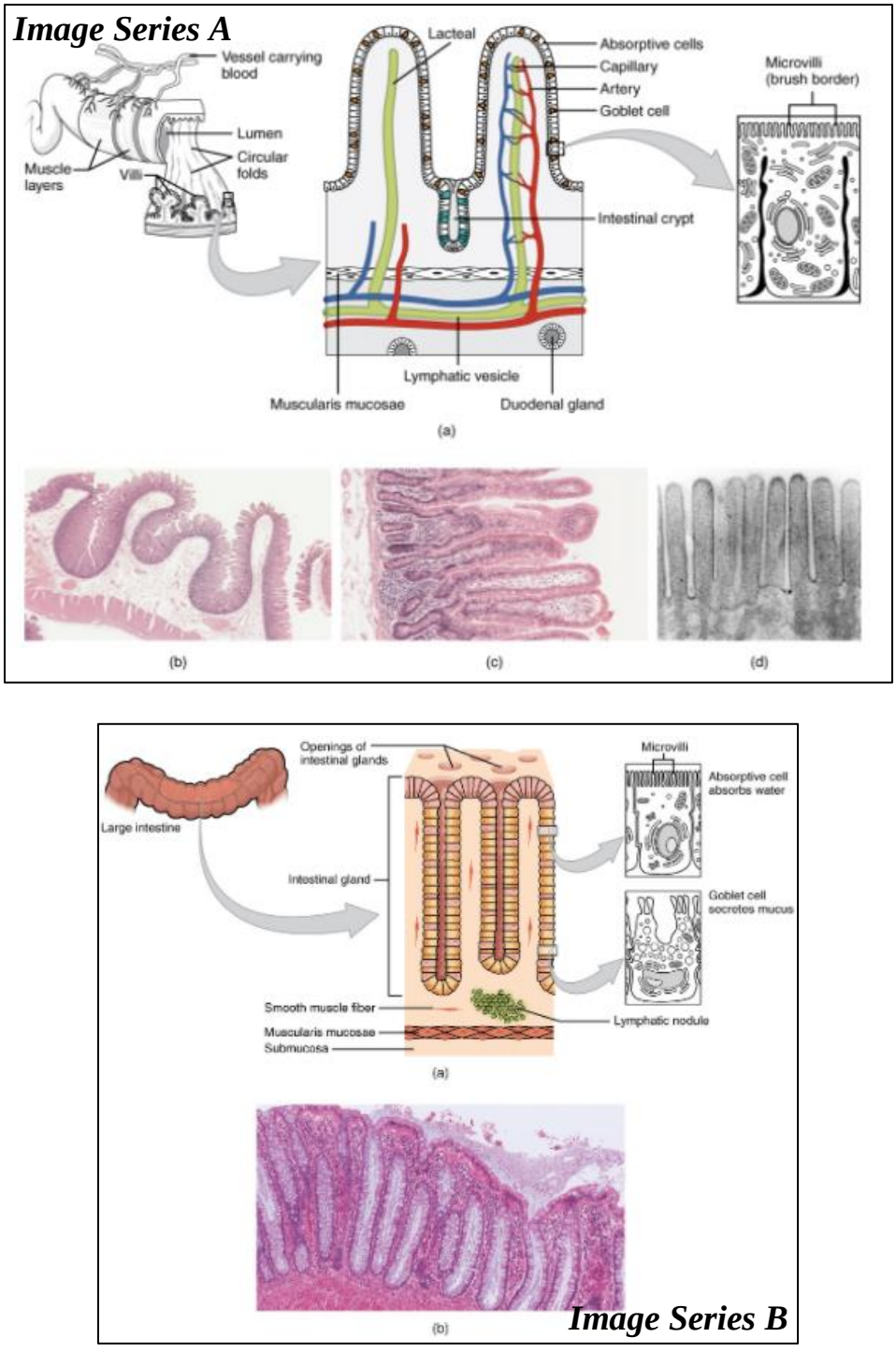


Figure 1-4: Small & large intestinal microanatomy

Image Series A depicts the microanatomy of the small intestine and Image Series B depicts the large intestine. Note the distinguishing the presence of villi in the small intestine. Image courtesy of OpenStax (2019).

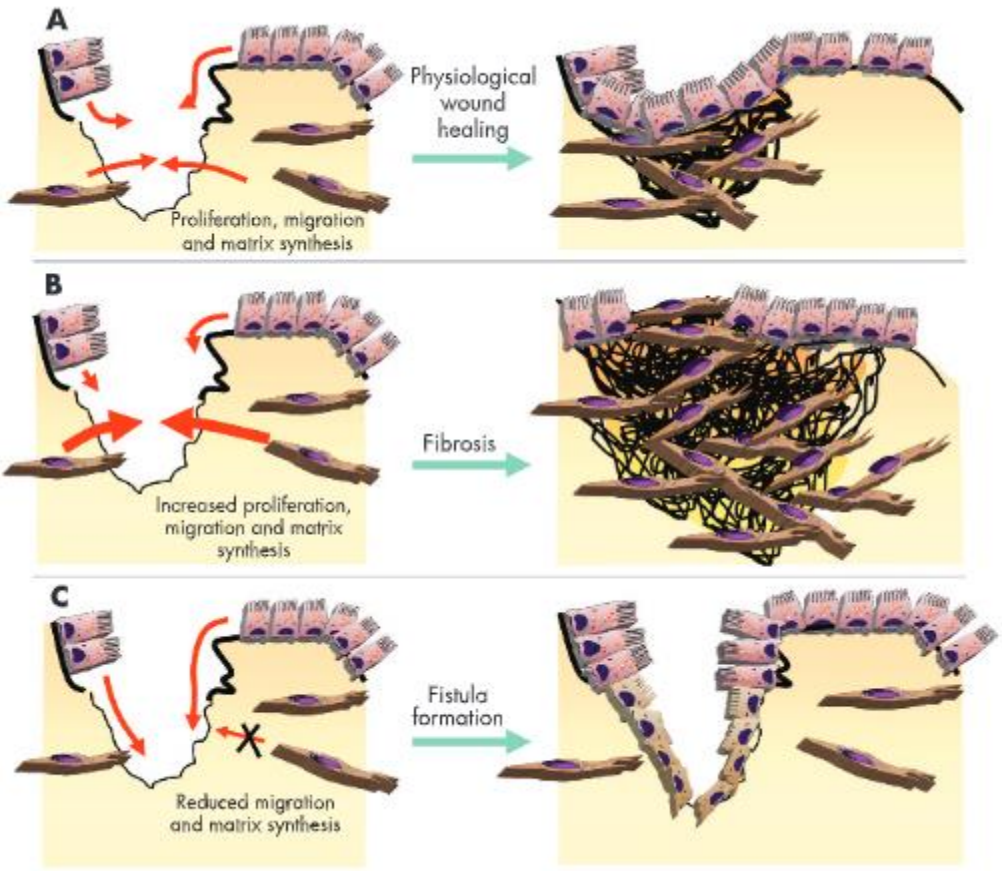


Figure 1-5: Fibrous tissue and ulcer formation in the intestine

Fibrosis (A) at an intestinal injury site is essentially an over-exuberance of normal repair processes, whereas fistula formation (B) is the result of reduced migration of myofibroblasts and production of ECM [78]. Image courtesy of Rieder *et al.* (2007).

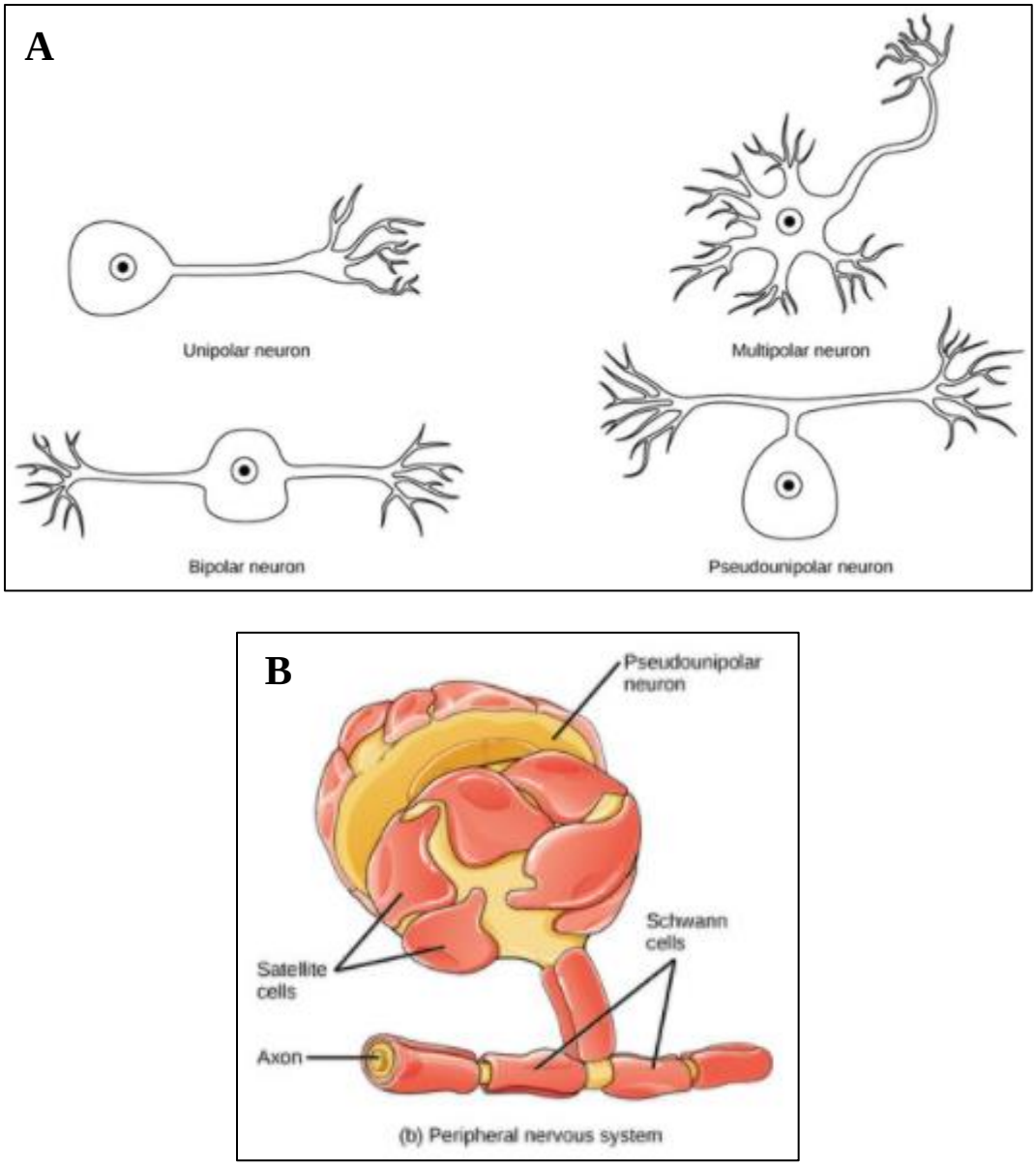


Figure 1-6: Neuronal & glial cells

Image (A) depicts neuronal cell morphologies and (B) depicts positioning of Schwann cells on the axonal surface. Image courtesy of Boundless Biology [99].

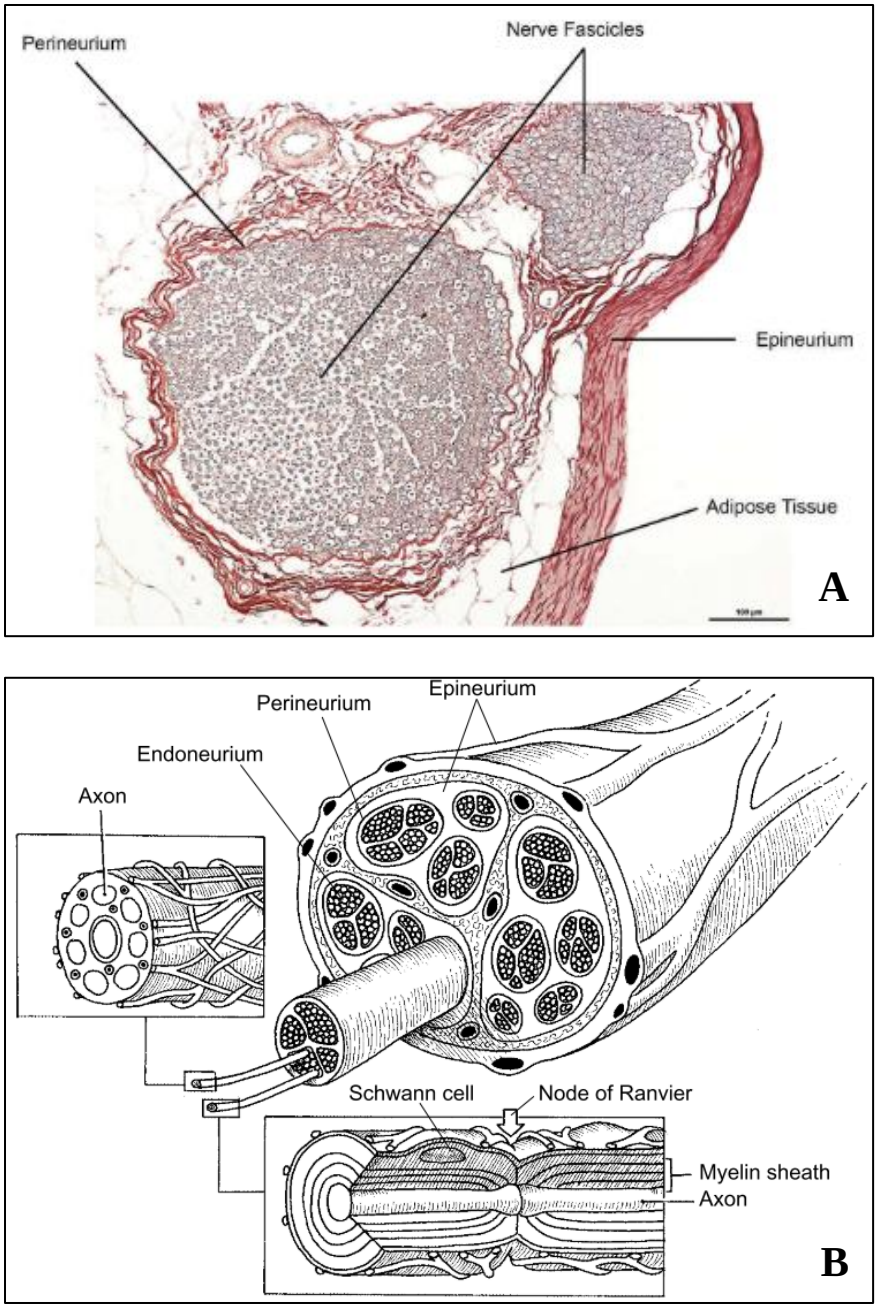


Figure 1-7: Microanatomy of the peripheral nerve

Image (A) depicts a histologic cross-section of a peripheral nerve and (B) depicts an anatomic illustration. Image (A) is courtesy of Wang et al (2019) and (B) is courtesy of Lee & Wolfe (2000), which was originally published in Lundborg (1988) [153].

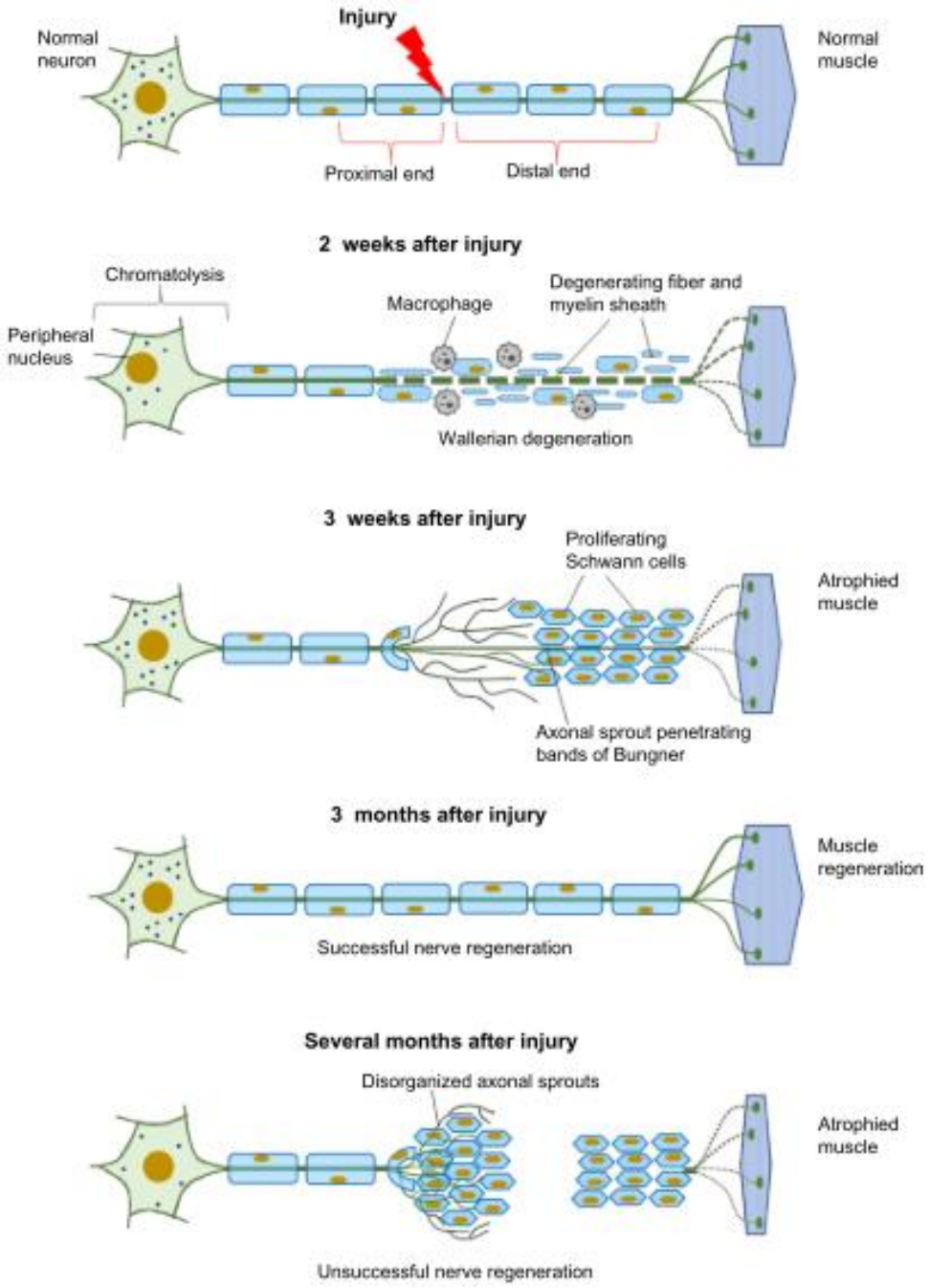


Figure 1-8: Peripheral nerve regeneration process

The peripheral nerve regeneration process is characterized by chromatolysis and swelling of the neuron's nucleus and body immediately after injury and progressive swelling within the axonal stump over several days, followed by Wallerian degeneration, Schwann cell proliferation and myelination, and axonal sprouting and growth [104, 105]. Image courtesy of Arslantuli *et al.* (2014).

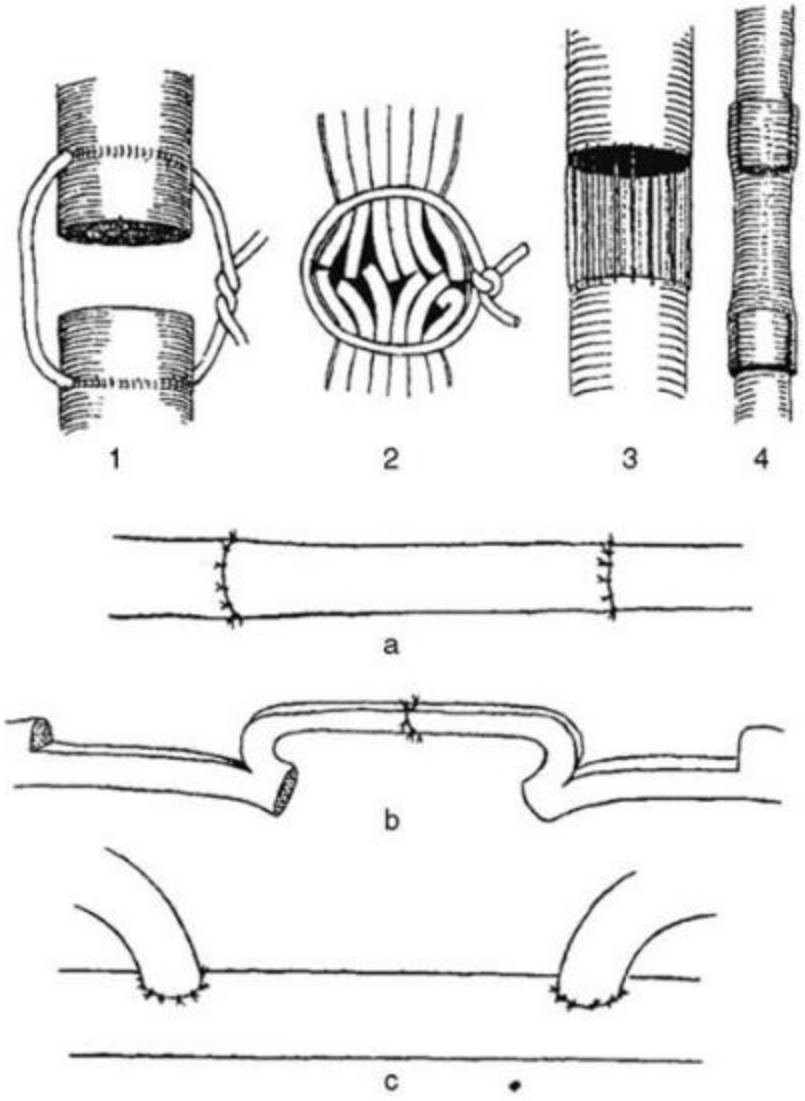


Figure 1-9: Drawings of early peripheral nerve repair techniques

Published in Battiston *et al.* (2009) [110], originally extracted from Babcock (1927) [154]. Images depict the following: (1) and (2) anastomotic suturing techniques; (3) and (4) gap repairs; (a) grafting; (b) nerve flap repair; (c) end-to-side repair.

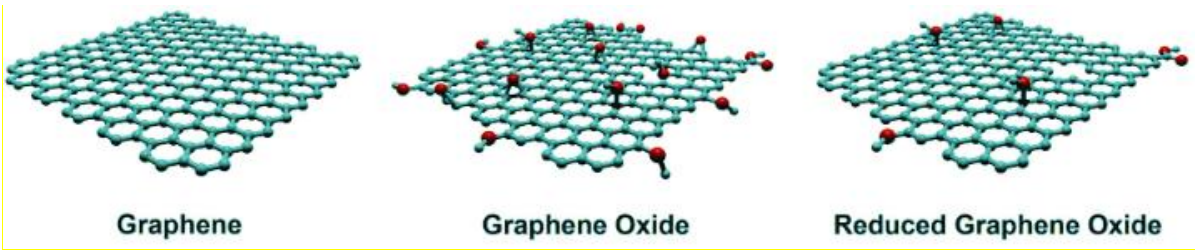


Figure 1-10: Structure of several members of the graphene family

Chemical structures of single-layer sheets of graphene, graphene oxide, and reduced graphene oxide. Blue hexagonal grids represent a carbon monolayer and red spheres represent oxygen. Image courtesy of Reina *et al.* (2017).

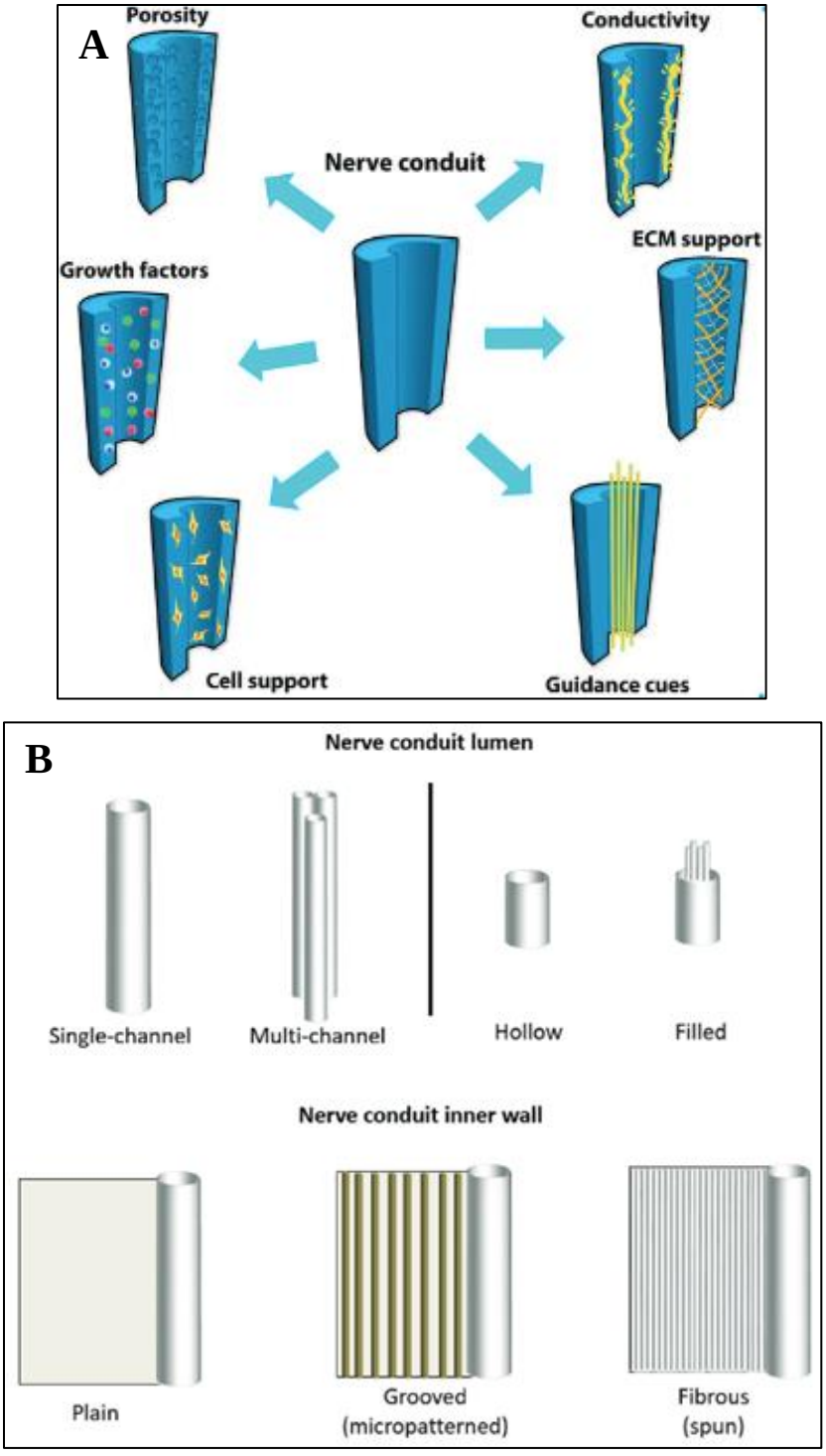


Figure 1-11: Example nerve conduit features

Nerve conduits can feature a variety of intraluminal and topographic features. Images courtesy of Magaz *et al.* (2018).

CHAPTER 2 : *Pilot Study*: Collapsible Guide for Use in Small Intestinal Anastomosis

Statement on Utilization of Published Manuscript:

The contents of this chapter (exclusive of the *ex vivo* study and additional figures) were originally published in *Frontiers in Surgery, Visceral Surgery* on November 11, 2020, under the research topic *Bioengineering Solutions in Surgery: Advances, Applications and Solutions for Clinical Translation*. Alisha Pedersen and Karrer Alghazali were equal co-authors in the production of the manuscript, with Alisha taking first authorship at time of publication.

Citation:

[1] Pedersen AP, Alghazali KM, Hamzah RN, Mulon P-Y, McCracken M, Rifkin RE, Mhannawee A, Nima ZA, Griffin C, Donnell RL, Biris AS and Anderson DE (2020). Development and *in vivo* Assessment of a Rapidly Collapsible Anastomotic Guide for Use in Anastomosis of the Small Intestine: A Pilot Study Using a Swine Model. *Front. Surg*. 7:587951. doi.org/10.3389/fsurg.2020. 587951



frontiers in Surgery

ORIGINAL RESEARCH
published: 11 November 2020
doi: 10.3389/fsurg.2020.587951

OPEN ACCESS

Edited by:
Pegah Mukherjee,
The University of Sydney, Australia

Reviewed by:
Ahmed Farag El-Kamel,
University of Mansoura, Egypt
Kenan Yanfarzade,
Independent Researcher, Baku,
Azerbaijan

*Correspondence:
Alisha P. Pedersen
apedi14@vols.utk.edu
Karrer M. Alghazali
karrer@mushcoss.com

†These authors have contributed equally to this work and share first authorship

Specialty section:
This article was submitted to Visceral Surgery, a section of the journal Frontiers in Surgery

Received: 21 July 2020
Accepted: 05 October 2020
Published: 11 November 2020

Citation:
Pedersen AP, Alghazali KM, Hamzah RN, Mulon P-Y, McCracken M, Rifkin RE, Mhannawee A, Nima ZA, Griffin C, Donnell RL, Biris AS and Anderson DE (2020) Development and in vivo Assessment of a Rapidly Collapsible Anastomotic Guide for Use in Anastomosis of the Small Intestine: A Pilot Study Using a Swine Model. Front. Surg. 7:587951. doi: 10.3389/fsurg.2020.587951

Development and *in vivo* Assessment of a Rapidly Collapsible Anastomotic Guide for Use in Anastomosis of the Small Intestine: A Pilot Study Using a Swine Model

Alisha P. Pedersen[1†], Karrer M. Alghazali[2,3*†], Rabab N. Hamzah[3], Pierre-Yves Mulon[1], Megan McCracken[4], Rebecca E. Rifkin[1], Anwar Mhannawee[3], Zeid A. Nima[3], Christopher Griffin[3], Robert L. Donnell[3], Alexandru S. Biris[3] and David E. Anderson[1]*

[1] Department of Large Animal Clinical Sciences, College of Veterinary Medicine, University of Tennessee, Knoxville, TN, United States, [2] Center for Integrative Nanotechnology Sciences, University of Arkansas at Little Rock, Little Rock, AR, United States, [3] NuCleonis BioSciences LLC, Little Rock, AR, United States, [4] Equine Hospital, Veterinary Health Center, University of Missouri College of Veterinary Medicine, Columbia, MO, United States, [5] Department of Biomedical and Diagnostic Sciences, College of Veterinary Medicine, University of Tennessee, Knoxville, TN, United States

Various conditions in human and veterinary medicine require intestinal resection and anastomosis, and complications from these procedures are frequent. A rapidly collapsible anastomotic guide was developed for small intestinal end-to-end anastomosis and was investigated in order to assess its utility to improve the anastomotic process and to potentially reduce complication rates. A complex manufacturing method for building a polymeric device was established utilizing biocompatible and biodegradable polyvinylpyrrolidone and polyurethane. This combination of polymers would result in rapid collapse of the material. The guide was designed as a hollow cylinder composed of overlaying shingles that separate following exposure to moisture. An *in vivo* study was performed using commercial pigs, with each pig receiving one standard handsewn anastomosis and one guide-facilitated anastomosis. Pigs were sacrificed after 13 days, at which time burst pressure, maximum luminal diameter, and presence of adhesions were assessed. Burst pressures were not statistically different between treatment groups, but *in vivo* anastomoses performed with the guide withstood 10% greater luminal burst pressure and maintained 17% larger luminal diameter than those performed using the standard handsewn technique alone. Surgeons commented that the addition of a guide eased the performance of the anastomosis. Hence, a rapidly collapsible anastomotic guide may be beneficial to the performance of intestinal anastomosis.

Keywords: end-to-end anastomosis, anastomotic guide, side-to-side anastomosis, polyvinylpyrrolidone, polyurethane

Abstract

Various conditions in human and veterinary medicine require intestinal resection and anastomosis, and complications from these procedures are frequent. A rapidly collapsible anastomotic guide was developed for small intestinal end-to-end anastomosis and was investigated in order to assess its utility to improve the anastomotic process and to potentially reduce complication rates. Small intestinal hand-sewn, end-to-end anastomoses (EEA) were initially performed with or without the use of a prototype intraluminal guide in an *ex vivo* study utilizing swine cadavers. Time of completion, burst pressure, and intestinal diameter were assessed. *Ex vivo* data revealed up to a 37% decrease in procedure completion time and a mean 15.2% reduction in EEA site stricture. A complex manufacturing method for building a polymeric device was established utilizing biocompatible and biodegradable polyvinylpyrrolidone and polyurethane. This combination of polymers would result in rapid collapse of the material. The guide was designed as a hollow cylinder composed of overlaying shingles that separate following exposure to moisture. An *in vivo* study was performed using commercial pigs, with each pig receiving one standard handsewn anastomosis and one guide-facilitated anastomosis. Pigs were sacrificed after thirteen days, at which time burst pressure, maximum luminal diameter, and presence of adhesions were assessed. Burst pressures were not statistically different between treatment groups, but *in vivo* anastomoses performed with the guide withstood 10% greater luminal burst pressure and maintained 17% larger luminal diameter than those performed using the standard handsewn technique alone. Surgeons commented that the addition of a guide eased the performance of the anastomosis. Hence, a rapidly collapsible anastomotic guide may be beneficial to the performance of intestinal anastomosis.

Introduction

Small intestinal anastomosis is a relatively common procedure that may be performed in either emergency or elective situations and commonly involves resection of a diseased or damaged segment of the bowel [2-6]. Numerous pathological conditions indicate the need for an intestinal anastomosis, including vascular compromise, bowel gangrene, obstruction, intussusception, volvulus, polyps, neoplasia, impaction, perforation due to trauma, severe inflammatory bowel disease refractory to medical therapy, chronic constipation, various congenital abnormalities, and severe inflammation due to disease. There are several techniques for performing an intestinal anastomosis. The operative technique chosen is at the discretion of the surgeon and is often based on the particular situation, personal preference, benefits or hindrances of specific techniques, cost, feasibility, availability of instruments, the diameter of the affected area of bowel, presence or lack of edema, location within the abdominal cavity, type of disease or condition, and time constraints [2, 3]. Regardless of the techniques used, practices that provide the best post-operative recovery include adequate accessibility of the affected bowel segment, gentle manipulation of the bowel and surrounding abdominal structures, appropriate hemostasis and maintenance of vascularization following transection, avoidance of tension at the anastomotic site, proper surgical technique, and prevention of contamination of the abdomen with intestinal contents [3].

The most common anastomotic techniques can be divided into two broad categories, handsewn and stapled, within which are numerous sub-categories. Categories of handsewn anastomoses include simple continuous suture pattern versus interrupted suture pattern [6-9]; single-layered or double-layered closure [10-12]; inverting, everting, or appositional pattern[13-16]; end-to-end (EEA) or side-to-side (SSA) positioning of intestinal segments; use of absorbable versus non-absorbable suture material and choice of a specific type of suture material; extramucosal or full-thickness suturing; and choice of spacing between suture placements [17, 18]. Categories of stapled anastomoses include: end-to-end or side-to-side positioning; oversewing the stapled area or burying it; and choice of stapling device used [2]. No matter the technique, several potential complications may occur during or after an intestinal anastomosis procedure, some of which are life-threatening. A complication that may present itself early in the recovery period is leakage from the anastomotic site. During the first 5-7 days of recovery, the efficacy of the

anastomotic site largely relies on the integrity of the suture material or staples to holdfast in the tissues. Leakage that occurs within the first day or two after surgery is often associated with the techniques utilized to perform the anastomosis. If leakage occurs beyond the first 5-7 days in the postoperative recovery period, it is more likely to be associated with poor intestinal healing [3]. Leakage may take the form of diffuse peritonitis or localized abscess formation. Peritonitis has a high morbidity and mortality rate and requires additional surgical intervention [3]. Leakage has been reported to increase the expected mortality rate after bowel anastomosis from 7.2% to 22% [2, 19].

Another commonly encountered complication is excessive bleeding from the anastomotic site, either intraoperatively or postoperatively. The integrity of the anastomosis should be re-evaluated if this occurs and hemostasis achieved as needed. Postoperative bleeding can be evident as hematemesis, melena, bleeding through an intra-abdominal drain, progressive anemia, and abdominal distension, among other signs. These cases may need to be treated with medical management or, if persistent or severe, surgical intervention. Stapled anastomoses in particular have been shown to result in disruption of mesenteric blood vessels, increasing the risk of ischemia of the bowel [3]. Stricture of the intestine at the anastomosis is a serious complication that has been reported to occur more frequently after stapled EEA than handsewn EEA [3, 20]. Medical management of anastomotic leakage after surgery is a significant risk factor contributing to the development of a stricture, and dilatation or surgical revision may be necessary to treat this complication [3].

We hypothesized that the use of an anastomotic guide (AG), placed within the lumen of the intestine during surgery would improve the accuracy of EEA by providing a means to appose the cut ends of the intestine so that precise sutures could be placed. This precision surgery would result in increased lumen diameter and reduced potential for leakage after anastomosis. The device was designed such that it would rapidly collapse after surgery so as not to be predisposed to complications associated with other intraluminal intestinal devices. Intraluminal stents have been used to expand and maintain the lumen size of strictured bowel after colon resection and anastomosis. To date, intestinal stents used to expand the intestinal wall contain non-degradable or slowly degraded materials [21]. Intestinal stents may increase morbidity rates associated with interruption of intestinal motility, impaction of the stent by digesta, stent migration, and re-

obstruction [21-23]. A slowly degrading (up to 3 months) intraluminal colonic stent was described for treatment of strictures of the colon after anastomotic leakage [24]. A rapidly degraded or collapsed intraluminal device would eliminate post-operative morbidity associated with the use of the device. We aimed to assess the feasibility of a rapidly collapsible, intraluminal small intestinal AG to reduce the potential for post-operative complications, as well as to improve the accuracy and efficiency of the anastomotic procedure [24]. A simulated intraluminal guide was used for a preliminary *ex vivo* study to demonstrate proof-of-concept that the use of a guide could improve the accuracy and ease of performance of an anastomosis. A prototype AG was then fabricated and underwent numerous characterization assessments prior to application in an *in vivo* swine model, which was established in order to assess post-surgical complications when compared with a standard handsewn EEA method.

Materials and Methods

Ex Vivo *Investigation*

Freshly harvested small intestinal segments from swine cadavers were cut along the mesentery and maintained in cooled saline or water until immediately prior to testing. Segments were trimmed to approximately 20-cm long, and intestinal lumens were evacuated and rinsed. Each segment was transected and the halves laid end-to-end so that the cut edges were aligned. Anastomoses were performed using #3-0 PDS suture (Ethicon, INC., Somerville, New Jersey) placed in one of two techniques: 1) simple continuous suturing using two suture segments (each segment hemicircumferential) or 2) simple continuous suturing using two suture segments (each segment hemicircumferential) with the addition of an anastomotic guide (AG) placed prior to the performance of the anastomosis. For the purposes of *ex vivo* concept studies, a 0.5-inch diameter PVC pipe segment was used to mimic the function of an AG. This was placed into the lumen of each half of the intestinal segment, and the cut edges of the bowel aligned. Other than the presence of an intraluminal guide, the technique for both groups was identical. The suture line began at the mesenteric side and continued in a simple continuous pattern 180^{o} around to the anti-mesenteric side. This procedure was repeated on the remaining cut edge on the opposite side (Figure 2-1). If

any obvious gap was noticed, a single interrupted suture was placed.

Procedure time: Time for completion of each EEA was measured, with the timer being set just before the first suture was placed and stopped immediately after the last knot was tied.

Burst pressure: Pressure within the bowel lumen was measured by instilling saline into the anastomotic region and observing for leakage. Burst pressure withstood by the anastomotic sites was assessed using a digital pressure monitor (Surgivet® V6400 Invasive Blood Pressure Monitor, Smiths Medical PLC, Minneapolis, MN). Intraluminal guides were removed from segments in which they were employed, and the open ends of all segments were closed using surgical clamps, leaving an approximately 12-cm long segment centered on the anastomosis. A 16-gauge needle and IV line were used to instill saline solution into one side of this region, and a second 16-gauge needle was placed into the opposing side and attached to the pressure monitor. The lumen was gradually distended with saline while the anastomosis was observed for leaks (Figure 2-2). Once a leak occurred, the pressure reading was recorded and considered the maximum burst pressure withstood by the anastomotic site for that specimen.

Bowel diameter: Diameter difference was calculated based on diameter measurements of the intestinal regions proximally and distally adjacent to the anastomosis, as well as at the anastomotic site, while saline remained infused in the segments following burst pressure measurement. Diameters were measured at six locations: three anti-mesentery to mesentery axes (proximal to anastomosis, at anastomosis, and distal to anastomosis) and three side-to-side axes (proximal to anastomosis, at anastomosis, and distal to anastomosis). From these measurements, the diameter difference (%) between the proximal and distal regions versus the anastomotic site was determined.

Anastomotic Guide Composition and Fabrication

Non-degradable 3D-printed models of an intraluminal guide were initially designed with Autodesk 123D software (Autodesk Inc., San Rafael, CA) and fabricated based on expected bowel size in

an approximately 70-kg pig, as well as the length predicted to be of greatest benefit to the technical performance of an anastomosis (Figure 2-3). A hollow cylindrical tube was determined to be the ideal shape. These prototypes were used as models for creation of a rapidly collapsible, intraluminal AG. The desired specifications were that the guide would collapse no less than 30 minutes and no longer than 3 hours after implantation within the intestine.

A guide was fabricated using a hollow cylindrical tube composed of layers of biocompatible polymer polyurethane (PU) (HydroMed:AdvanSource Biomaterials; Wilmington, MA) and moisture/fluid-degradable polymer polyvinylpyrrolidone (PVP) (polyvinylpyrrolidone : Sigma-Aldrich: Average MW 10000, St. Louis, MO). These polymers were chosen based on their water responses (water uptake and ability to dissolve in water). The polymer layers were produced using a modified salt leaching method. Briefly, the PU polymer was dissolved in 90/10 ethanol/deionized water to form medium 1, then 10 g of 75-150-μm particles (porosity agents—medium 2) for each 1 g of PU were added (Figure 2-4). The material was mixed extensively, poured over a glass mold, and transferred into a water bath to remove the salt particles. The resulting polymer film was dried and cut into a small laminate (3 x 1.5 cm). Next, the porous polymer laminate was saturated with PVP. The polymer laminates were then assembled to form multilayers over the support mold. The mold was removed, and the samples were left to dry (Figure 2-5).

The device was fabricated to serve as a temporary supportive intraluminal anastomotic guide that can rapidly lose its integrity after becoming wet and within the desired time. The desired specifications were that the guide would lose its integrity in no less than 30 minutes and no more than 3 hours after implantation within the intestine. To test the device's ability to meet these specifications, the fabricated samples were immersed in a water bath, and the integrality was observed over time.

In Vivo *Investigation*

In vivo studies were done after approval by the Institutional Animal Care and Use Committee (IACUC protocol #2522) at the University of Tennessee, Knoxville. Six domestic cross-bred pigs, weighing 35 to 70 kg, were housed in separate adjacent pens and acclimated to their environment

for twelve days. Each pig was fasted for a minimum of 12 hours prior to surgery, and water access was restricted a minimum of 2 hours before surgery. Peri-operative analgesia was provided by placement of transdermal fentanyl patches (1 µg/kg) along the dorsal midline in the mid-thoracic region at least 12 hours prior to surgery. Subjects were pre-medicated with xylazine (2 mg/kg, IM), induced with a combination of midazolam (0.1-0.2 mg/kg, IM) and ketamine (10 mg/kg, IM), an endotracheal tube was placed, and anesthesia maintained using isoflurane (range 1 to 5 %) vaporized into oxygen (100%). Each subject was placed into dorsal recumbency, clipped, and aseptically prepared along the ventral midline. The surgical model, briefly depicted in Figure 2-6, consisted of a 10-cm ventral midline laparotomy with subsequent exteriorization of 20-40 cm of jejunum. The bowel was milked free of intraluminal contents and a 15 cm segment was isolated with Doyen intestinal clamps. A complete, transverse enterotomy was performed at a 90º angle and single interrupted sutures of #3-0 PDS (Ethicon, INC., Somerville, New Jersey) were placed at the mesenteric and anti-mesenteric margins of the cut edges for stabilization and to aid in apposition of the edges. The anastomosis was completed with an interrupted simple continuous appositional pattern (two suture segments, each placed hemi-circumferentially) using #3-0 PDS. Integrity, blood perfusion, and complete closure of the anastomosis was evaluated. Approximately 20 cm distal to the first anastomosis, a second enterotomy was performed in like manner, except after the first single interrupted suture was placed and before closing the cut edges of the bowel with the same technique, the collapsible intraluminal anastomotic guide was placed within the lumen traversing and centered on the cut edges. Following replacement of the jejunum within the abdominal cavity, the linea alba was closed using #0 PDS, the subcutaneous layer with #2-0 PDS, and finally the skin with #1 polypropylene, all utilizing a simple continuous pattern. Surgeons were consulted regarding their subjective opinion of the utility of the AG during surgery.

Pigs received intramuscular ceftiofur (Excede, Zoetis Services LLC, Parsippany, New Jersey; 5 mg/kg dose) prior to surgery. The pigs were monitored frequently for signs of pain, incision site abnormalities, vomiting, abdominal distention, diarrhea, or constipation. Peri-operative analgesia was managed using fentanyl patches (1 µg/kg, TD, 72 hours) and meloxicam (0.4 mg/kg, PO, q24h x 5d). Pigs were monitored for activity, appetite, and clinical signs of pain through day 13 at which time the study was terminated.

All pigs were sacrificed 13 days after surgery, and necropsy examinations performed to

assess the gross appearance of the bowel and anastomoses, as well as the surrounding abdominal cavity. Burst pressure withstood by the anastomotic sites was determined by instilling saline into the anastomotic region and observing for leakage. Fluid pressure was assessed using a digital pressure monitor (Surgivet® V6400 Invasive Blood Pressure Monitor, Smiths Medical PLC, Minneapolis, MN). The vicinity of the anastomotic site was occluded using surgical clamps, leaving an approximately 12-cm long segment centered on the anastomosis. A 16-gauge needle and IV line were used to instill saline solution into one side of this region, and a second 16-gauge needle was placed into the opposing side and attached to the pressure monitor. The lumen was gradually distended with saline while the anastomosis was observed for leaks. Once a leak occurred, the pressure reading was recorded and considered the maximum burst pressure withstood by the anastomotic site for that sample.

The external diameter of the bowel was also measured for the assessment of stricture of the anastomotic site. Diameter difference was calculated based on diameter measurements of the intestinal regions just proximally and distally adjacent to the anastomosis, as well as at the anastomotic site, utilizing calipers while saline remained infused in the segments following burst pressure measurement. Histologic evaluation included hematoxylin and eosin and trichrome stains to assess fibrosis and collagen deposition, presence and characterization of inflammation at the anastomotic sites and within the adjacent tissue, approximate width of anastomotic sites, serosal thickness, and any additional abnormalities.

Results

Ex Vivo *Investigation*

Time required for completion of the EEA procedure, burst pressure achieved at the anastomotic site, maximum diameter of the anastomotic site, and maximum diameter of the intestine immediately proximal and distal to the EEA are summarized (Table 2-1). Procedure time required to perform an EEA without an AG was significantly longer as compared with those performed using the AG ($p < 0.05$). Burst pressure was similar for each treatment group. The maximum diameter % difference at the EEA site compared with the adjacent proximal and distal intestinal

regions was significantly less when an AG was used resulting in 14.7 to 15.2% less stricture at the site of AG anastomoses compared to anastomoses performed without a guide. Qualitative evaluation by individuals performing the anastomoses described that the procedure was easier to perform when there was a guide within the lumen.

Anastomotic Guide Characteristics

3D Keyence Laser Microscope Analysis: Three-dimensional (3D) laser microscopy (LSCM, VK-X260K, Keyence, Itasca, IL) was used to evaluate the surface morphology and topography of the samples, allowing visualization of the porous structure of the polymer laminate. The porous polymer laminate was examined using 20X and 10X lenses. The data was analyzed with Keyence's Multi-File Analyzer software. 3D microscopy confirmed that the polymer laminate has a porous structure, as shown in Figure 2-7.

Device Testing: Generally, when dry, the device is a rigid structure due to the solidification of PVP. The fabricated samples were immersed in a water bath, and the integrality was observed over time. The device lost its integrity as a function of the water/fluid response of its two polymers, causing it to collapse.

In Vivo *Investigation*

Morbidities observed after surgery included minimal incidences of diarrhea, mild pyrexia that resolved after treatment with antibiotics, and mild swelling at the incision site. No remnants of the AGs were recovered in feces.

Following sacrifice of the pigs, gross examination of the anastomoses and surrounding abdominal cavity was performed. Adhesions were discovered at eleven out of the twelve EEA sites and at adjacent regions within the abdominal cavity in five out of the six pigs. There were no significant differences in adhesion development between the anastomotic sites that involved the AG and those that did not. A standard handsewn EEA in one pig was noted to have had minor dehiscence, and no leakage or dehiscence was noted in any of the EEA performed with the AG.

The gross appearance of the healed margins of the bowel were similar for all EEA sites.

Burst pressure was found to be approximately 10% greater at AG-facilitated anastomotic sites than those of standard handsewn EEA sites (Table 2-2); however, this difference was not statistically significant. The maximum diameter achieved at the anastomotic sites that utilized an AG was significantly greater than that achieved with the standard handsewn anastomoses (Table 2-2). Subjective evaluation by surgeons performing the anastomoses noted that the guide aided in the placement of more evenly spaced sutures and eased the performance of the EEA. The surgeons noted that there was some difficulty placing the guide within the lumen due to its pliability (accountable to submersion in saline prior to surgery).

Histologic evaluation revealed characteristics of expected healing within all of the samples, including suture granulomas adjacent to anastomotic sites, fibrosis and collagen deposition within sites, serosal thickness at sites between 2-4 times that of the adjacent normal tissue, and sites ranging in width from less than 0.5 to 5 mm. All anastomotic sites contained a normal expected amount of mild-to-moderate inflammatory cell infiltration, typically mixed eosinophilic and lymphocytic inflammation. Two anastomotic sites (one standard and one AG) in two separate pigs appeared to have features of both jejunum and ileum, dependent on the section examined. The standard handsewn anastomosis in one pig demonstrated a focal region of ulceration and marked inflammatory infiltrates, including dead or degenerate segmented eosinophils and neutrophils. This sample demonstrated an increased presence of macrophages within an area of fibrosis. Within this same pig, the bowel edges of the AG site appeared to be overlapped in one region. Another standard handsewn anastomosis in a different pig similarly demonstrated an area of ulceration, along with the presence of hemorrhage, imbedded plant material or suture, and marked suppurative and eosinophilic inflammation. Hemorrhage was found within the serosa of this sample. Within the standard handsewn site of an additional pig, there was a focal region of pyogranulomatous inflammation, and in the AG site of this same pig, there was a mild-to-moderate amount of inflammation and hemorrhage within the serosa which was deemed likely not significant.

Discussion

During post-mortem assessment, anastomotic site diameter was deemed to be improved in the sites in which an AG was used. Although small, this difference may be clinically significant, resulting in a decreased likelihood of stricture and impaction at surgical sites. A meta-analysis examining complications following sutured and stapled colorectal anastomosis in 1233 human patients determined that strictures occurred in 2% and 8% of patients, respectively [2, 25]. One limitation to evaluating the diameter difference by measuring the external diameter with calipers is that any inverted mucosa resulting in a further narrowed intraluminal diameter would not be accounted for. Two alternative methods of assessing the intraluminal diameter and anastomotic index are by instillation of a contrast agent into the delineated region of the anastomosis and subsequent radiographic imaging [26, 27], or by measurement of the wall thickness at the anastomotic site and proximally and distally to it utilizing calipers [27].

Differences in burst pressure between the groups were not significantly different. This suggests that the healing process in the intestine with EEA is similar regardless of the technique employed. Maximum burst pressures achieved were physiologically appropriate, and in fact were in excess to normal physiological pressures [28, 29], so it does not appear that the performance of anastomoses produced a risk of bowel disruption during motility, at least when assessed two weeks post-operatively.

Adhesion development occurred at nearly all anastomotic sites and within local areas of the abdominal cavity. It was difficult to differentiate which anastomotic site may have incited the additional adhesions within the abdomen, and the approximately 20 cm distance between the two anastomoses may ultimately have been too close in proximity to allow this determination. Intraluminal appearance of each anastomosis was not noticeably different, supporting the likelihood that the methods did not adversely affect the normal process of intestinal healing. One pig appeared to have developed a small dehiscence at the standard handsewn anastomotic site, which was sealed with an adhesion. Histologic evaluation of the samples did not reveal any substantial concerns in regards to integrity of the anastomotic sites or presence of excessive inflammation that would be expected to progress to significant disease, including within the samples that demonstrated focal regions of inflammation. All samples revealed anticipated

indicators of healing, including granuloma formation at suture sites, fibrosis and collagen deposition within the anastomotic sites, and thickening of the serosa.

The EEA technique was noted by the surgeons to be easier to perform with the use of the AG. This is likely owing to the ability to place sutures more easily within the cut edges of bowel due to the edges being dilated by the guide as opposed to the natural contraction and eversion that occurs when the bowel is transected. Precision and accuracy in reconstruction of the continuity and patency of the bowel is critical to ensuring that devastating dehiscence or stricture does not occur [3, 30]. The only concern noted with the use of the AG regarded difficulty placing the guide within the lumen due to its pliability. The guides were briefly soaked in saline prior to surgery, which likely accounts for the majority of this pliability. However, sturdiness of the guide may also be addressed in modified designs by altering the thickness or polymer composition. Time to collapse of the guide was assessed in hydration studies prior to placement within the subjects and was deemed appropriate. No remnants remained within the lumen upon necropsy evaluation, which further supports that the guides broke apart.

One concern about placement of a medical device within the bowel lumen is the potential for complications associated with the device itself. Non-degradable or slowly degrading intestinal stents that have been previously available or investigated may increase morbidity rates associated with hindrance to normal peristalsis, dislodgement, blockage of the intestinal lumen with the stent, and impaction of the lumen of the stent with digesta [21-23]. We designed a rapidly collapsible polymeric device to avoid these potential complications. Should the guide dislodge shortly after the surgery, it would quickly break apart with the passage of digesta within the bowel. The testing of the device by water bath immersion demonstrated that the device lost its integrity over time as a function of the water/fluid response of its two polymers, causing it to collapse. Generally, the two polymers have different responses to fluid. PU uptakes fluid into its structure, with the ability to increase in mass by about 300% of its dry weight and expand in size by about 60%, as shown in Figure 2-8. In contrast, PVP dissolves when exposed to fluid, causing the device to lose its polymer-polymer bonds.

The ability of an intraluminal anastomotic guide to aid in increasing the diameter of an intestinal anastomosis site, as well as ease the performance of the technique itself, without presenting any additional complications, supports the use of guides for this particular procedure.

This could ultimately reduce complications that occur post-operatively, including dehiscence, leakage, peritonitis, stricture, and impaction. Any reduction in time of performance would also be beneficial as some patients undergoing this procedure may be physiologically and anesthetically unstable. The use of a swine model is advantageous for translation to human medicine, as swine have gastrointestinal tracts that are comparable to humans. Continued research is warranted to develop a collapsible or degradable intraluminal guide for small intestinal anastomosis for use in human and animal patients, and the data from this study will be utilized in the planning of a follow-up validation study employing a larger number of swine with assignment of animals to a single treatment group rather than the performance of both procedures within the same animal.

Acknowledgements

Additional thanks for technical support during these investigations is given to Dr. Madhu Dhar, Dr. Xiaocun Sun, Dr. Tom Doherty, Dr. Christopher Smith, Katie Waller, Sara Root, Paxton Parker, Richard Steiner, Austin Bow, Steven Newby, Rachel Rodriguez, Tammy Howard, Kaitlin Siegfried, Phil Snow, and Wampler's Farm Sausage.

References

[1] Pedersen, A.P., Alghazali, K.M., Hamzah, R.N., Mulon, P.-Y., McCracken, M., Rifkin, R.E., Mhannawee, A., Nima, Z.A., Griffin, C., Donnell, R.L., Biris, A.S., and Anderson, D.E., *Development and in vivo Assessment of a Rapidly Collapsible Anastomotic Guide for Use in Anastomosis of the Small Intestine: A Pilot Study Using a Swine Model.* Frontiers in Surgery, 2020. **7**.

[2] Goulder, F., *Bowel anastomoses: The theory, the practice and the evidence base.* World journal of gastrointestinal surgery, 2012. **4**(9): p. 208-213.

[3] *Intestinal Anastomosis Technique*. 2016 [cited 2017 June 30]; Available from: https://emedicine.medscape.com/article/1892319-technique.

[4] Tobias, K. and Ayres, R., *Key gastrointestinal surgeries - Intestinal anastomosis.* Veterinary Medicine -Bonner Springs then Edwardsville-, 2006. **101**: p. 226-229.

[5] Ralphs, S.C., Jessen, C.R., and Lipowitz, A.J., *Risk factors for leakage following intestinal anastomosis in dogs and cats: 115 cases (1991-2000).* J Am Vet Med Assoc, 2003. **223**(1): p. 73-7.

[6] Weisman, D.L., Smeak, D.D., Birchard, S.J., and Zweigart, S.L., *Comparison of a continuous suture pattern with a simple interrupted pattern for enteric closure in dogs and cats: 83 cases (1991-1997).* J Am Vet Med Assoc, 1999. **214**(10): p. 1507-10.

[7] Burch, J.M., Franciose, R.J., Moore, E.E., Biffl, W.L., and Offner, P.J., *Single-layer continuous versus two-layer interrupted intestinal anastomosis: a prospective randomized trial.* Annals of surgery, 2000. **231**(6): p. 832-837.

[8] Ellison, G.J., MP; Park, RD, *End-to-end approximating intestinal anastomosis in the dog: A comparative fluorescein dye, angiographic and histopathologic evaluation.* Journal of the American Animal Hospital Association, 1982. **18**: p. 729-736.

[9] Allen, D., Smeak, D.D., and Schertel, E., *Prevalence of small intestinal dehiscence and associated clinical factors: a retrospective study of 121 dogs.* Journal of The American Animal Hospital Association, 1992. **28**: p. 70-76.

[10] Shikata, S., Yamagishi, H., Taji, Y., Shimada, T., and Noguchi, Y., *Single- versus two-layer intestinal anastomosis: a meta-analysis of randomized controlled trials.* BMC surgery, 2006. **6**: p. 2-2.

[11] Garude, K., Tandel, C., Rao, S., and Shah, N.J., *Single layered intestinal anastomosis: a safe and economic technique.* Indian J Surg, 2013. **75**(4): p. 290-3.

[12] Sajid, M.S., Siddiqui, M.R., and Baig, M.K., *Single layer versus double layer suture anastomosis of the gastrointestinal tract.* Cochrane Database Syst Rev, 2012. **1**: p. Cd005477.

[13] Getzen, L.C., Roe, R.D., and Holloway, C.K., *Comparative study of intestinal anastomotic healing in inverted and everted closures.* Surg Gynecol Obstet, 1966. **123**(6): p. 1219-27.

[14] Goligher, J.C., Morris, C., McAdam, W.A., De Dombal, F.T., and Johnston, D., *A controlled trial of inverting versus everting intestinal suture in clinical large-bowel surgery.* Br J Surg, 1970. **57**(11): p. 817-22.

[15] Holt, D.S., DH, *Large intestines*, in *Textbook of Small Animal Surgery*. 2003, Saunders: Philadelphia, PA.

[16] Bellenger, C.R., *Comparison of inverting and appositional methods for anastomosis of the small intestine in cats.* Vet Rec, 1982. **110**(12): p. 265-8.

[17] Deveney, K.E. and Way, L.W., *Effect of different absorbable sutures on healing of gastrointestinal anastomoses.* Am J Surg, 1977. **133**(1): p. 86-94.

[18] Milovancev, M., Weisman, D.L., and Palmisano, M.P., *Foreign body attachment to polypropylene suture material extruded into the small intestinal lumen after enteric closure in three dogs.* J Am Vet Med Assoc, 2004. **225**(11): p. 1713-5, 1701.

[19] Fielding, L.P., Stewart-Brown, S., Blesovsky, L., and Kearney, G., *Anastomotic integrity after operations for large-bowel cancer: a multicentre study.* Br Med J, 1980. **281**(6237): p. 411-4.

[20] Leung, T.T., MacLean, A.R., Buie, W.D., and Dixon, E., *Comparison of stapled versus handsewn loop ileostomy closure: a meta-analysis.* J Gastrointest Surg, 2008. **12**(5): p. 939-44.

[21] Wang, Z., Li, N., Li, R., Li, Y., and Ruan, L., *Biodegradable intestinal stents: A review.* Progress in Natural Science: Materials International, 2014. **24**(5): p. 423-432.

[22] Brightwell, N.L., McFee, A.S., and Aust, J.B., *Bowel obstruction and the long tube stent.* Arch Surg, 1977. **112**(4): p. 505-11.

[23] Son, S.R., Franco, R.A., Bae, S.H., Min, Y.K., and Lee, B.T., *Electrospun PLGA/gelatin fibrous tubes for the application of biodegradable intestinal stent in rat model.* J Biomed Mater Res B Appl Biomater, 2013. **101**(6): p. 1095-105.

[24] Wang, Y., Cai, X., Jin, R., Liang, Y., Huang, D., and Peng, S., *Experimental study of primary repair of colonic leakage with a degradable stent in a porcine model.* J Gastrointest Surg, 2011. **15**(11): p. 1995-2000.

[25] Lustosa, S.A., Matos, D., Atallah, A.N., and Castro, A.A., *Stapled versus handsewn methods for colorectal anastomosis surgery.* Cochrane Database Syst Rev, 2001(3): p. Cd003144.

[26] Gandini, M., *In vitro evaluation of a closed-bowel technique for one-layer hand-sewn inverting end-to-end jejunojejunosotomy in the horse.* Vet Surg, 2006. **35**(7): p. 683-8.

[27] Zilling, T.L., Jansson, O., Walther, B.S., and Ottosson, A., *Sutureless small bowel anastomoses: experimental study in pigs.* Eur J Surg, 1999. **165**(1): p. 61-8.

[28] Coolman, B.R., Ehrhart, N., Pijanowski, G., Ehrhart, E.J., and Coolman, S.L., *Comparison of skin staples with sutures for anastomosis of the small intestine in dogs.* Vet Surg, 2000. **29**(4): p. 293-302.

[29] Ellison, G., *End-to-end anastomosis in the dog: A comparison of techniques.* Compendium on Continuing Education for the Practising Veterinarian -North American Edition-, 1981. **3**: p. 486-494.

[30] Shandall, A., Lowndes, R., and Young, H.L., *Colonic anastomotic healing and oxygen tension.* Br J Surg, 1985. **72**(8): p. 606-9.

Appendix
Tables & Figures

Table 2-1: Comparison of Completion Time, Burst Pressure, and Diameter Difference for Each Anastomotic Technique (*Ex Vivo)*

	Hand-Sewn EEA	Anastomotic Guide EEA
Number of Trials	10	9
Time for Completion (min:sec)[a]	15:04 ± 1:43	10:50 ± 0.50
Burst Pressure (mmHg)[b]	48 ± 11	43 ± 9
Average Maximum Diameter Proximal to EEA (mm)	34.7 ± 2.4	33.5 ± 2.2
Average Maximum Diameter Distal to EEA (mm)	35.5 ± 2.8	33.5 ± 1.5
Average Maximum Diameter at EEA (mm)	27.3 ± 3.0	31.2 ± 2.5
Diameter Difference of Site and Adjacent Regions (%)[a]	78.0 ± 8.6	93.2 ± 3.3

Average maximum diameter values are calculated as the mean of the anti-mesentery-to-mesentery and side-to-side diameters determined with calipers. Diameter difference represents the difference between the average diameter of the bowel proximal and distal to the anastomotic site and the diameter of the anastomotic site itself. One extreme outlier was removed from the Hand-Sewn EEA group for calculations of time for completion and burst pressure. Diameter measurements were able to be performed on only 7 samples for each technique.

[a]Statistically significant difference ($p < 0.05$), [b]No significant difference

Table 2-2: Comparison of Adhesion Number, Burst Pressure, and Maximum Diameter for Each Anastomotic Technique (*In Vivo*)

	Standard Handsewn EEA	Anastomotic Guide EEA
Average Number of Adhesions at Site	1	1
Average Burst Pressure (mmHg)[b]	150.6 ± 49.3	166.0 ± 47.5
Average Maximum Diameter at Anastomotic Site (mm)[a]	22.73 ± 2.0	26.59 ± 3.9
Diameter Difference of Anastomotic Sites (%)[a]		+17%

Burst pressure was obtained at only five of the six anastomotic sites of each technique due to perforation of the anastomotic site or adjacent bowel in two samples. Presence of adhesions at the anastomotic sites and local regions of the abdominal cavity was assessed grossly. Burst pressure was measured by instilling saline into the anastomotic region and observing the maximum pressure withstood by the anastomosis *via* a digital pressure monitor. Maximum diameter at each anastomotic site was measured while saline remained infused in the segments following burst pressure measurement. Diameter difference is the difference between the average diameter of the anastomoses performed with and without the use of an AG.

[a]Statistically significant difference ($p < 0.05$), [b]No significant difference

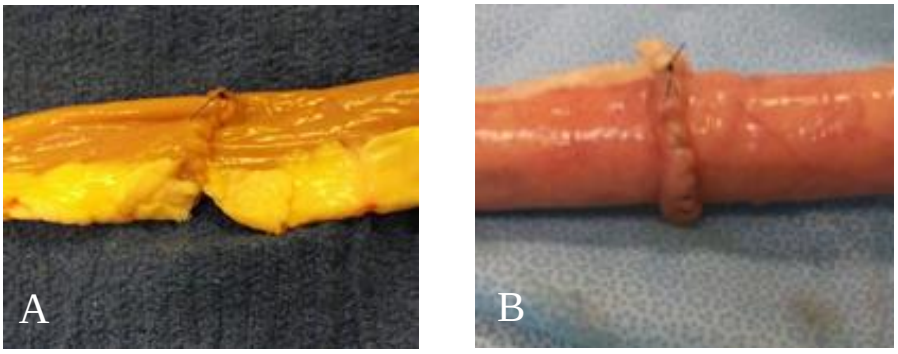


Figure 2-1: *Ex vivo* intestinal anastomoses

(A) Anastomosis performed with no intraluminal guide; (B) anastomosis performed with an intraluminal guide (guide still located within lumen)

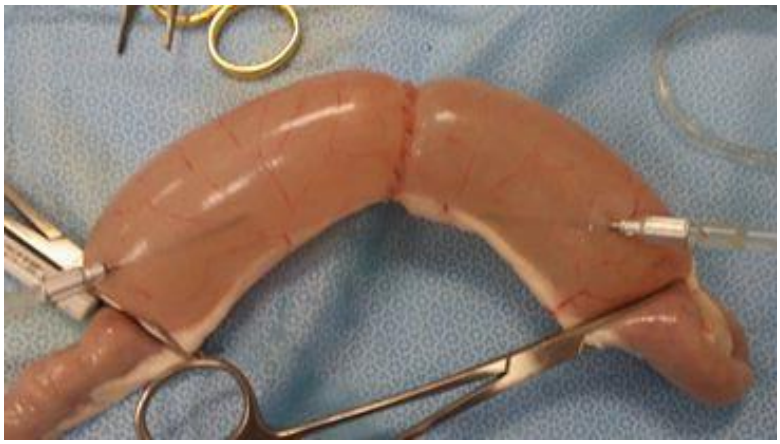


Figure 2-2: *Ex vivo* burst pressure testing

An intestinal segment distended with saline to assess pressure able to be withstood by the anastomotic site.

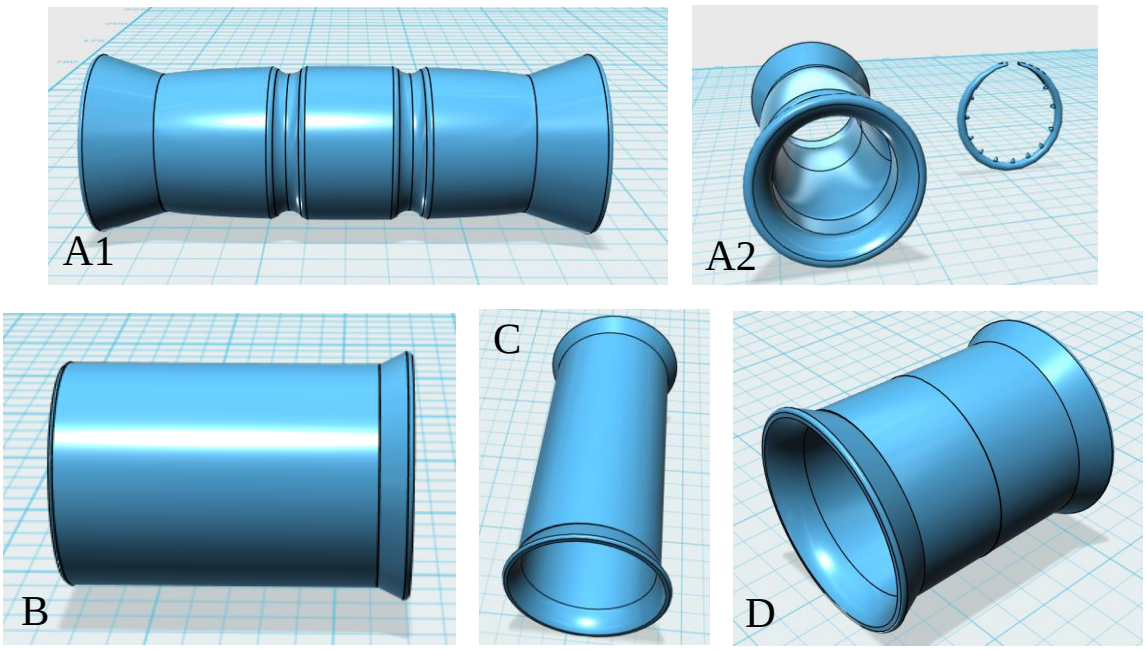


Figure 2-3: 3D-printed non-degradable intraluminal guide designs

Designs generated with Autodesk 123D software (Autodesk Inc., San Rafael, CA); (A1) lateral view of prototype employing external fixator; (A2) end-on view of prototype employing external fixator, with external fixator depicted to the right; (B) prototype with flange on single end; (C) prototype with flange on each end and expanded length; (D) prototype with flange on each end and shortened length.

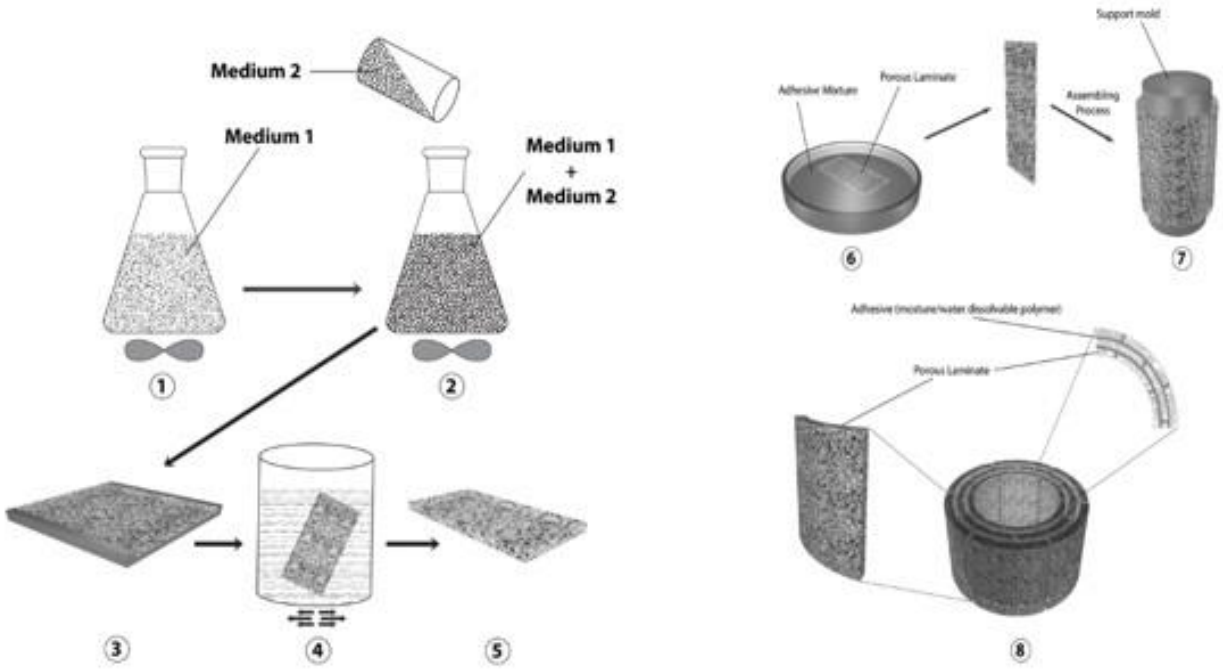


Figure 2-4: Intestinal guide fabrication protocol

General protocol used to fabricate the device. Medium 1 refers to PU dissolved in 90/10 ethanol/deionized water. Medium 2 refers to salt porosity agents with 75-150-μm diameter.

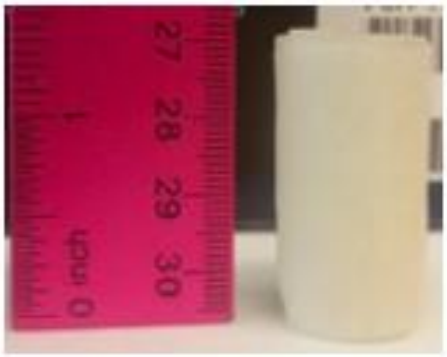


Figure 2-5: Fabricated intestinal anastomotic guide

Fabricated device measures 3 x 1.5-cm

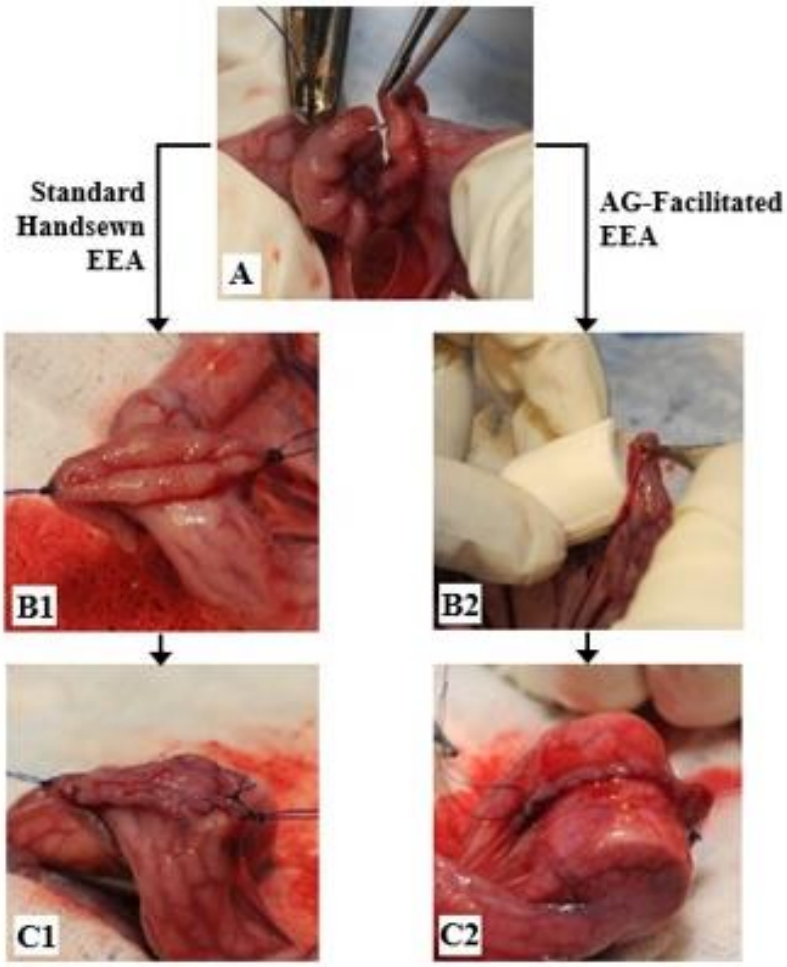


Figure 2-6: End-to-end anastomosis procedure

(A) a single interrupted suture is placed on the anti-mesenteric margin of the bowel immediately following performance of a transverse enterotomy; (B1) single interrupted sutures are secrured on both the anti-mesenteric and mesenteric margins, and the bowel edges are apposed for further suturing; (C1) a row of simple continuous sutures is placed hemi-circumferentially; (B2) an AG is placed into the lumen of the bowel; (C2) the anastomosis is performed overtop the AG after complete placement within the lumen.

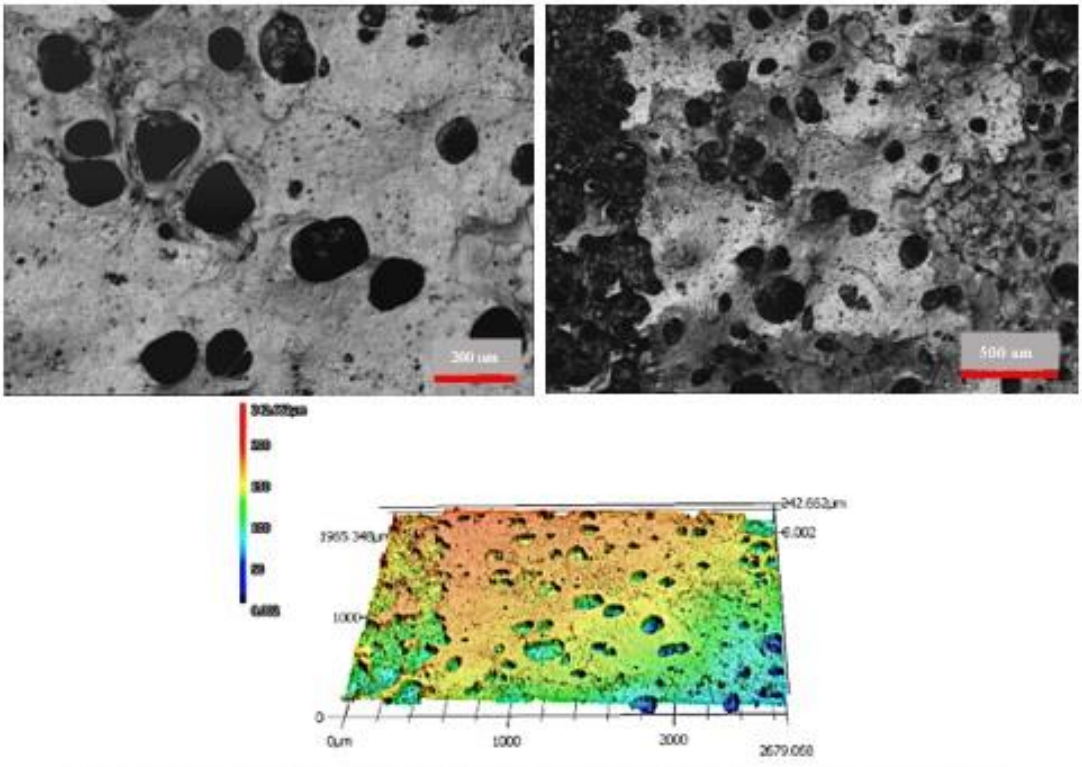


Figure 2-7: 3D LSCM results for the porous polymer laminate used to fabricate the device

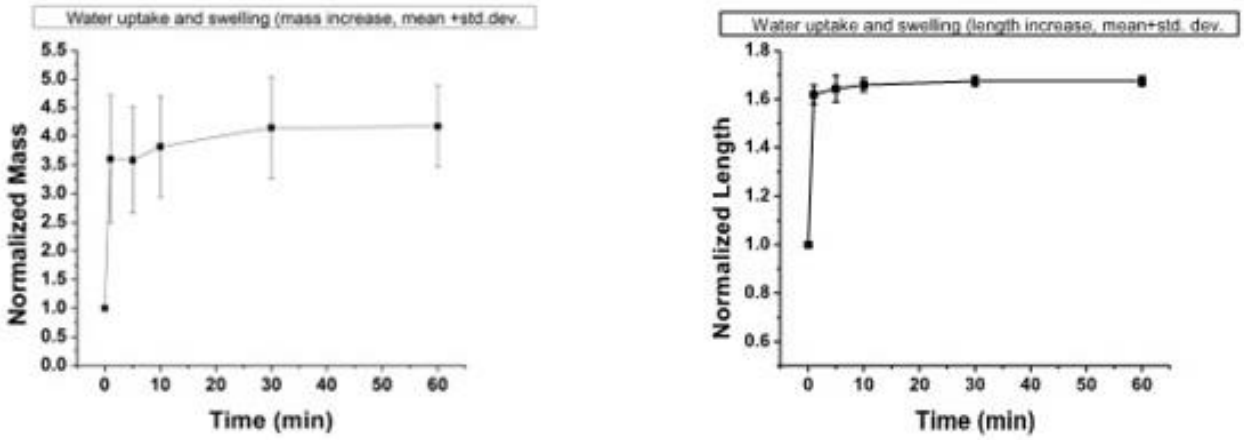


Figure 2-8: Water uptake and swelling behavior of the device

Water uptake and swelling behavior of the device porous polymer laminate used to fabricate the device. Left: normalized mass; right: normalized length.

CHAPTER 3 : *Feasibility Study*: Second-Generation Collapsible Guide for Use in Small Intestinal Anastomosis

Statement on Utilization of Pre-Publication Manuscript:

The contents of this chapter are anticipated to be published in a journal with a biomaterials focus in 2021. Karrer Alghazali and Alisha Pedersen were co-authors in the production of the manuscript, with Karrer taking first authorship.

Anticipated Title and Authorship:

Surgical application of a rapidly degradable, intraluminal anastomotic guide for enhanced surgical performance of end-to-end small intestinal anastomosis

Karrer M. Alghazali, PhD[1,2*]; Alisha Pedersen, DVM[3*]; Rabab N. Hamzah[1]; Pierre-Yves Mulon, DVM, DES, Dipl. ACVS[3]; Rebecca E. Rifkin, DVM, PhD[3]; Anwer Mhannawee, PhD[1]; Zeid A. Nima, PhD[1]; Christopher Griffin[1]; Robert L. Donnell, DVM, PhD, DACVP[4]; Alexandru S. Biris, PhD, MS[1]; David Anderson, DVM, MS, DACVS[3]

[*]Co-first authors, equal work and with equal credit.
[1]Center for Integrative Nanotechnology Sciences, University of Arkansas at Little Rock, Little Rock, AR
[2]NuShores Biosciences LLC, Little Rock, AR
[3]Department of Large Animal Clinical Sciences, College of Veterinary Medicine, University of Tennessee, Knoxville, TN
[4]Department of Biomedical and Diagnostic Sciences, College of Veterinary Medicine, University of Tennessee, Knoxville, TN

Abstract

Hand-sewn, end-to-end anastomosis of the small intestine remains a commonly performed surgical procedure. The aim of this study was to assess the application of a novel intraluminal, rapidly degradable anastomotic guide used for the purpose of enhancing intestinal alignment and placement of sutures in the small intestine *in vivo* using a swine small intestinal anastomosis model. An anastomotic guide was designed to improve handleability during creation of an end-to-end small intestinal anastomosis. The anastomotic guide construct was designed to rapidly degrade (< 3 hours) and manufactured as a hollow cylinder, composed of layers of polyurethane and polyvinylpyrrolidone. The guide was designed to reliably degrade yet maintain sufficient rigidity so as to support manipulation during surgery. Each pig underwent a single hand-sewn end-to-end small intestinal anastomosis, either with or without the use of the anastomotic guide. Qualitative surgeon's observational data revealed improved visibility for suture placement and intestinal alignment, as well as greater surgeon confidence in the integrity of the anastomosis when a guide was employed. Total procedure time, intestinal diameter, and intestinal burst pressure was similar for both techniques. Utilization of a guide for small intestinal anastomosis appeared to enhance the surgical technique without prolonging the operative time and without post-operative morbidities.

Introduction

Intestinal anastomosis is a relatively common procedure performed in human and veterinary patients, often including resection of a diseased segment of bowel prior to reconnection of the remaining viable ends in order to reestablish bowel continuity [1, 2]. Despite a variety of minimally invasive and stapled anastomosis techniques, hand-sewn end-to-end anastomosis of the small intestine remains a common technique used to re-establish intestinal patency and flow of digesta after intestinal resection. Indications for intestinal resection and anastomosis include obstruction, such as that from foreign bodies, pathologic strictures, or chronic constipation; inadequate segmental functionality due to neurologic dysfunction; traumatic or ulcerative perforation; or other disease processes, including intussusception, neoplasia, volvulus, torsion, chronic inflammatory bowel disease, and Crohn's disease [1, 2]. Post-operative complications are commonly encountered, the most significant of these being dehiscence, leakage, peritonitis, ileus, tissue necrosis, obstruction, tissue hypoxia, stricture, and death [1-5]. Dehiscence and leakage from the anastomotic site, causing septic peritonitis, is one of the most serious complications and is reported to occur as frequently as 1 to 24% of cases [6, 7]. Despite medical advancements including automated devices, these complications persist.

Recently, we developed an intraluminal, rapidly degrading anastomotic guide (AG) as a means of improving the surgical technique for hand-sewn anastomosis of the small intestine [8]. This anastomotic device was developed for placement within the lumen of bowel at the site of end-to-end small intestinal anastomosis to serve as a guide for alignment and suturing of hand-sewn anastomoses. The AG was designed to rapidly degrade such that impaction or interruption of intestinal motility would not occur. The guide serves to expand the lumen at the anastomotic site, resulting in precise apposition of the cut edges of the intestine, increased visibility of suture placement, and improved tissue handling. The AG then rapidly disassembles and exits the bowel with the flow of normal digesta.

Stricture of the intestine at the anastomosis site is a routine consequence of intestinal resection and anastomosis, regardless of the technique used [5]. Non-degradable metal or plastic intraluminal stents have been utilized in the treatment of strictures, but there are numerous associated morbidities, including secondary stricture, stent migration, hyperplasia of intestinal

mucosa, perforation of the stent through the intestinal wall, and the necessity for repeated endoscopic procedures [5]. In patients where intraluminal support is only needed during the immediate operative period and without the need for continued intraluminal support during the convalescent period, a rapidly degradable, intraluminal medical device may be used to minimize complications of hand-sewn anastomosis in order to prevent procedural- and device-associated morbidities. Based on our prototype research, the AG used in this study was improved and designed to aid in the performance of the procedure and then rapidly degrade during the immediate post-operative period. This is expected to eliminate morbidities requiring placement of an indwelling non-degradable stent at a later date.

We propose several benefits to incorporating an AG in the performance of a hand-sewn technique. One essential feature impacting the acceptance of the AG by surgeons is that it allows for the surgeon to apply the same hand-sewn suturing technique to which they are accustomed. The AG expands the lumen of the bowel so that the edges that frequently evert following transection resume a more normal conformation. When suturing results in an inverted anastomosis, the size of the intestinal lumen is reduced; mucosal eversion may increase the incidence of adhesion development [1]. Visualization of the delineation between the layers of the bowel wall is enhanced with the AG, ensuring that submucosa is contained in each suture. This is imperative as the submucosa is the holding layer of the intestinal anastomosis and is the most resistant to the tensile forces exerted on the site [3, 4]. Expansion of the bowel provided by the AG allows for the entirety of the anastomotic site to be better visualized and ensures that no aspect of the circumference is missed in the anastomosis, including at the mesenteric border where most post-operative anastomotic leaks occur [4]. This enhanced visualization is not only important for assurance of complete circumferential closure of the anastomosis, but for reduction of excessive suture material that may be incorporated due to concerns about tissue integrity [3]. The guide eliminates the possibility of engaging the posterior wall of the intestine during placement of sutures, a recognized complication of hand sewn anastomosis when the bowel is collapsed during the procedure [4]. Due to the rapid degradability of the guide and its composition of polymers with demonstrated biocompatibility, there are no anticipated complications associated with the utility of the AG reported here.

The objectives of this study were to assess the use of a rapidly degradable anastomotic guide

applied in the performance of end-to-end small intestinal anastomoses as compared to those completed without use of an AG. This study evaluated parameters including enterotomy time, total procedure time, and subjective assessment of the technical aspects of the procedure as indicated by surgeons performing the surgeries. Post-surgery parameters included fecal consistency and AG elimination time. Post-mortem parameters included determination of lumen diameter at the anastomotic site compared to the surrounding bowel and intestinal burst pressure of the intestine in the region of the anastomotic site. We hypothesized that anastomoses performed with an AG would enhance the technical performance and outcomes of the procedure compared to anastomoses performed without the use of an AG.

Materials and Methods

Anastomotic Guide Fabrication & Hydration/Degradation Testing

Anastomotic guide fabrication: The device (patent pending) was fabricated by assembling layers of porous polymer laminate to the form of a cylindrical shape. Each individual laminate was saturated with water dissolvable polymer which acts as an adhesive to bond the polymer layers. Briefly, a novel method was used to fabricate the porous polymer film (Figure 3-1). The technique was based on using high air pressure spraying to deposit the microfiber structure of the polymer from its solution. Chloroform was used as a solvent to blend two immiscible polymers with ratio polycaprolactone (PCL) 70% and polyurethane (PU) 30%. The instant solvent evaporation and the high injection air pressure were able to homogenize both PCL and PU to form a microfiber structure. The resulting film was cut to form 1.5-cm by 3-cm laminates. These polymer laminates were used to form a hollow cylindrical tube, where each individual laminate was saturated with 20% polyvinylpyrrolidone (PVP) solution in water for 1 minute, then assembled over a cylindrical mold to form a multilayered structure. After that, the mold was removed and the hollow cylindrical sample left to dry for 48 hours. The completely dried device has a rigid structure as an effect of the presence of PVP polymer (Figure 3-2).

Assessment of surface morphology and topography: A 3D Keyence Laser Microscope (LSCM,

VK-X260K, Keyence, USA) was used to evaluate the surface morphology and topography of the guide samples. 3D measurement data collected were analyzed with Keyence's Multi-File Analyzer software. Samples were examined in the following order: polymer laminate before saturation with PVP, polymer laminate after saturation with PVP. Both sets of samples were examined using 20X lens and 100X lens.

Mechanical testing of the device: Compression tests of the samples were performed using the ADMET expert 7601 universal testing system (ADMET, Inc., Norwood, Massachusetts). Briefly, the hollow cylindrical tube with a dimension 20-mm diameter and 30-mm length was placed in the sample holder. It was then subjected to a preload of 1 Lbf before starting the compression test, with a displacement rate of 10-mm/minute and a maximum load applied of 250 Ibf. The sample was compressed up to 100% of its initial height. After the data was collected, the stress/strain curve was plotted.

In vitro *device degradation or disassembly method:* The device was fabricated to serve as a temporary supportive intraluminal anastomotic guide that can be rapidly degraded or disassembled within a desired timeframe. The desired specifications were that the guide would degrade in not less than 30 minutes and not longer than 3 hours after implantation in the intestine. To test the device's ability to disassemble, we used a water bath as a medium. The fabricated samples were immersed in the water bath, and device integrality was visualized with time.

Surgical Procedure

Utilization of pigs for this study was approved by the Institutional Animal Care and Use Committee (IACUC) at the University of Tennessee, Knoxville (#2522). Twelve mixed-breed, white production pigs weighing between 14 and 40 kg (median 30.9 kg, mean 28.6 ± 7.2 kg) were acclimated to individual indoor pens for a minimum of 7 days. Prior to surgery, pigs were fasted for at least 12 hours and withheld from water for approximately 2 hours. Transdermal fentanyl patches (1 µg/kg TD, approximately 72-hour duration) were applied to the dorsum a minimum of 12 hours before surgery. If any fentanyl patch was removed or dislodged during that period, a new

fentanyl patch was placed prior to surgery. Pigs were pre-medicated with a combination of midazolam (0.1-0.2 mg/kg IM), xylazine (2 mg/kg IM), and ketamine (10 mg/kg IM). Once anesthetized, pigs were intubated and maintained on inhalant isoflurane and placed into dorsal recumbency for aseptic surgical site preparation. Ceftiofur CFA (Excede, Zoetis Services LLC, Parsippany, New Jersey; 5 mg/kg IM), maropitant citrate (Cerenia, Zoetis Services LLC, Parsippany, New Jersey; 1 mg/kg IV), and flunixin meglumine (Prevail, VetOne®, Boise, Idaho; 2.2 mg/kg IV) were administered para-operatively for prevention of infection, control of nausea, and mitigation of inflammation/pain management, respectively.

A laparotomy incision approximately 10-cm long was made along the ventral midline and a 20 to 30-cm long segment of jejunum was exteriorized. From the center of the jejunal segment directing orad and aborad, the bowel was gently compressed to move intraluminal contents away from the planned site of enterotomy. Intestinal clamps were placed on either side of the surgical site, delineating an approximately 10-cm section.

Hand-sewn enterotomy group (control): A complete, transverse enterotomy was performed across the jejunum perpendicular to the mesenteric border. Single interrupted stay sutures (#3-0 PDS, Ethicon, INC. Somerville, New Jersey), without knotting, were placed on the mesenteric and anti-mesenteric edges in order to hold the cut edges apposed. Anastomoses performed without the use of a guide were initiated using 2 single full-thickness simple interrupted sutures of #3-0 PDS, one each placed on the mesenteric and anti-mesenteric borders. Then, a single row of full-thickness simple continuous sutures of #3-0 PDS were placed coursing from the anti-mesenteric margin to the mesenteric margin, followed by, in like manner, a single row on the opposing side from the mesenteric margin to the anti-mesenteric margin.

Hand-sewn enterotomy with AG group: For anastomoses that were facilitated with an anastomotic guide, the guide was placed into the lumen on one side of the enterotomy and then into the opposing side so that the bowel edges were opposed overtop of the guide (Figure 3-3). The suturing process was identical to that of the non-guide-aided anastomoses. Occasionally, an additional simple interrupted suture was placed between the mesenteric and anti-mesenteric edges to further secure the guide within the lumen.

The integrity of each anastomosis was assessed by releasing the intestinal clamps and gently compressing contents from the surrounding bowel into the surgical site and monitoring for leakage. The bowel was rinsed with sterile saline and replaced into the abdomen after which the linea alba was closed in a simple continuous pattern (#0 PDS, Ethicon, INC. Somerville, New Jersey). The skin and subcutaneous layers were closed together in a simple continuous pattern (#1 polypropylene, Ethicon, INC. Somerville, New Jersey). Total procedure time, starting with the initiation of the skin incision, and enterotomy time, starting with the first cut into the intestine, was recorded for all surgeries.

Post-operative analgesia consisted of maintaining fentanyl patches until at least 60 hours after surgery and administration of meloxicam (0.4 mg/kg PO, q24hr x 5 days). Post-operative monitoring was comprised of daily physical examinations, pain and incision assessments, observations of feed intake and hydration status, monitoring fecal and urine output, and body weight measurements. Fecal output was monitored with a scoring system performed twice daily to analyze trends in consistency for the duration of the study, as well as to track elimination of the anastomotic guides. The scale, adapted from Wen *et al.* (2018) [9], ranged from 0 to 3, with (0) indicating normal/semi-firm feces, (1) pasty, (2) semi-liquid, and (3) liquid feces. If any pig were not to have defecated at the time of observation, no score was given.

Post-Mortem Data Collection

Pigs were sacrificed 1 month (range 29 to 33 days) after surgery. Necropsies were performed to assess the overall appearance of the abdomen, including signs of peritonitis, and to detect the presence of any adhesions at the anastomotic sites. A segment of jejunum approximately 20-cm long and with the anastomotic site centrally-located was clamped at either end with intestinal clamps and infused with saline until dilated to a turgid state. The diameters of the anastomotic site and the bowel immediately orad and aborad were measured with calipers. A pressure monitor (Surgivet® V6400 Invasive Blood Pressure Monitor, Smiths Medical PLC, Minneapolis, MN) attached to a 16-gauge needle that penetrated into the region was then utilized to measure intraluminal pressure within the bowel lumen as saline was continuously infused through another 16-gauze needle penetrating the opposing side. The maximum pressure achieved within the lumen,

before loss of integrity in the anastomosis or bowel wall, was measured as the maximum burst pressure.

Anastomotic sites were harvested and preserved in 10% neutral buffered formalin, then sectioned to create 5 µm-thick tissue slides for histology. Histology specimens were stained with hematoxylin and eosin (H&E) and Masson's trichrome stain and evaluated by a veterinary pathologist. Characteristics that were assessed included deposition of collagen, inflammatory cell infiltration, width of the anastomotic site, and thickening of the serosa at the anastomotic site.

Statistical Analysis

All quantitative analyses (total procedure time, total enterotomy time, return to fecal production, anastomotic site diameter compared to surrounding bowel, and burst pressure) were analyzed using a one-tailed student's *t*-test with p-value < 0.05 considered statistically significant. Averages are presented with standard deviations. Incidence of fecal score type post-surgery is presented as a percent of all fecal production recordings.

Results

Anastomotic Guide Material Characteristics

Surface morphology and topography results: Surface morphology and topography of samples were evaluated using 3D laser microscopy. Two sets of samples were evaluated; the first set being the polymer laminate alone and the second being the polymer laminate after saturation with PVP. The results confirmed that the polymer laminate in the first set has a porous structure consisting of micro-sized fibers, as shown in Figure 3-4. The results also indicate the second set of samples show micro-sized fiber structure for the polymer laminate used to fabricate the device after it is saturated with PVP. The PVP-coated polymer laminate also demonstrates a porous structure, as it clearly shows that the fiber structure is partially coated with PVP polymer (Figure 3-4).

Mechanical compression results: The compression test for the samples was used to investigate

the device's durability and the ability to maintain its structure during manipulation. The results indicated that the device can withstand up to 6 Lbf when compressed up to 20% of the initial diameter, and up to 12 Lbf when compressed up to 50% of its initial diameter (Figure 3-5).

In vitro *device degradation or disassembly results:* The degradability or disassembly of the device when it comes into contact with water was evaluated using a water bath. The result shows that the device loses its integrity gradually after exposure to water. The device was fabricated by assembling porous layers of polymer laminate and by saturating them with the water dissolvable polymer as an adhesive. The disassembly steps start when the water attaches to the adhesive polymer, which leads to softening of its structure, followed by separation of the outer layer of the device after 10 minutes. The device completely collapses or disassembles after about 30 minutes (Figure 3-6).

Intra-Operative Data

Operative times: During the surgical procedures, times were recorded at the start of the skin incision ("procedure start"), transection of the bowel ("enterotomy start"), placement of the last knot within the anastomosis ("enterotomy end"), and placement of the last knot within the skin incision ("procedure end"). Total surgical time and total enterotomy time were determined and are displayed in Figure 3-7. The average procedure time for control anastomoses was 47.2 minutes (± 5.3 minutes), compared to 48.8 minutes (± 5.8 minutes) for AG-facilitated anastomoses ($p = 0.33$). Enterotomy time for control anastomoses was 17.4 minutes (± 3.4 minutes) compared with AG anastomoses, which required a mean of 24.7 minutes (± 4.4 minutes). This difference was statistically significant ($p < 0.05$).

Surgeon's observation: Subjective data from surgeons revealed an initial delay in adaptation to utilizing the guide for anastomosis because of its novelty, but once placed within the lumen and the initial interrupted sutures completed, surgeons rated the performance of the anastomosis to be enhanced as compared with that of controls. The AG allowed for improved ease of placement of sutures and increased visualization of mucosal and serosal edges.

Post-surgical period: There were no clinical indications of pain in any of the pigs post-operatively. Three control pigs developed a fever within the first five days after surgery, all of which responded to treatment with flunixin meglumine (1.1 mg/kg PO). One of these pigs simultaneously developed moderate incisional swelling and was treated successfully with antibiotics (tulathromycin, tulathromycin, Zoetis Services LLC, Parsippany, New Jersey; 2.5 mg/kg IM once). Four pigs (three control, one AG) experienced mild-to-moderate swelling of the incision site beyond the first week and an additional three AG pigs developed mild incisional swelling. These pigs were successfully treated with antibiotics (Ceftiofur CFA, 5 mg/kg IM once or tulathromycin, 2.5 mg/kg IM once). Five pigs (3 control, 2 AG) developed signs of respiratory disease and were successfully treated with antibiotics (Ceftiofur CFA, 5 mg/kg IM once, or tulathromycin, 2.5 mg/kg IM once). Transient vomiting occurred in 5 pigs which resolved quickly and did not require treatment. One pig (AG group) had multiple episodes of vomiting and was speculated to have developed gastric ulcers. Vomiting resolved with ulcer treatment including bismuth subsalicylate (Pepto Bismol, Proctor & Gamble, Cincinnati, OH, 3 oz PO once), omeprazole (1 mg/kg PO q24h), sucralfate (2 grams PO q12h), and probiotics (Proviable, Nutramax Laboratories Veterinary Sciences, Inc., Lancaster, SC). All pigs gained weight throughout the study.

Fecal scoring: Fecal scoring (Figure 3-8) and time to first fecal elimination (Figure 3-9) revealed that fecal output returned by the second day after surgery in all pigs. On some occasions, feces exhibited different scores at different times on the same day. The highest fecal score was recorded for these samples and used for analysis. All pigs returned to fecal production at similar times and with similar fecal consistency. Of the pigs that received an AG, 3 passed the AG within 30 hours of the procedure, 1 between 31 and 42 hours, 1 between 43 and 54 hours, and 1 between 90 and 102 hours. All AGs were eliminated as individual, disbanded sheets. One of the pigs that had evidence of AG elimination within 30 hours of the procedure passed additional remnants between 43-54 hours.

Postmortem Data

Gross examination: Pigs were sacrificed one month after surgery (range, 29 to 33 days).

Occasionally, anastomoses were difficult to locate as a result of advanced incisional healing and minimal-to-no adhesion development. Seven pigs (3 control, 4 AG) had mild or moderate adhesions at the anastomotic site, and five pigs (2 control, 3 AG) had an adhesion elsewhere in the abdomen. Adhesions had no sign of impairment of intestinal function and would likely not have resulted in motility disturbances in any of the pigs.

Intestinal diameter: Segments of jejunum orad and aborad to the anastomotic site were clamped using Doyen forceps such that the anastomotic sites were located centrally. The segments were infused with saline until turgid and the diameters of the anastomotic site, bowel diameter approximately 2-cm orad and 2-cm aborad to the EEA site were measured with calipers. These values were considered the "maximum diameter" of the bowel in the respective regions. Within each sample, the average of the diameters of the orad and aborad segments was calculated and compared to the diameter of the anastomotic site, and the resulting percentage reflected the size of the anastomotic site in comparison to the surrounding bowel. A percentage less than 100 equivocates to relative stenosis at the anastomotic site, indicative of limited expandability from fibrous tissue. The range of anastomotic site diameter, as a percentage compared to the surrounding bowel, in the AG-facilitated group was 59 to 89% (mean, 72% ± 11%; Figure 3-10). Range within the control group was 50 to 78% (mean, 70% ± 7%; Figure 3-10). Anastomotic size was similar among treatment groups ($p > 0.05$). Additionally, percent difference between diameters of orad and aborad regions compared to diameters of anastomotic sites was determined and the averages revealed statistically similar % difference on either side: 142% and 141% for the AG groups' orad and aboard regions, respectively, and 149% and 139% for the control groups' orad and aborad regions, respectively.

Bursting pressure: Intestinal wall burst pressure was obtained by infusing the segment with additional saline and monitoring the pressure within the lumen with a digital pressure monitor. Intestinal burst occurred at the anastomotic site in 4 out of 11 specimens (3 AG, 1 control). Bursting occurred in the bowel adjacent to the anastomotic site in 4 out of 11 specimens (2 AG, 2 control). Failure to reach burst pressure occurred in three specimens (1 AG, 2 control). Burst pressure was statistically similar for both treatment groups. The maximum value recorded was

used as the maximum pressure for those specimens. AG burst pressures ranged from 97 to 284 mm-Hg (AG, mean, 176.8 ± 59.9 mmHg) and control burst pressures ranged from 120 to 248 mmHg (mean, 192.8 mmHg ± 46.7 mmHg), as shown in Figure 3-11.

Histopathology: Slides were stained with hematoxylin and eosin (H&E) stain in order demonstrate overall tissue architecture and cellularity. Histologic evaluation by a board-certified veterinary pathologist revealed minimal differences between samples overall and no profound abnormalities. The majority of samples displayed mild mucosal and/or submucosal mixed inflammation (eosinophils, lymphocytes, plasmocytes), at a level not unexpected in the porcine species. Most samples also revealed the presence of suture granulomas, distinguished by multilobulated macrophages, lymphocytes, and eosinophils congregated in an area where suture was previously present (or remained). Several samples, without a trend in group designation, also displayed mild lymphatic dilation. Two samples within the AG group had an area of hemorrhage, the cause of this being unknown, but at least one of which may have been due to manipulation of the tissue during harvesting and burst pressure testing. One sample from the control group was removed from evaluation due to improper sectioning.

Discussion

Fabrication of the AG was successful to the specifications desired; that being initial sturdiness but rapid degradation once exposed to water or digesta. Application of the AG during surgery improved the surgeons' ability to perform the hand-sewn EEA without significantly prolonging the total surgery time. The enterotomy time was slightly longer with use of the AG and this is potentially associated with initial learning because of its novelty. Despite this learning curve, once the AG was secured within the lumen, the performance of the anastomosis was enhanced in the surgeons' opinion. The AG allowed for enhanced visualization of the mucosa and serosa of the cut edges of the bowel, which may increase surgeon confidence that their suture was correctly placed. The ability of the AG to slightly dilate the bowel aids in the prevention of gaps within the repair, which can further increase surgeon confidence that post-operative leakage will not occur. All but one pig receiving an AG eliminated the device within 54 hours. The remaining pig that experienced

the longest delay in AG elimination also experienced the longest delay in return to fecal output. Post-mortem results showed that there were no significant differences between the two groups in regard to adhesions, bowel diameter, intestinal burst pressure, or infection/leakage of the anastomosis.

Biomaterials are increasingly investigated as alternatives for traditional indwelling medical devices because of the frequency of morbidities associated with devices that remain in the body long-term. Biomaterials are substances or devices developed to interact with and direct living systems for therapeutic or diagnostic purposes [5, 10]. Benefits of utilizing a biomaterial for an AG include the ability for the material to be fabricated for rapid degradation, eliminating concerns for interference with intestinal motility, dislodgement, and obstruction. The AG was tailored to have mechanical features suitable for the needs of lumen expansion within the brevity of the procedure [5]. Although hydration tests were performed with the AG to assess disbanding of the sheets composing the AG, one limitation of the study is the inability to determine the disbanding rate *in vivo*. This is likely variable and dependent on the amount of digesta within the small intestine and the degree of peristalsis or presence of ileus within the bowel post-operatively. While testing revealed that the AG became disassembled around 30 minutes, this data was collected from conditions in which the non-sterilized guide was fully saturated and was exposed to frequent fluid flow dynamics. Another limitation is that since the guides are hand-fabricated and gas sterilized prior to implantation, there could have been differences between them in their degradation characteristics.

Some biodegradable stents have been proposed and fabricated, but the typical timeframe that these remain within the intestine (weeks to months) exceeds that which would be needed solely for the anastomotic procedure, and may present morbidities of their own [5]. As elucidated by Wang *et al.* (2014), intraluminal stents composed of magnesium alloys have been fabricated, but have a high corrosion rate. Polymer-based stents, such as those composed of poly(ι-lactide) (PLLA), polydioxanone (PDS), or glycolide-co-ε-caprolactone (PGACL), are reported to have degradation rates ranging from weeks to months, and are at risk of dislodgement during this timeframe. Several case series utilizing PDS-based stents revealed migration rates ranging from 0 to 36% [5]. Kuo *et al.* [11] assessed the application of a short-duration agarose-based stent for intestinal anastomosis in rabbits. Anastomoses performed with the use of the agarose stent were

reported to result in significantly shorter operating times, greater collagen deposition and vessel formation at the anastomotic site, and increased bursting pressure of the anastomosis 21 days after surgery as compared with anastomoses performed without the stent. This supports the potential benefits of using an intraluminal guide for the procedure without the need for sustained presence of stents.

Ultimately, the anastomotic technique chosen by a surgeon is largely based on ease, cost, constraints and requirements of the patient, and the surgeons' personal experience [3]. Ideally, a technique would be employed that could achieve primary healing with the cut edges of bowel in precise apposition to one another [3, 11]. Primary healing can promote more rapid bridging of the apposed tissue with collagen and vascular development, ultimately reducing the inflammatory period of healing [11]. Achievement of primary healing results in minimal scarring, less risk of dehiscence, and minimal stricture formation. With the currently used techniques, however, this is not generally feasible and secondary healing takes place with a typical timeline characterized by a period dominated by inflammation (days 0 to 4 post-surgery), followed by fibroplasia and immature collagen deposition (days 3 to 14), and finally tissue remodeling (day 10 and onwards) [3]. Until mature collagen has been established at the anastomotic site, the anastomosis relies on the surgical technique employed [3].

Factors that affect the healing and ultimate outcome of an intestinal anastomosis include local blood perfusion, apposition and alignment of the cut edges of bowel, tension at the anastomotic site, presence of contamination, and, most importantly, surgical technique used [3, 7]. The most ideal technique for intestinal anastomosis would include precise alignment of the cut edges of the bowel, maintenance of local vasculature, eliminating foreign material at the surgical site, and applying sufficient tensile force when placing sutures to keep tissues aligned without gap or dehiscence [3, 4, 12]. Hand-sewn anastomosis using a two-layer technique (mucosal and serosal layers) has been the standard method utilized; however, currently, the standard of practice has shifted to a single-layer serosa-submucosa technique because of the reduced amount of suture material required for this technique and the decreased time requirement [3]. The two-layer approach may contribute to reduced lumen size, inadequate apposition of bowel edges, reduced local tissue perfusion, and delayed healing [1, 3]. A single-layer anastomosis may be performed with an interrupted or continuous technique, and, in uncomplicated cases, each are considered

suitable choices [3]. In animals, the incidence of post-operative anastomotic leakage is greater (11%) in those patients receiving an interrupted pattern as compared with that of a continuous pattern (3%) [1]. Histologically, 66% of anastomoses repaired with a simple interrupted pattern had mucosal eversion, while only 38% of anastomoses repaired with a simple continuous pattern demonstrated eversion, inversion, or inappropriate apposition [1].

While a hand-sewn technique continues to be the most often pursued method for intestinal anastomosis, the repair can also be facilitated with a stapling device. Stapled anastomotic devices can be used to create end-to-end or side-to-side anastomoses. Stapled anastomosis can reduce the time of the procedure and may be useful in cases with restricted accessibility, a significant difference in bowel diameter, or when the procedure must be completed rapidly [3, 6, 12-14]. Despite these benefits, technical problems more frequently occur when utilizing staplers, and the incidence of stenosis at the anastomotic site may be higher than for hand-sewn anastomosis [3]. In a study of stapled versus hand-sewn anastomosis in 1120 emergency cases [14], there were no significant differences in incidences of anastomotic leakage, abscess development, fistulation, post-operative hospitalization timeframe, or mortality between the two methods. Numerous studies have found no significant difference in post-operative complications between stapled and hand-sewn anastomosis, and an extensive systematic review of stapling versus suturing techniques for various surgical procedures only detected a difference in the average time of completion between the two methods in regards to intestinal anastomosis [6, 12, 13, 15, 16]. There are particular situations in which a stapling technique would be less advantageous than suturing, such as when the bowel is edematous, friable, or afflicted with severe pathology that requires “fine tuning” of the technique [6, 12-14]. Additionally, stapling devices often present a considerably greater expense to the completion of the procedure [6, 13].

Ultimately, this study has demonstrated the ability for a rapidly degradable AG to expand the lumen at the anastomotic site, resulting in enhanced apposition of bowel edges, increased visibility of suture placement, and improved tissue handling, without introducing any added morbidities. This device may prove a beneficial addition to the surgical technique of small intestinal anastomosis.

Acknowledgements

These studies were supported by the University of Tennessee, College of Veterinary Medicine Center of Excellence Summer Research Program and the Center of Excellence in Livestock Diseases and Human Health. Additional thanks for technical support during these investigations is given to Dr. Tom Doherty, Elizabeth Croy, Dr. Remigiusz Grzeskowiak, Dr. Natalie Chow, Dr. Urshulaa Dholakia, Dr. Madhu Dhar, Kassandra Willoughby, Samuel Good, Rachel Clark, Laura Freeman, Desmond Coates, Phil Snow, Sarah Wingo, Kristina Kravchenko, Emma Horn, Lacey Duarte, Rebecca Davis, Austin Bow, Steven Newby, Richard Steiner, Tammy Howard, Shannon Tissot, and Alex Anderson.

References

[1] Tobias, K. and Ayres, R., *Key gastrointestinal surgeries - Intestinal anastomosis.* Veterinary Medicine -Bonner Springs then Edwardsville-, 2006. **101**: p. 226-229.

[2] Cha, J., Shademan, A., Le, H.N., Decker, R., Kim, P.C., Kang, J.U., and Krieger, A., *Multispectral tissue characterization for intestinal anastomosis optimization.* J Biomed Opt, 2015. **20**(10): p. 106001.

[3] Ashkanani, F. and Krukowski, Z.H., *Intestinal Anastomosis.* Surgery (Oxford), 2002. **20**(5): p. 104-107.

[4] Chassin, J.L., *Small Bowel Resection and Anastomosis*, in *Operative Strategy in General Surgery: An Expositive Atlas*. 1994, Springer New York: New York, NY. p. 267-272.

[5] Wang, Z., Li, N., Li, R., Li, Y., and Ruan, L., *Biodegradable intestinal stents: A review.* Progress in Natural Science: Materials International, 2014. **24**(5): p. 423-432.

[6] Yao, L., Li, C., Zhu, X., Shao, Y., Meng, S., Shi, L., and Wang, H., *An Effective New Intestinal Anastomosis Method.* Medical science monitor : international medical journal of experimental and clinical research, 2016. **22**: p. 4570-4576.

[7] Kaska, M., Blazej, S., Turek, Z., Ryska, A., Jegorov, B., Radochova, V., Bezouska, J., and Paral, J., *The effect of three different surgical techniques for colon anastomosis on regional postoperative microperfusion: Laser Doppler Flowmetry study in pigs.* Clin Hemorheol Microcirc, 2018. **68**(1): p. 61-70.

[8] Pedersen, A.P., Alghazali, K.M., Hamzah, R.N., Mulon, P.-Y., McCracken, M., Rifkin, R.E., Mhannawee, A., Nima, Z.A., Griffin, C., Donnell, R.L., Biris, A.S., and Anderson, D.E., *Development and in vivo Assessment of a Rapidly Collapsible Anastomotic Guide for Use in Anastomosis of the Small Intestine: A Pilot Study Using a Swine Model.* Frontiers in Surgery, 2020. **7**.

[9] Wen, X., Wang, L., Zheng, C., Yang, X., Ma, X., Wu, Y., Chen, Z., and Jiang, Z., *Fecal scores and microbial metabolites in weaned piglets fed different protein sources and levels.* Anim Nutr, 2018. **4**(1): p. 31-36.

[10] Williams, D.F., *On the nature of biomaterials.* Biomaterials, 2009. **30**(30): p. 5897-5909.

[11] Kuo, W.-Y., Huang, H.-C., Huang, S.-W., Yu, K.-H., Cheng, F.-P., Wang, J.-H., and Wu, J.-T., *Benefits of Intraluminal Agarose Stents during End-to-End Intestinal Anastomosis in New Zealand White Rabbits.* Comparative medicine, 2017. **67**(6): p. 504-507.

[12] Kano, M., Hanari, N., Gunji, H., Hayano, K., Hayashi, H., and Matsubara, H., *Is "functional end-to-end anastomosis" really functional? A review of the literature on stapled anastomosis using linear staplers.* Surg Today, 2017. **47**(1): p. 1-7.

[13] Catena, F., La Donna, M., Gagliardi, S., Avanzolini, A., and Taffurelli, M., *Stapled versus hand-sewn anastomoses in emergency intestinal surgery: results of a prospective randomized study.* Surg Today, 2004. **34**(2): p. 123-6.

[14] Naumann, D.N., Bhangu, A., Kelly, M., and Bowley, D.M., *Stapled versus handsewn intestinal anastomosis in emergency laparotomy: a systemic review and meta-analysis.* Surgery, 2015. **157**(4): p. 609-18.

[15] Hemming, K., Pinkney, T., Futaba, K., Pennant, M., Morton, D.G., and Lilford, R.J., *A systematic review of systematic reviews and panoramic meta-analysis: staples versus sutures for surgical procedures.* PLoS One, 2013. **8**(10): p. e75132.

[16] Chandramohan, S.M., Gajbhiye, R.N., Agwarwal, A., Creedon, E., Schwiers, M.L., Waggoner, J.R., and Tatla, D., *A randomized study comparing outcomes of stapled and hand-sutured anastomoses in patients undergoing open gastrointestinal surgery.* Indian J Surg, 2013. **75**(4): p. 311-6.

Appendix
Figures

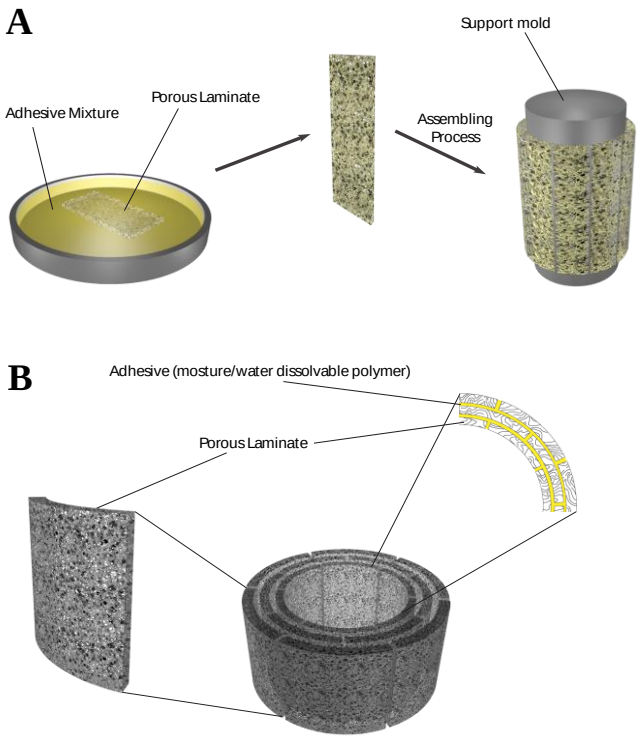


Figure 3-1: Steps for fabrication of the device

(A) The porous polymer laminates were saturated with adhesive solution then assembled over support mold; (B) the support mold was removed, and the device left to dry for 48 hours.

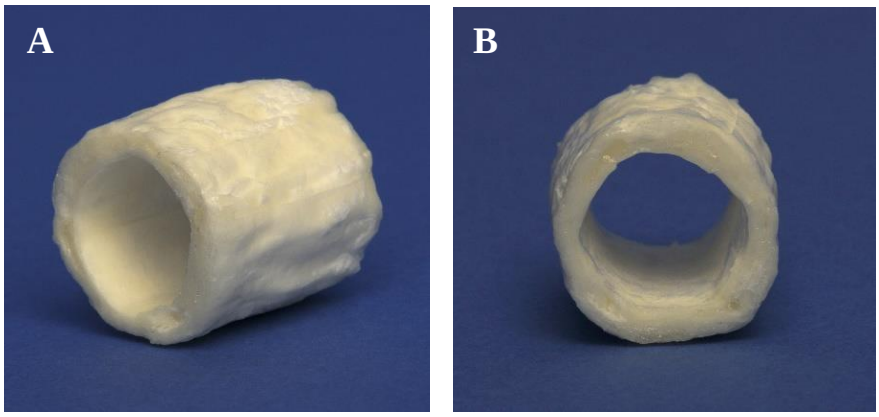


Figure 3-2: Images of pre-sterilized anastomotic guide

A) pre-sterilized AG viewed obliquely; B) pre-sterilized AG viewed end-on.

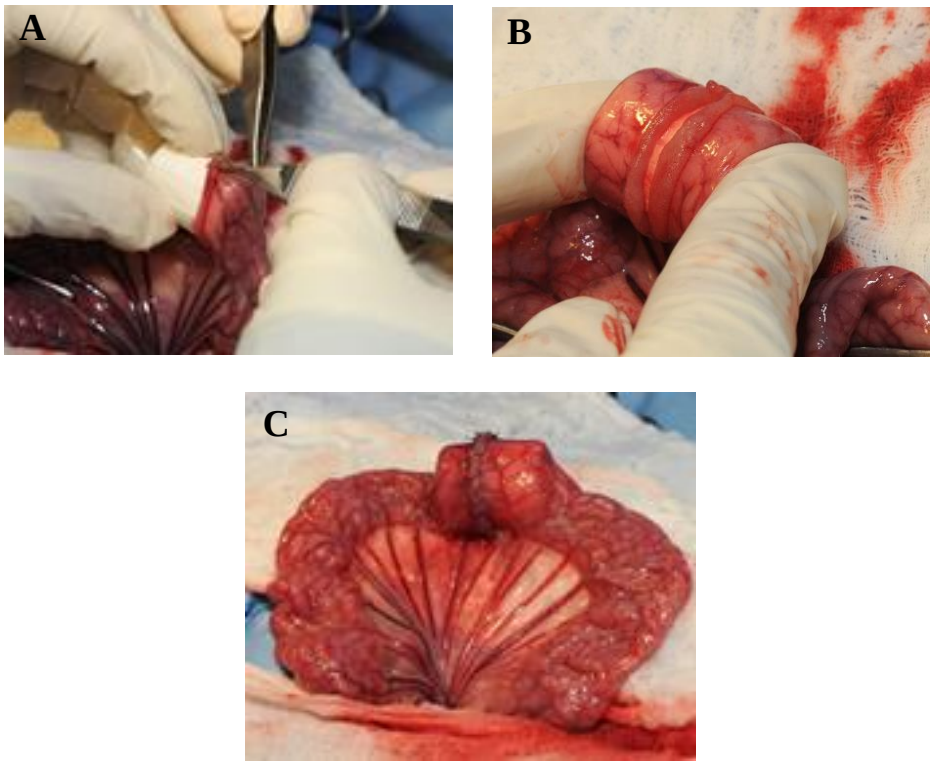


Figure 3-3: Images of anastomotic guide placement during surgery

A) AG being placed into the cut edge of one side the bowel; B) apposition of both cut edges of bowel overlying AG within the lumen; C) completed anastomosis with AG within the lumen.

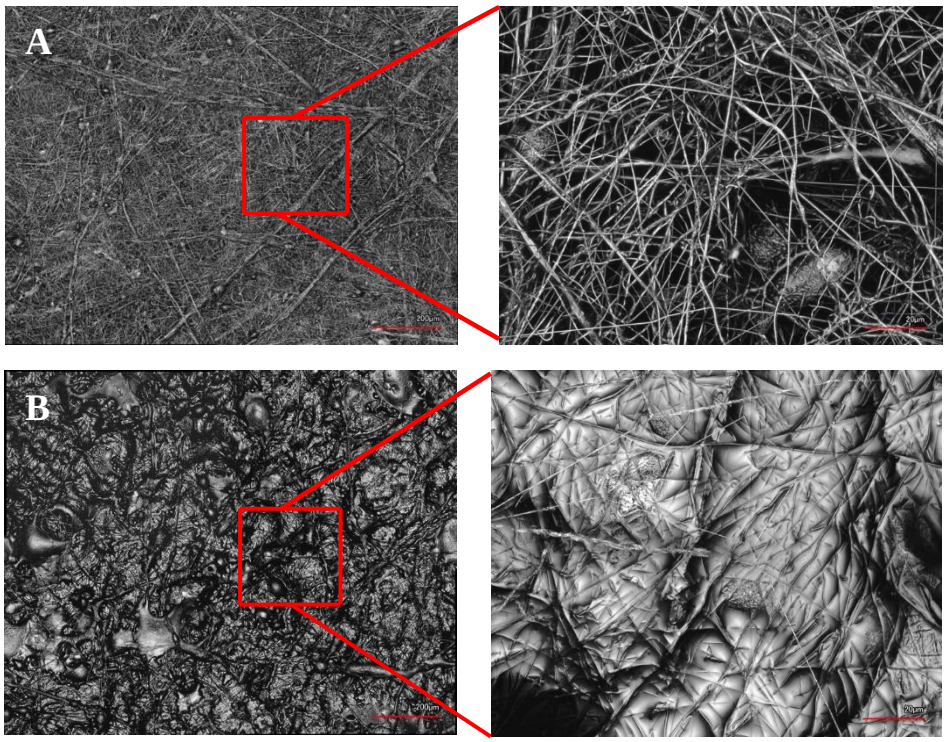


Figure 3-4: Representative 3D laser microscopy images of polymer

(A) The polymer laminate used to fabricate the device before saturation with PVP polymer; the insert clearly shows the fiber structure; (B) the polymer film used to fabricate the device after saturation with PVP; the insert clearly shows the fiber structure where the laminate is partially coated with PVP polymer.

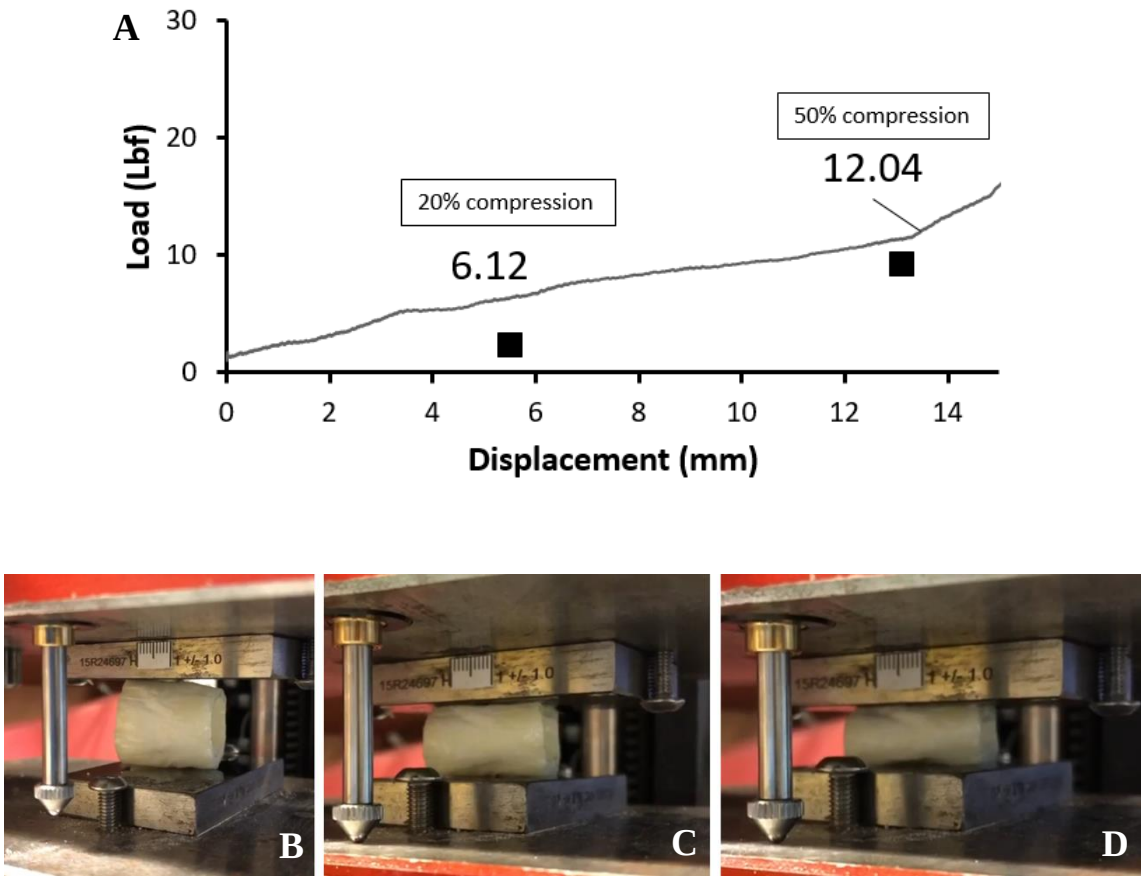


Figure 3-5: Mechanical compression results

(A) Strain/stress curve, (B) the samples before compression, (C) the samples after 20% compression of its dimeter, (D) the samples after 50% compression of its diameter.

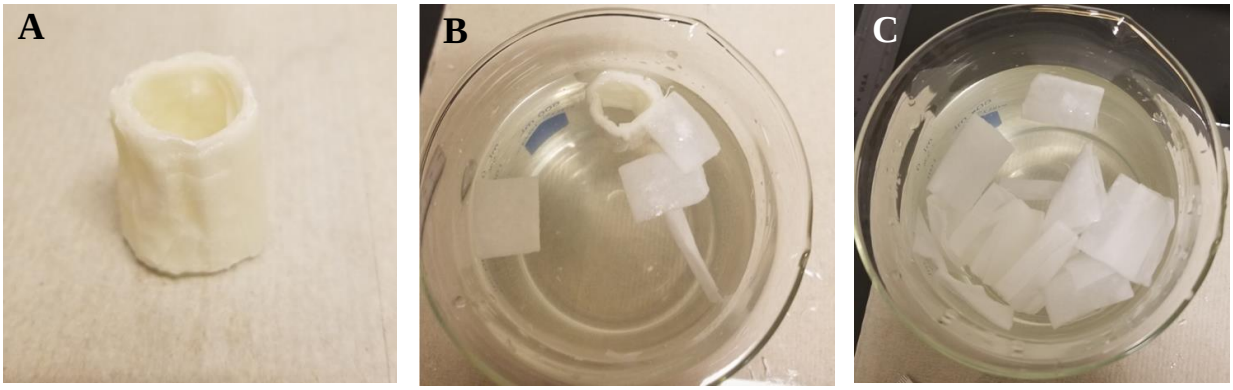


Figure 3-6: Hydration testing

(A) The fabricated device prior to placement in water bath, (B) the device starting to collapse after 10 minutes in water, (C) the device totally collapsed after 30 minutes.

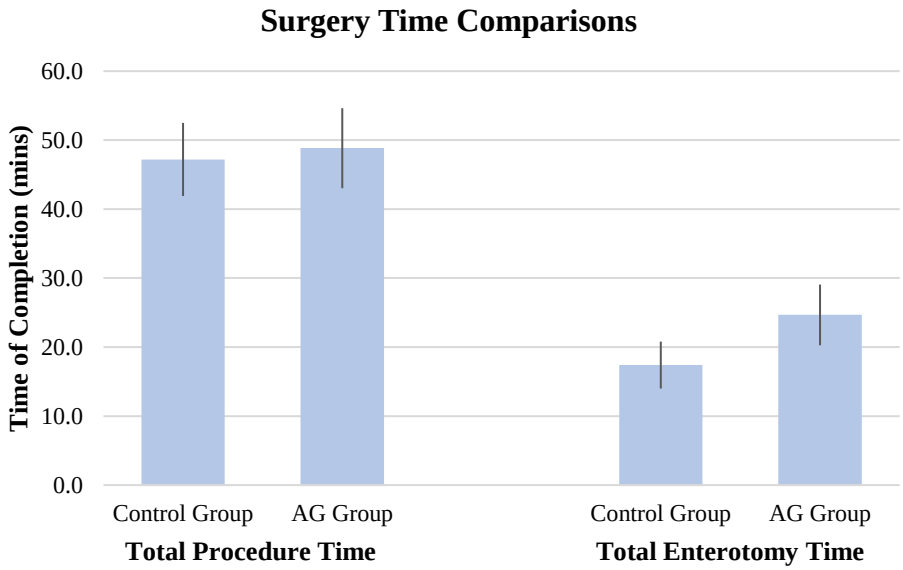


Figure 3-7: Surgical duration comparison

Comparison of average total surgical time and total enterotomy time for anastomoses performed with or without an anastomotic guide. Error bars demonstrate the standard deviation of each average.

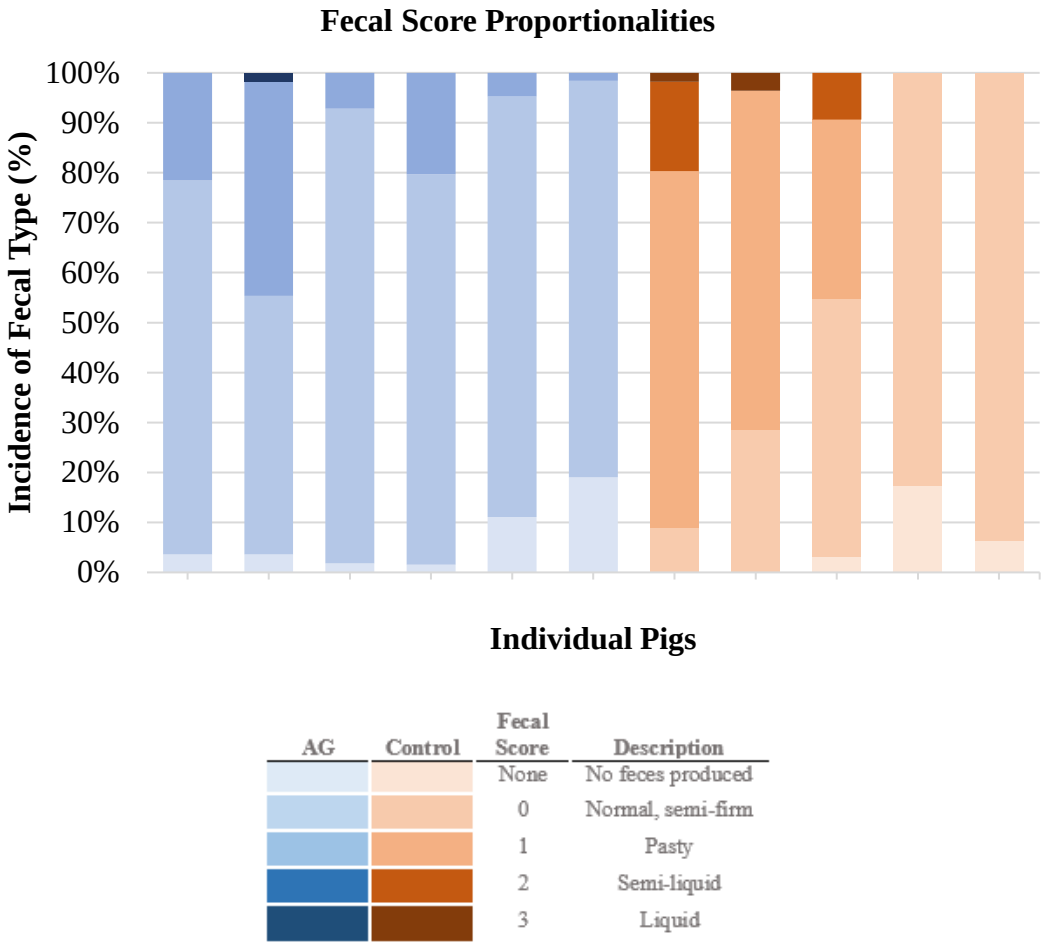


Figure 3-8: Fecal scoring results

Incidence of fecal quality type within individual pigs based on fecal scoring performed at least twice daily. Incidence is represented as a percentage and refers to the number of fecal scores that were recorded within each category as compared to the total number of observations. Fecal score scale derived from Wen et al (2018).

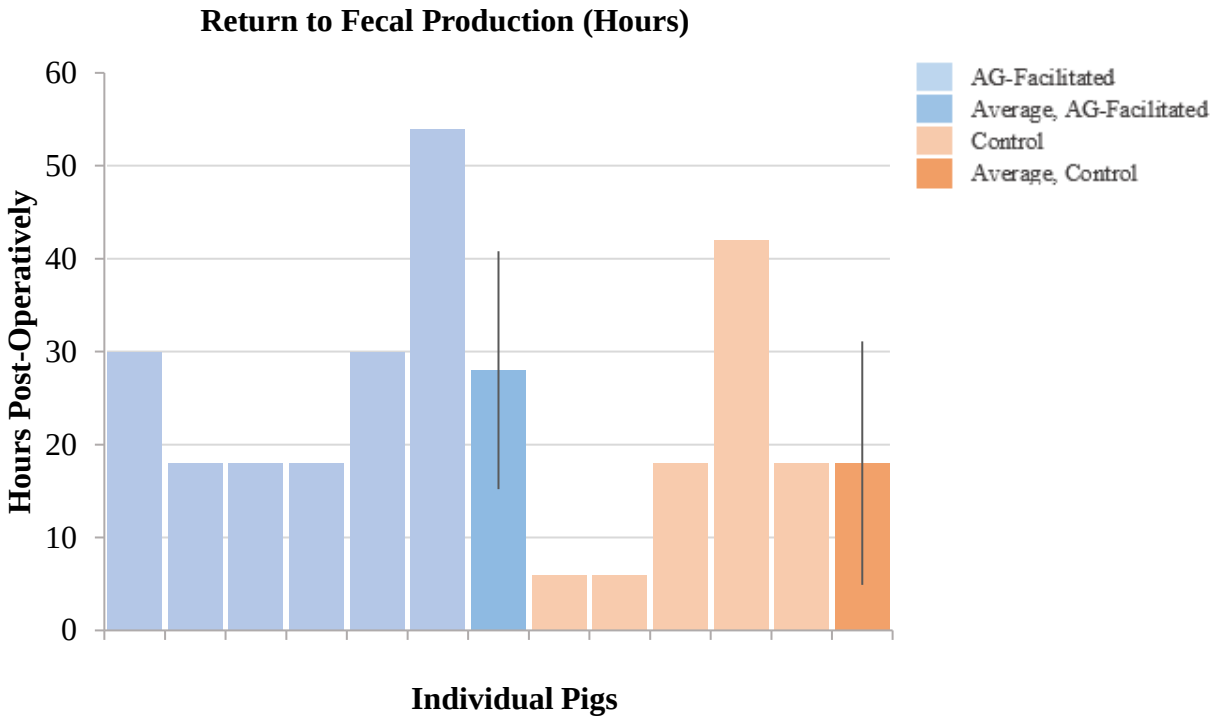


Figure 3-9: Return to fecal production

Hours post-operatively that individual pigs returned to fecal production. Error bars represent the standard deviations of the averages for each group.

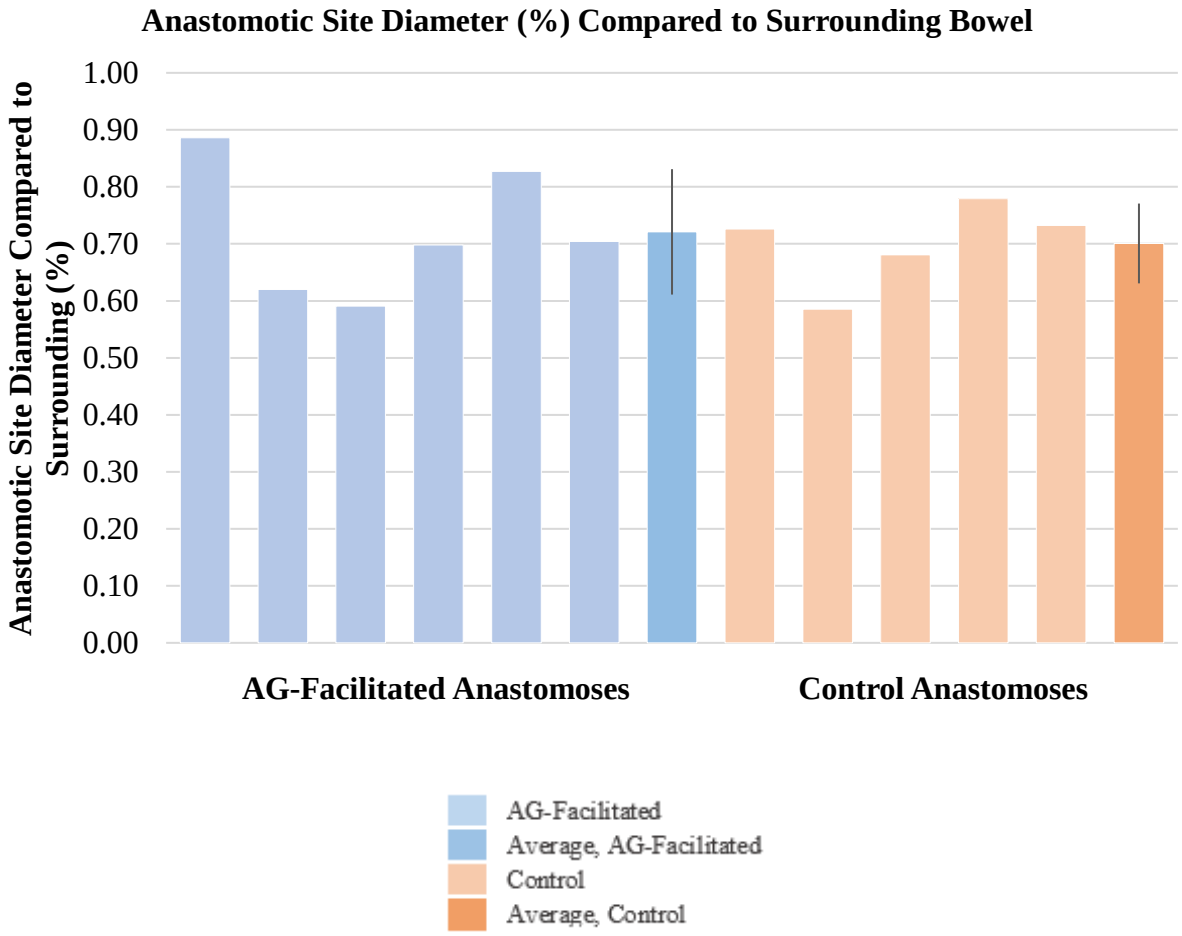


Figure 3-10: Post-mortem anastomotic site diameter results

Diameter of anastomotic site in comparison to surrounding bowel for each pig. Percentage diameter reflects the percent that the anastomotic site was when compared to the average diameter of the adjacent bowel (orad and aborad). Error bars demonstrate the standard deviations of the averages for each group.

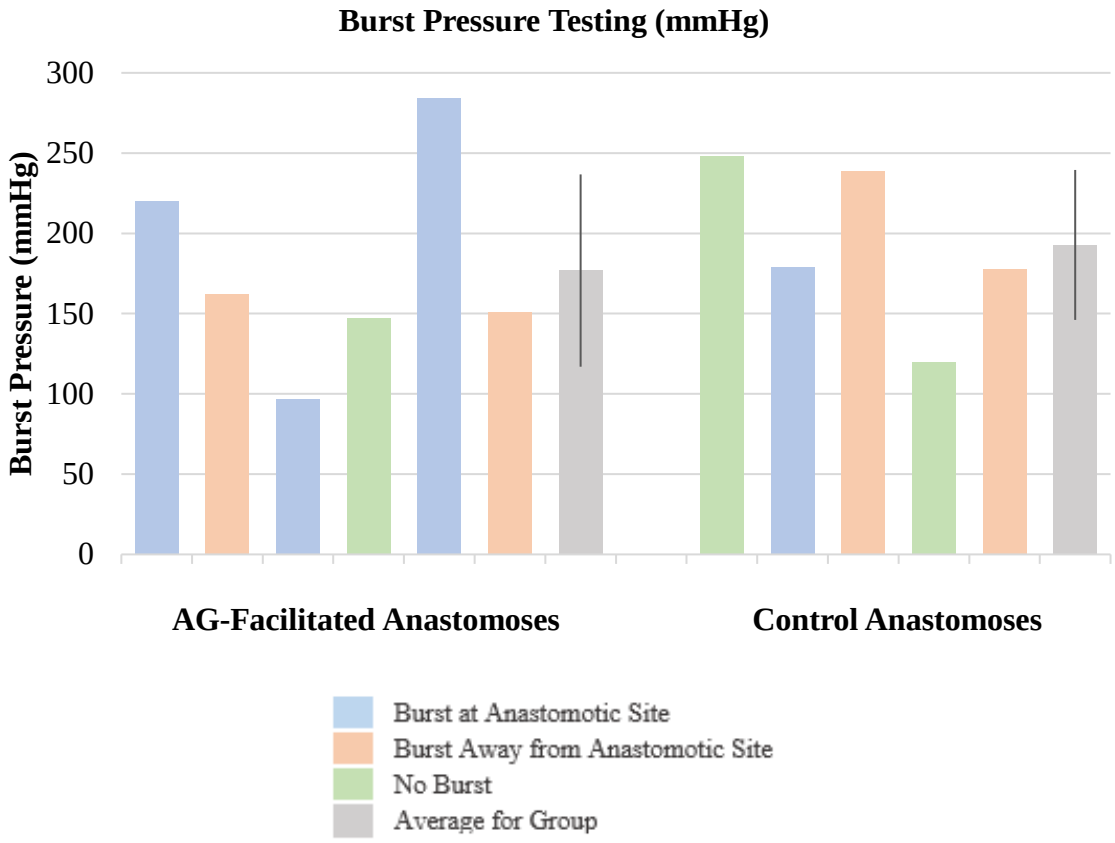


Figure 3-11: Burst pressures achieved by each anastomosis

Bars in blue represent samples in which bursting occurred at the anastomotic site. Orange bars represent samples in which bursting occurred at the bowel adjacent to the anastomotic site and where the anastomotic site remained intact. Green bars represent the maximum pressure achieved within the bowel lumen but with no burst achieved. Grey bars signify the average for each group and error bars represent their corresponding standard deviations.

CHAPTER 4 : Design, Fabrication, & Preliminary *In Vitro* Validation of a Degradable Scaffold for Peripheral Nerve Defects

Abstract

Peripheral nerve injury (PNI) is an unfortunate, yet common, occurrence associated with severe trauma and various peripheral neuropathic disorders. Critical-sized defects of peripheral nerve, those being too large to heal by the body's inherent repair mechanisms, are of particular concern as current therapeutic options are suboptimal. The standard repair method is autologous grafting, consisting of transposition of a nerve from another region of the patient's body to the injury site. Unfortunately, this presents additional comorbidities at the donor site and frequently produces poor motor and sensory outcomes. Development of a biocompatible and degradable nerve scaffold has gained attention amongst biomedical researchers as a promising alternative therapy. The intentions of this multi-phase study were to conceptualize and design a bioprinted poly(lactic-co-glycolic acid) (PLGA)-graphene oxide (GO) composite nerve scaffold, assess iterations of PLGA-GO material with varying proportions of GO to elucidate any differences in human mesenchymal stem cell viability or neural differentiation, and assess varying hydrogel samples and neural growth factor combinations and concentrations with anticipated application in a neural growth factor-eluting hydrogel product for addition to the lumen of the nerve scaffold. Cytotoxicity and morphology assessments revealed that, while GO proportions ranging from 0.25 to 2% consistently appear to support cell adherence and growth, 0.25% and 0.5% wt. GO iterations may facilitate a greater propensity for cells to adapt a neural-like morphology with a more extensive webbing morphology. Growth factor experiments showed that, when Schwann cells are seeded at a low density (750 cells/well), exposure to 30 ng/mL of bFGF may result in inhibition of cell proliferation, but exposure to CNTF in a range of 25 to 50 ng/mL induces greater proliferation than in control samples. Hydrogel experiments revealed that Biogelx hydrogel products display a burst release of impregnated protein, which is most accurately quantified with the BCA assay as opposed to the Bradford's assay. Ultimately, this series of experiments lays a foundation for further fabrication of a novel bioprinted carbon nanomaterial-composite nerve scaffold with the potential to evoke enhanced neuroinductive effects on regenerating nerve, with the aid of a neural growth factor-eluting hydrogel infused into the lumen.

Background, Significance, & Innovation

Peripheral nerve injury (PNI) is a relatively common disorder, with more than 200,000 new cases occurring in the U.S. annually due to trauma alone [1]. While there are numerous etiologies of peripheral nerve damage and disease, it is estimated that a staggering 20 million Americans are afflicted with a peripheral neuropathic disorder [2]. Classifications of PNI include neuropraxia, resulting from compression or traction of the nerve, axonotmesis, due to a disruption of nerve axons, and neurotmesis, caused by full-thickness damage to the nerve [3]. Any classification of PNI may necessitate surgical intervention depending on the consequent symptoms, but is particularly common in cases of neurotmesis where there is a complete impediment to signal transduction. Critically-sized peripheral nerve defects, defined as those greater than between 1 and 3-cm [4, 5], are especially dependent upon surgical intervention as gaps of this magnitude are unable to heal by the body's inherent repair mechanisms. The etiology of such significant defects include severe traumatic incidents, warfare, neoplasia, infections, autoimmune disorders, and focal vascular damage [2].

Despite much research being devoted to this critical area of need, repair of nerve defects continues to be suboptimal in many cases. Approximately 33% of all PNIs ultimately result in inadequate recovery, often due to aberrant healing and propagation of scar tissue which impedes Schwann cell proliferation and axon sprouting [3, 6]. Poor motor and/or sensory functionality can be displayed symptomatically in the form of chronic pain, deranged temperature sensitivity, muscle atrophy, weakness, loss of reflexes, incoordination, and reduced limb functionality [2, 3], all of which directly affect an individual's physical capacity for self-sufficiency and overall quality of life. For very minute nerve gaps, it may be technically feasible to directly anastomose, or conjoin, the severed nerve stumps [3], depending on the ability of the healthy nerve segments to extend over the region; however, this may not be an option in even relatively small nerve injuries. The gold standard method of repair is the utilization of an autologous nerve graft, harvested from another region of the patient's body. Benefits of this method include the elimination of the potential for an adverse immunogenic reaction to the graft and ready availability notwithstanding any co-morbid conditions that may prevent surgery at the donor site. Unfortunately, additional complications are associated with the harvesting procedure itself. Allogeneic nerve grafts, which

are harvested from a human organ donor, are another available option, but pose the risk of inducing an adverse immunogenic reaction which may result in rejection of the graft. Patients receiving an allogeneic graft typically undergo a systemic immunosuppression regimen to prevent this complication, but such drugs are often administered for months or years and may induce their own side effects; for example, tacrolimus can induce nephrotoxicity, neurotoxicity, and gastrointestinal disorders [7].

Alternative options to nerve grafting have been explored in the fields of biomedical, neurological, and regenerative medicine research. The common theme amongst many of these investigations has been the conceptualization and development of an artificial nerve tunnel, often referred to as a "conduit", "guide", "wrap", or "scaffold", to which the severed nerve ends can be anastomosed and through which the nerve can regenerate. A variety of concepts have been proposed that emphasize unique elements of the physicochemical and behavioral characteristics of the device, including utilization of diverse composite materials, manipulation of surface topography, incorporation of bioactive agents, alternative methods of implantation, inclusion of electro-stimulation, etc. Utilization of biodegradable materials coated in or impregnated with a neurostimulatory substance is a method which in particular poses great potential. Members of our research group have previously investigated poly-ε-caprolactone (PCL)-based nerve wraps coated in high-oxygen graphene (HOG) or graphene oxide (GO) for peripheral nerve repair [8]. While valuable information was acquired from this preliminary study, we are now transitioning to what we believe will be a far more satisfactory concept to mitigate the critical deficiency in peripheral nerve therapeutics. The following is an outline of the preliminary experiments performed as a foundation for the ultimate fabrication of a novel bioprinted poly(lactic-co-glycolic) acid (also called poly(D,L-lactide-co-glycolide); PLGA) [9], nerve scaffold with imbedded graphene oxide (GO), as well as a neural growth factor-eluting hydrogel to be used in conjunction with the scaffold for amplified nerve regeneration.

In an ideal circumstance, a nerve scaffold for repair of a critical-sized peripheral nerve defect would serve as a structural support for nerve ingrowth, feature bioactive properties to enhance nerve regeneration, remain *in situ* for a duration appropriate for the site of application, and ultimately degrade into nontoxic by-products. These are the pivotal goals for our device. PLGA has been selected as the base polymer as opposed to PCL due to PCL having a variable

degradation timeframe, most often years [10], which would be excessively long in many nerve defect applications. Additionally, the newest nerve scaffold iteration will be tubular rather than a sheet-like wrap, which was previously fabricated from PCL. Our research group has heavily utilized PLGA in bioprinted bone scaffold applications and has developed reliable methods for this material's manipulation that we have felt confident can be successfully applied to fabrication of the nerve scaffold. Graphene is a carbon lattice monolayer (2D) nanomaterial that has acquired great intrigue in the biomedical field over the past several years due to its biocompatibility, flexibility, transparency, mechanics, and thermal and electrical conductive capacity, leading it to be a prospective material for drug delivery, bioelectrodes, stem cell differentiation, and tissue engineering applications [11, 12]. Graphene applications have become especially promising in the realm of peripheral nerve repair. For example, graphene oxide materials in composites with polymers have demonstrated enhanced adherence, proliferation, and differentiation of neural stem cells and Schwann cells [12-14].

In addition to the materials used, the novelty of the proposed device is especially evident in the utilization of a bioprinter (Aether 1 Bioprinter; Aether, San Francisco, CA, USA; or Cellink Bio X6; Cellink, Boston, MA, USA) for fabrication of the device, which not only allows for production of a construct in any design we deem optimal, but displays extreme sensitivity in the printing of the design down to 0.2-mm resolution. This extremely sensitive resolution not only enables us to print constructs that will be utilized in initial small mammal *in vivo* testing, but also prospectively demonstrates the capacity for printing constructs for utility in repair of nerves with small diameters. Imbedding GO into the construct as opposed to coating the interior surface allows for persistent presence of GO throughout the degradation process of the scaffold, resulting in a constant neuroinductive stimulation. Additionally, a growth factor-eluting hydrogel to be injected into the lumen of the scaffold at time of implantation will be synthesized in order to potentiate the scaffold's nerve regeneration capacity. The following is a description of the preliminary scaffold design efforts and experiments performed for delineation of the optimal composite material ratio, growth factor(s) to impregnate into the hydrogel adjunct product, and hydrogel elution behavior.

Scaffold Design Conceptualizations

Design Phase

The first goal in the entirety of this study was to design the nerve scaffold to be fabricated. Several design features were initially considered with respect to the inherent behavior of axons to traverse surfaces in a linear fashion [15, 16], including tubular conduits with multiple linear tube-like channels, multiple divisions to form "chambers", or complete hollowness. Based on the resolution capacity of the bioprinter, scale of the scaffold for implantation in a rat model, and propensity for PLGA composites to swell slightly, the designs were narrowed down to a tubular shape with either a completely hollow lumen, bi-chambered lumen (lumen divided into two equal halves linearly with a single partition), or quad-chambered lumen (lumen divided into four equal parts linearly with two partitions that intersect perpendicularly). The motivation for considering the addition of dividers was to increase the wall surface area within the scaffold, affording more area for neural cell attachment and linear axonal growth.

CAD software (AutoCAD 2020, Autodesk Inc., San Rafael, CA, USA) was used to generate each of the designs along with the code for the initial scaffold printing (Figure 4-1). Multiple prototypes were printed using acrylonitrile butadiene styrene (ABS) plastic [17] in varying diameters ranging from 2.0 to 3.5-mm outer wall diameter and 15-mm length. While the sciatic nerve defect is anticipated to be only 10-mm, the additional 2.5-mm at either end permits space for tucking of the severed nerve ends for anastomosis. The smaller diameter also reduces the likelihood that the nerve ends will require stretching, and hence introduce a risk of fraying, during the suturing process. In the chambered designs, the partitions were situated only within the central 10-mm, with the 2.5-mm sections at either end being hollow. With input from Dr. Stacy Stephenson, consideration of the size of the rat sciatic nerve, and concern about occlusion of the lumen in the chambered designs, we elected to proceed with development of a hollow conduit with 2.5-mm external diameter, 2.0-mm internal diameter, 0.25-mm wall thickness, and 15-mm length.

Material Selection

The pivotal material of interest for our nerve scaffold is GO because of its demonstrated neuroinductive properties and biocompatibility. The powder-like consistency of GO, which is in actuality nanoscale fragmentation of 2-D layer sheets, necessitates incorporation into a material to provide structure and maintenance at the site of implantation. PLGA was selected due to its exceptional biocompatibility, FDA-approval status, malleability in composites, and ability to be melted and extruded from a bioprinter. Furthermore, a ratio of 75:25 PLGA (lactide groups to glycolide groups) was selected due to its favorable degradation profile and physical properties [9], as well as familiarity with it in other applications within our research group. Strength, swelling behavior, and degradation of PLGA are affected by its crystallinity, which varies between the different molar ratio products, and the higher the proportion of glycolide groups, the faster the material degrades [18, 19]. Both PLGA alone and PLGA-GO composites have demonstrated a degradative process facilitated by hydrolysis of ester bonds and subsequent auto-catalysis by carboxylic functional groups to form lactic acid, glycolic acid, and other acidic groups [20, 21]. Darestani *et al.* (2005) prepared disks of 50:50 PLGA for degradation profiling over a 56 day period, and found that the hydrolytic process occurred in a series of seven distinct phases: hydrolysis of the material surface; hydrolysis of the outer layers of the material; water soluble oligomer formation within the outer layers; exiting of the water soluble oligomers formed in the outer layers; hydrolysis of the bulk of the material with exiting of by-products; catalyzation of hydrolysis of the bulk material; and finally, fragile structure formation of the porous remnant of the material. This process in 75:25 PLGA would likely proceed similarly, but with an altered ratio of lactic acid and glycolic acid by-products and an increased timeframe for degradation due to the reduced proportion of hydrophilic glycolic acid groups [22].

Having elected to develop a nerve scaffold comprised of a homogenous mixture of PLGA and GO, rather than PLGA being coated in a thin film of GO, the initial step of the composite formulation was to determine the specific solvent, and its proportion, to be utilized in the facilitation of homogenization during the melting process and ease extrusion from the bioprinter. It was imperative to select a solvent that would either be entirely removed from the composite prior to implantation, or if residue were to remain, that it would be entirely biocompatible with

demonstrated *in vitro* and *in vivo* compatibility in the anticipated proportions remaining within the composite.

DMSO is a highly polar organosulfur compound with the formula $(CH_3)_2SO$ [23]. DMSO is frequently encountered in biomedical research in applications where samples or materials require cryoprotection due to its ability to prevent crystal formation in cells during freezing [24]. DMSO is also a profitable solvent, not only for its ability to dissolve polar and non-polar compounds, but for its utility in bioprinting because it can facilitate an extensive decrease in the melting point of composites, which greatly reduces the energy required for the printer to reach the threshold temperature [23]. For example, experience amongst members of our lab have revealed that composites of PLGA and GO combined with chloroform may require temperatures of up to 140ºC to reach a melted state, whereas similar composites combined with DMSO have required temperatures of only 45 to 85ºC. Although DMSO may prove to impair cell viability at concentrations as low as 0.5% to 10% DMSO in solution, depending on conditions and cell lineage utilized [25-27], previous experiments in our lab and labs of consulted investigators have revealed that the bulk of the solvent is evaporated during melting and subsequent freezing at -20ºC. Hence, we felt comfortable in the employment of DMSO for the purposes of homogenizing the composite constituents and facilitating a greatly reduced melting temperature for bioprinting.

Composite Fabrication Techniques

Assessment of Composite Formulations for Bioprinting Compatibility

Fabrication of Variable Composite Ratios

The initial phase of *in vitro* testing with the material was geared towards assessment of the proportion of GO imbedded within the PLGA in order to delineate any differences in neuroinductivity depending on amount of GO present; however, the first step in the set-up of this experiment was determining the volume of DMSO that would be sufficient to homogenize the material and allow it to be extruded from the bioprinter, without excess that may result in cytotoxicity in the cell cultures. A GO-PLGA blend at an arbitrary, yet relevant, proportion of 1% weight (wt.) GO was utilized for the base polymer. 1 gram PLGA was combined with 10 mg GO

for each of four samples, to which DMSO was added in one of the following quantities: 0.3, 0.4, 0.5, and 0.6 mL. These were placed in a rotational oven set to 85ºC and were stirred frequently to homogenize the material. Once homogenized, the samples were frozen at -20ºC overnight. Samples were then allowed to come to room temperature and the materials were manipulated to assess their malleability, flexibility, and overall consistency. The samples incorporating 0.4 mL and 0.5 mL were subjectively the most optimal consistencies for printability, as deemed from experienced personnel in our lab group. Ultimately, the prototype formulation for first trial printing was selected to be 1 gram PLGA, 10 mg GO, and 0.425 mL DMSO.

Initial Bioprinting Attempts of Composite

Printing was attempted with a sample of the prototype formulation and was successful up to approximately 1-mm in height, with a "volcano-like" collapse occurring at approximately 2-mm. Issues arising due to suboptimal depressurization points warranted reconfiguration of the CAD coding, following which printing was reattempted and appeared more successful. Since the sample for trial printing was exhausted before a complete construct was printed, it was elected to discontinue further printing until the *in vitro* assays for determination of GO quantity to imbed in the composite were completed.

Fabrication of Material with Variable Graphene Oxide Proportions

Necessitation of Evaluating Variable PLGA-GO Proportions

PLGA-GO proportions were evaluated in variable ratios for three main purposes: to (1) confirm the biocompatibility of GO when hMSCs are exposed to the material in a range of concentrations, (2) delineate any differences in effects on cells between concentrations, and (3) remove arbitration in selection of the GO ratio for the composite. Obtaining this information is essential for elucidation of the proportion of GO ultimately to be incorporated into the scaffold construct, with the intent of selecting a concentration that will sustain cellular proliferation and support, or even induce, differentiation of cells into a neural lineage morphology. Achieving these goals first entailed fabricating material with a range of GO imbedded, followed by exposing the material to hMSCs. We hypothesized that GO films or smears ranging from 0-5% concentration or weight,

respectively, would be non-cytotoxic to hMSCs, and that at least one GO proportion would appear more neuroinductive or supportive of neural-differentiated cells than the others. Various investigators have previously investigated polymer composites with GO proportions in this range, and our motivations were to elucidate whether distinct cellular effects may occur at these different proportions and to justify selection of a specific proportion for our material. Drop-coated thin films and polymer smears were both investigated rather than only a single method because surface area density and weight percent of GO are not directly proportional with one another due to GO's 2D monolayer structure, and we believed that analyzing both physical characteristics could provide a wealth of knowledge regarding the bioactivity of GO that has yet to be elucidated.

Composite Drop-Coating Techniques & Materials

GO and ethanol (EtOH) were utilized for fabrication of one series of coverslips because the solution, once the EtOH has completely evaporated, leaves a thin film comprised entirely of GO. This technique was considered potentially useful for evaluating the surface area density impact of GO on cells as the solutions can be diluted to selected concentrations of GO; in this case, 0.25-5%. The 2D nature of GO imparts an immense surface area in even minute samples, with an estimated value of nearly 7,400 cm^2 per milligram [28]. For this reason, serial dilutions were required for synthesis of extremely low concentration GO-EtOH solutions.

In a modified approach inspired by Newby *et al.* [29], first diluted EtOH was prepared using 200-proof EtOH and nanopure water. A stock solution of GO and diluted EtOH was then made at a concentration of 10 μg/mL and bath sonicated for 30 minutes for homogenization. For synthesis of EtOH-GO solutions which were applied to coverslips with a surface area of 1.8 cm^2 for targeted thin films of 0.25, 0.5, 1, 2, and 5% coverage, concentrations of EtOH-GO, prepared from the stock solution and additional EtOH, were 3, 6, 12, 24, 60 μL per 5 mL volume. Samples were then bath sonicated for 30 minutes and aliquoted in approximately 100 μL increments on glass coverslips. Coverslips quickly air-dried, eliminating the necessity of placement into a vacuum oven.

Composite Smear Techniques & Materials

GO and PLGA were utilized for fabrication of the second series of coverslips because this allowed

for evaluation of the weight percent impact of GO on cells, in the range of 0.25-5% wt. GO, and was directly applicable to the ultimate material to be utilized for the scaffolds. PLGA-GO coverslips were fabricated utilizing a melted polymer smear technique. Weight proportions of 0.25, 0.5, 1, 2, 5% GO were added to 75:25 PLGA to synthesize 1-gram samples (e.g. 5 mg GO and 1995 mg PLGA for 0.25% weight GO). An additional PLGA-only sample was used as a positive control. DMSO served as the solvent to aid in the melting and homogenization process, as well as in anticipation of later extrusion from the bioprinter since DMSO greatly reduces the melting point of the material. DMSO also serves as a cryoprotectant when freezing the material and, as demonstrated in other experiments by members of our group, displays no apparent cytotoxicity in the low concentrations present following evaporation of the majority of the solvent during the fabrication processes.

The samples of GO, PLGA, and DMSO were placed into a rotational oven set to 85ºC, with periodic mixing of the samples for homogenization. After complete melting, which in some cases of the high GO concentration samples was facilitated by the addition of approximately 0.1 mL DMSO, small droplets of the material were applied to glass coverslips and smeared using a glass rod or metal spreader. Smears were made so that a minimum of 60-70% of the coverslip was coated in the material.

Composite Results & Discussion

Production of uniformly coated EtOH-GO coverslips was unsatisfactory due to discrepancies between properties of the glass surface of the coverslips and the rapid evaporation of the ethanol. Instead of uniform evaporation across the surface, leaving a thin film residue of GO, the solvent formed small droplets as the total quantity of ethanol gradually reduced. The concentration of GO in these droplets was therefore higher than the concentration of the initially deposited volume, and resulted in island formation of GO on the coverslip. While the total mass of GO remained the same, the distribution was uneven, and there would have been limited value in applying cells to these coverslips since individual island density would be comparable between samples.

Before resorting to complete reliance on the PLGA-GO smears for *in vitro* assays, alternative solvents were assessed in order to determine if any would facilitate more even distribution of GO. Solutions of 95%, 90%, and 80% EtOH and 90% and 80% methanol were

prepared from pure ethanol and methanol, respectively. 50 μL droplets of these solutions, in addition to pure ethanol, pure methanol, and water, were applied to individual glass coverslips and observed for wettability (affinity for the glass surface and spread of the solution) and evaporative behavior (Figure 4-2). Solutions with less water content were found to "wet", or spread across, the surface more, but after approximately fifteen minutes or less, all samples except for water resulted in island formation. With no optimal solvent being found, the smear fabrication technique was elected for further utility in the *in vitro* experiments.

There were two particular benefits to employing smears versus films for these assays. One is that the material would be more closely matched to the nature of the material anticipated to be fabricated for the nerve scaffolds. While the surface texture of the smears are different from the bioprinted material, the inherent physicochemical properties of the material are similar, and so these samples take into account additional factors that would have been eliminated in the EtOH-GO film experiments. Secondly, the nature of the surface characteristics would be highly different between EtOH-GO films and GO imbedded in PLGA. GO powder is composed of minute fragments of single-layer GO sheets. In a thin film, GO sheets would be predisposed to lying down flat on the surface and stacking upon one another. When embedded in a polymer, the GO sheets would be positioned randomly, some even likely protruding from the surface. Kaliavaradhan, Rukmanikrishnan, & Muthusamy (2018) found that surface appearance of epoxy-phthalonitrile composites with 0, 1, 3, and 5% wt. GO were dramatically different, as demonstrated by scanning electron microscopy and transmission electron microscopy (Figure 4-3) [30]. Specifically, the greater proportion of GO demonstrated more agglomeration of GO layers on the surface. Distribution of GO in polymer resulting in surface roughness could potentially present itself as more advantageous or disadvantageous for cell migration and adherence, and so it is important to determine cell response early in the assessment of this material before proceeding with more complex fabrication techniques.

Fabrication of PLGA-GO smears was performed with successful homogenization of GO and the polymer (Figure 4-4-A). In some of the composites with a higher proportion of GO, additional DMSO was needed to facilitate melting and homogenization. Due to the high viscosity of the melted material, smears typically featured some level of visible surface roughness.

Composite Sterilization & Limitations

Coverslips were placed into 24-well plates prior to sterilization. Both ultraviolet (UV) irradiation and gas sterilization methods were performed on individual plates, but due to material malformations (i.e. bubble formation; Figure 4-4-B) and cell death, possibly induced by the sterilization method itself or an increased volume of DMSO used in fabrication of the material, the gas sterilization method was discontinued. Experiments previously performed in our group have found that gas sterilized PLGA-GO materials should remain dormant for a minimum of 48-hours before seeding with cells in order for residual adsorbed hydrogen peroxide to evaporate. In our experiment, the waiting period was performed, and samples were also rinsed with HBSS or media prior to seeding with cells; however, they still did not perform successfully as did the UV-irradiated samples. UV irradiation for a minimum of 4 hours is the now the confirmed mechanism for sterilization of these PLGA-GO composites.

A final important consideration is the behavior of the material once exposed to fluid. After seeding with cells, submersion in media, and incubation, some samples were found to take on a rolled or "crinkled" conformation (Figure 4-4-C), which in some cases inhibited the ability for the material to serve as a platform for the cells. This is discussed further in the *in vitro* results and discussion section.

In Vitro **Analyses of Composites for Delineation of Optimal Neuroinductivity**

Cell Culture Conditions

Human adipose-derived mesenchymal stems cells (hMSCs) were employed for assessment of neuroinductivity of the material as these cells have the capacity to assume a multitude of lineages, including osteocytes, chondrocytes, adipocytes, and neural-lineage cells. Cells utilized in these experiments have been previously characterized with the capacity for tri-lineage differentiation by our lab [31]. The intention of applying these cells to material with a range of imbedded GO is to determine if a particular threshold of GO induces cellular differentiation to a neural lineage as qualified with cellular morphologic staining and neural cell markers. Two series of conditions were evaluated: hMSCs seeded on PLGA-GO smears ranging from 0 to 5% wt. GO in the presence of

neuroinduction media (serving as positive control), and hMSCs seeded on PLGA-GO smears ranging from 0 to 2% wt. GO in the presence of standard media. The 5% wt. GO sample was eliminated from the standard media series as this iteration of smears proved to have a suboptimal consistency and was difficult to visualize cells on when utilized in the initial series of experiments performed with neuroinduction media.

Composite smears on glass coverslips were placed into 24-well plates and UV sterilized for a minimum of 4 hours. Plates were constructed as follows: three WST-8 assay plates with samples in duplicate and endpoints at Day 3, 5, and 7; calcein green AM (CAM) assay plates with samples in duplicate and Day 3, 5, and 7 endpoints for neuroinduction samples and Day 7 only for standard media samples; one vimentin immunofluorescence staining plate with samples in duplicate and Day 7 endpoint. Replicates and timepoints between the two series varied depending on availability of total cell number once passaged. MSCs of no greater than passage six were passaged using 0.05% trypsin and seeded onto the smears at 10,000 cells/well. Standard media was comprised of Dulbecco's Modified Eagle's Medium fortified with 2.5 mM L-glutamine (DMEM/F-12 1:1 Modified; Hyclone, Logan, UT), 10% fetal bovine serum, 1% penicillin/streptomycin, and 0.1% amphotericin. Neuroinduction media was comprised of standard media, 0.5 mM 3-isobutyl-1-methylxanthine (IBMX; Sigma-Aldrich, St. Louis, MO), and 1.0 mM N^6,'-O-dibutyryladenosine 3',5'-cyclic monophosphate sodium salt (dbcAMP or Bucladesine; Sigma-Aldrich, St. Louis, MO) [8]. Each well was fed with 0.5 mL of media, with a media change every two to three days. Cells were incubated in standard culture conditions at 37ºC and 5% CO_2. Individual assay procedures are described below.

WST-8 Assay for Assessment of Cell Viability

Assays for Quantitation of Cellular Viability & Proliferation

A variety of live cell quantification assays exist which can be utilized to assess cell viability and track cell proliferation over time. These assays are tailored to take advantage of a multitude of cell functionalities, including enzyme activity, permeability, adherence, production of ATP or co-enzyme, and nucleotide uptake ability [32]. Selection of the specific assay is influenced by cell number, cell lineage, anticipated outcome, and specific intention, such as monitoring number of

cells over time, quantifying cellular divisions, or assessing metabolism or DNA synthesis [33]. Collectively, there are eight main categories of cell viability assays, which rely on dye exclusion, metabolic activity, ATP levels, sulforhodamine B binding, protease viability, clonogenic cell survival, DNA synthesis, or Raman micro-spectroscopy for quantification of cells [32]. One of the most commonly employed of these assay categories is dye exclusion, particularly the trypan blue assay, which relies on application of a negatively charged diazo-dye that can penetrate permeable membranes of dead cells, but is impermeable to membranes of live cells, allowing quantification of clear "live" cells versus blue "dead" cells [32, 34]. This method is often employed when quantifying viable cells in suspension [34], and is used in our passaging protocols.

One of the other most commonly employed categories of cell viability assays includes assays that rely on cellular metabolic activity. Common assays in this category include MTT, MTS, WST, calcein AM, and alamar blue [32]. MTT, MTS, and WST assays all rely on tetrazolium salts of similar structure, hence their comparable abbreviations, which are converted to insoluble formazan crystals by mitochondrial enzyme reduction reactions [32]. The formazan product is then quantified using a spectrophotometer, making these colorimetric in nature. Pitfalls to these assays include limited sensitivity and prolonged incubation time [32].

Alamar blue (also called "resazurin") is a dye which is capable of entering into the cytosol of cells, upon which it is reduced to resorufin, a red fluorescent molecule [32]. The greater proportion of reduction in metabolically-active live cells versus dead cells results in a fluorescence differential that allows for live cell determination [32]. The dye is added to the media at the onset of the culture, and allows for viability assessment for the duration of the experiment without discontinuing samples at selected timepoints, as in many other assays [35, 36]. While this is a highly sensitive assay, there can be some fluorescence interference and substantial optimization protocols may be warranted [32]. While calcein green is commonly used in fluorescence assays, the non-fluorescent derivative, calcein-acetomethoxy (calcein AM; CAM), can be utilized in cytotoxicity assays employing flow cytometry [32]. CAM is permeable to cell membranes, regardless of their viability, but only experiences cleavage into the fluorescent calcein and non-fluorescent acetomethoxy by esterases in the cytoplasm of live cells [32]. Disadvantages to this assay include reduced sensitivity to adherent cells and the requirement of a more highly sensitive microscope [32].

Selection of WST-8 Assay

The WST-8 metabolic assay was elected for quantitative assessment of cell proliferation for the PLGA-GO material rather than the MTS assay, as are typically utilized by our lab, due to evidence that the specific tetrazolium reagent used in MTT assays (3-(4,5-dimethylthiazol-2-yl)-2,5-diphenyltetrazolium bromide), which is very similar to the MTS reagent (3-(4,5-dimethylthiazol-2-yl)-5-(3-carboxymethoxyphe-nyl)-2-(4-sulfophenyl)-2H-tetrazolium), has confounding interactions with GO that may result in false positive readings [37, 38]. Several investigators have found that carbon-family materials in general interact with the MTT reagent to artificially inflate cell viability [39, 40]. Marques *et al*. (1995) described the process by which the [MTT]+ cation may undergo reduction from electrons or protons, the mechanism of which was exemplified with graphene by Liao *et al.* (2011) and is depicted in Figure 4-5 [37, 41, 42]. The multi-step reduction of the MTT reagent by graphene, which produces the purple formazan product traditionally formed from interaction with live cells, explains the aberrant results when this reagent is used in the presence of graphene-based materials [37]. Liao *et al.* (2011) also performed both WST-8 and trypan blue exclusion assays with a range of GO concentrations and found that these were both reliable methods of assessing cell viability.

WST-8 Assay Experimental Techniques & Materials

A preliminary calibration assessment of a range of cell densities was performed, serving as a confirmation of handling technique and assay reliability. This procedure is described under "in Vitro *Growth Factor Experiments – Experimental Techniques & Materials*". For each series of assays (neuroinduction media and standard media), a plate was dedicated to performance of a WST-8 assay on Days 3, 5, and 7. Media was carefully removed from each well and replaced with 300 µL of fresh media, sufficient to cover all or the majority of the individual smears. 30µL of WST-8 reagent was then applied to each well, making the final media to reagent volume ratio 1:10. Plates were swirled for mixing of media and reagent, then incubated for approximately 2.5 hours before being read by the spectrophotometric plate reader at 450 nm. The resulting absorbance readings were vetted for any outliers, averaged, and plotted for relative live cell number over time (i.e. comparison of proportions between timepoints rather than direct quantification of cell numbers from absorbance value).

Calcein Green AM for Morphology & Qualitative Assessment of Cell Proliferation

Assays for Morphology & Qualitative Assessment of Cell Proliferation

Several of the aforementioned cell viability and proliferation assays simultaneously permit observance of cellular morphology to a limited extent. Historic methods of assessing cell phenotype have largely relied on these cell viability assays or levels of luminescence reporter genes, but recent advancements have been made in automated microscopy that have amplified the capacity to visualize a great host of phenotypes in samples with a high density of cells [43]. Cellular staining continues to be a reliable technique that can permit visualization of cells or cellular components, and in some cases, multiple stains can be combined for broader delineation of cellular components in individual cells [44]. These stains also vary in their applicability to fixed cells or live cells, and microscopy technique (light versus fluorescent) for visualization [44]. Immunofluorescence (IF) staining also permits elucidation of cellular phenotype by application of specific antibodies tagged with fluorophores that are targeted to bind to specified cell component antigens [45]. These antigens can be components of a broad range of cells, such as vimentin intermediate filament protein found in cells of mesenchymal origin, or components very specific to certain cell types, such as S100 in neurons and astrocytes [46-48]. The IF method can be either direct (primary), where the fluorophore is directly attached to the primary antibody which targets the antigen, or indirect (secondary), where the fluorophore is attached to a secondary antibody which targets an antigen-bound primary antibody [45]. For these experiments, calcein green AM was selected for subjective assessment of cell proliferation and morphology. Cells were also fixed for performance of immunofluorescent staining with vimentin secondary antibody and neural cell-specific markers.

Experimental Techniques & Materials

For each series of assays (neuroinduction media and standard media), a plate was dedicated to performance of CAM staining on Days 3, 5, and 7. CAM (CellTrace Calcein Green, AM, Invitrogen, Thermo Fisher Scientific) was reconstituted by adding 10 μL DMSO to each 20 μg vial. CAM solution was prepared in a ratio of 2 μL CAM/DMSO to 1 mL Hank's Balanced Salt Solution (HBSS; VWR, Radnor, PA), in sufficient volume to apply 0.5 mL of the solution per

well. Prior to this, media was carefully removed from each well and samples were washed once with HBSS. CAM solution was applied and samples incubated for approximately 5 minutes before being imaged on a fluorescent microscope with a green filter (488 nm).

For each series of assays (neuroinduction media and standard media), a plate was dedicated to performance of vimentin staining of Day 7 cells. Media was removed from the wells and samples were washed twice or thrice with HBSS before being fixed with 4% paraformaldehyde (PFA) for a minimum of 10 minutes. PFA was removed, samples washed twice or thrice with HBSS, and lastly covered in HBSS for refrigerated storage until the time of proceeding with the immunofluorescence staining process.

The protocol for vimentin staining was performed with practice plates and is as follows: HBSS is removed and samples are washed once with fresh HBSS. 0.1% Triton is applied to samples for 10 minutes to induce cell permeabilization and then washed with two or three applications of HBSS. 0.5 mL protein block per well is applied for 30 minutes before addition of 1 μL of the primary antibody (purified mouse anti-vimentin 0.5 mg/mL; BD Biosciences, Franklin Lakes, NJ), which is allowed exposure to the samples overnight in the refrigerator. The following day, samples are washed two or three times with HBSS and 0.5 mL protein block with two drops of secondary antibody (donkey anti-mouse IgG (H+L) antiprobes secondary antibody, AlexaFluor 488; Invitrogen, Thermo Fisher Scientific, Waltham, MA) is applied to each well, making the final secondary antibody ratio approximately 1:500. After 30 minutes, samples are washed two to three times with HBSS and DAPI (ProLong Gold Antifade Mountant with DAPI; Molecular Probes, Thermo Fisher Scientific, Waltham, MA) is applied. DAPI is allowed to dry for minimum of 24 hours before florescence imaging.

Results & Discussion

WST-8 Assays

WST-8 assays were performed in duplicate for both neuroinduction media and standard media-exposed samples. Any inconsistent absorbance readings were eliminated from the data set, which occurred minimally. Averages and standard deviations were used to generate bar graphs for comparison of cell number differences between timepoint within each material iteration subset, as

well as trends between material iterations. Of note, absorbance values are unable to be compared between the neuroinduction media-exposed sample set and standard media-exposed set due to non-cellular media and WST-8 reagent blank sample values, or an approximated value, being subtracted from each timepoint of the standard media-exposed set but not the neuroinduction media-exposed set. Additionally, as growth factor trials were being performed simultaneously, the media utilized for blanks was that utilized by Schwann cells, which is very similar in coloration and constituents.

As several of the smears adapted a rolled or substantially crinkled conformation due to exposure to fluid and physiologic temperature, inhibiting cells to utilize at least a portion of the material as a surface for adherence and growth, and smears not covering the entirety of the surface even in proper conformation, these assays are less accurate for direct quantitation of cell proliferation, but rather serve better as assessments of cytotoxicity. WST-8 assay results from neuroinduction media-exposed samples (Figure 4-6-A) demonstrated progressive cell proliferation or stability in all samples, indicating that none of the material iterations were cytotoxic to cells, despite WST-8 assay results of the standard media-exposed samples (Figure 4-6-B) revealing a decrease in cell number of the 0.5% wt. GO and 1.0% wt. GO samples. The cause of the decline in cell number of each of these samples is unknown and unexplained by CAM images, which clearly show a substantial number of cells present.

CAM Assays

Morphology of cells between samples exposed to neuroinduction media (Figure 4-7) and standard media (Figure 4-8) featured both similarities and differences. Cells from the neuroinduction media-exposed samples evoked a clearly neural-like spindle morphology with extensive webbing and close association of cells with one another. Webbing appeared slightly less prevalent in the PLGA-only samples compared to the samples with GO imbedded. Cells from the standard-media exposed samples also appeared spindle shaped with some cells having no webbing and some featuring a range of mild to extensive webbing. PLGA-only samples appeared to induce cells with a more thinly spindled shape with minimal webbing evident. Similar to the confounding of the WST-8 assay results, abnormal conformation of the material in some cases inhibited optimal imaging, as did samples with higher proportions of GO due to their deep black coloration. Trends in these

samples suggest that the material not only serves as an acceptable surface for cell attachment and proliferation, but GO-imbedded material in particular appears to influence cells to form web-like structures, potentially facilitating better communication with neighboring cells and more cohesive tissue architecture. Additionally, though the capabilities of imaging multiple areas of each sample was often impeded, from the images that were obtained of standard media-exposed samples, it appears that cells on 0.25% wt. GO and 0.5% wt. GO demonstrate the greatest proportion of webbing. For example, in Figures 4-8-C2 and 4-8-C3, there is an obvious transition of the cell morphology at the periphery of the material, where cells are more spindle shaped with less webbing, to cells on the material with extensive webbing. With collective considerations of cytotoxicity results, appearance of cells on material, and reduced GO proportion more easily facilitating imaging of cells, it is recommended that material iterations of 0.25% wt. GO or 0.5% wt. GO be pursued for fabrication of the nerve scaffold.

Preliminary Experiments for Development of a Growth Factor-Eluting Hydrogel

Growth Factor Hydrogel Conceptualization

Growth Factor Delivery

Growth factors are intracellular signaling proteins that induce such physiologic responses as cellular recruitment and differentiation [49]. Growth factor delivery devices have become a great area of interest in biomedical research, with a multitude of methods and mechanisms being explored [49, 50]. Tissue engineering applications in the field of peripheral nerve repair have found promising results in the administration of growth factors, such as the capacity to stimulate neuronal cell proliferation and differentiation, enhance myelination, and advance axonal growth [51]. Utilization of hydrogels in biomedical applications has also gained much attention in recent years, owing to the wide array of polymers and adjunct materials from which they can be fabricated, the variety of physical and chemical properties they can be tailored to feature, and their diverse applicability. Hydrogels with growth factors impregnated for subsequent delivery to a specific tissue site is one such application. Growth factors may be incorporated into a hydrogel by a variety of mechanisms including direct addition prior to or during hydration of the dry hydrogel

formulation, incorporation into microspheres with subsequent addition to the hydrogel, and cross-linking to the hydrogel structure (chemically, enzymatically, or mechanically) [49, 50]. An additional consideration pertains to the mechanism of growth factor release from the hydrogel, which can include elution from a stable hydrogel, elution from a hydrogel as it degrades or swells, and release upon a particular stimuli (e.g. heat, pH) [50].

We conceptualized development of a neural growth factor-eluting hydrogel to serve as an adjunct to our nerve scaffold with the intent of enhancing neural cell growth in the early regeneration period. We proposed that the hydrogel would contain between one to three neural cell growth factors which would be directly incorporated into a commercially-available hydrogel product. The growth factor hydrogel would be stored within a tuberculin syringe and injected into the lumen of the scaffold at the time of surgery, then elute the growth factors as the hydrogel progressively degrades.

Neural-Specific Growth Factors & Selection

There are several categories of growth factors that impart action on neural cells, some of which are specific to neural-lineage cells, and others which act on many cell types including neural-lineage cells [52]. These categories are neurotrophins, neurokines, fibroblast growth factors, transforming growth factor β superfamily, epidermal growth factor superfamily, and a non-distinct "others" group, the growth factors belonging to which are provided in Table 4-1 [52]. Neurotrophins contribute to the development, survival, functionality, and morphologic plasticity of neural cells [51, 53]. One of the most studied neurotrophins, nerve growth factor (NGF), features an ability to stimulate growth and is required for neuronal cell survival [52]. Interestingly, NGF is synthesized in the tissues surrounding neurons involved in innervation to that region [52]. Following peripheral nerve injury, cytokines released by inflammatory cells induce synthesis of NGF in Schwann cells and fibroblasts of the injured nerve, as well as in local mast cells [53]. Cell response to NGF is mediated through several members of the Trk family of receptor tyrosine kinases, as well as p75NTR, a TNF receptor [53].

Ciliary neurotrophic factor (CNTF), a neurokine, demonstrates a broad range of actions on a multitude of neuronal cell types, which includes sustainment of cells within the peripheral nervous system and control of neurotransmitter release in the central nervous system [52]. CNTF

is produced in muscle tissue, where it can then be utilized by motor neurons, the mechanism of which has facilitated prevention of motor neuron death and partial reversal of neuromuscular disease in animal models when CNTF was applied to injured nerves [52]. CNTF is typically found in high levels within normal, healthy peripheral nerve, but CTNF mRNA experiences a decline in less than 24 hours post-injury, followed by a steep decrease to five times below normal levels thereafter [51]. For comparison, the mRNA of neurokine interleukin 6 elevates to thirty-five times normal levels in the distal damaged nerve segment immediately after injury, followed by return to normal levels at 24 hours [51].

There are two specific FGFs within the nervous system, acidic FGF (also termed FGF-1) and basic FGF (also termed FGF-2), and these are extremely abundant in proportion to other neural growth factors [52]. bFGF displays mitogenic activity within the peripheral nervous system [54]. Insulin-like growth factor I (IGF-I), a growth factor which falls within the "other" classification, has been heavily utilized for its trophic and survival roles in *in vitro* studies of neural cells [52]. IGF-I not only promotes proliferation, differentiation, and survival of neuronal and glial cells, but has been shown to reduce motor neuron cell death and enhance axonal repair after injury [52]. Lewis *et al.* (1993) reported that subcutaneous injections of IGF-I were capable of enhancing function recovery of a sciatic nerve crush injury in mice [55].

Based on encouraging results accumulated from the literature, which have demonstrated that neurotrophic factors can enhance the survival rate of injured nerves [51], we elected to proceed with assessment of three neural growth factors in varying combinations for potential impregnation into a hydrogel adjunct to the peripheral nerve scaffold. CNTF was selected based on its interesting behavior of sharply decreased expression post-injury. The potential to retain this growth factor at the site of the nerve injury when typically there is a deficiency may greatly aid in facilitating immediate enhancement of nerve recovery. Choi *et al.* (2008) assessed the effects of combinations of four different neural growth factors in relation to their proliferative effects and inducement of differentiation of neural stem cells, and found that not only do cultures exposed to more than a single growth factor demonstrate additive effects on cellular differentiation, but bFGF and IGF-I together elicit the most profound response [54]. The authors suggest that this may be due to a synergism between the mitogenic effects of bFGF and post-mitotic action of IGF-I. Hence, bFGF and IGF-I were selected as the second and third growth factors for assessment in our study.

Commercially-Available Hydrogel Product Selection

Investigation into commercially available hydrogel products lead to selection of the Biogelx range of hydrogels (Lanarkshire, NL, Scotland, UK), a synthetic peptide-based product formulated as a powder to which fluid is added for reconstitution and gel formation. The resulting gel produces a nanofibrous network, intended to emulate ECM, and which can be tailored to feature a variety of mechanical properties depending on the volume of fluid added [56]. Two products were utilized for our experiments: Biogelx-S, a standard, non-functionalized formula, and Biogelx-IKVAV, a laminin-functionalized formula.

In Vitro *Growth Factor Experiments*

Experimental Groups

Immortalized rat neuronal Schwann cells (NSCs; RT4-D6P2T; ATCC, Manassas, VA) were utilized for all *in vitro* growth factor assays [57-59]. Two series of experiments were performed, the first evaluating combinations of the three selected growth factors with cumulative concentration of growth factor being 30 ng/mL, and the second solely evaluating varying concentrations of CNTF (10, 25, and 50 ng/mL) based on results from the first experiments suggesting this to be a potentially beneficial growth factor *in vitro*. Two trials were performed for each series, one with an initial cell seeding density of 750 cells/well, and another with 2000 cells/well. Concentrations of growth factors utilized in *in vitro* experimentation have been reported to fall within the range of 10 to 20 ng/mL [51, 54, 60]. In the growth factor comparison experiment, the eight group designations were as follows: IGF-I (30 ng/mL), bFGF (30 ng/mL), CNTF (30 ng/mL), IGF-I+bFGF (15 ng/mL of each), IGF-I+CNTF (15 ng/mL of each), bFGF+CNTF (15 ng/mL of each), IGF-I+bFGF+CNTF (10 ng/mL of each), no growth factor (media alone). In the CNTF concentration gradient experiment, group designations were as follows: no growth factor (media alone), 10 ng/mL, 25 ng/mL, and 50 ng/mL CNTF.

Experimental Techniques & Materials

The growth factor products utilized for growth factor testing were recombinant mouse IGF-I (Sigma-Aldrich, St. Louis, MO), recombinant rat bFGF (Sigma-Aldrich, St. Louis, MO), and

recombinant rat CNTF (Sigma-Aldrich, St. Louis, MO). Lyophilized growth factors were reconstituted with sterile water, and stock solutions of 1 ng per uL of media were prepared, aliquoted, and frozen at -20ºC. At each feeding, solutions of the designated growth factor concentrations were freshly prepared with the stock growth factor solutions and high glucose standard media, which was comprised of high glucose DMEM, fortified with 4 mM L-glutamine (ATCC, Manassas, VA), 10% fetal bovine serum, 1% penicillin/streptomycin, and 0.1% amphotericin.

NSCs were passaged with 0.25% trypsin and seeded at either 750 or 2000 cells/well in 24-well plates. The reduction of cells than is typically seeded (10,000 cells/well) was based on preliminary experiments which demonstrated that, due to the extreme proliferative nature of the cells, lower seeding density aids in preventing premature confluency of cells and permits greater spacing of assay timepoints. Growth factor-spiked media in the appropriate concentrations were applied to each well, and plates were constructed as follows for all experiments: three WST-8 assay plates for three timepoints (varied depending on cell seeding density) with samples in triplicate and three CAM staining assay plates for the same three timepoints with samples in duplicate. Timepoints in the growth factor comparison experiment were Day 0.5, 2, and 3.5 for Trial 1 (750 cells/well seeded) and Day 2, 4, and 5.5 for Trial 2 (2000 cells/well seeded). Timepoints in the CNTF concentration gradient experiment were Day 1, 3, and 6 for Trial 1 (750 cells/well) and Day 2, 4, and 5.5 for Trial 2 (2000 cells/well). Samples discontinued at the latter timepoints received one exchange of fresh growth factor-spiked media mid-way through their culture period. Timepoints were variable between trials based on variances in when they were performed and cell proliferation behavior.

WST-8 assays were performed utilizing the same protocol as employed for the PLGA-GO composite experiments, with a reduced volume of media and WST-8 reagent (though remaining in a 10:1 ratio), due to submersion of material not being a factor. A preliminary calibration assessment of a range of cell densities was also performed, serving as a confirmation of handling technique and assay reliability. For this procedure, passaged NSCs were seeded into wells at densities of 0, 500, 1000, 1500, 3000, 5000, and 10,000 cells/well in triplicate. 100 μL of media and 10 μL of WST-8 reagent were added and the plate was then incubated for approximately 2.5 hours. The plate was read with the spectrophotometric plate reader at 450 nm, values averaged,

and then a calibration curve was generated. CAM assays were also performed identically to the protocol employed for the PLGA-GO composite experiments.

In Vitro *Growth Factor Results & Discussion*

Calibration Curve

An initial WST-8 calibration curve of NSCs was performed with assessment of 0 to 10,000 cells/well, as shown in Figures 4-9 and 4-17-A. The linearity of the graph serves as confirmation of the cell counting and handling technique, as well as the validity of the assay for this particular cell lineage and application.

Growth Factor Trials 1 & 2

Cells were exposed to growth factors (IGF-I, bFGF, and CNTF) in total concentrations of 30 ng/mL, with samples evaluating only one growth factor containing 30 ng/mL of that growth factor, samples evaluating two growth factors containing 15 ng/mL of each, and samples evaluating all three growth factors containing 10 ng/mL of each. Trial 1 and Trial 2 evaluated growth factors in these proportions applied to 750 cells/well and 2000 cells/well, respectively, which would typically be considered extremely low cell seeding densities; however, NSCs grow extraordinarily fast compared to most lineages. Based upon previously performed cultures, seeding densities of typical proportions (e.g. 10,000 cells/well) exceed the capacity of the well within a few days and confound interpretation of results.

Trial 1 WST-8 results (Figure 4-10-A) revealed the greatest cell proliferation in final timepoint (Day 3.5) samples to be those exposed to 30 ng/mL of CNTF; however, one-tailed student's *t*-tests assuming unequal variances revealed no significant difference ($p < 0.05$) in these samples compared to all other samples except for 30 ng/mL bFGF [61]. Unfortunately, since the higher proliferative growth factor samples did not produce significantly different results than the control sample, it is possible that this less proliferative sample was actually inhibitory to NSC growth. Trial 2 produced quite different results at the final timepoint (Day 5.5; Figure 4-10-B), with 15 ng/mL each of IGF-I and CNTF resulting in the greatest proliferation of cells and this being significantly different ($p < 0.05$) than the other samples. Note that absorbance values

between Trial 1 and 2 samples cannot be compared because non-cellular media and WST-8 reagent blanks were subtracted from Trial 2 values, whereas they were not for Trial 1 values.

Cell morphology, as depicted with CAM imaging (Figures 4-11 & 4-12), appeared similar in cells of all samples in both trials, and cell density was obviously increased in the progression of timepoints and between the two trials with variability in their initial cell seeding density. One limitation to the Trial 2 results is that, based on CAM image appearance, cells were so confluent at the last timepoint that it is very likely cell death and/or sloughing may have occurred in small regions. This may have confounded the results of the final WST-8 assay timepoint for this trial. Alternatively evaluating the WST-8 assay results of the mid-way timepoint (Day 4), there was no significant difference ($p < 0.05$) between the most proliferative sample (10 ng/mL of all three growth factors) and the next five most proliferative samples, and the sample of 15 ng/mL each of IGF-I and CNTF unexpectedly demonstrated the least proliferation, completely opposite to the Day 5.5 results. While it is difficult to make definitive interpretations from these data, results from Trial 1 appear more reliable in consideration of culture conditions and Trial 2 limitations.

In order to elucidate if any of the significantly more proliferative samples of Trial 1 demonstrate any beneficial effects over control samples, alternative cell seeding densities and/or timepoints could be evaluated; for example, experiments of seeding with 2000 cells/well would benefit from an earlier final timepoint than Day 5.5 in order to reduce the chances of cell death and sloughing. Additionally, alternative growth factor concentrations could be evaluated. Cumulative 30 ng/mL growth factor concentrations do not necessarily directly correspond to physiologic conditions; however, performing every range and combination between 10 to 30 ng/mL of each growth factor would have resulted in several dozen combinations, which was out of the constraints of this study. Although 30 ng/mL of CNTF did not produce significantly higher proliferation, it inherently inducing the highest magnitude of proliferation stimulated another series of experiments evaluating the impact of varying concentrations of CNTF on NSCs, as described to follow.

CNTF Concentration Gradient Trials 1 & 2

Cell seeding density differences between Trial 1 and 2 were identical to that of the IGF-I, bFGF, and CNTF growth factor experiments: Trial 1 consisted of an initial 750 cells/well, and Trial 2 an

initial 2000 cells/well. Cells were exposed to CNTF concentrations of 10, 25, or 50 ng/mL, or were exposed to control media in the absence of CNTF. WST-8 results of the final timepoint of Trial 1 (Day 6; Figure 4-13-A) revealed the greatest inherent cell proliferation in samples exposed to 25 ng/mL of CNTF; however, this was only a significant difference ($p < 0.05$) when compared to control samples. There was minimal variability in earlier timepoints, so comparing these does not elucidate any benefits of the growth factors in the early proliferation phase. Trial 2 final timepoint (Day 5.5) results (Figure 4-13-B) showed a similar greater cell proliferation effect in samples exposed to 25 ng/mL CNTF, but this was only significantly different than the 50 ng/mL samples, and variability in absorbance amongst all samples was fairly low. As a similar situation of excessive cell confluency occurred in the final timepoint wells of those initially seeded with 2000 cells/well, the mid-way timepoint (Day 4) was evaluated and revealed no significant difference ($p < 0.05$) between the most proliferative samples (25 ng/mL) and all others. Similar to the IGF-I, bFGF, and CNTF experiments, absorbance values between Trials 1 and 2 cannot be directly compared due to non-cellular media and WST-8 reagent blank values being subtracted from only Trial 2 samples.

CAM images (Figures 4-14 & 4-15) demonstrate similar cell morphology between samples and cell density appearance that is sensical to the WST-8 results. Collectively from the WST-8 and CAM image data, the most notable observance is that there is greater proliferation in samples exposed to CNTF concentrations of 25 ng/mL or 50 ng/mL than control samples exposed to no growth factors when initial cell seeding density is low (750 cells/well). This suggests that in cases of a reduced number of viable cells in a local tissue environment, such as post-injury within a peripheral nerve, administration of CNTF may stimulate greater proliferation of those cells and may ultimately enhance the speed of regeneration.

Hydrogel Optimization & Elution Studies

Biogelx Product Optimization Techniques & Materials

Development of our growth factor-eluting hydrogel first relied on selecting the optimal product based on tangible consistency, to include the ability to be extruded through a small-gauge syringe (i.e. 25G) and to remain situated where extruded without leakage so that the product can be

maintained within the nerve scaffold lumen. Biogelx hydrogel products can be hydrated with variable volumes of fluid to evoke alternative densities and viscosities, and, as we speculated, with the possibility of featuring different degradation profiles. Hence, the first phase of characterizing the hydrogel products was to manipulate the volumes of saline (Normosol-R) added to samples of the powdered gel product, with qualitative assessment of the resulting physical characteristics. A range of hydration volumes were first examined based on suggestions from the product specifications, resulting in final concentrations of 4.4, 8.8, and 12.2 mg gel powder in 1 mL saline. 0.5 mL samples were prepared and evaluated in regards to their extrusion capacity from a 25G syringe, viscosity during extrusion, maintenance of shape when extruded into a culture plate well, and appearance and viscosity over a period of time (less than 30 minutes).

Based on the results of the three initial trial samples, two formulations were developed for the first series of elution studies: 14.7 mg/mL (Gel Formula 1) and 23.3 mg/mL (Gel Formula 2). Gel Formula 1 had a greater fluid to gel powder ratio, resulting in a slightly thinner, less viscous product, whereas Gel Formula 2 had a greater proportion of gel powder to fluid volume, and hence was denser and more viscous. Samples of gel were prepared so that the elution study would be run in triplicates of 0.15 mL BSA solution (200 ng/mL) to 2.2 mg or 3.5 mg gel powder for Gel Formula 1 and 2, respectively. The resulting samples each contained 30 ng of BSA total. Samples were placed into the center of a 6-well plate, covered with 3 mLs of saline, and were placed into an incubator with designated timepoints for sample retrieval. Due to erroneous results, as discussed in the results section, the trial was discontinued and repeated a second time, but with impregnation of 150 ng of BSA into each sample and half of the volume of saline coverage (1.5 mL).

A third trial consisted of increasing the impregnated mass of BSA, as well as altering the gel formulas to produce more hydrated samples that could potentially facilitate increased release of the impregnated BSA. The modified formulas contained 12 mg/mL (Gel Formula 3) and 17 mg/mL (Gel Formula 4) of gel powder and were impregnated with 400 ng BSA. Samples were prepared with 0.2 mL BSA solution (2 μg/mL) and 2.4 mg or 3.4 mg gel powder, respectively. Additionally, a non-BSA containing gel sample was created as a control to determine if the synthetic peptides constituting the gel powder were capable of eliciting a signal in the protein quantification assays. Saline served as an additional control. All samples were placed into 12-well plates, covered in 1 mL saline, and were incubated. A final trial of the elution studies employed

the same parameters as Trial 3, but with impregnation of 10 μg/mL of BSA per sample, being greatly increased in order mitigate possible sensitivity issues with the colorimetric assays.

Protein Quantification Assays

In order to gain an understanding of the capacity for the hydrogel product to store and release additives overtime, a series of elution assays were performed. Growth factors are quite expensive, typically costing several hundred dollars for microgram quantities, so an alternative molecule was utilized for the initial elution studies. As growth factors are protein in nature, bovine serum albumin was selected as a substitutionary protein. Though BSA is a larger protein than any of the growth factors under evaluation (approximately 66 kDa versus approximately 7.7 kDa to 22.8 kDa) [62-65], it is still of a comparable size and was a beneficial selection in regards expense and availability of reliable assay options.

There are numerous protein quantification assays available, each with their intricacies, sensitivities, advantages, and disadvantages, which are broadly divided into categories based on their dependence of ultraviolet absorption, fluorescence, or color change for quantification [66]. Ultraviolet light absorption can be utilized for quantification of protein without the necessity for added reagents; however, this method is highly implicated in erroneous results with the potential for interference from free nucleic acids [66, 67]. Fluorescent assays, such as EZQ (Invitrogen, Thermo Fisher Scientific, Waltham, MA) and Qubit (Invitrogen, Thermo Fisher Scientific, Waltham, MA), utilize a specialized proprietary dye that, once bound to protein in solution, elicits an increased fluorescence proportional to the quantity of bound dye [66, 68, 69]. Substantial benefits of these assays include that they require incredibly small quantities of sample (as minimal as 1 μL) while maintaining high sensitivity, and are minimally affected by non-proteinaceous substances in solution (e.g. salts, urea, reducing agents, solvents) [66, 68, 69].

Colorimetric assays are commonly utilized for protein quantification. Biuret methods, including bicinchoninic acid (BCA) and Lowry's assays, rely on protein-copper chelation, whereas dye-based methods, such as the Bradford's (Coomassie Blue) assay, rely on protein-dye binding [66]. Biuret methods have less protein-to-protein variation than dye-binding methods, but require an incubation waiting period in order for the copper complexes to form and are slightly less sensitive; for example, the BCA assay has a detection threshold of 5 μg/mL with an advanced

protocol, but requires a concentration of 20 μg/mL with the standard assay method [66, 70, 71]. Dye-binding methods are more sensitive (detection threshold of 1 μg/mL) and evoke an immediate color change when the reagent is combined with the sample, but can result in highly variable results depending on the nature of the protein(s) being evaluated [66, 71]. For this reason, developing a protein calibration curve is especially essential.

We elected to utilize the Bradford's assay initially for quantification of bovine serum albumin released into solution from the hydrogel, with later adoption of the BCA assay for parallel testing with the Bradford's assay. The Bradford's assay employs Coomassie Blue dye, which is brown in its unconjugated appearance, but transitions to blue when bound to protein. This color change is accountable to Coomassie Blue ligands binding to positively charged regions on the protein, in addition to formation of hydrophobic and Van der Waals interactions between the dye and protein [71]. The spectrophotometer setting for a Bradford's assay sample is 595 nm [72-74]. The BCA assay employs a two-step process. First, Cu^{2+} is reduced to Cu^{+} by the protein in solution, which produces a mildly blue complex; then, the bicinchoninic acid component reacts with the reduced copper to elicit a profound purple color that is substantially more profound than the color change produced from the first reaction step [70]. The spectrophotometer setting for this assay is 562 nm [70].

Bradford's & BCA Assay Techniques & Materials

The methods employed for the Bradford's assay were a conglomeration of methodologies utilized by several sources [72-74]. In order to select an optimal Coomassie Blue reagent to sample ratio, a calibration experiment was performed using 250 μL increments of Coomassie Blue (Coomassie Protein Assay Reagent, Thermo Scientific, Thermo Fisher Scientific, Waltham, MA) with either 10 or 20 μL of BSA solution added in an array of known concentrations. A stock solution of BSA and saline (Normosol-R) was made at a concentration of 400 μg/mL, and serially diluted to created samples with final concentrations of 0.1 ng, 1 ng, 10 ng, 100 ng, 1 μg, and 10 μg/mL. Retrieving samples from these individual solutions, rather than from a single stock solution, permitted an equal volume of solution to be added to sample wells (either 10 or 20 μL), preventing erroneous results due to inconsistent ratios of Coomassie Blue to sample volume, and resulting in final target quantities of 0.001, 0.01, 0.1, 1, 10, 100 ng BSA being added to the wells in the 10 μL samples,

and double these amounts in the 20 μL samples. The refrigerated Coomassie Blue reagent was allowed to sit at room temperature briefly before addition of BSA samples, and all samples were read in a 96-well plate, in triplicate, by an Epoch spectrophotometric plate reader set to 595 nm wavelength. Samples from hydrogel elution tests were performed in the same manner with 10 μL samples of the extraneous solution being added to 250 μL of Coomassie Blue.

A second calibration study was performed for the Bradford's assay and BCA assay in parallel. BSA solutions were prepared in concentrations of 1 μg/mL, 10 μg/mL, 100 μg/mL, 1 mg/mL, 5 mg/mL, 10 mg/mL, in addition to a saline control. As the Bradford's assay utilizes 10 μL of sample per well and the BCA assay utilizes 25 μL of sample per well, total masses of BSA added to wells for each assay were 10 ng, 100 ng, 1 μg, 10 μg, 50 μg, 100 μg, and 25 ng, 250 ng, 2.5 μg, 25 μg, 125 μg, 250 μg, respectively. The Bradford's assay calibration was performed in the same manner as previously explained. The BCA assay (Pierce BCA Protein Assay Kit, Thermo Scientific, Thermo Fisher Scientific, Waltham, MA), performed as designated in the product specifications [75], required initial mixture of the working reagent, composed of a 50:1 ratio of BCA Reagent A, which includes bicinchoninic acid and buffers, and BCA Reagent B, containing 4% cupric sulfate. 25 uL of each BSA solution was added to 200 μL of the working reagent in a 96-well plate. For increased sensitivity, the enhanced protocol was utilized, which required placement of the plate into a 60ºC oven for 30 minutes. The plate was then cooled to room temperature and read by the spectrophotometer at 562 nm. The same protocol was utilized for the elution study samples of Trial 4, in parallel with performance of Bradford's assays.

Samples from the elution trials were retrieved from wells in triplicate (Trial 1) or duplicate (Trials 2 through 4) at designated timepoints, one to two initial samples being retrieved within 6 hours of immersion of the gels in saline, a minimum of two subsequent samples being retrieved at 24-hour increments, and any subsequent samples ranging from 24 to 72 hours. Extraneous fluid was not replaced at each timepoint due to gel fragility, but rather remained with the gel sample for the duration of the elution test. Absorbance outputs were accumulated, outliers removed, and averages of replicates were graphed to track cumulative changes in elution. From the raw absorbance outputs, corrected absorbance values were calculated. As the combined unbound Coomassie reagent and saline has its own absorbance value, all samples necessitated correction to "true" absorbance values reflecting the absorbance of the reagent color change alone due to the

presence of protein. While simple subtraction of the daily combined Coomassie reagent and saline absorbance value would provide an estimate of the corrected absorbance, this is not entirely accurate due to the logarithmic nature of absorbance as a measurement. Proper absorbance correction requires a series of conversions from the outputted absorbance values to transmittance values, absorbtance values, corrected absorbtance in comparison to absortance of Coomassie reagent with saline, corrected transmittance, and finally corrected absorbance. Absorbance is the amount of light absorbed by the sample proportional to the sample thickness and concentration, whereas absorptance is the inherent absorptive property of the solution being evaluated [76, 77]. Transmittance is the amount of light that passes through the sample [76]. Absorbance correction is required in this phase of the study rather than in the previous spectrophotometric assays described because the end goal of these assays is to *quantify* the substance producing the color change, in this case BSA, rather than demonstrating relative differences between timepoints and sample groups. Below is the series of equations involved in this correction:

$A_S = absorbance\ of\ sample$ $A_R = absorbance\ of\ reference\ soln.\ (reagent/saline)$

$T_R = transmittance\ of\ sample$ $T_R = transmittance\ of\ reference\ solution$

$T_S' = \ absorbtance\ of\ sample$ $T_R' = absorbtance\ of\ reference\ solution$

$T_{S,cor}' = corrected\ absorbtance$ $T_{S,cor} = corrected\ transmittance$

$A_{S,cor} = corrected\ absorbance$

(1) *Convert absorbance outputs to transmittance:* $T_S = 10^{-A_S}$ $T_R = 10^{-A_R}$

(2) *Convert transmittance to absorptance:* $T_S' = 1 - T_S$ $T_R' = 1 - \ T_R$

(3) *Correct absorptance:* $T_{s,cor}' = \ T_S' - \ T_R{}'$

(4) *Convert to corrected transmittance:* $T_{S,cor} = 1 - \ T_{S,cor}'$

(5) *Convert to corrected absorbance:* $A_{S,cor} = \ -\log\left(T_{S,cor}\right)$

From corrected absorbance values, corresponding quantities of BSA present in extraneous solution were calculated. In calculation of BSA quantities in the extraneous fluid, decline in total extraneous fluid volume was accounted for as samples were removed overtime.

Hydrogel Studies Results & Discussion

Bradford's Assay Initial Calibration

The two initial calibration assays performed with 10 μL and 20 μL samples of BSA solution, ranging from 0 to 200 ng supplemented into wells, showed similar curves, with minimal differences between absorbance values of the individual BSA solutions despite the 20 μL samples containing double the quantity of BSA as the 10 μL samples. Since removal of less volume from wells with each timepoint is optimal, as the fluid volume was not replaced, 10 μL volumes were selected for future experiments. Trends in the calibration curve (see Figure 4-16) reveal that the Bradford's assay is not sensitive to quantities of BSA below 0.1 ng. Visual appearance of the assay is depicted in Figure 4-17-A.

Hydrogel Trials 1-3

Trials 1 and 2 evaluated the elution behavior of Gel Formulas 1 and 2 when impregnated with 30 ng of BSA (Trial 1; Figure 4-18) or 150 ng of BSA (Trial 2). In Trial 1 (Figure 4-20-A), there appeared to be a decrease in the quantity of BSA detected between 20 minutes and 4 hours, followed by an increase at 24 hours, and then a decrease at 48 hours, for the majority of the samples. Such a trend is confounded by the nature of the assay being a cumulative release assessment, rather than an assessment of actual release between timepoints. Out of concerns that the amount of eluted BSA was too low to reach the sensitivity level of the assay and hence produced erroneous results, the impregnated mass was increased to 150 ng and the immersion fluid volume was decreased from 3 mL of saline to approximately 1.5 mL of saline in Trial 2. A blank saline sample was also evaluated at each timepoint. As shown in Figure 4-20-B, Bradford's assays demonstrated a gradual increase in absorbance of nearly all samples between 6 hours and 24 hours, and then a decrease at the 48 hour timepoint, a trend also evident in the blank saline samples.

With continued concerns about the sensitivity of the assay, Trial 3 was attempted with an increased loading mass of 400 ng of BSA and immersion fluid volume reduction to 1 mL of saline (Figure 4-19). A control gel sample without any BSA was also evaluated to assess any effects of the synthetic peptide on the protein quantification outputs. Additionally, speculation that the loading volume of saline into the gels may have been too minimal to allow large enough pores to

develop to permit elution of the BSA, the concentration of each gel formula was reduced, allowing a higher saline to gel powder ratio. Trial 3 results (Figure 4-20-C) showed that the first two days experienced an increase in absorbance readings, and then a decline over the Day 4 and Day 7 timepoints, for all samples including the control gel and saline. Two possible etiologies of the erroneous results were considered: inherently inadequate performance of the hydrogel product for this application, or a disadvantageous response from the protein quantification assay selected. Due to the saline samples featuring the same trends as the samples with impregnated BSA, the latter potential etiology was further investigated by evaluating an alternative assay: the BCA assay. Of note, Table 4-2 describes the cumulative subjective qualities of the aforementioned gel formulations.

Bradford's and BCA Assay Calibrations with Higher BSA Concentrations

In preparation for impregnating high concentrations of BSA into the hydrogel samples in order to eliminate the sensitivity factor from the list of potential confounders, new calibration curves were generated with a range of 0 to 100 μg BSA (Bradford's assay) and 0 to 250 μg BSA (BCA assay) being added to wells. Differences in BSA mass between assays was due to the volume required for the individual samples: 10 μL for the Bradford's assay and 25 μL for the BCA assay. Raw and corrected absorbance curves are depicted in Figure 4-21 for the Bradford's assay and Figure 4-22 for the BCA assay, and the appearance of the BCA assay is depicted in Figure 4-17-C. Of note, the 250 μg value for the BCA assay is not depicted in the curve as the maximum absorbance reading was surpassed with this high of a concentration of protein.

Both curves demonstrate an initially steep slope until a threshold protein concentration is reached, following which a more linear and gradual slope is visible. With the ultimate goal of translating absorbance values from extraneous fluid samples into mass of BSA eluted, it was necessary to produce trendline equations for each curve. With the two distinct slopes present in each curve, the curves were divided into two separate trendlines with their respective equations applicable to absorbance values above and below particular thresholds (Figure 4-23): for the Bradford's assay, absorbance values ≤ 0.053 (equivalent to BSA mass ≤ 1 μg) or > 0.053 (> 1 μg), and for the BCA assay, absorbance values ≤ 0.448 (≤ 25 μg) or > 0.448 (> 25 μg). Absorbance outputs from hydrogel samples were then compared to the appropriate range before converting to

BSA mass within the assay sample (10 or 25 μL for Bradford's and BCA assays, respectively), which was then converted to total amount eluted into the extraneous solution after accounting for the approximate volumes removed each day for the assays.

Hydrogel Trial 4

Gel Formulas 3 and 4 were evaluated in Trial 4, being impregnated with a greatly increased mass of 2 mg BSA and immersed in 1 mL of saline. Both Bradford's and BCA assays were performed simultaneously. Each assay produced different results: the Bradford's assay (Figure 4-24-A) showing an increase in absorbance for most samples over the first day, and then a progressive decrease, whereas the BCA assay (Figure 4-24-B) showed a very gradual, yet relatively stable, decrease in all samples over the course of each timepoint with nearly identical values for all samples. In converting the absorbance values to total mass of BSA eluted, the Bradford's assay (Figure 4-25-A) suggests that the maximum amount eluted from the majority of samples (Day 1 reading) was approximately 4 mg, whereas the maximum amount detected in the BCA assay (at 5 hours; Figure 4-25-B) was approximately 0.9 mg. The impossibility of 4 mg of BSA being eluted from samples with only 2 mg of BSA being impregnated eliminates the Bradford's assay as being a reliable method of protein quantification for this application. Additionally, the extreme similarity in outputs of all samples as seen with the BCA assay suggests this to be a more reliable assay for this particular assessment. While the results are still somewhat unexpected from a cumulative release perspective, as the quantity of BSA released from the samples declined from approximately 0.9 mg to 0.5 mg over the course of four days, there are possible explanations for this. The initially high BSA concentration was likely due to a burst release of the additive from the gel, a phenomenon commonly seen in drug delivery devices. Additionally, due to the fragility of the hydrogels, they could not be homogenized before retrieving extraneous fluid samples at each timepoint, potentially resulting in lack of access to eluted BSA that settled out of solution at the bottom of the well. It is also possible that the hydrogels initially experienced a burst release of the BSA, but as the gels fragmented and dispersed in the fluid, the fragments re-uptook some of the free-floating BSA. An additional limitation in the set-up of this elution study is the possibility that fluid release from the hydrogel sample contributed to a volume increase of the extraneous fluid, which would have reduced the total calculated concentrations of BSA which were based on the

original 1 mL immersion volume. Although this may have occurred, the effect is expected to be minimal with the hydrogel fluid volumes being only 0.2 mL.

Cumulative Interpretation

From the four trials and varied protein quantification assays performed, it is apparent that the BCA assay is a better mechanism of assessment for this particular application. Why the Bradford's assay consistently produced erroneous results, despite consistent methodology and assessment of samples in a wide range of concentrations, remains to be elucidated. The behavior of the hydrogel even in the most optimal circumstances of Trial 4 and despite the limitations mentioned suggests a suboptimal performance for application in our growth factor-eluting hydrogel. Ideally, when applied *in vivo*, such a product should remain *in situ* for a minimum of one week post-surgery, with elution of additives over that duration and with minimal burst release. The Biogelx products are produced for *in vitro* cell culture conditions, and hence are not manufactured to meet *in vivo* drug delivery specifications. However, in order to confirm the behavior of this hydrogel in more optimal conditions, including in a dynamic environment and using non-cumulative assessment, individual samples could be fabricated for discontinuation at each timepoint, with gels being placed on a rocker at a low setting for set periods of time each day to facilitate fluid flow and being "strained" from their respective wells prior to homogenization of extraneous fluid and subsequent analysis with the BCA assay.

Conclusions & Future Steps

Conclusions

Although there were certainly limitations and quandaries with each individual experiment, collectively several overarching conclusions can be made: PLGA-GO material in proportions of 0.25% to 2% wt. GO can permit cell attachment and growth, without cytotoxic effects, and with neural cell-like differentiation being most evident on iterations imbedded with 0.25% and 0.5% GO; when seeded at a low density, exposure of NSCs to 30 ng/mL of bFGF may lead to inhibition of cell proliferation, but exposure to CNTF in a range of 25 to 50 ng/mL induces greater proliferation than in control samples; and Biogelx hydrogel products demonstrate a burst release

of impregnated protein, which is most accurately quantified with the BCA assay as opposed to the Bradford's assay.

Future Steps

The next requirements in this investigation will be to commence bioprinting iterations of the PLGA-GO material to ensure it can feasibly be printed into the proposed construct shape and at the necessary dimensions; perform additional growth factor experiments with a similar gradient assessment as was performed for CNTF; and to optimize the Biogelx hydrogel product with further experimentation or determine alternative options. Additionally, further characterization of the PLGA-GO material will be imperative in the prediction of its behavior *in vivo*. This includes surface characterization with atomic force microscopy, degradation experiments in hydrated conditions *via* scanning electron microscopy [20], and swell testing to ensure the scaffold lumen does not become constricted when the material is exposed to fluid. With the successful fabrication of a PLGA-GO nerve scaffold, and with thorough characterization, preparations can be made for implantation of the scaffold into a rat sciatic nerve defect model, a reliable archetypal for simulating peripheral nerve injury.

Acknowledgements

Funding for these preliminary experiments was graciously provided through a SEED grant awarded by the Office of Research Engagement at the University of Tennessee, Knoxville. Much thanks is extended to Steven Newby, Lisa Amelse, Madhu Dhar, David Anderson, Stacy Stephenson, Tom Masi, and Andrew Pedersen, for their assistance and advisement in the areas of material fabrication, cell culturing and imaging, prototype planning, and physical/materials chemistry.

References

[1] Kubiak, C.A., Kung, T.A., Brown, D.L., Cederna, P.S., and Kemp, S.W.P., *State-of-the-Art Techniques in Treating Peripheral Nerve Injury.* Plastic and Reconstructive Surgery, 2018. **141**(3): p. 702-710.

[2] NINDS, N.I.o.N.D.a.S. *Peripheral Neuropathy Fact Sheet*. 2018 [cited 2020 October 8]; Available from: https://www.ninds.nih.gov/Disorders/Patient-Caregiver-Education/Fact-Sheets/Peripheral-Neuropathy-Fact-Sheet#3208_1.

[3] Wang, M.L., Rivlin, M., Graham, J.G., and Beredjiklian, P.K., *Peripheral nerve injury, scarring, and recovery.* Connective Tissue Research, 2019. **60**(1): p. 3-9.

[4] Gonzalez-Perez, F., Hernández, J., Heimann, C., Phillips, J.B., Udina, E., and Navarro, X., *Schwann cells and mesenchymal stem cells in laminin- or fibronectin-aligned matrices and regeneration across a critical size defect of 15 mm in the rat sciatic nerve.* Journal of Neurosurgery: Spine, 2018. **28**(1): p. 109-118.

[5] Gaudin, R., Knipfer, C., Henningsen, A., Smeets, R., Heiland, M., and Hadlock, T., *Approaches to Peripheral Nerve Repair: Generations of Biomaterial Conduits Yielding to Replacing Autologous Nerve Grafts in Craniomaxillofacial Surgery.* BioMed Research International, 2016. **2016**: p. 1-18.

[6] Lopez, J., Xin, K., Quan, A., Xiang, S., Leto Barone, A.A., Budihardjo, J., Musavi, L., Mulla, S., Redett, R., Martin, R., Mao, H.-Q., Lee, W.P.A., Ibrahim, Z., and Brandacher, G., *Poly(ε-Caprolactone) Nanofiber Wrap Improves Nerve Regeneration and Functional Outcomes after Delayed Nerve Repair.* Plastic and Reconstructive Surgery, 2019. **144**(1): p. 48e-57e.

[7] Fox, I.K. and Mackinnon, S.E., *Experience with nerve allograft transplantation.* Seminars in plastic surgery, 2007. **21**(4): p. 242-249.

[8] Steiner, R., *Graphene-Based Nanomaterials in the Design of Nerve Wraps for Regenerative Medicine Applications* in *Comparative and Experimental Medicine*. 2019, University of Tennessee, Knoxville: TRACE: Tennessee Research and Creative Exchange. p. 122.

[9] *Poly(D,L-lactide-co-glycolide)*. [cited 2021 Mar 13]; Available from: https://www.sigmaaldrich.com/catalog/product/sigma/p1941?lang=en&region=US.

[10] Bartnikowski, M., Dargaville, T.R., Ivanovski, S., and Hutmacher, D.W., *Degradation mechanisms of polycaprolactone in the context of chemistry, geometry and environment.* Progress in Polymer Science, 2019. **96**: p. 1-20.

[11] Bramini, M., Alberini, G., Colombo, E., Chiacchiaretta, M., Difrancesco, M.L., Maya-Vetencourt, J.F., Maragliano, L., Benfenati, F., and Cesca, F., *Interfacing Graphene-Based Materials With Neural Cells.* Frontiers in Systems Neuroscience, 2018. **12**.

[12] Zhang, Y., Liu, X., Michelson, K., Trivedi, R., Wu, X., Schepp, E., Xing, Y., Darland, D., and Zhao, J.X., *Graphene Oxide-Based Biocompatible 3D Mesh with a Tunable Porosity and Tensility for Cell Culture.* ACS Biomaterials Science & Engineering, 2018.

[13] Zhao, Y., Wang, Y., Niu, C., Zhang, L., Li, G., and Yang, Y., *Construction of polyacrylamide/graphene oxide/gelatin/sodium alginate composite hydrogel with bioactivity for promoting Schwann cells growth.* Journal of Biomedical Materials Research Part A, 2018. **106**(7): p. 1951-1964.

[14] Li, G., Zhao, Y., Zhang, L., Gao, M., Kong, Y., and Yang, Y., *Preparation of graphene oxide/polyacrylamide composite hydrogel and its effect on Schwann cells attachment and proliferation.* Colloids and Surfaces B: Biointerfaces, 2016. **143**: p. 547-556.

[15] Hoffman-Kim, D., Mitchel, J.A., and Bellamkonda, R.V., *Topography, Cell Response, and Nerve Regeneration.* Annual Review of Biomedical Engineering, 2010. **12**(1): p. 203-231.

[16] Griffin, M.F., Malahias, M., Hindocha, S., and Khan, W.S., *Peripheral Nerve Injury: Principles for Repair and Regeneration.* The Open Orthopaedics Journal, 2014. **8**(1): p. 199-203.

[17] *Acrylonitrile Butadiene Styrene (ABS) and its Features*. Available from: https://omnexus.specialchem.com/selection-guide/acrylonitrile-butadiene-styrene-abs-plastic.

[18] Makadia, H.K. and Siegel, S.J., *Poly Lactic-co-Glycolic Acid (PLGA) as Biodegradable Controlled Drug Delivery Carrier.* Polymers, 2011. **3**(3): p. 1377-1397.

[19] Vey, E., Rodger, C., Booth, J., Claybourn, M., Miller, A.F., and Saiani, A., *Degradation kinetics of poly(lactic-co-glycolic) acid block copolymer cast films in phosphate buffer solution as revealed by infrared and Raman spectroscopies.* Polymer Degradation and Stability, 2011. **96**(10): p. 1882-1889.

[20] Park, J.J., Yu, E.J., Lee, W.-K., and Ha, C.-S., *Mechanical properties and degradation studies of poly(D,L-lactide-co-glycolide) 50:50/graphene oxide nanocomposite films.* Polymers for Advanced Technologies, 2014. **25**(1): p. 48-54.

[21] Darestani, M., Entezami, A., Mobedi, H., and Abtahi, M., *Degradation of Poly(D,L-lactide-co-glycolide) 50:50 Implant in Aqueous Medium.* Iran Polym J, 2005. **14**.

[22] Lu, L., Garcia, C.A., and Mikos, A.G., *In vitro degradation of thin poly(DL-lactic-co-glycolic acid) films.* Journal of Biomedical Materials Research, 1999. **46**(2): p. 236-244.

[23] *Dimethyl Sulfoxide (DMSO) (CH3)2SO*. [cited 2021 Mar 13]; Available from: https://www.sigmaaldrich.com/chemistry/solvents/dimethyl-sulfoxide-center.html.

[24] Sargent, B. *DMSO – Cryopreservation Comes With a Cost*. 2011 [cited 2021 Mar 13]; Available from: https://cellculturedish.com/dmso-cryopreservation-comes-with-a-cost/#:~:text=Dimethyl%20sulfoxide%20(DMSO)%20is%20frequently,cells%20during%20the%20freezing%20process.&text=DMSO%20is%20almost%20always%20used%20in%20the%20banking%20of%20cord%20blood%20cells.

[25] Da Violante, G., Zerrouk, N., Richard, I., Provot, G., Chaumeil, J.C., and Arnaud, P., *Evaluation of the Cytotoxicity Effect of Dimethyl Sulfoxide (DMSO) on Caco2/TC7 Colon Tumor Cell Cultures.* Biological and Pharmaceutical Bulletin, 2002. **25**(12): p. 1600-1603.

[26] Hebling, J., Bianchi, L., Basso, F.G., Scheffel, D.L., Soares, D.G., Carrilho, M.R.O., Pashley, D.H., Tjäderhane, L., and De Souza Costa, C.A., *Cytotoxicity of dimethyl sulfoxide (DMSO) in direct contact with odontoblast-like cells.* Dental Materials, 2015. **31**(4): p. 399-405.

[27] De Abreu Costa, L., Henrique Fernandes Ottoni, M., Dos Santos, M., Meireles, A., Gomes De Almeida, V., De Fátima Pereira, W., Alves De Avelar-Freitas, B., and Eustáquio Alvim Brito-Melo, G., *Dimethyl Sulfoxide (DMSO) Decreases Cell Proliferation and TNF-α, IFN-γ, and IL-2 Cytokines Production in Cultures of Peripheral Blood Lymphocytes.* Molecules, 2017. **22**(11): p. 1789.

[28] Montes-Navajas, P., Asenjo, N.G., Santamaría, R., Menéndez, R., Corma, A., and García, H., *Surface Area Measurement of Graphene Oxide in Aqueous Solutions.* Langmuir, 2013. **29**(44): p. 13443-13448.

[29] Newby, S.D., Masi, T., Griffin, C.D., King, W.J., Chipman, A., Stephenson, S., Anderson, D.E., Biris, A.S., Bourdo, S.E., and Dhar, M., * Functionalized Graphene Nanoparticles Induce Human Mesenchymal Stem Cells to Express Distinct Extracellular Matrix Proteins Mediating Osteogenesis *. International Journal of Nanomedicine, 2020. **Volume 15**: p. 2501-2513.

[30] Kaliavaradhan, K., Rukmanikrishnan, B., and Muthusamy, S., *Investigation of the effect of graphene oxide on the properties of epoxy-phthalonitrile nanocomposites.* Advances in Polymer Technology, 2018. **37**(5): p. 1256-1267.

[31] Alghazali, K.M., Newby, S.D., Nima, Z.A., Hamzah, R.N., Watanabe, F., Bourdo, S.E., Masi, T.J., Stephenson, S.M., Anderson, D.E., Dhar, M.S., and Biris, A.S., *Functionalized gold nanorod nanocomposite system to modulate differentiation of human mesenchymal stem cells into neural-like progenitors.* Scientific Reports, 2017. **7**(1).

[32] Adan, A., Kiraz, Y., and Baran, Y., *Cell Proliferation and Cytotoxicity Assays.* Current Pharmaceutical Biotechnology, 2016. **17**(14): p. 1213-1221.

[33] *Cell Viability and Proliferation Assays*. [cited 2021 Mar 5]; Available from: https://www.sigmaaldrich.com/technical-documents/articles/biofiles/cell-viability-and-proliferation.html.

[34] Strober, W., *Trypan blue exclusion test of cell viability.* Curr Protoc Immunol, 2001. **Appendix 3**: p. Appendix 3B.

[35] Ahmed, S.A., Gogal, R.M., Jr., and Walsh, J.E., *A new rapid and simple non-radioactive assay to monitor and determine the proliferation of lymphocytes: an alternative to [3H]thymidine incorporation assay.* J Immunol Methods, 1994. **170**(2): p. 211-24.

[36] Al-Nasiry, S., Geusens, N., Hanssens, M., Luyten, C., and Pijnenborg, R., *The use of Alamar Blue assay for quantitative analysis of viability, migration and invasion of choriocarcinoma cells.* Hum Reprod, 2007. **22**(5): p. 1304-9.

[37] Liao, K.-H., Lin, Y.-S., Macosko, C.W., and Haynes, C.L., *Cytotoxicity of Graphene Oxide and Graphene in Human Erythrocytes and Skin Fibroblasts.* ACS Applied Materials & Interfaces, 2011. **3**(7): p. 2607-2615.

[38] Rai, Y., Pathak, R., Kumari, N., Sah, D.K., Pandey, S., Kalra, N., Soni, R., Dwarakanath, B.S., and Bhatt, A.N., *Mitochondrial biogenesis and metabolic hyperactivation limits the application of MTT assay in the estimation of radiation induced growth inhibition.* Scientific Reports, 2018. **8**(1).

[39] Monteiro-Riviere, N. and Inman, A., *Challenges for assessing carbon nanomaterial toxicity to the skin.* Carbon, 2006. **44**(6): p. 1070-1078.

[40] Wörle-Knirsch, J.M., Pulskamp, K., and Krug, H.F., *Oops They Did It Again! Carbon Nanotubes Hoax Scientists in Viability Assays.* Nano Letters, 2006. **6**(6): p. 1261-1268.

[41] Liao, K.-H., Lin, Y.-S., Macosko, C.W., and Haynes, C.L., *Supporting Information - Cytotoxicity of Graphene Oxide and Graphene in Human Erythrocytes and Skin Fibroblasts.* ACS Applied Materials & Interfaces, 2011. **3**(7): p. 1-12.

[42] Marques, E.P., Zhang, J., Tse, Y.-H., Metcalfe, R.A., Pietro, W.J., and Lever, A.B.P., *Surface electrochemistry of 3-(4,5-dimethylthiazol-2-yl)-2,5-diphenyl-2H-tetrazolium bromide ([MTT]Br) adsorbed on a graphite electrode.* Journal of Electroanalytical Chemistry, 1995. **395**(1-2): p. 133-142.

[43] Boutros, M., Heigwer, F., and Laufer, C., *Microscopy-Based High-Content Screening.* Cell, 2015. **163**(6): p. 1314-1325.

[44] Bruckner, M.Z. *Microscopy*. Microbial Life Educational Resources 2021 Jan 14, 2021; Available from: https://serc.carleton.edu/microbelife/research_methods/microscopy/index.html.

[45] Im, K., Mareninov, S., Diaz, M.F.P., and Yong, W.H., *An Introduction to Performing Immunofluorescence Staining*. 2019, Springer New York. p. 299-311.

[46] Eriksson, J.E., Dechat, T., Grin, B., Helfand, B., Mendez, M., Pallari, H.-M., and Goldman, R.D., *Introducing intermediate filaments: from discovery to disease.* Journal of Clinical Investigation, 2009. **119**(7): p. 1763-1771.

[47] Bogush, T.A., Kaliuzhny, S.A., Basharina, A.A., Grishanina, A.N., Dyakova, Y.B., Bogush, E.A., Kirsanov, V.Y., and Davydov, M.M., *Immunofluorescence Analysis of the Vimentin Expression in Epithelial Cells.* Moscow University Chemistry Bulletin, 2019. **74**(6): p. 290-295.

[48] Ning, H., Lin, G., Lue, T.F., and Lin, C.-S., *Neuron-like differentiation of adipose tissue-derived stromal cells and vascular smooth muscle cells.* Differentiation, 2006. **74**(9-10): p. 510-518.

[49] Blackwood, K.A., Bock, N., Dargaville, T.R., and Ann Woodruff, M., *Scaffolds for Growth Factor Delivery as Applied to Bone Tissue Engineering.* International Journal of Polymer Science, 2012. **2012**: p. 1-25.

[50] Peppas, N.A., Hilt, J.Z., Khademhosseini, A., and Langer, R., *Hydrogels in Biology and Medicine: From Molecular Principles to Bionanotechnology.* Advanced Materials, 2006. **18**(11): p. 1345-1360.

[51] Önger, M.E., Delibaş, B., Türkmen, A.P., Erener, E., Altunkaynak, B.Z., and Kaplan, S., *The role of growth factors in nerve regeneration.* Drug Discoveries & Therapeutics, 2016. **10**(6): p. 285-291.

[52] Landreth, G.E., *Classes of Growth Factors Acting in the Nervous System.*, in *Basic Neurochemistry: Molecular, Cellular, and Medical Aspects*, Siegel, G.J., Agranoff, B.W., Uhler, M.D., Albers, R.W., and Fisher, S.K., Editors. 1999, Lippincott-Raven Publishers: Philadelphia.

[53] Huang, E.J. and Reichardt, L.F., *Neurotrophins: Roles in Neuronal Development and Function.* Annual Review of Neuroscience, 2001. **24**(1): p. 677-736.

[54] Choi, K.-C., Yoo, D.-S., Cho, K.-S., Huh, P.-W., Kim, D.-S., and Park, C.-K., *Effect of Single Growth Factor and Growth Factor Combinations on Differentiation of Neural Stem Cells.* 2008. **44**(6): p. 375.

[55] Lewis, M.E., Neff, N.T., Contreras, P.C., Stong, D.B., Oppenheim, R.W., Grebow, P.E., and Vaught, J.L., *Insulin-like growth factor-I: potential for treatment of motor neuronal disorders.* Exp Neurol, 1993. **124**(1): p. 73-88.

[56] biogelx. *Hydrogel Product Range*. October 2020]; Available from: https://www.biogelx.com/peptide-hydrogel-products-2/.

[57] Kostic, M., Paridaen, J.T.M.L., Long, K.R., Kalebic, N., Langen, B., Grübling, N., Wimberger, P., Kawasaki, H., Namba, T., and Huttner, W.B., *YAP Activity Is Necessary and Sufficient for Basal Progenitor Abundance and Proliferation in the Developing Neocortex.* Cell Reports, 2019. **27**(4): p. 1103-1118.e6.

[58] *Rat Schwann Cells (RSC)*, in *ScienCell Research Laboratories*. ScienCell Research Laboratories, Inc.: https://www.sciencellonline.com/.

[59] Andersen, N.D., Srinivas, S., Piñero, G., and Monje, P.V., *A rapid and versatile method for the isolation, purification and cryogenic storage of Schwann cells from adult rodent nerves.* Scientific Reports, 2016. **6**(1): p. 31781.

[60] Jhaveri, S.J., Hynd, M.R., Dowell-Mesfin, N., Turner, J.N., Shain, W., and Ober, C.K., *Release of Nerve Growth Factor from HEMA Hydrogel-Coated Substrates and Its Effect on the Differentiation of Neural Cells.* 2009. **10**(1): p. 174-183.

[61] Glen, S. *T Test in Excel: Easy Steps with Video*. 2013 [cited 2021 Mar 26]; Available from: https://www.statisticshowto.com/how-to-do-a-t-test-in-excel/.

[62] Sigma, M. *Bovine Serum Albumin*. October 2020]; Available from: https://www.sigmaaldrich.com/catalog/product/sigma/a8531?lang=en&region=US.

[63] Laron, Z., *Insulin-like growth factor 1 (IGF-1): a growth hormone.* Molecular Pathology, 2001. **54**(5): p. 311-316.

[64] Yu, P.-J., Ferrari, G., Galloway, A.C., Mignatti, P., and Pintucci, G., *Basic fibroblast growth factor (FGF-2): The high molecular weight forms come of age.* Journal of Cellular Biochemistry, 2007. **100**(5): p. 1100-1108.

[65] Sigma, M. *Ciliary Neurotrophic Factor human*. October 2020]; Available from: https://www.sigmaaldrich.com/catalog/product/sigma/c3710?lang=en&region=US.

[66] *Overview of Protein Assays Methods*. [cited 2021 Feb. 24]; Available from: https://www.thermofisher.com/us/en/home/life-science/protein-biology/protein-biology-learning-center/protein-biology-resource-library/pierce-protein-methods/overview-protein-assays.html.

[67] *Fluorescence-based Total Protein Determination using the Compound CBQCA* 2001, BioTek. p. 1-4.

[68] *Qubit® Protein Assay Kits*, in *Molecular Probes*. 2015, Thermo Fisher Scientific: Thermo Fisher. p. 1-10.

[69] *EZQ ® Protein Quantitation Kit (R33200)*, in *Molecular Probes*. 2005, Thermo Fisher Scientific: Thermo Fisher. p. 1-4.

[70] *Pierce™ BCA Protein Assay Kit*. [cited 2021 Feb. 24]; Available from: https://www.thermofisher.com/order/catalog/product/23227#/23227.

[71] *Pierce™ Coomassie (Bradford) Protein Assay Kit*. [cited 2021 Feb. 24]; Available from: https://www.thermofisher.com/order/catalog/product/23200?ef_id=Cj0KCQiAj9iBBhCJARIsAE9qRtB-DNdEUterMwnV1_Kj-0z1GvppC9uGrOQOUgDfp-clKATh7wn0up8aAgCiEALw_wcB:G:s&s_kwcid=AL!3652!3!437211904039!b!!g!!&cid=bid_pca_sbu_r01_co_cp1359_pjt0000_bid00000_0se_gaw_dy_pur_con&gclid=Cj0KCQiAj9iBBhCJARIsAE9qRtB-DNdEUterMwnV1_Kj-0z1GvppC9uGrOQOUgDfp-clKATh7wn0up8aAgCiEALw_wcB#/23200?ef_id=Cj0KCQiAj9iBBhCJARIsAE9qRtB-DNdEUterMwnV1_Kj-0z1GvppC9uGrOQOUgDfp-clKATh7wn0up8aAgCiEALw_wcB:G:s&s_kwcid=AL!3652!3!437211904039!b!!g!!&cid=bid_pca_sbu_r01_co_cp1359_pjt0000_bid00000_0se_gaw_dy_pur_con&gclid=Cj0KCQiAj9iBBhCJARIsAE9qRtB-DNdEUterMwnV1_Kj-0z1GvppC9uGrOQOUgDfp-clKATh7wn0up8aAgCiEALw_wcB.

[72] *Quick Start™ Bradford Protein Assay - Instruction Manual*, in *Bio-Rad Laboratories, Inc.*, Bio-Rad Laboratories, Inc.: bio-rad.com.

[73] *Technical Bulletin - Bradford Reagent*, in *Sigma-Aldrich*. Sigma-Aldrich, Inc.: sigma-aldrich.com.

[74] Martz, E., *Bradford Assay for Protein*, in *Microbiology 542, Immunology Lab*, Amherst, U.o.M., Editor., The University of Massachusetts Biology Computer Resource Center: Biology Department, University of Massachusetts Amherst.

[75] *BCA Protein Assay Kit*, in *Pierce*. Thermo Fisher Scientific. p. 1-4.

[76] Bertrand, G.L. *Spectrophotometry*. [cited 2021 Mar 8]; Available from: https://web.mst.edu/~gbert/Color_Lg/spec/Aspec.html.

[77] bababian. *Optical density, absorbance, absorptance*. [cited 2021 Mar 9]; Available from: https://ioptic.wordpress.com/2011/11/01/optical-density-absorbance-absorptance/.

Appendix
Tables & Figures

Table 4-1: Growth Factors Utilized in the Nervous System

Growth Factor Classifications	Growth Factor
Neurotrophins	Nerve growth factor
	Brain-derived neurotrophic factor
	Neurotrophin 3
	Neurotrophin 4 (also called Neurotrophin 5)
	Neurotrophin 6
	Neurotrophin 7
Neurokines	Ciliary neurotrophic factor
	Leukemia inhibitory factor
	Interleukin (IL-6)
	Cardiotrophin 1
Fibroblast growth factors	Fibroblast growth factor-1 (acidic FGF)
	Fibroblast growth factor-2 (basic FGF)
Transforming growth factor β superfamily	Transforming growth factors β
	Bone morphogenetic factors
	Glial-derived neurotrophic factor
	Neurturin
Epidermal growth factor superfamily	Epidermal growth factor
	Transforming growth factor α
	Neuregulins (GGF, ARIA, SMDF, etc.)
Other growth factors	Platelet-derived growth factor
	Insulin-like growth factor I

Table reproduced from Landreth (1999) [1] with information included from Huang & Reichardt (2001) [2].

Table 4-2: Subjective Qualities of Hydrogel Samples

Gel Formula Number	Mass of Hydrogel Powder (mg)	Volume of BSA Solution (mL)	Concentration of Powder (mg/mL)	Quality After Extrusion	Quality After Immersed	Quality After Incubation
3	2.4	0.2	12	Spreads extensively but maintains puddle	Disperses with feathered edge	Disperses
1	2.2	0.15	14.7	Maintains globule form with slight spread	Feathered edge	Shape somewhat maintained; transparent appearance
4	3.4	0.2	17	Slight globule shape maintained with spreading	Maintains shape fairly well	Disperses
2	3.5	0.15	23.3	Globule shape maintained well	Maintains globule shape	Maintains shape well with slight dispersion; opaque appearance

Appearance of gel samples after extrusion, immediately after submersion in extraneous saline, and after incubation are described. Gel samples are arranged in ascending order by concentration.

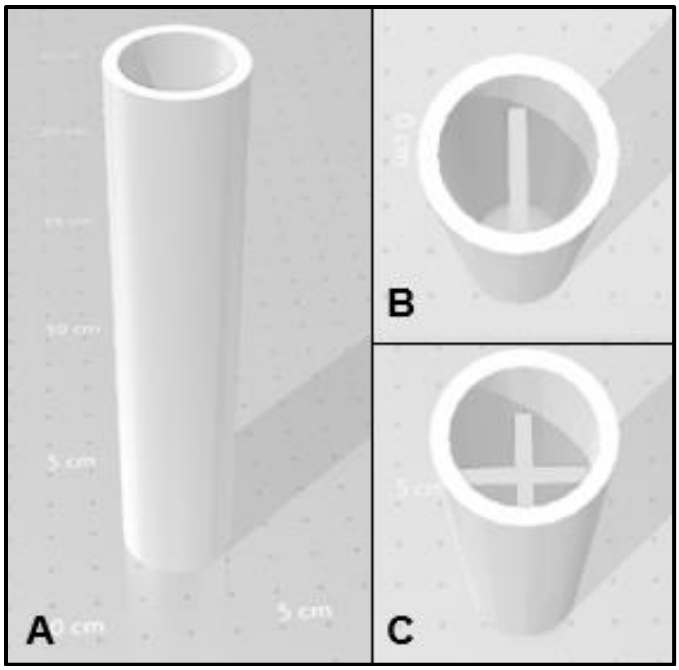


Figure 4-1: CAD images of proposed nerve scaffold constructs

Representative images of potential nerve scaffold designs from various angles: A) exterior view; (B) end-on view of a bi-chambered lumen; (C) end-on view of a quad-chambered lumen.

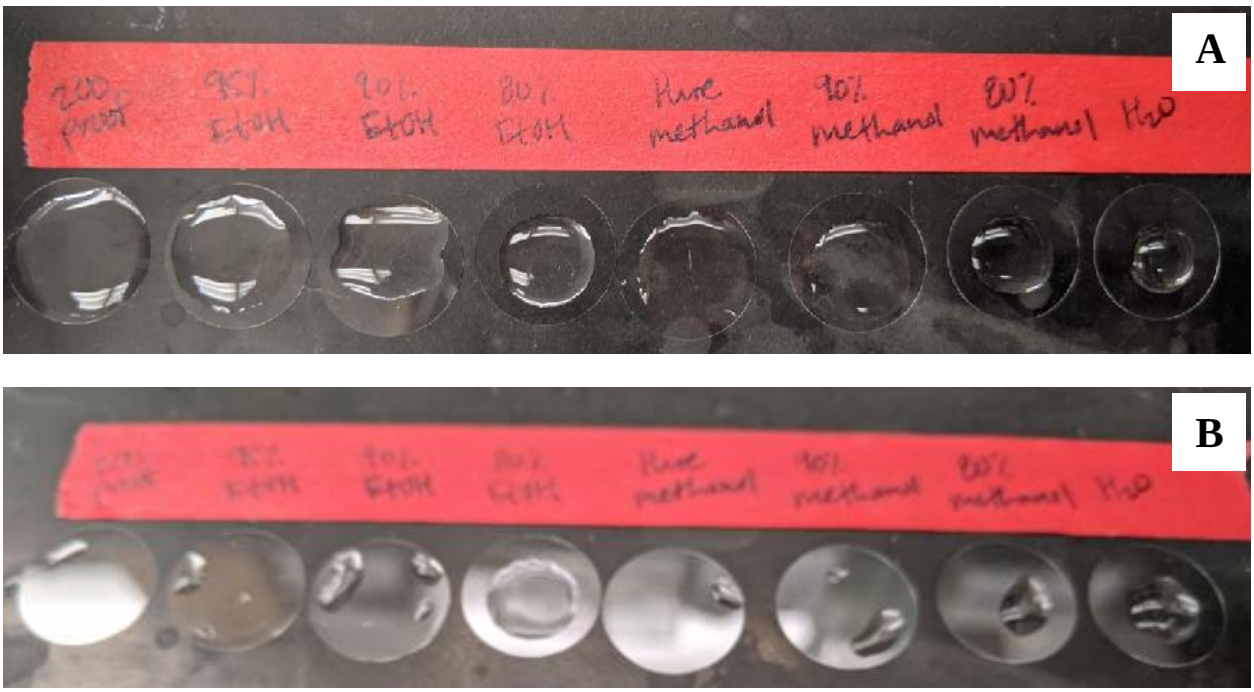


Figure 4-2: Wettability assessment of potential solvents for drop-coating

Solutions of 95%, 90%, and 80% ethanol and 90% and 80% methanol, as well as pure ethanol, methanol, and water, were applied to glass coverslips in 50 µL volumes (A) in order to assess their wettability. Pure ethanol and methanol "wet" the surface the most extensively at first application, and wettability decreased with increased water content. After approximately 15 minutes (B), samples with no or less water demonstrated an evaporative process characterized by island formation.

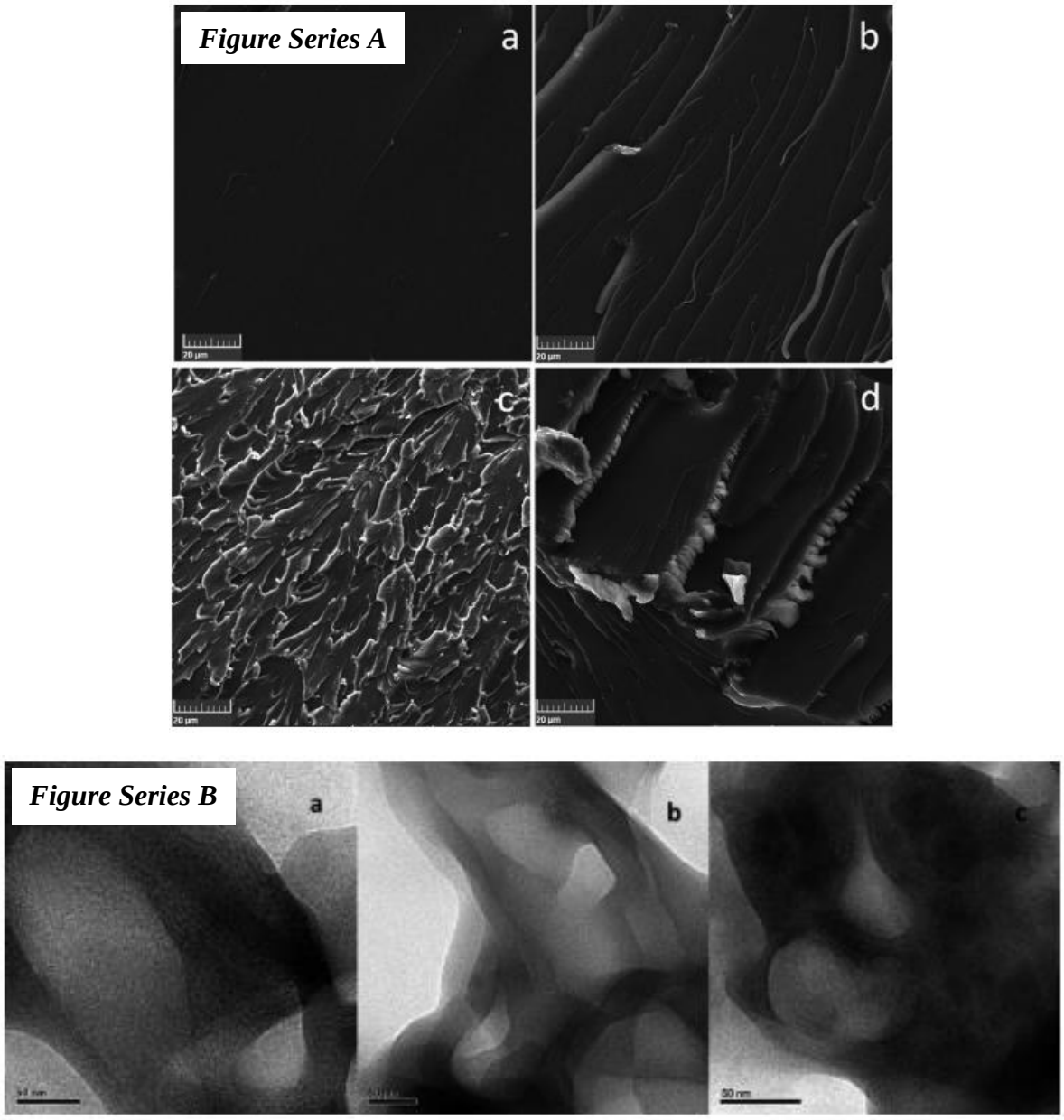


Figure 4-3: SEM and TEM images of polymer-GO composites of varying % wt. GO

Scanning electron microscopy images of epoxy-phthalonitrile-GO composites are depicted in Figure Series A: (a) 0% wt. GO; (b) 1% wt. GO; (c) 3% wt. GO; (d) 5% wt. GO. Transmission electron microscopy images of epoxy-phthalonitrile-GO composites are depicted in Figure Series B: (a) 1% wt. GO; (b) 3% wt. GO; (c) 5% wt. GO. Images are courtesy of Kaliavaradhan, Rukmanikrishnan, & Muthusamy (2018).

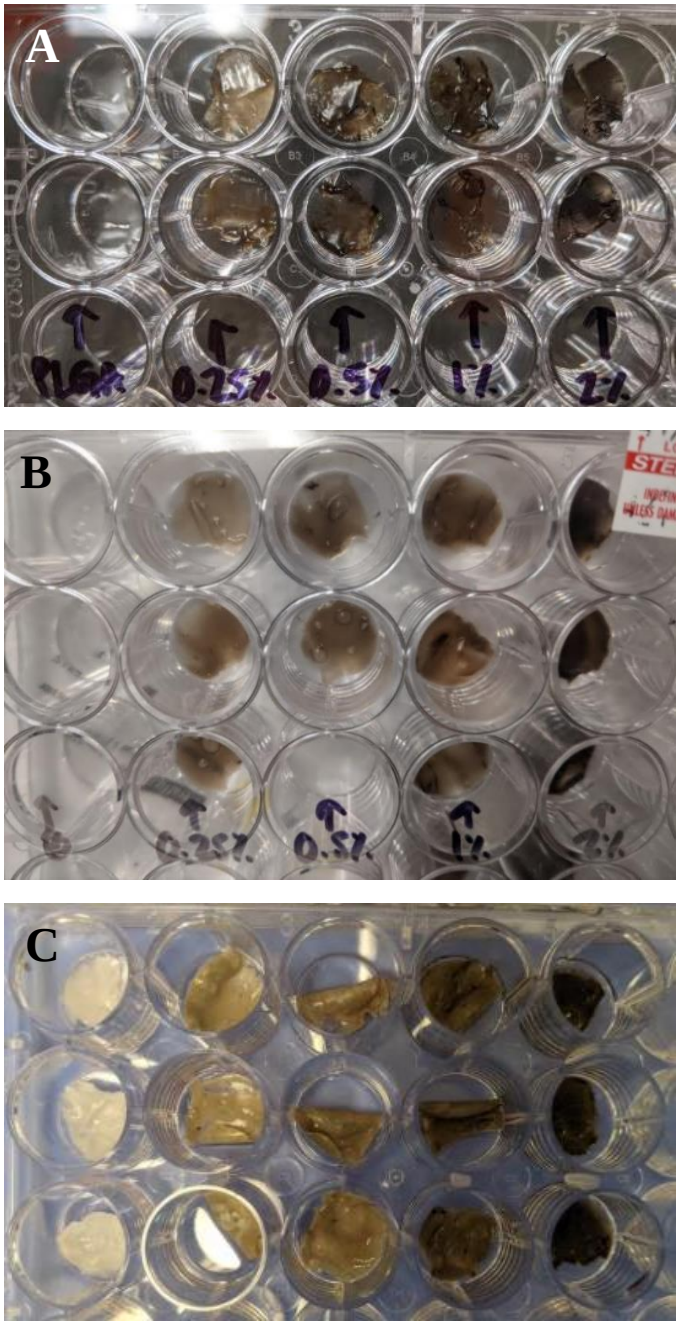


Figure 4-4: Appearance of PLGA-GO smears

Images represent varying conditions of smears: (A) following fabrication; (B) following gas sterilization (note the bubble formation); (C) following exposure to media and incubation (note the rolled and crinkled appearance of a proportion of the samples).

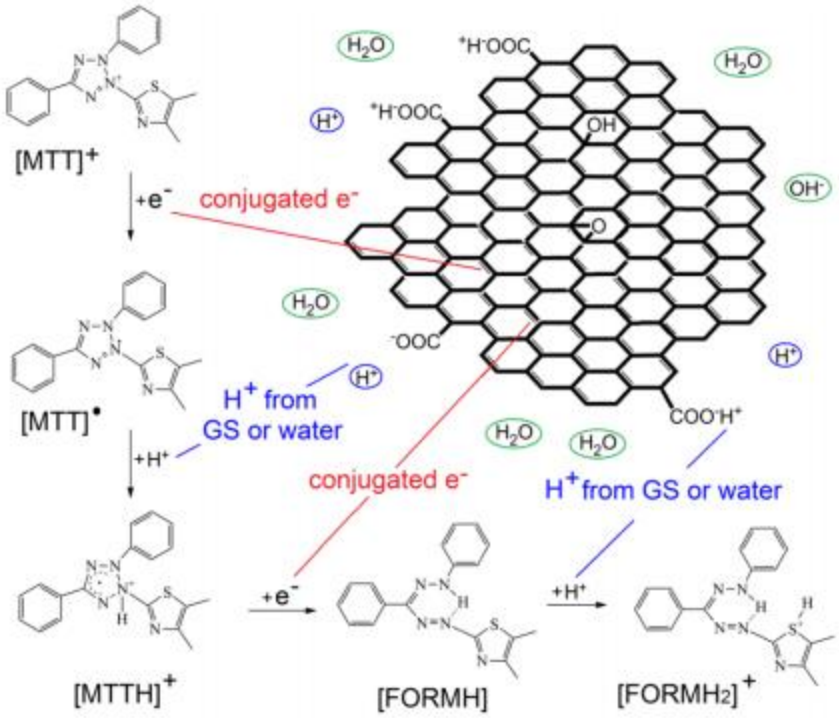
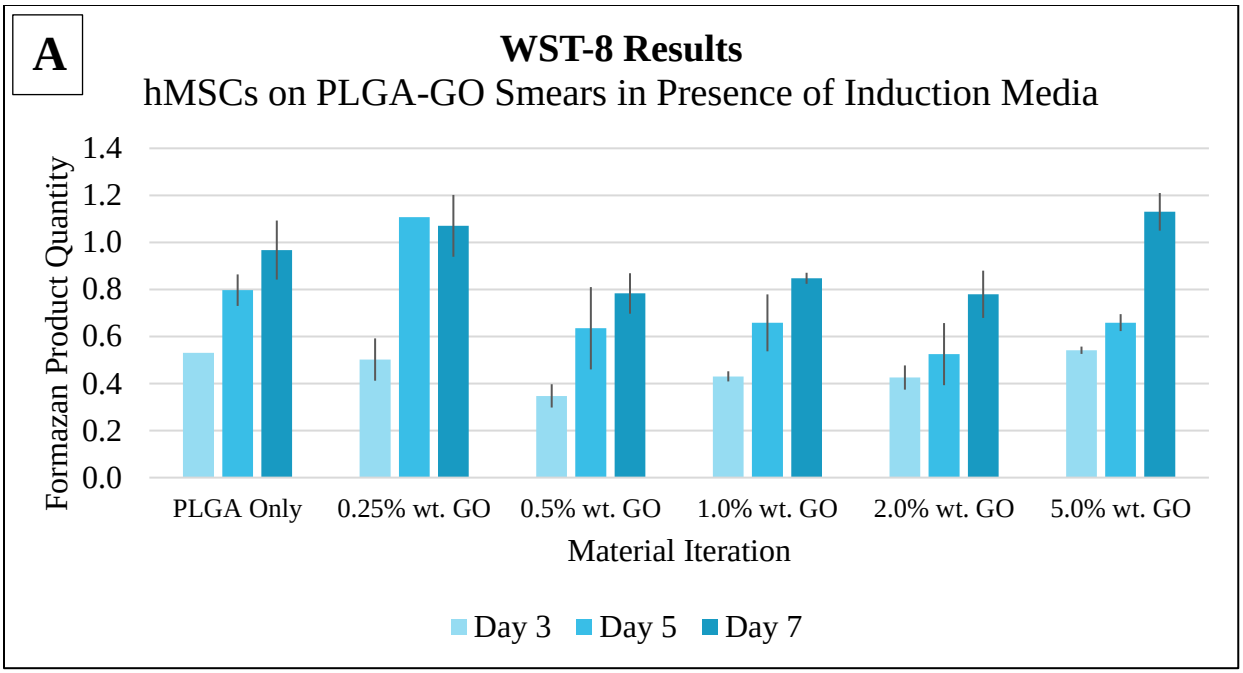


Figure 4-5: Reduction mechanism of MTT assay reagent

Depicted is the mechanism of reduction of the MTT assay reagent in the presence of graphene materials. The MTT cation may undergo reduction from electrons or protons, and a purple formazan product is ultimately produced which confounds cell quantification. Image is courtesy of Liao *et al.* (2011).



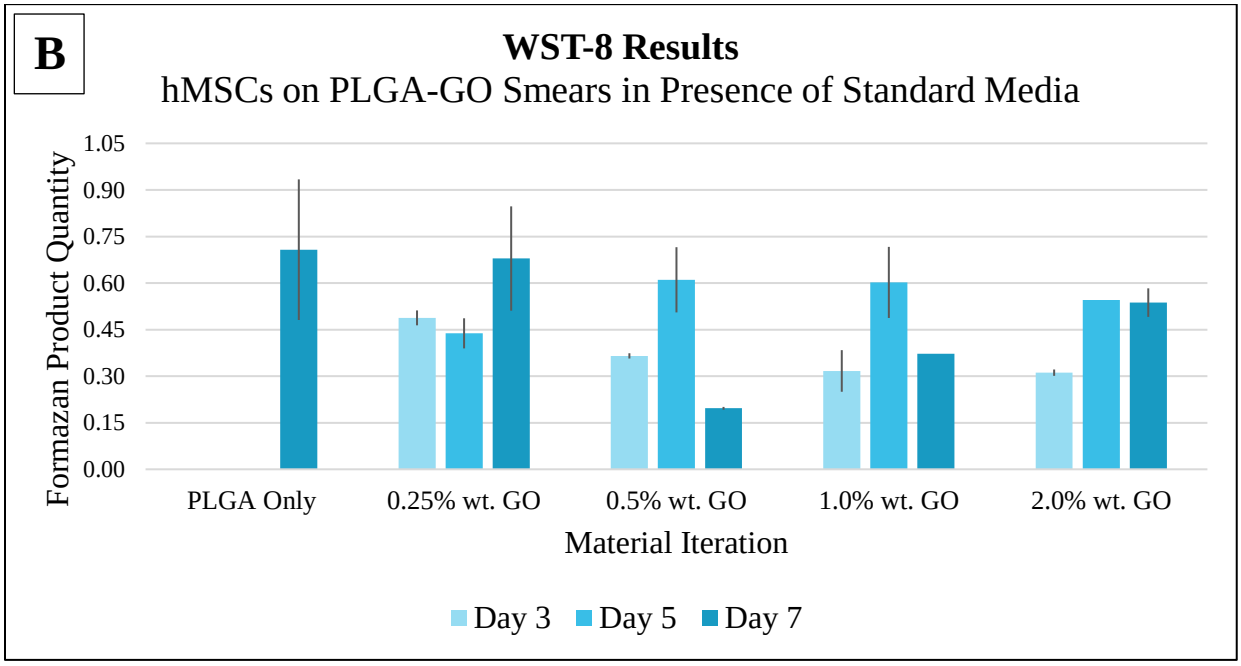


Figure 4-6: WST-8 assay results for PLGA-GO smears

Assay results in (A) reveal that all material iterations are cytocompatible, as evidenced by gradual increase or stability in cell count. Causes of downward trends in cell count of samples in (B) remain to be elucidated. PLGA samples for Days 3 and 5 are absent from (B) due to bubbles in the sample which were unable to be eliminated and which confounded absorbance readings.

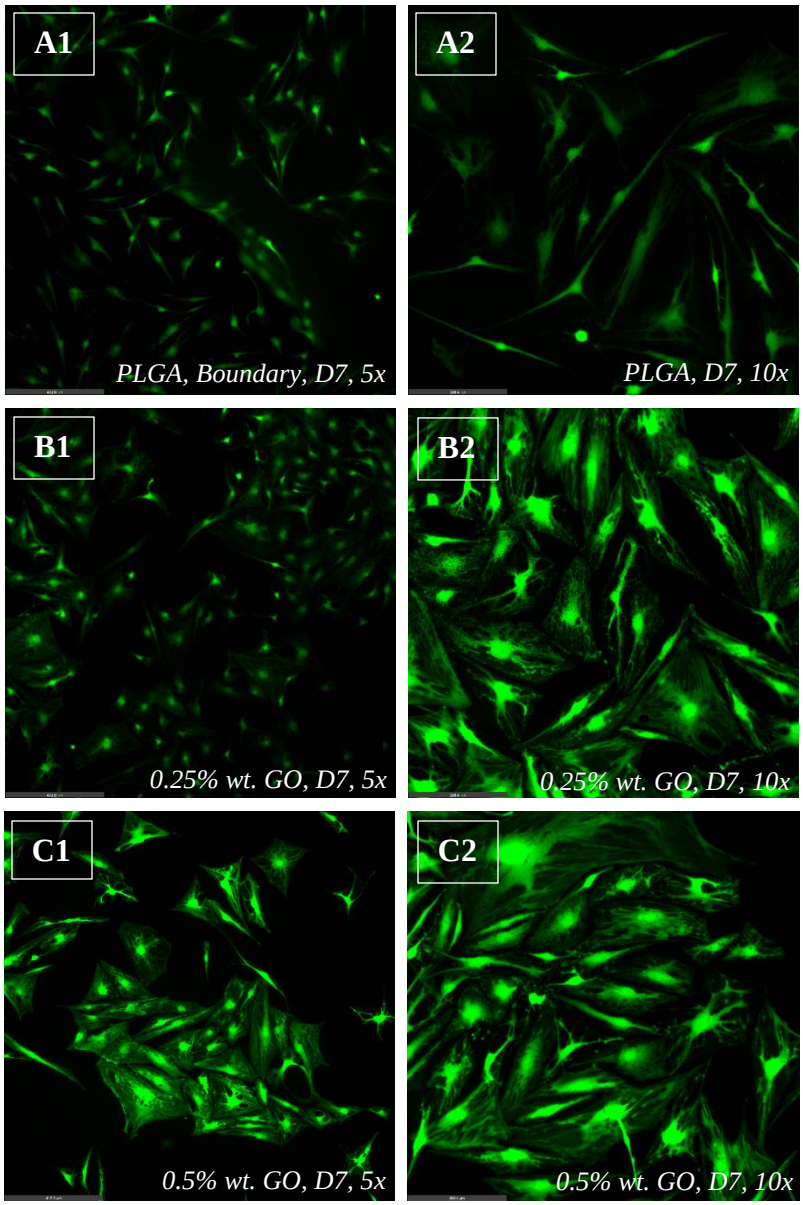


Figure 4-7: Day 7 CAM images of PLGA-GO composites exposed to neuroinduction media

Figure continued on following page; Samples in respect to the material to which hMSCs were applied to are as follows: (A) PLGA only; (B) 0.25% wt. GO; (C) 0.5% wt. GO; (D) 1% wt. GO; (E) 2% wt. GO; (F) 5% wt. GO. All images depict cells on material unless otherwise noted. Individual image captions denote the magnification represented.

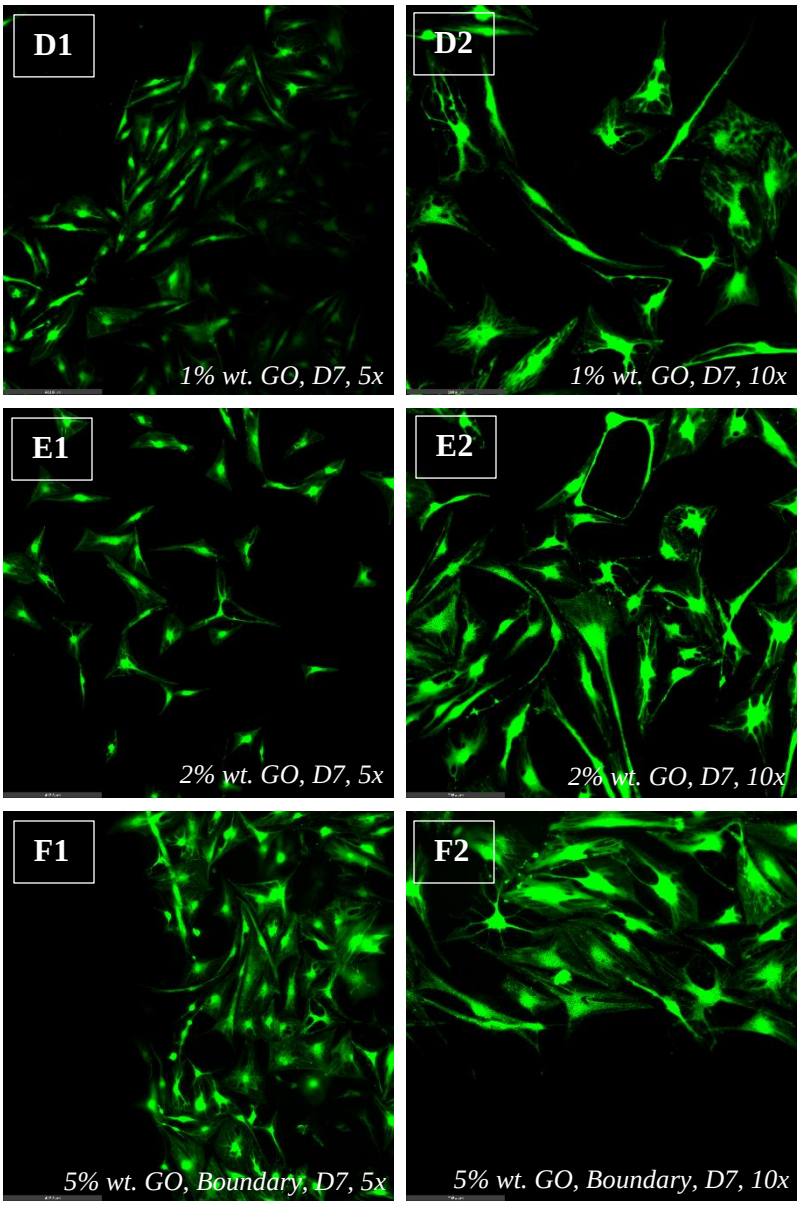


Figure 4-7 (*continued*)

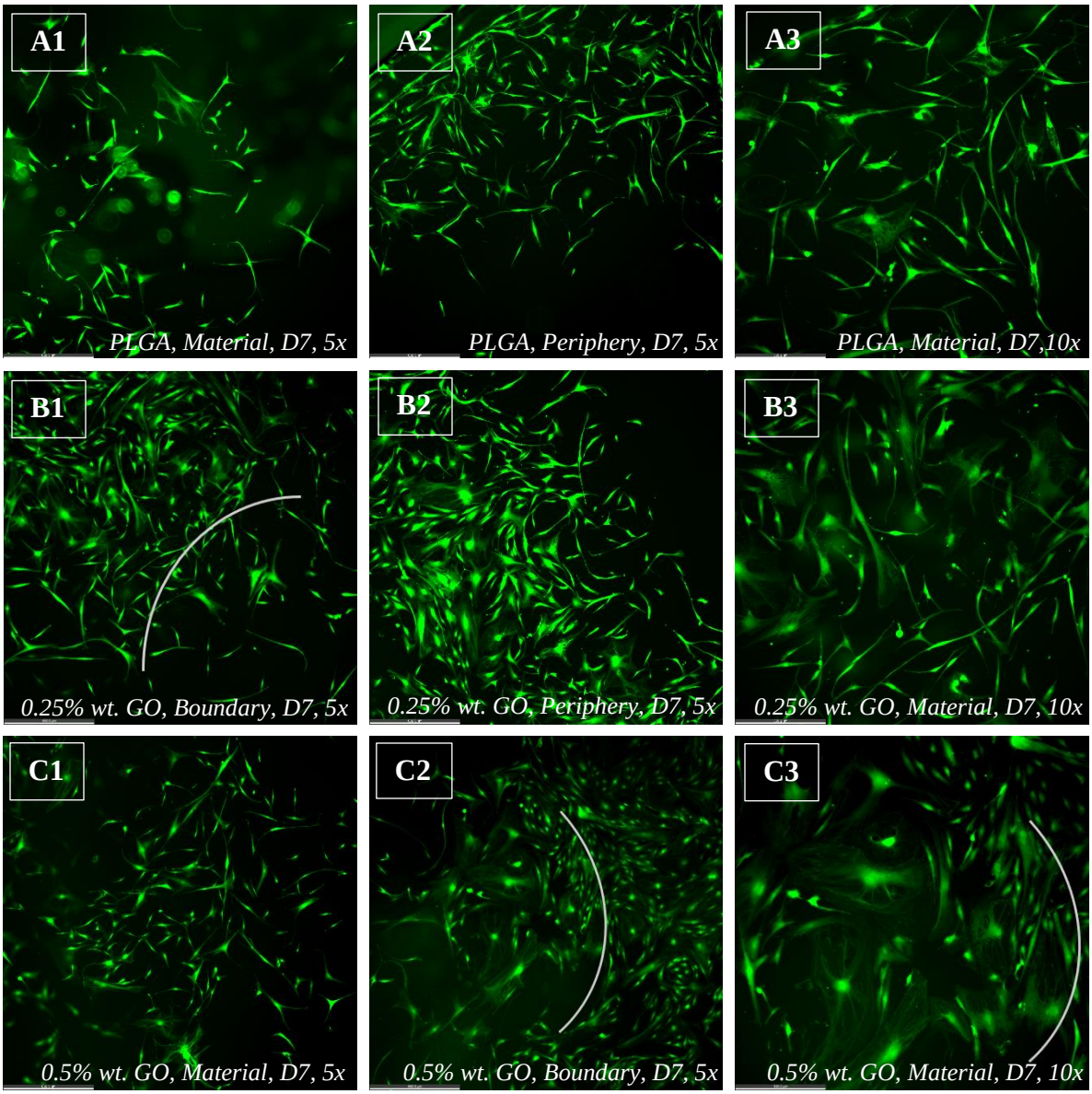


Figure 4-8: Day 7 CAM images of PLGA-GO composites exposed to standard media

Figure continued on following page; Samples in respect to the material to which hMSCs were applied to are as follows: (A) PLGA only; (B) 0.25% wt. GO; (C) 0.5% wt. GO; (D) 1% wt. GO; (E) 2% wt. GO. Individual image captions denote the magnification and the particular surface represented, whether of the material, peripheral to the material on the glass coverslip, or at the boundary between material and glass coverslip. Semi-circular lines in some images approximate this boundary, when applicable.

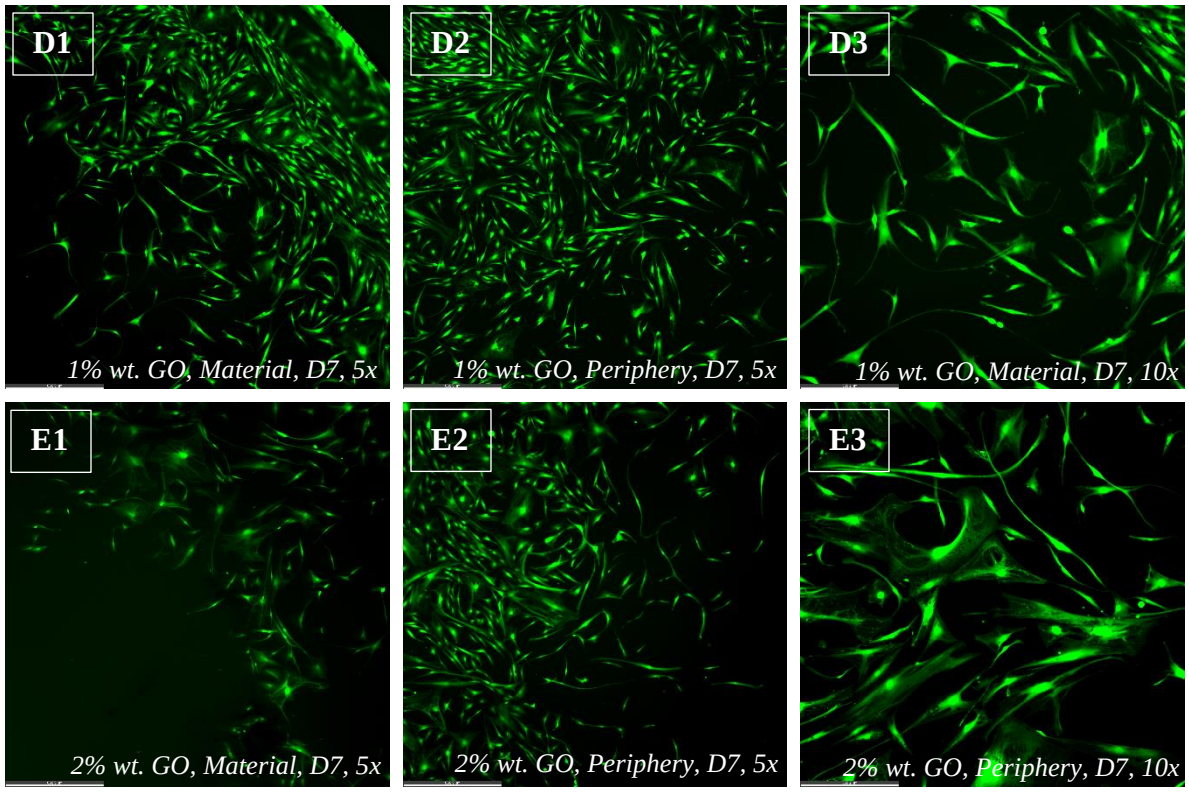


Figure 4-8 (*continued*)

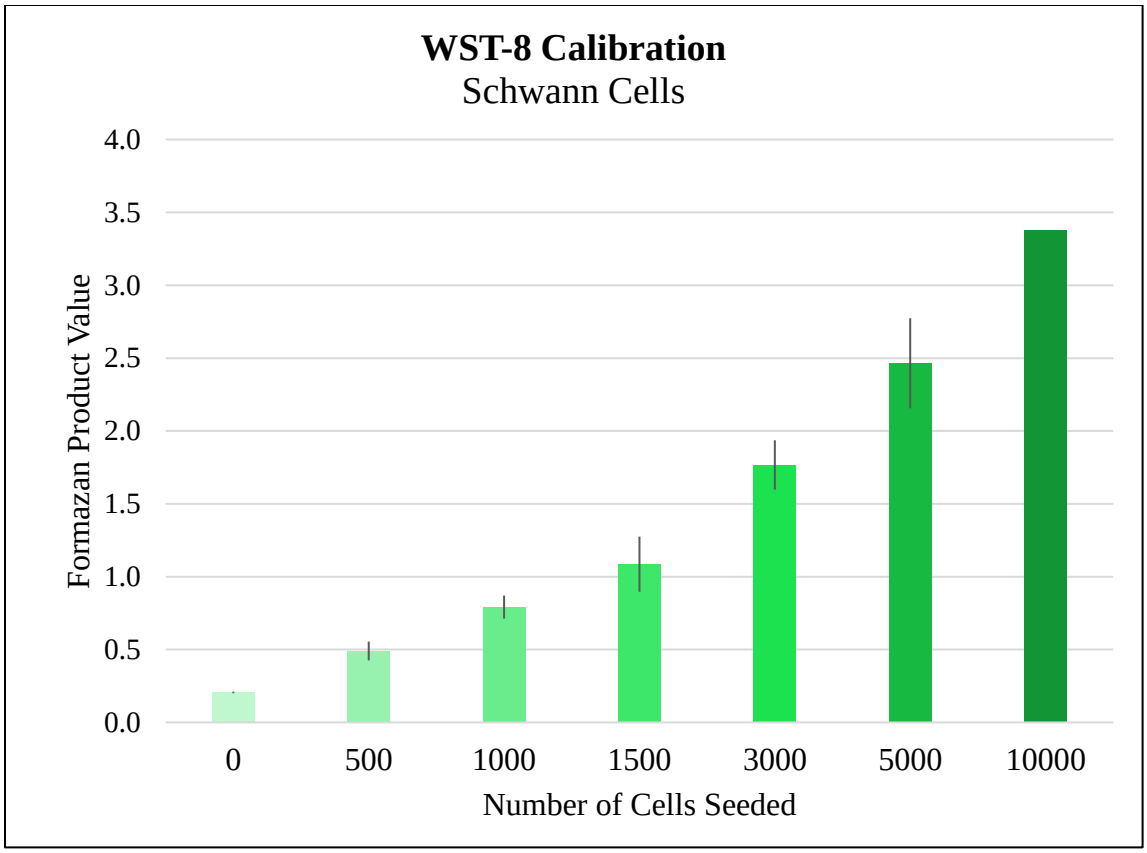


Figure 4-9: WST-8 calibration with Schwann cells

Cells were seeded in samples ranging from 0 to 10,000 cells per well. WST-8 assays were performed in a standard protocol and absorbance read at 450 nm. Results are depicted in the above bar graph with standard deviations. "Formazan product value" is translatable to the absorbance output.

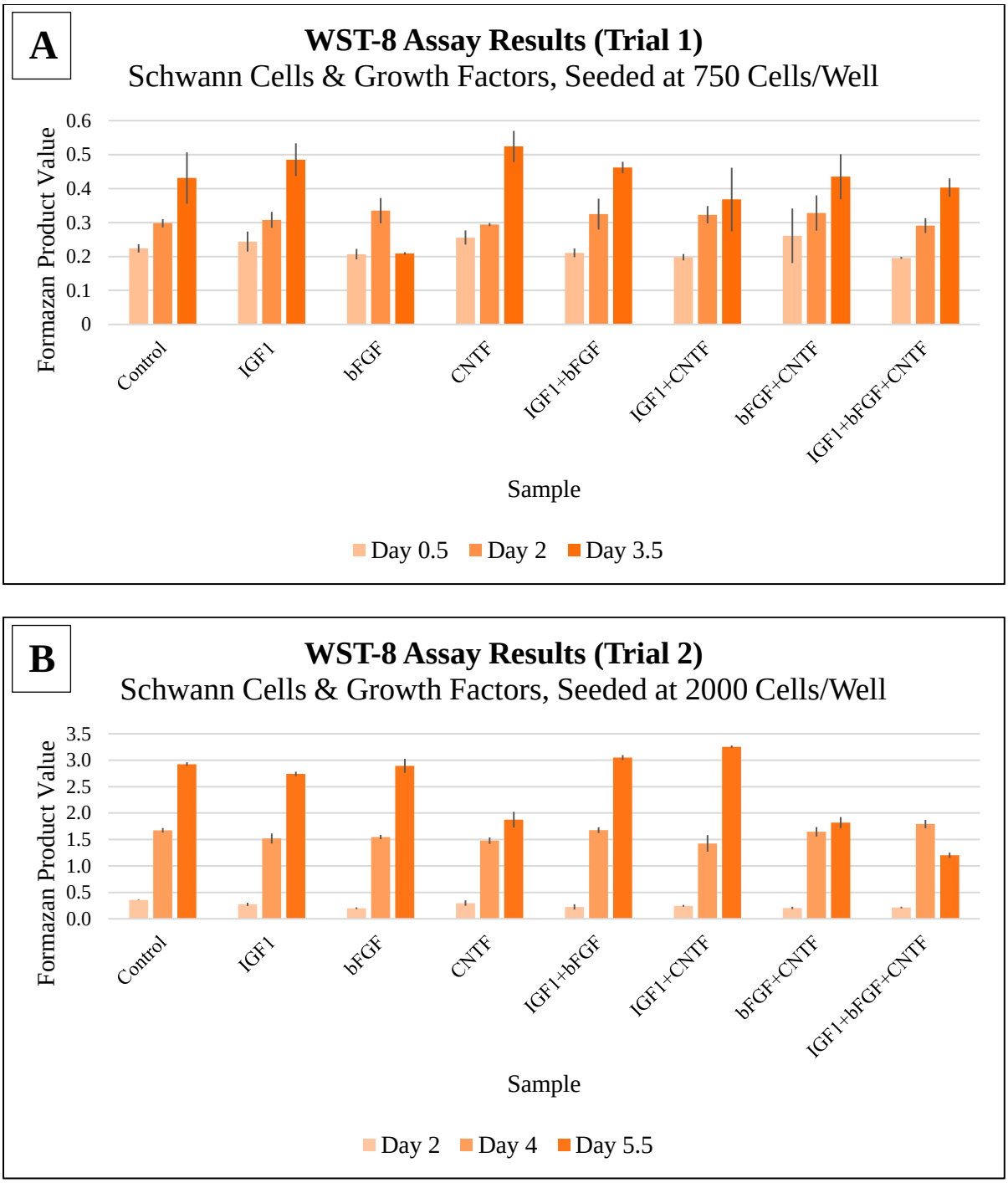


Figure 4-10: WST-8 assay results for growth factor experiments

When NSC density is low (A), 30 ng/mL bFGF and 10 ng/mL each of IGF-I, bFGF, and CNTF result in an inhibitory effects, with all other combinations producing comparable results to controls. Results in (B) at the final timepoint are confounded by extreme confluency of cells.

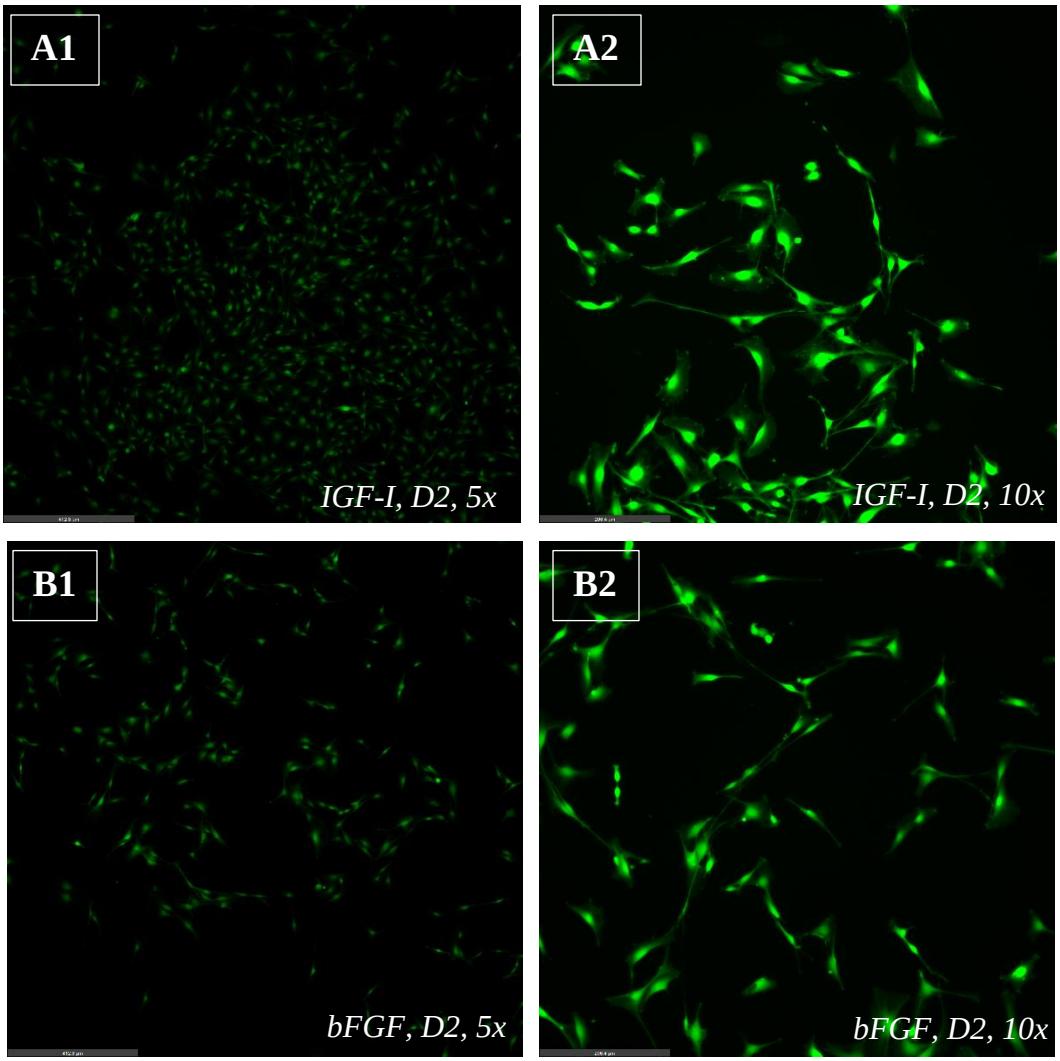


Figure 4-11: Day 2 CAM images of NSCs (750 cells/well), exposed to growth factors

Figure continued on following two pages; Representative images of Day 2 timepoint NSC samples, initially seeded at 750 cells/well, and exposed to growth factors. Images with "1" are taken at 5x magnification, and images at "2" are taken at 10x. Day 2 samples are represented rather than the final timepoint (Day 3.5) due to abnormalities in the samples of the Day 3.5 CAM well plate. Samples in respect to exposure to growth factors are as follows: (A) 30 ng/mL IGF-I, (B) 30 ng/mL bFGF, (C) 30 ng/mL CNTF, (D) 15 ng/mL IGF-I and 15 ng/mL bFGF, (E) 15 ng/mL IGF-I and 15 ng/mL CNTF, (F) 15 ng/mL bFGF and 15 ng/mL CNTF, (G) 10 ng/mL IGF-I, 10 ng/mL bFGF, and 10 ng/mL CNTF, (H) Control (no growth factors).

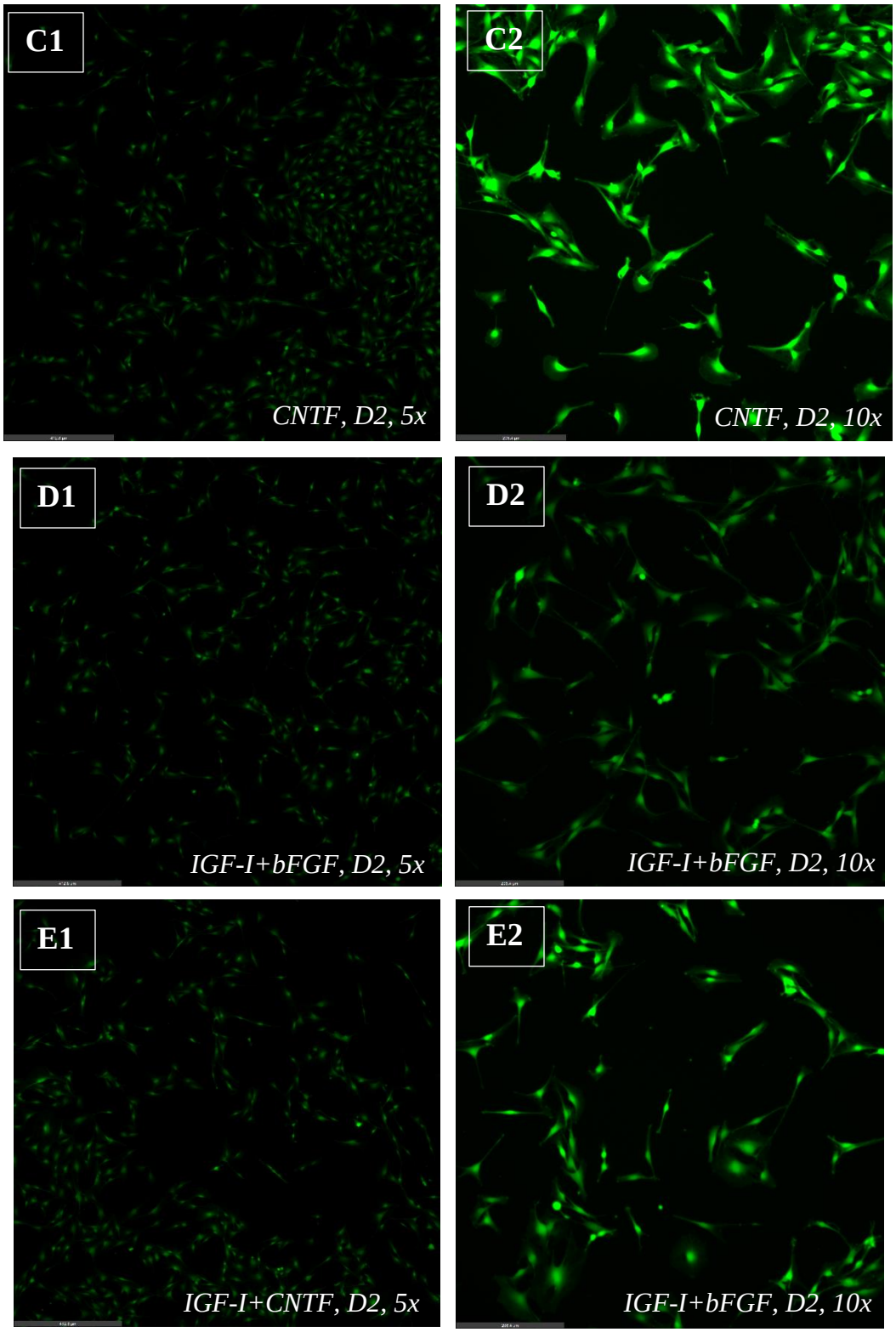


Figure 4-11 (*continued*)

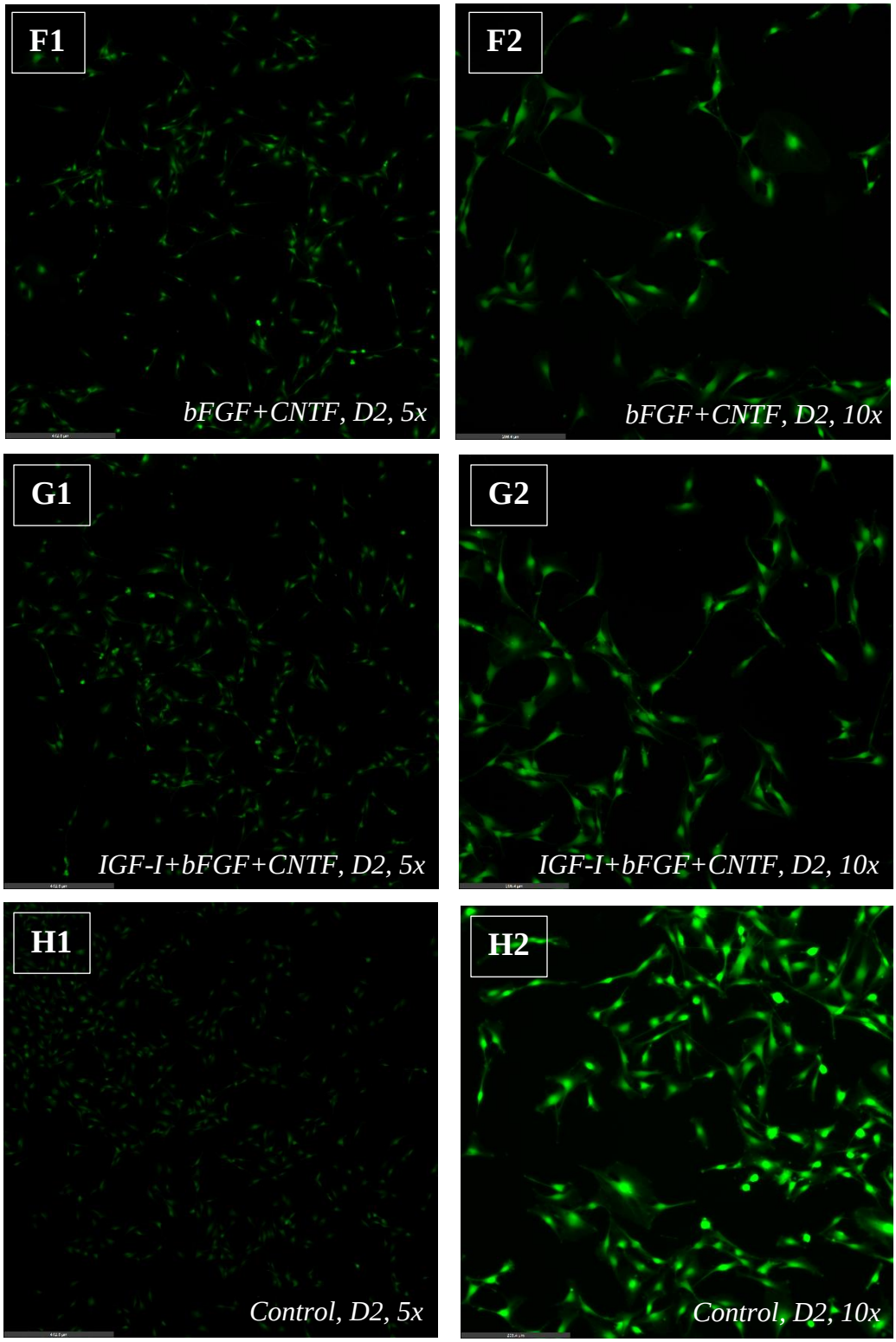


Figure 4-11 (*continued*)

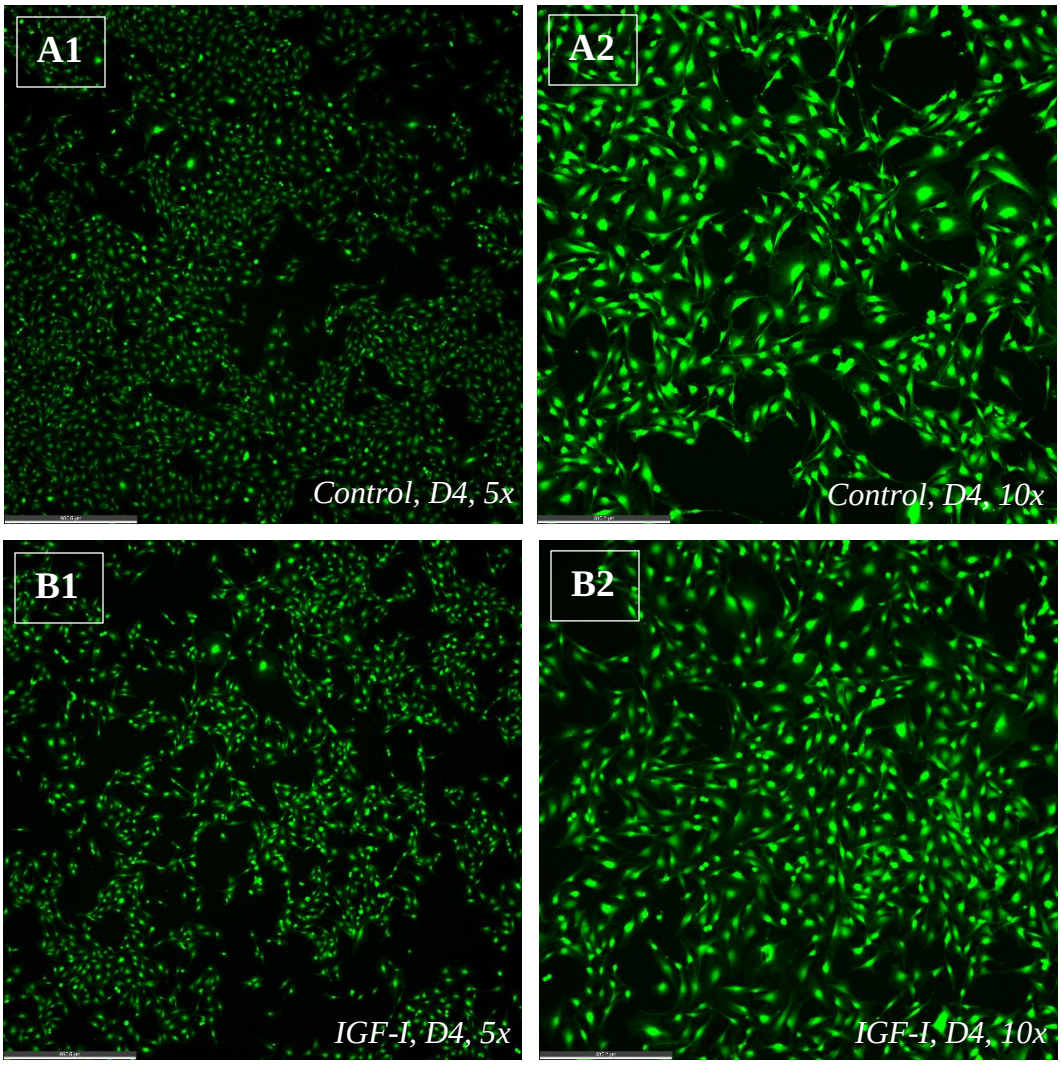


Figure 4-12: Day 4 CAM images of NSCs (2000 cells/well), exposed to growth factors

Figure continued on following two pages; Representative images of Day 4 timepoint NSC samples, initially seeded at 2000 cells/well, exposed to growth factors. Images with "1" are taken at 5x magnification, and images at "2" are taken at 10x. Day 4 is represented rather than the final timepoint (Day 5.5) due to extreme confluency of cells limiting sufficient visualization of cell morphology. Samples in respect to exposure to growth factors are as follows: (A) Control (no growth factors), (B) 30 ng/mL IGF-I, (C) 30 ng/mL bFGF, (D) 30 ng/mL CNTF, (E) 15 ng/mL IGF-I and 15 ng/mL bFGF, (F) 15 ng/mL IGF-I and 15 ng/mL CNTF, (G) 15 ng/mL bFGF and 15 ng/mL CNTF, and (H) 10 ng/mL IGF-I, 10 ng/mL bFGF, and 10 ng/mL CNTF.

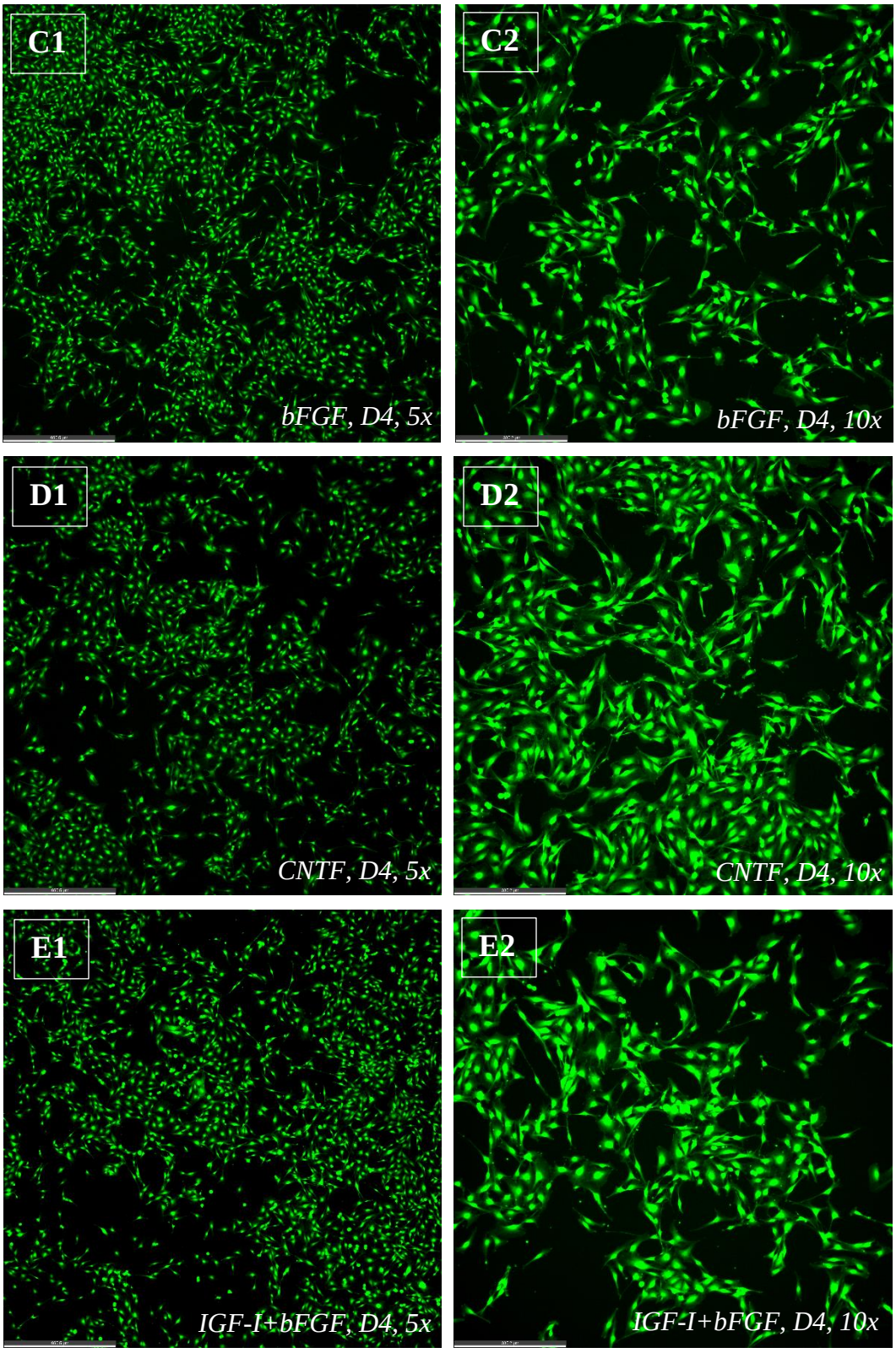


Figure 4-12 (*continued*)

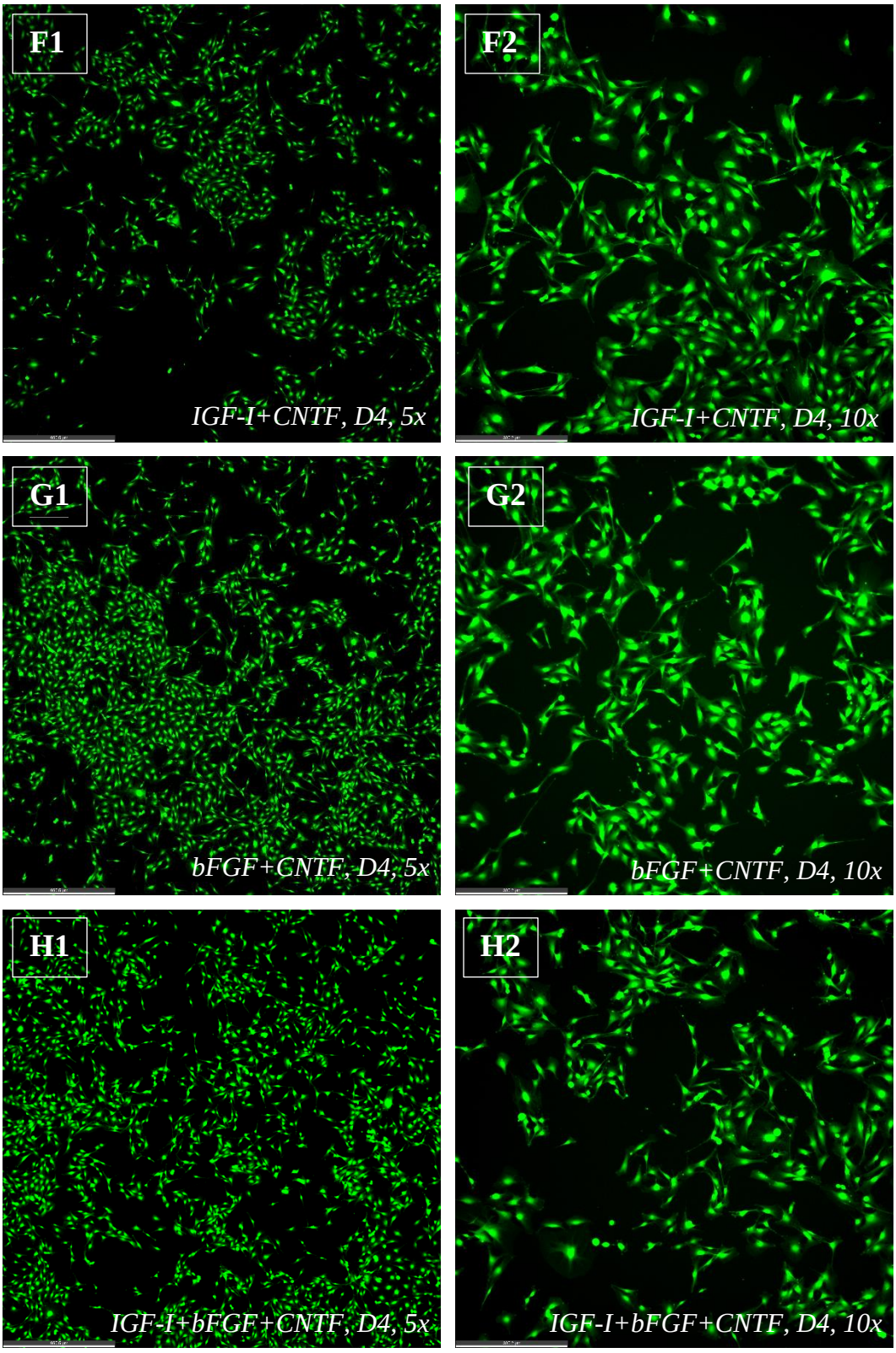


Figure 4-12 (*continued*)

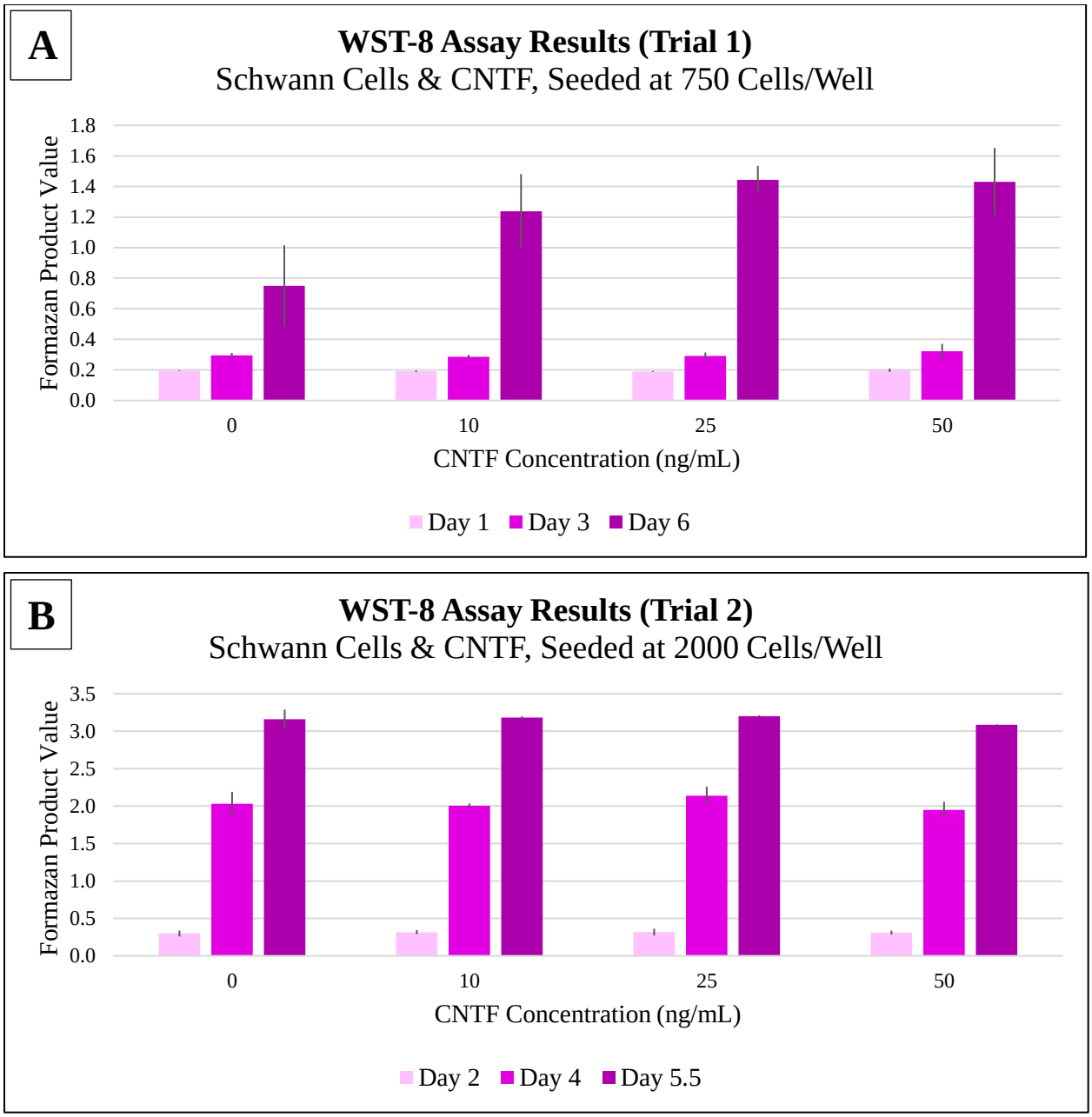


Figure 4-13: WST-8 assay results for CNTF concentration gradient experiments

WST-8 assays of NSCs exposed to CNTF in concentrations ranging from 10 to 50 ng/mL reveal that at a low cell seeding density (A), CNTF appears to enhance cell proliferation at any of the evaluated concentrations compared to control samples, whereas at a higher cell seeding density (B), there is no clear benefit in the addition of CNTF.

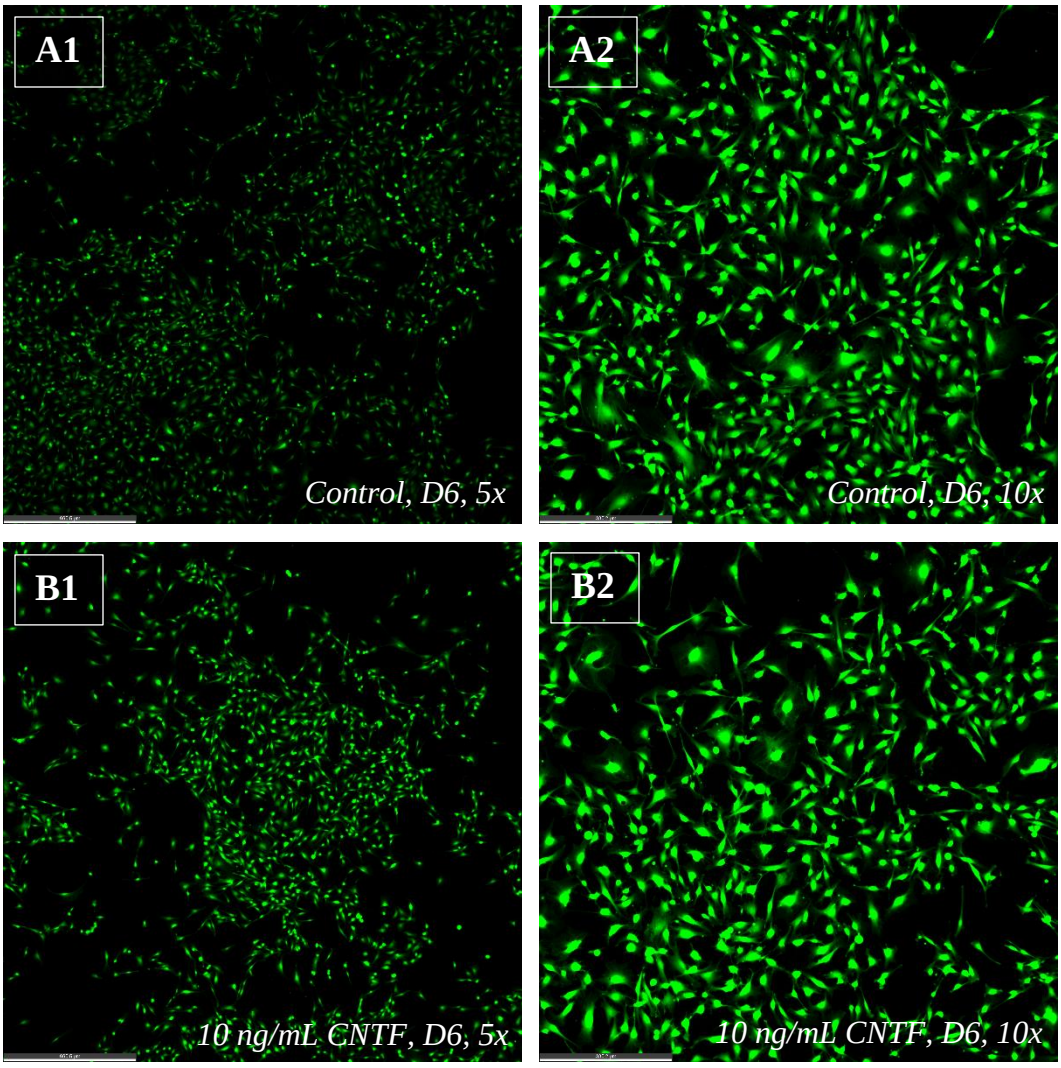


Figure 4-14: Day 6 CAM images of NSCs (seeded at 750 cells/well), exposed to CNTF

Figure continued on following page; Representative images of the Day 6 timepoint NSC samples, initially seeded at 750 cells/well, exposed to CNTF in varying concentrations. Images with "1" are taken at 5x magnification, and images at "2" are taken at 10x. Samples in respect to exposure to growth factors are as follows: (A) control (no growth factor), (B) 10 ng/mL CNTF, (C) 25 ng/mL CNTF, (D) 50 ng/mL.

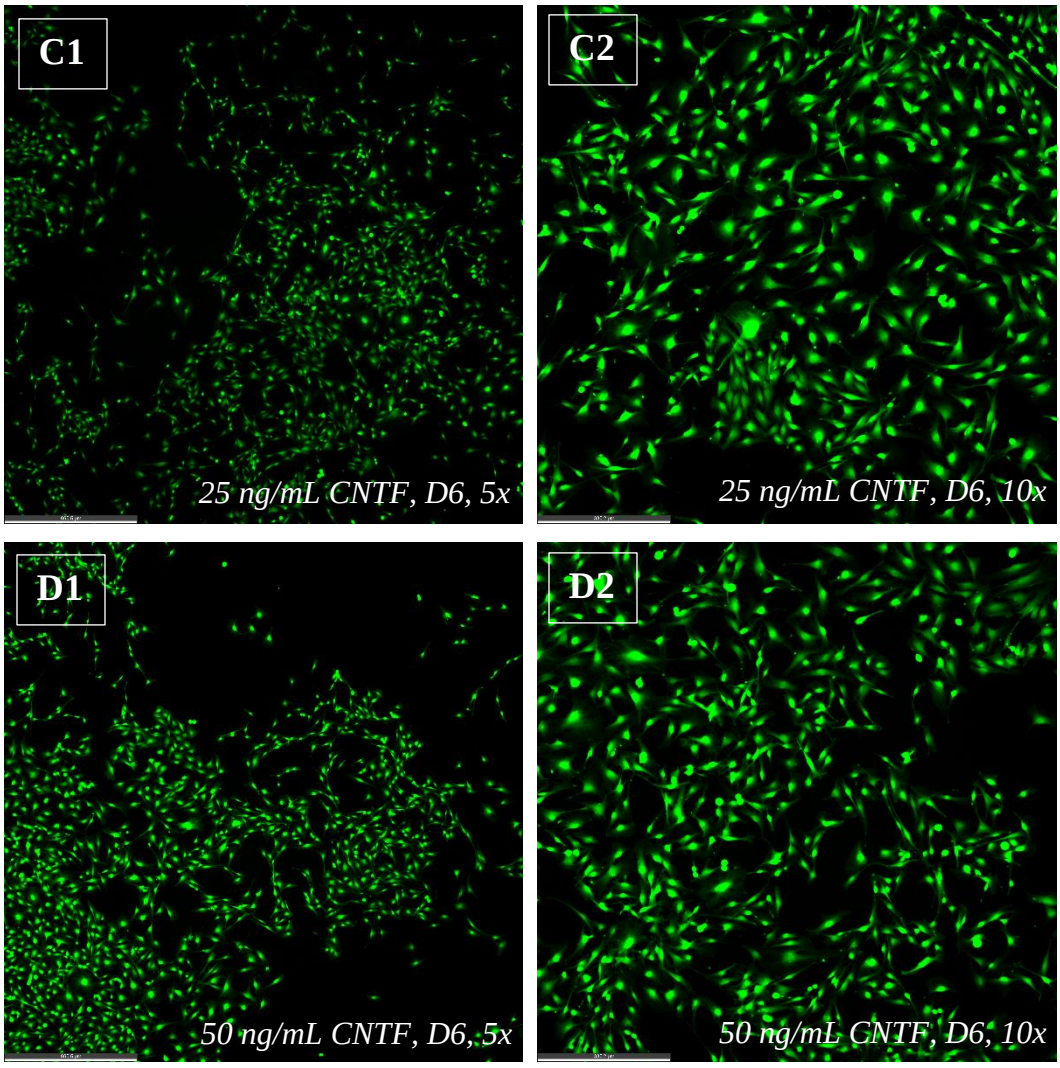


Figure 4-14 (*continued*)

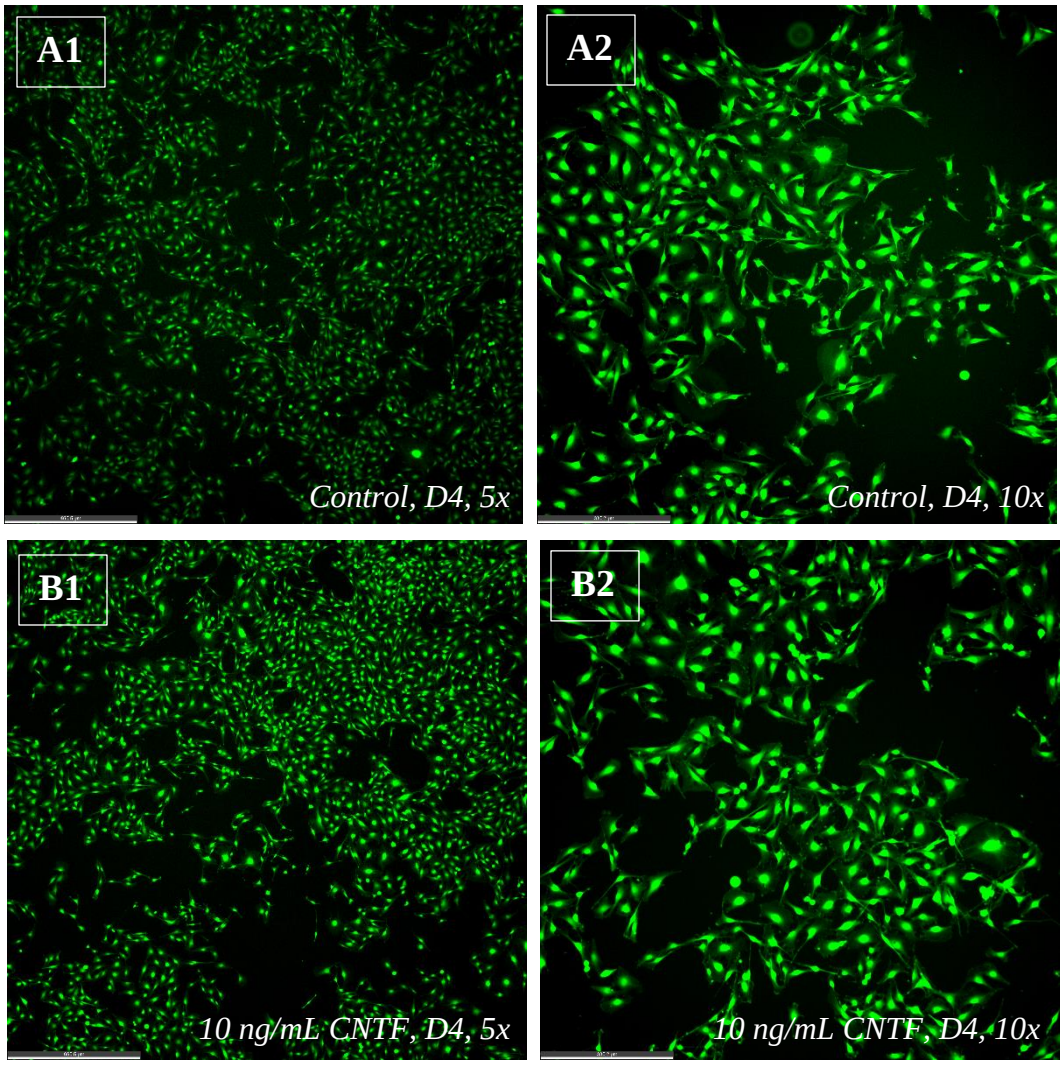


Figure 4-15: Day 4 CAM images of NSCs (seeded at 2000 cells/well), exposed to CNTF

Figure continued on following page; Representative images of the Day 4 timepoint NSC samples, initially seeded at 2000 cells/well, exposed to CNTF in varying concentrations. Day 4 images are represented rather than the final timepoint (Day 5.5) due to extreme confluency of cells impeding visualization of cell morphology. Images with "1" are taken at 5x magnification, and images at "2" are taken at 10x. Samples in respect to exposure to growth factors are as follows: (A) control (no growth factor), (B) 10 ng/mL CNTF, (C) 25 ng/mL CNTF, (D) 50 ng/mL.

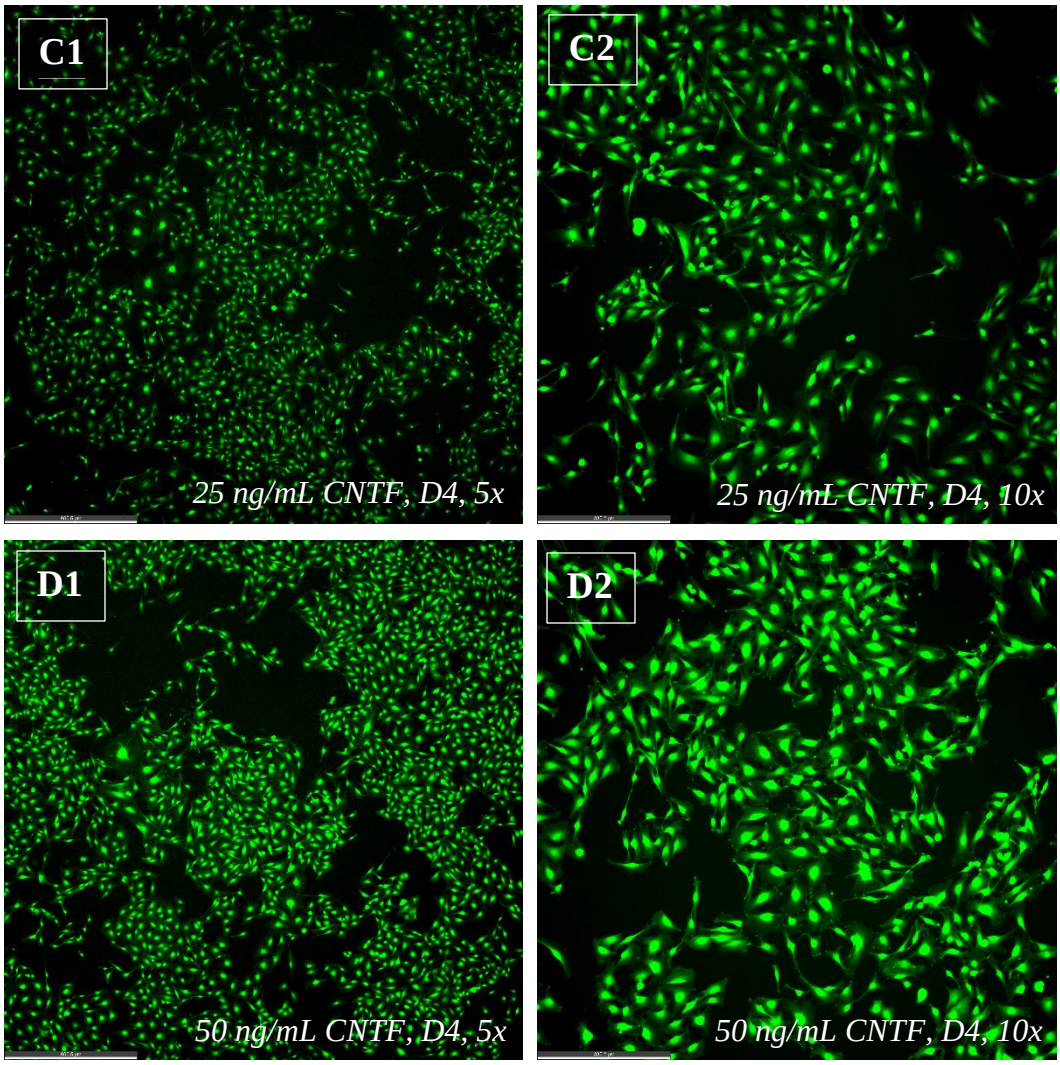


Figure 4-15 (*continued*)

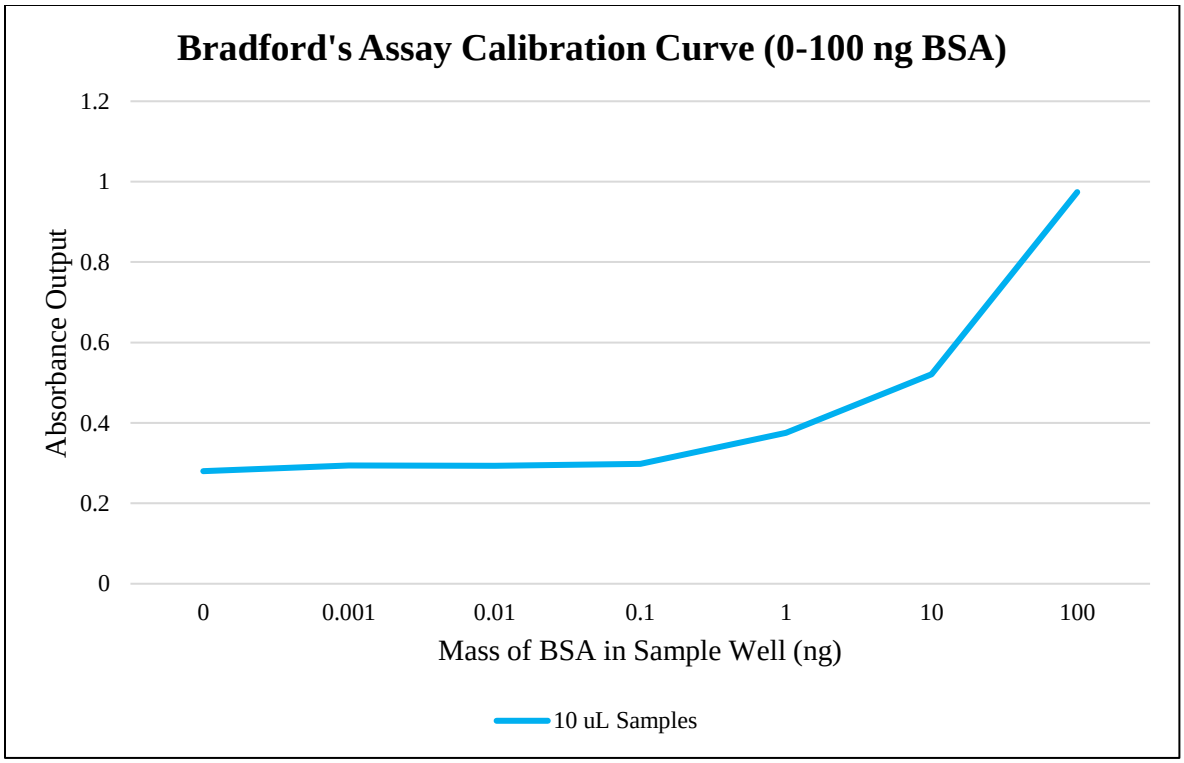


Figure 4-16: Bradford's assay initial calibration data

Calibration curve depicted for a Bradford's assay performed with samples ranging from 0 to 100 ng of BSA. It is apparent that the assay is insensitive to quantities of BSA below 0.1 ng.

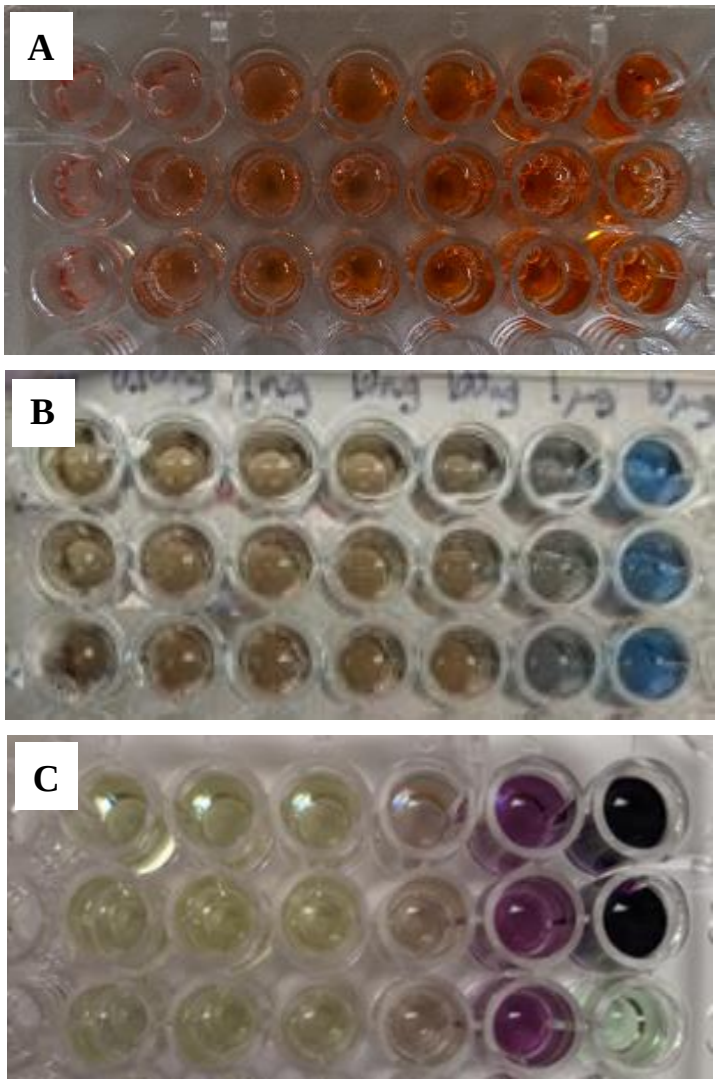


Figure 4-17: Appearances of colorimetric assays

Example images of colorimetric assay calibration plates: (A) WST-8 assay; (B) Bradford's assay; (C) BCA assay.

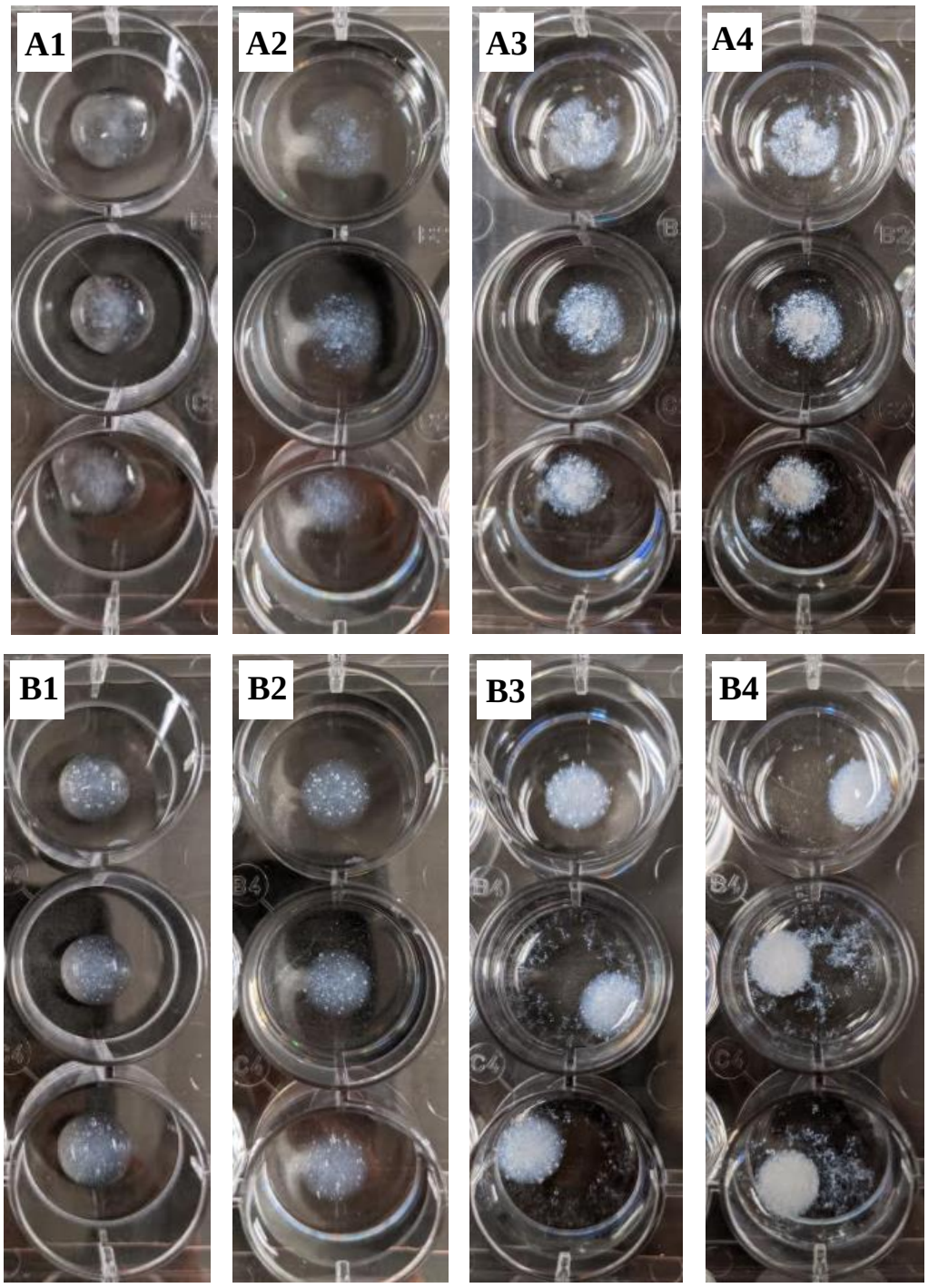


Figure 4-18: Appearances of Gel Forumla 1 and 2 in varying conditions

Hydrogel samples in the "A" series correspond to Gel Formula 1 replicates, whereas samples in the "B" series correspond to Gel Formula 2 replicates. Timepoint "1" is immediately after extrusion into wells; "2" after addition of extraneous saline to wells; "3" at approximately 4 hours; and "4" at two days.

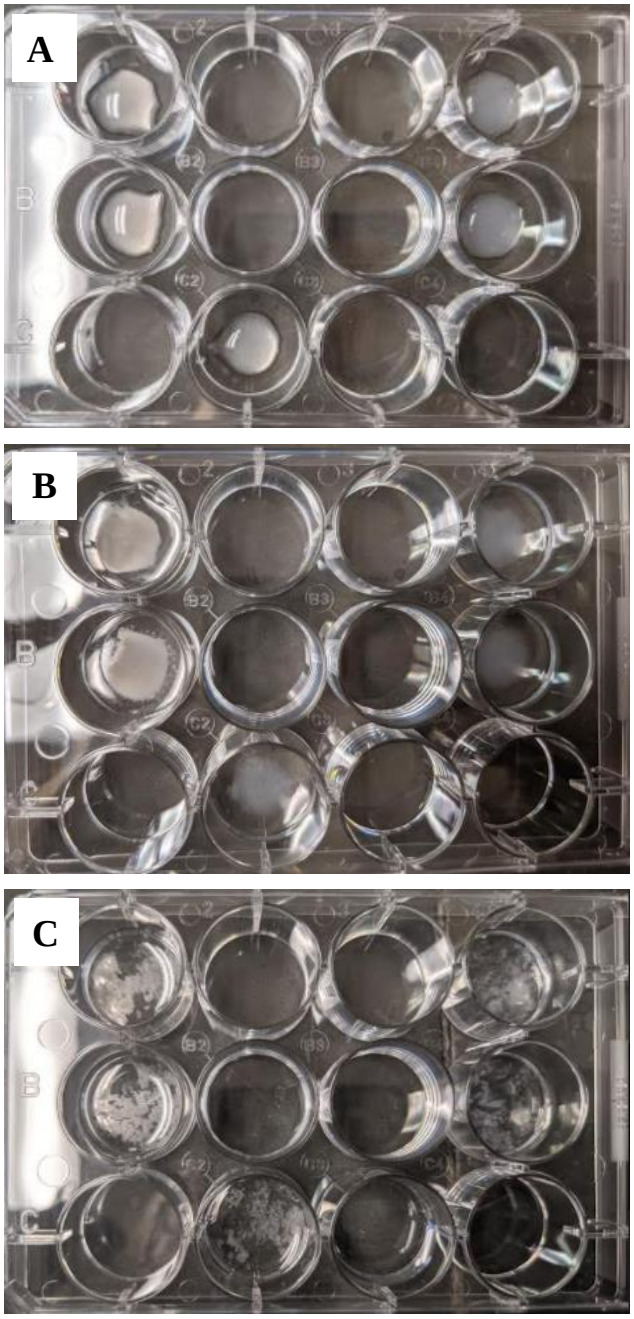


Figure 4-19: Appearances of Gel Forumla 3 and 4 in varying conditions

Hydrogel samples are arranged in plates as follows: left-hand samples are replicates of "Gel Formula 3"; right-hand samples are replicated of Gel Formula 4"; bottom-most sample is a control (non-BSA impregnated) gel sample. Images are representative of gel appearance (A) after extrusion into wells, (B) immediately after addition of extraneous saline to wells, and (C) at the Day 1 timepoint.

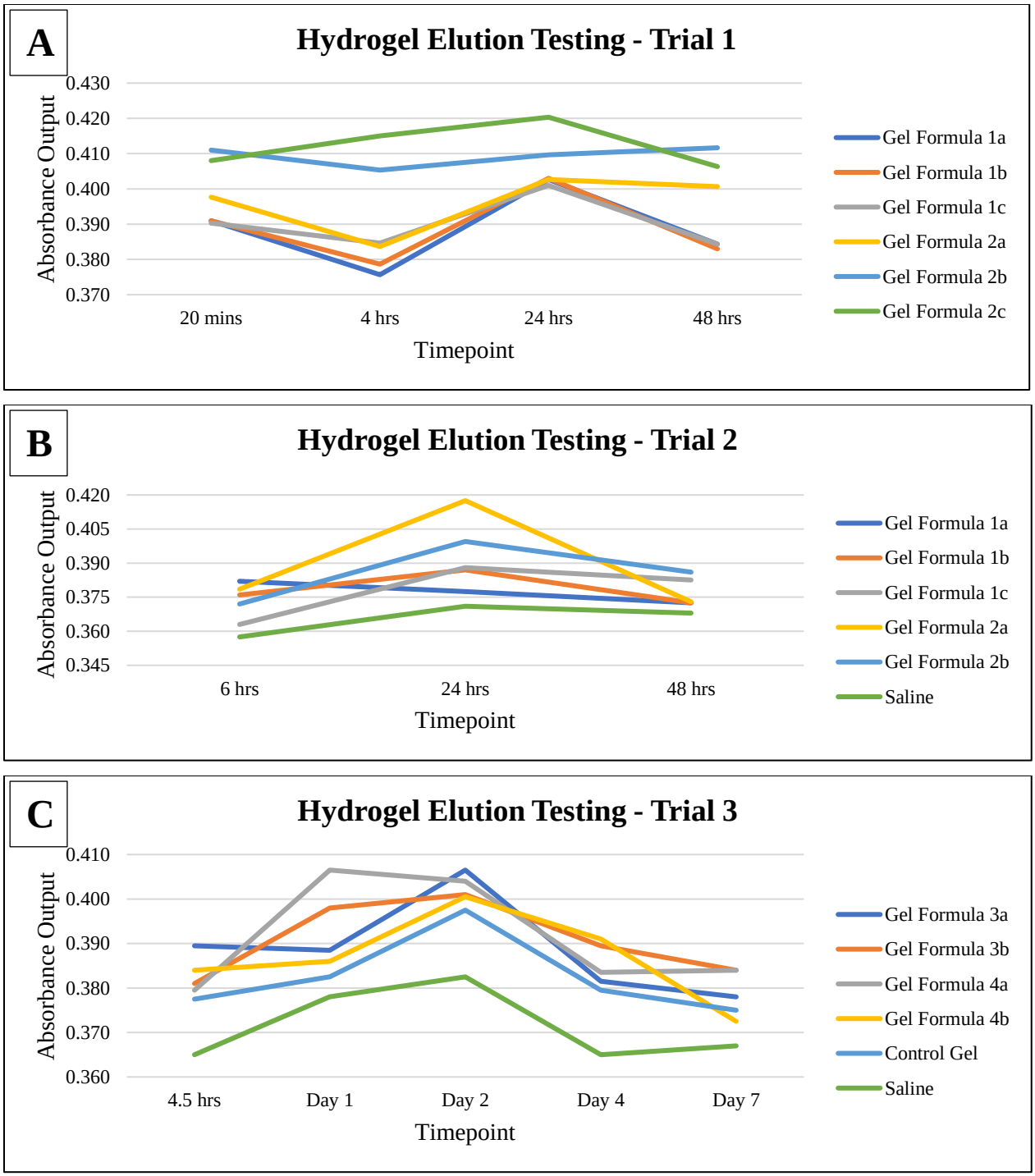


Figure 4-20: Hydrogel elution results for Trials 1-3

Figures represent Bradford's assay absorbance outputs detected over timepoints. Samples with "a", "b", or "c" represent replicates of the same gel formula.

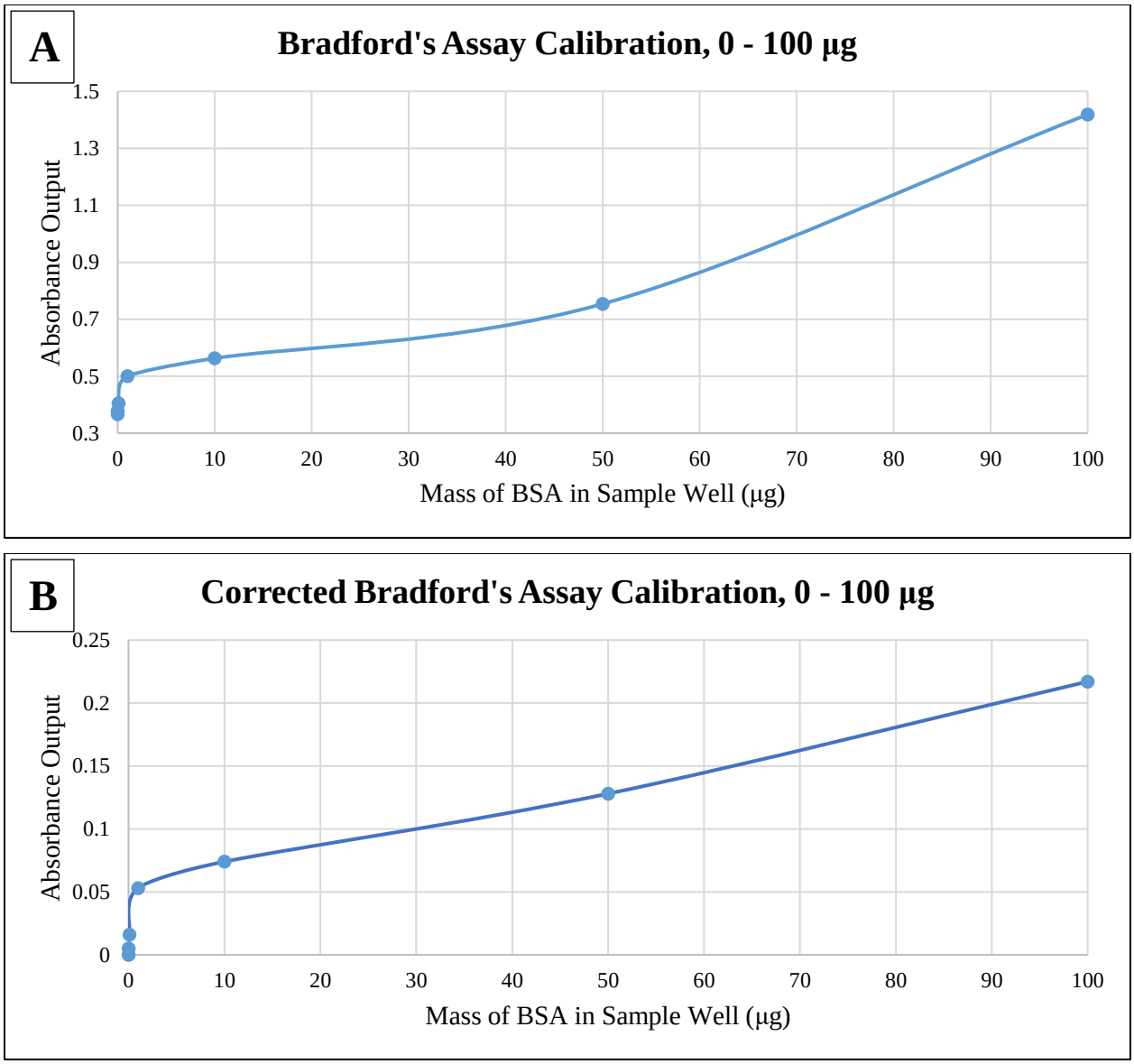


Figure 4-21: Bradford's assay calibration data with higher concentrations of BSA

Another Bradford's assay calibration was performed, but with a greater range BSA (0 to 100 µg). Both raw (A) and corrected (B) absorbances are depicted.

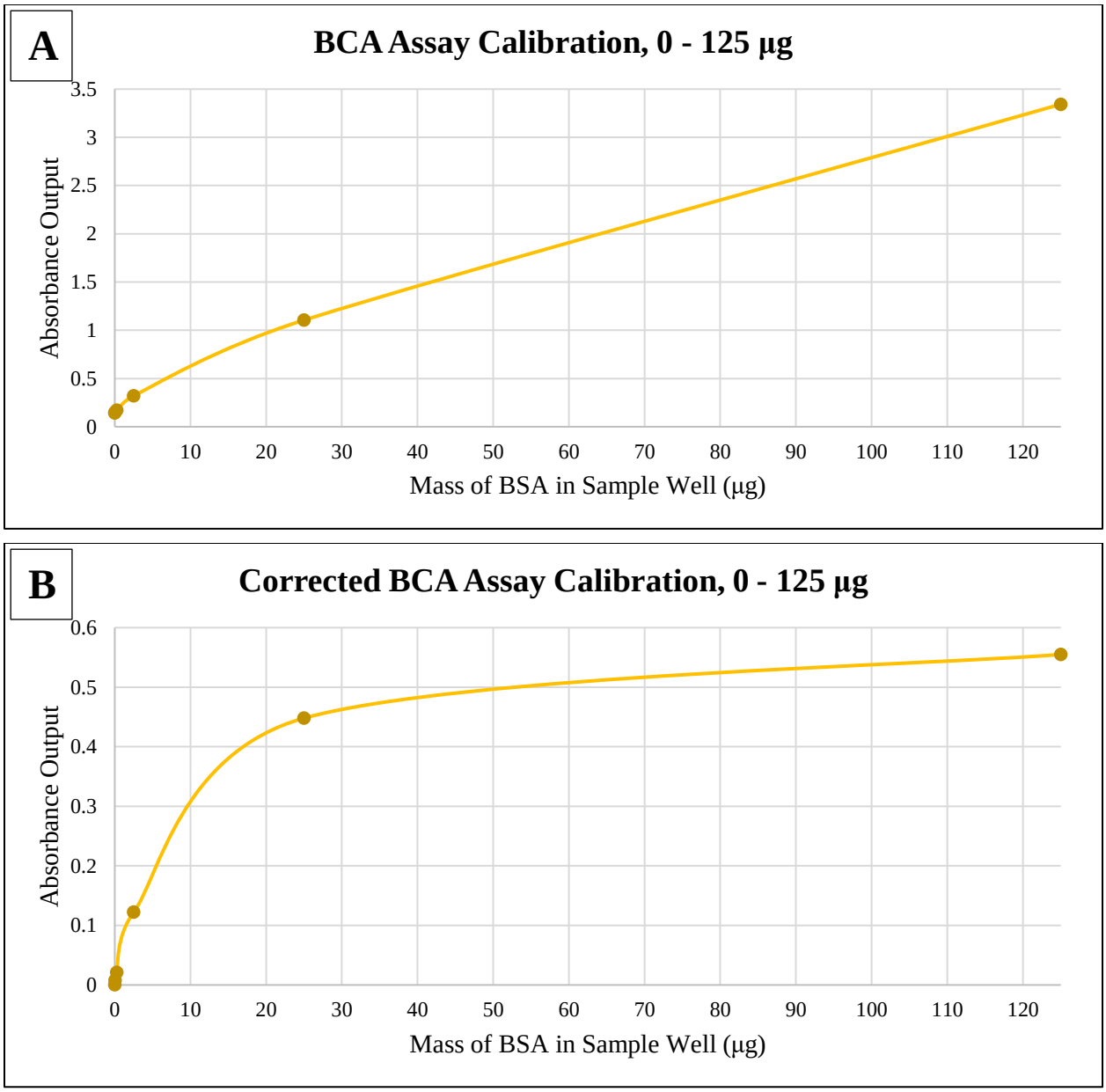


Figure 4-22: BCA assay calibration data

A BCA assay calibration was performed with a range of 0 to 100 µg BSA. Both raw (A) and corrected (B) absorbances are depicted. Absorbance output for 250 µg BSA, though performed, is not depicted as the amount of protein present surpassed the maximum threshold of the absorbance reader.

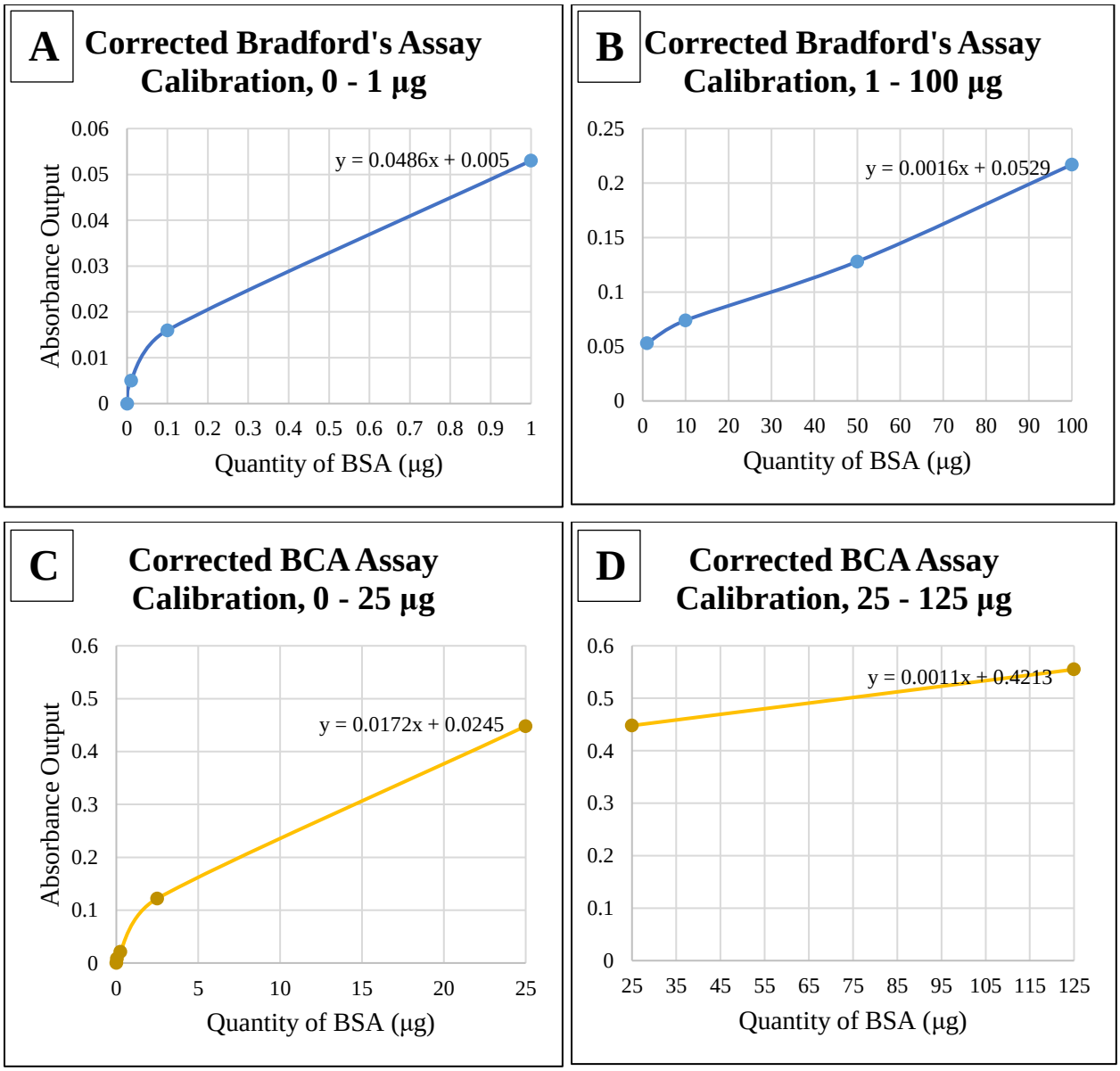


Figure 4-23: Bradford's and BCA assays (corrected) with divided trendlines

As two distinct slopes were represented in each of the calibration curves, separate graphs were generated to permit calculations of the quantity of BSA in samples from the hydrogel experiments. (A) and (B) together represent the complete Bradford's assay curve, and (C) and (D) together represent the BCA assay curve.

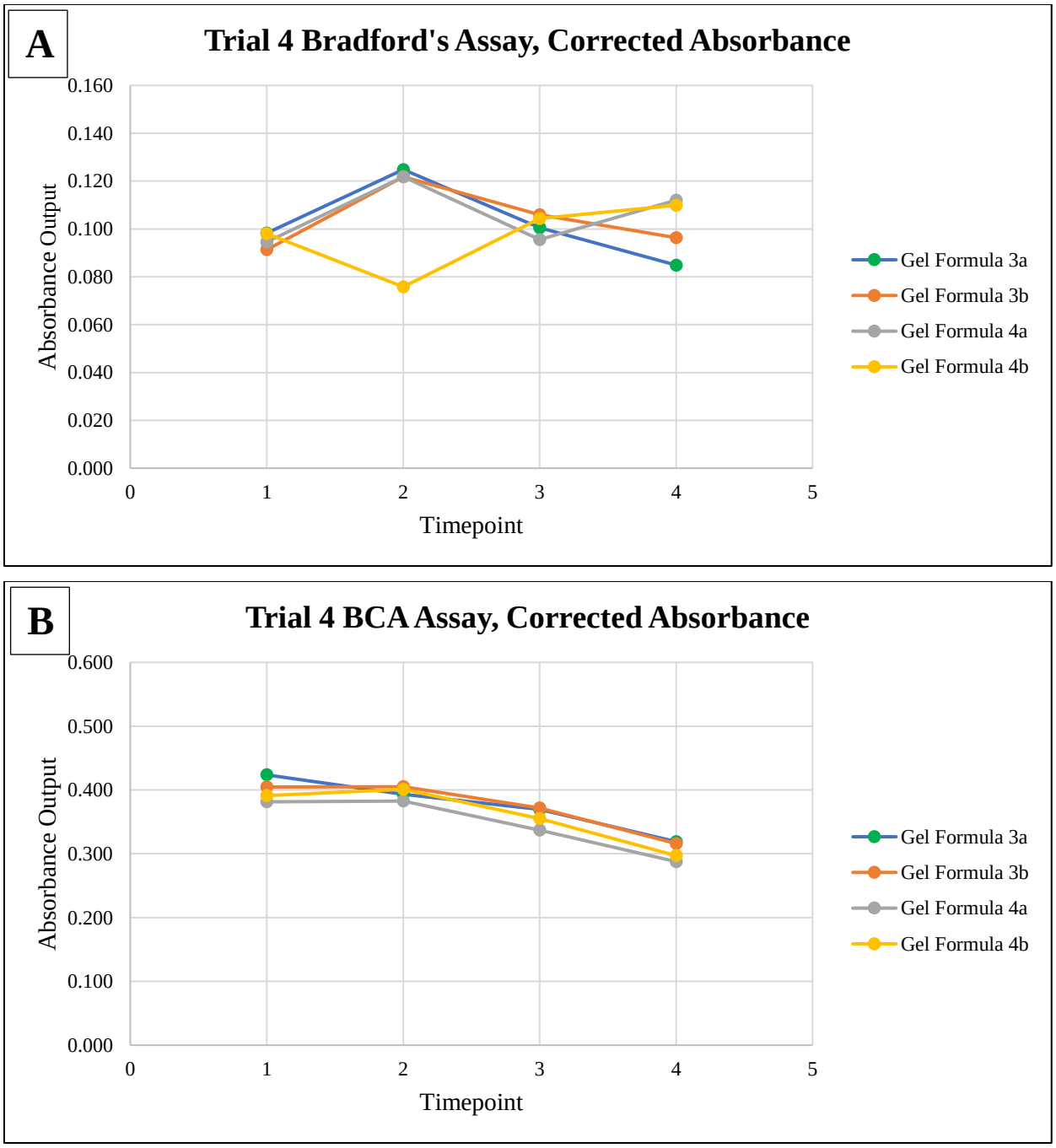


Figure 4-24: Absorbance values for Trial 4 hydrogel samples

Results of Bradford's (A) and BCA (B) assays, both corrected, are depicted for Trial 4 hydrogel samples. "a" and "b" samples represent replicates of the same gel formula. Timepoint 1 = 5 hours; 2 = 1 day; 3 = 2 days; 4 = 4 days. BCA assay trends appear similar between all samples.

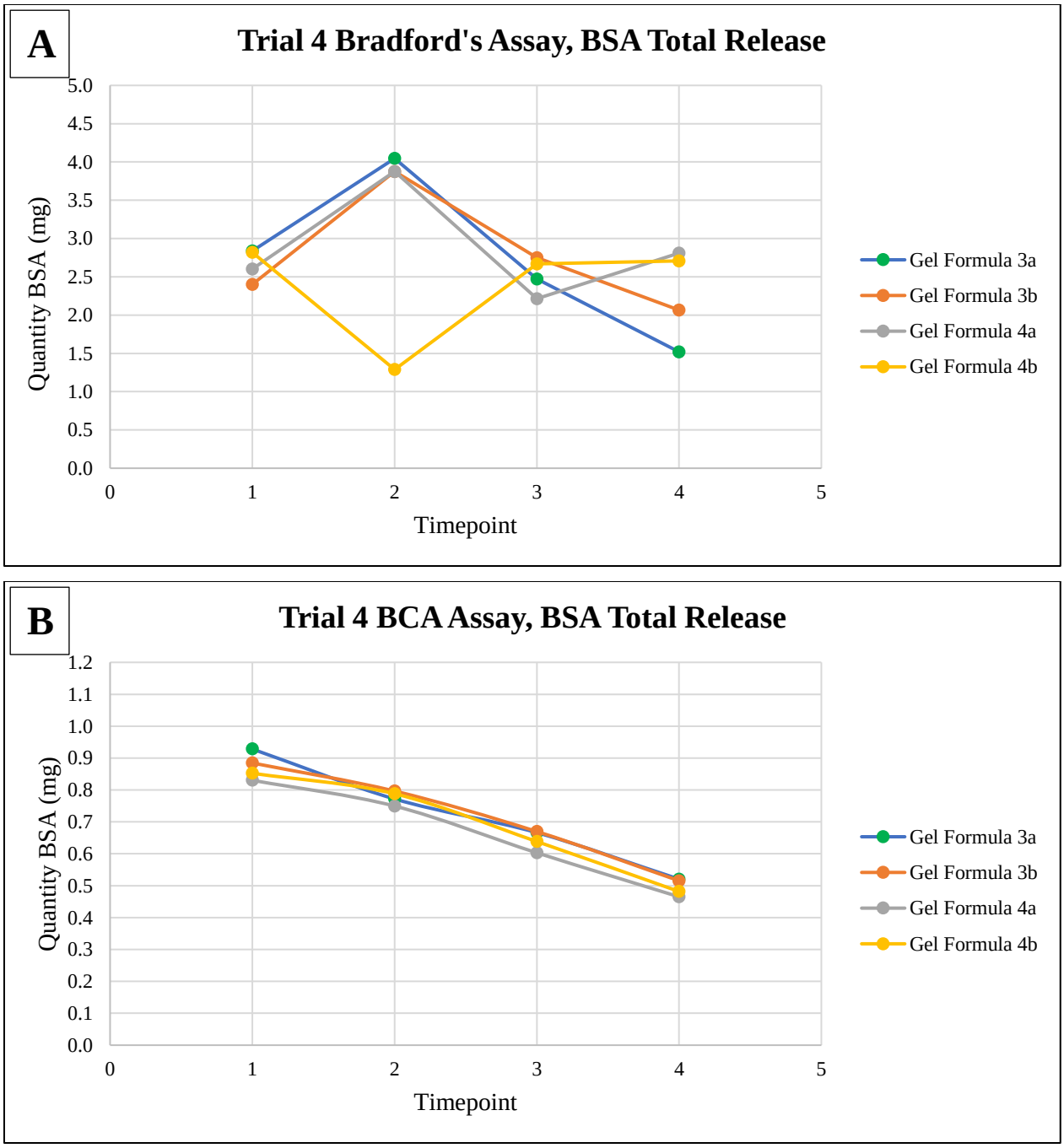


Figure 4-25: Total BSA mass release Trial 4 hydrogel samples

Total BSA release determined from Bradford's (A) and BCA (B) assays are depicted for Trial 4 hydrogel samples. "a" and "b" samples represent replicates of the same gel formula. Timepoint 1 = 5 hours; 2 = 1 day; 3 = 2 days; 4 = 4 days. BCA assay quantities are more sensical in comparison to the loading mass of BSA (2 mg), and it appears that there is a burst release of BSA from the gel.

Vita

Alisha Potter Pedersen, born in April of 1993 in Charlotte, North Carolina, spent the majority of her youth desiring to become a teacher, but after a life-altering event during the summer before her senior year of high school, a new passion for veterinary medicine was ignited. Alisha graduated from the University of North Carolina at Charlotte in May of 2015, earning a Bachelor of Arts in Chemistry and a Bachelor of Science in Psychology. She then enrolled at the University of Tennessee College of Veterinary Medicine, where she developed a special interest in large animal medicine, surgery, and biomedical research. After spending a summer in the COE Summer Research Program under the mentorship of Dr. David Anderson, Alisha enrolled in the Dual DVM-PhD Program, focusing her research largely on regenerative biomaterial applications in large and small mammal models. Alisha graduated with her DVM in May of 2015 and immediately transitioned into completing her PhD in Comparative and Experimental Medicine.

During her time at UTCVM, Alisha has been first author of one publication (Chapter 2 of this document) and co-author of an additional publication. Alisha has presented her research at several college-level symposia, as well as at the National Veterinary Scholars Symposium, held at the National Institutes of Health. Alisha is now preparing for graduation in May 2021 and hopes to pursue a position in academia.

[1] Landreth, G.E., *Classes of Growth Factors Acting in the Nervous System.*, in *Basic Neurochemistry: Molecular, Cellular, and Medical Aspects*, Siegel, G.J., Agranoff, B.W., Uhler, M.D., Albers, R.W., and Fisher, S.K., Editors. 1999, Lippincott-Raven Publishers: Philadelphia.

[2] Huang, E.J. and Reichardt, L.F., *Neurotrophins: Roles in Neuronal Development and Function.* Annual Review of Neuroscience, 2001. **24**(1): p. 677-736.